Tracer and model constraints on the ventilation of the deep Pacific Ocean

Bruno Millet

université
PARIS-SACLAY

Tracer and model constraints on the deep Pacific ventilation

Contraintes apportées par les traceurs et modèles sur la ventilation profonde de l'océan Pacifique

Thèse de doctorat de l'université Paris-Saclay

École doctorale n°129, sciences de l'environnement d'Île-de-France (SEIF)
Spécialité de doctorat: Géosciences
Graduate School : Géosciences, climat, environnement et planètes.
Référent : Université de Versailles-Saint-Quentin-en-Yvelines

Thèse préparée dans l'unité de recherche **LSCE (Université Paris-Saclay, CNRS, CEA, UVSQ)**, sous la direction de **Didier ROCHE**, Directeur de recherche CNRS, la co-direction de **William GRAY**, chercheur CEA et le co-encadrement de **Casimir DE LAVERGNE** chercheur CNRS.

Thèse soutenue à Paris-Saclay, le 26 septembre 2024, par

Bruno MILLET

Composition du jury

Membres du jury avec voix délibérative

Masa KAGEYAMA Directrice de Recherche, CNRS, LSCE	Présidente
David FERREIRA Associate Professor, Meteorology department, University of Reading, UK	Rapporteur & Examinateur
Elaine McDONAGH Research Professor, NORCE, Bergen	Rapporteur & Examinatrice
Juliette MIGNOT Chargée de Recherche, LOCEAN, Paris	Examinatrice

THESE DE DOCTORAT

NNT : 2024UPASJ019

université PARIS-SACLAY

ÉCOLE DOCTORALE
Sciences de l'Environnement d'Île-de-France (SEIF)

Titre: Contraintes apportées par les traceurs et modèles sur la ventilation profonde de l'océan Pacifique
Mots clés: Ventilation de l'océan, Océan Pacifique, Isotopes de l'oxygène

Résumé: L'Océan Pacifique représente environ 50% du volume global des océans, ce qui en fait un acteur essentiel des cycles biogéochimiques globaux et de leur réponse aux perturbations. En particulier, l'Océan Pacifique profond abrite des réservoirs majeurs de carbone et de nutriments, dont la taille et les variations sont largement contrôlées par les transports physiques de traceurs. Dans cette thèse, je cherche à mieux comprendre et contraindre le transport de traceurs dans l'Océan Pacifique profond à travers plusieurs états climatiques. Pour cela, j'ai à la fois généré de nouvelles données et utilisé des observations préexistantes, de traceurs conservatifs, notamment les isotopes de l'oxygène, ainsi que des modèles numériques de circulation océanique. Je montre que le mélange isopycnal exerce un contrôle essentiel sur la ventilation des profondeurs moyennes du Pacifique. Un retour des eaux abyssales vers la surface est identifié dans le Pacifique subarctique moderne. Cette voie de remontée semble avoir diminué pendant le dernier maximum glaciaire, il y a environ 20 000 ans, et le Pacifique Nord profond pourrait avoir été plus fortement stratifié. Cependant, les preuves de changements nécessaires dans le sud du bassin pour expliquer cette stratification profonde restent rares. Les modèles actuels de la circulation générale de l'océan peinent à reproduire les trajectoires des traceurs et les vitesses de ventilation dans le Pacifique Nord moderne déduites des observations. Cependant, ces circuits de traceurs restent insuffisamment contraints et la dynamique sous-jacente est mal comprise. L'analyse des mesures in situ du rapport isotopique de l'oxygène 18 (^{18}O) de l'eau de mer constitue un moyen efficace pour mieux contraindre les origines et les itinéraires des traceurs dans l'océan profond : les observations actuelles de ^{18}O dans les océans Austral, Indien et Pacifique permettent de mieux comprendre ces itinéraires. Je suggère que des mesures supplémentaires de ^{18}O à partir d'échantillons d'eau de mer modernes et de coquilles de calcite dans les carottes de sédiments fourniraient des contraintes précieuses sur les réservoirs et les flux de traceurs actuels et passés dans l'océan profond.

université PARIS-SACLAY

ÉCOLE DOCTORALE
Sciences de l'Environnement d'Île-de-France (SEIF)

Title: Tracer and model constraints on the ventilation of the deep Pacific Ocean
Keywords: Ocean Ventilation, Pacific Ocean, Oxygen isotopes

Abstract: The Pacific Ocean represents about 50% of the global ocean volume, making it an essential player in global biogeochemical cycles and their response to external perturbations. In particular, the deep Pacific Ocean hosts major reservoirs of carbon and nutrients, whose size and variations are largely controlled by physical tracer transports. In this thesis, I aim to better understand and constrain the transport of tracers in the deep Pacific Ocean across climate states. I use historical and generate new observations of conservative tracers, notably oxygen isotopes, combined with numerical models of ocean circulation. I show that isopycnal mixing is an essential control of the ventilation of Pacific mid-depths. A return of abyssal waters to the surface is identified in the modern subarctic Pacific. This upwelling pathway may have been weaker during the Last Glacial Maximum about 20,000 years ago, and the deep North Pacific may have been more strongly layered; however, evidence for the required end member changes in the south of the basin remains sparse. State-of-the-art prognostic models of global ocean circulation struggle to represent observationally inferred tracer pathways and turn-over times in the modern North Pacific. However, these tracer pathways remain insufficiently constrained and the underlying dynamics are poorly understood. Analysis of in-situ measurements of the oxygen isotope ratio of seawater ($\delta^{18}O$) provides an efficient means to better constrain the origins and routes of tracers in the deep ocean: insights on these routes are derived from existing $\delta^{18}O$ observations in the Southern, Indian, and Pacific Oceans. I suggest that additional measurements of $\delta^{18}O$ from modern ocean water samples, and from calcite shells in sediment cores, would provide valuable constraints on present-day and past tracer reservoirs and fluxes in the deep ocean.

REMERCIEMENTS

Je tiens dans un premier temps à remercier mes superviseurs qui m'ont encadré lors de cette thèse. Je salue leur disponibilité, et leur gentillesse. La passion qu'ils ont pour leur métier a grandement contribué à la joie que j'ai eu d'effectuer mes travaux de recherche.

Plus spécialement, je tiens à remercier Didier sans qui cette thèse n'aurait pu être possible. Casimir, partager un bureau avec toi, à défaut d'un thé ou d'un café, était un plaisir, ainsi que les discussions au bobo ou aux arènes. Je tiens à remercier ta motivation sans faille pour répondre à mes nombreuses interrogations. William, ton enthousiasme a été une source d'énergie non négligeable pour moi, et les nombreuses discussions de nos we respectifs une distraction très appréciée. Je tiens à te remercier tout particulièrement pour les opportunités que tu m'as donné pour que j'aille présenter ma recherche à l'international.

Je remercie également Elaine McDonagh et David Ferreira qui ont accepté d'être rapporteurs de ma thèse. Je leur en suis particulièrement reconnaissant, et leur souhaite bon courage. Je tiens à également remercier les examinatrices, Masa Kageyama et Juliette Mignot pour l'honneur qu'elles me font d'évaluer mon travail.

Toutes les personnes avec qui j'ai pu discuter à travers les différentes conférences en Italie, en Norvège, en Autriche, ou en France ont contribuées à la réussite de cette thèse et je leur en suis reconnaissant.

Je tiens à remercier également Elisabeth Michel et Claire Waelbroeck pour avoir suivi mon travail avec un œil intéressé et avisé, ainsi que pour les discussions enrichissantes que nous avons eues. Un remerciement supplémentaire pour Claire qui m'a acceuillie au LOCEAN et qui m'a aidé à réaliser une partie des mesures de ma thèse. Je remercie également James Rae et Kazuyo Tachikawa qui ont accepté de suivre le déroulé de ma thèse. Amy Wagner, pour son acceuil à Sacramento et sa bienveillance à mon égard.

Le LSCE m'a fourni un cadre idéal pour mener à bien cette thèse, et je remercie l'ensemble de l'équipe PALEOCEAN pour son accueil. Hélène, Patricia, Fatima, merci pour votre patience et votre aide qui a été précieuse. Hervé, s'il te plaît ne change rien. Sébastien, perdre au tournoi de volley du LSCE, ce n'est pas

si grave que ça. Gulay, merci infinimment pour la patience que tu as eu pour me présenter les différents petits organismes vivants au fond des océans; et surtout pour ta joie de vivre.

Je salue également les doctorants du LSCE avec qui j'ai pu partager de riches moments, Maureen, Stanley, Eva, Camille, Simon, Joséphine, Emma et bien d'autres. Enfin, certains doctorants extérieurs au labo auront marqué ma mémoire; David, je ne peux qu'être d'accord. Je remercie l'équipe du foot du jeudi et pour citer un grand homme: "Jacques, Anaïs, c'était bien".

Je tiens à remercier Marie et Marine pour tous ces moments partagés. Avec moi, vous trouverez toujours une oreille attentive pour vous plaindre de votre thèse (ou autre).

Un remerciement également pour mes "vrais amis", Nicolas et Julien, qui ont rendu ces 3 années au LSCE phénoménales. Des souvenirs impérissables. Des amitiés précieuses. N'oubliez pas d'y aller mollo.

Un remerciement tout particulier à mes parents, qui m'ont soutenu dans la réalisation de ces travaux. Ils ont su supporter mon envie dans les moments de doute; pour cela et bien d'autres choses je leur suis redevable. A mon frère et mes soeurs pour leur présence et leur joie de vivre.

Finalement, je tiens à remercier les personnes dont j'ai pu partager le quotidien au cours de ces 3 années. La maison d'Arceuil et ses soirées endiablées à tout jour et toute heure. La beberge pour ses riches discussions et joyeuses festivités. Et enfin, celle qui partage mon quotidien depuis maintenant une année, et je l'espère, pour de nombreuses à venir. Claire, ton soutien au travers de cette thèse n'a pas d'égal. Merci.

RÉSUMÉ EN FRANÇAIS

Contexte

Au cours des deux derniers millions d'années, le climat terrestre a alterné entre des périodes glaciaires (froides) et interglaciaires (chaudes). Ces cycles glaciaires-interglaciaires ont été accompagnées par des variations cycliques du dioxyde de carbone (CO_2) atmosphérique. L'origine de ces cycles est débattue, mais dépendrait principalement de la réponse combinée aux changements orbitaux du cycle du carbone, de la cryosphère et de la circulation océanique. Bien que la périodicité de ces cycles soit contrôlée par les forçages orbitaux (Imbrie et al., 1984), l'ampleur de la réponse du système climatique ne peut pas être expliquée par ces seuls forçages, et nécessite des rétroactions au sein de ce dernier pour expliquer les variations de CO_2 et de la température globale.

Le système climatique terrestre est constitué de plusieurs composants : l'atmosphère, l'océan, la cryosphère, les surfaces continentales (végétation et rivières), et la croûte océanique et continentale, qui stockent et échangent le CO_2 sur des échelles de temps très différentes (Sigman and Boyle, 2000). L'unique composant pouvant expliquer les variations de CO_2 atmosphérique au cours des cycles glaciaires-interglaciaires est l'océan profond, en raison de sa taille et de son temps de réponse aux perturbations atmosphérique (Broecker, 1982). Plusieurs mécanismes ont été proposés pour expliquer ces variations de CO_2, notamment des changements dans la circulation océanique (Ferrari et al., 2014; Kwon et al., 2012; Toggweiler et al., 2006), dans l'environnement de la couche de mélange (Abelmann et al., 2015; Stephens and Keeling, 2000), ou encore dans l'inventaire des nutriments (Shoenfelt et al., 2018; Wallmann et al., 2016). Expliquer la magnitude de ces variations ne représente plus une difficulté; le véritable défi n'est pas de trouver des mécanismes supplémentaires pouvant expliquer des changement de CO_2, mais plutôt de mieux contraindre la contribution de chacun de ces mécanismes (Galbraith and Skinner, 2020).

La ventilation océanique est définie comme la combinaison du mélange turbulent et du transport des masses d'eaux dans l'océan. Cet ensemble de phénomènes physique contrôle la distribution des différents traceurs, comme la chaleur et les nutriments, dans l'océan. Comprendre la ventilation océanique est essentiel pour comprendre la réponse future de l'océan à la perturbation induite par la combustion des combustibles fossiles. Etudier et analyser la ventilation océanique à différentes époques permet de mieux comprendre le

fonctionnements de l'océan, et comment celui-ci réagit en réponse aux perturbations. Cette thèse explore la ventilation de l'océan profond, avec un accent particulier sur l'océan Pacifique, sous conditions climatique moderne et glaciaire. Pour cette étude, j'utilise à la fois des données, pré-existantes et de nouvelles, ainsi que des modèles d'océans. Cette thèse s'intéresse également à l'évaluation des modèles numériques d'océan, pour comprendre le niveau de fidélité qu'ont ceux-ci à reproduire la ventilation océanique.

Problématique

Le transport de masse dans l'océan, ou "circulation océanique de retournement", ventile les profondeurs de l'océan par un renouvellement des eaux qui passe par la formation d'eaux denses. Seul deux endroits permettent aux eaux de surface de devenir suffisament denses et de plonger jusqu'au fond de l'océan: aux hautes latitudes de l'Atlantique Nord, appelées les eaux profondes de l'Atlantique Nord (NADW), et aux marges de l'Antarctique, appelées eaux Antarctique de fond (AABW). Ces eaux nouvellement formées se substituent progressivement aux anciennes eaux profondes, permettant au carbone séquestré dans l'océan de remonter vers l'océan supérieur et l'atmosphère. Le Pacifique Nord est éloigné des principales sources de formation des eaux profondes, et contient donc des eaux très anciennes, appauvries en oxygène et enrichies en carbone. Caractériser les mécanismes de la ventilation lente du Pacifique Nord est donc crucial pour comprendre le stockage du carbone dans l'océan.

Aujourd'hui, les eaux du Pacifique se situant sous la thermocline sont ventilées via trois branches de circulation principales (Figure 1). Aux profondeurs intermédiaires, jusqu'à environ 1 km, l'eau antarctique intermédiaire (AAIW) formée dans l'océan Austral domine la ventilation des eaux intermédiaires du Pacifique Sud, tandis que l'eau intermédiaire du Pacifique Nord (NPIW) formée au nord-ouest du bassin domine les profondeurs intermédiaires du Pacifique Nord. À des profondeurs plus importantes, la ventilation repose exclusivement sur les eaux provenant de l'océan Austral, en l'absence de formation d'eaux profondes dans le Pacifique Nord (Warren, 1983). Les moteurs et voies de cette ventilation profonde sont encore débattus (Holzer et al., 2021). Il existe deux visions différentes de la circulation profonde du Pacifique, représentées en Figure 1 : l'une voit les eaux denses antarctiques (AABW) remontant de manière diffuse jusqu'à environ 1,5 km sous l'influence du mélange diapycnal (mélange à travers les surfaces d'isodensité) et du chauffage géothermique avant de retourner vers le sud, transformées en eaux profondes du Pacifique (PDW). L'autre théorie propose que la remontée diffuse est confinée aux profondeurs abyssales où le fond marin est abondant, laissant une couche aux profondeurs moyennes exclue du retournement et faiblement ventilée par diffusion isopycnale (le long des surfaces d'isodensité) et recirculation (de Lavergne et al., 2017).

De multiples preuves indiquent des changements dans la circulation océanique profonde entre le LGM (Dernier Maximum Glaciaire) et l'époque moderne. Notre compréhension actuelle des changements possibles de la circulation océanique profonde pour le LGM par rapport à aujourd'hui sont (1) des eaux NADW moins dense (Curry and Oppo, 2005; Ferrari et al., 2014), (2) une augmentation de la production des eaux intermédiaires du Pacifique Nord (NPIW) (e.g. Keigwin, 1998; Matsumoto et al., 2002; Rae et al., 2020), et (3) un océan plus froid et plus salé, avec une augmentation de la stratification profonde en raison de la salinité plutôt que de la température (Adkins et al., 2002). D'autre part, la cellule de retournement abyssale pourrait avoir une structure largement inchangée, puisque celle-ci est déterminée par la topographie profonde (de Lavergne et al., 2017).

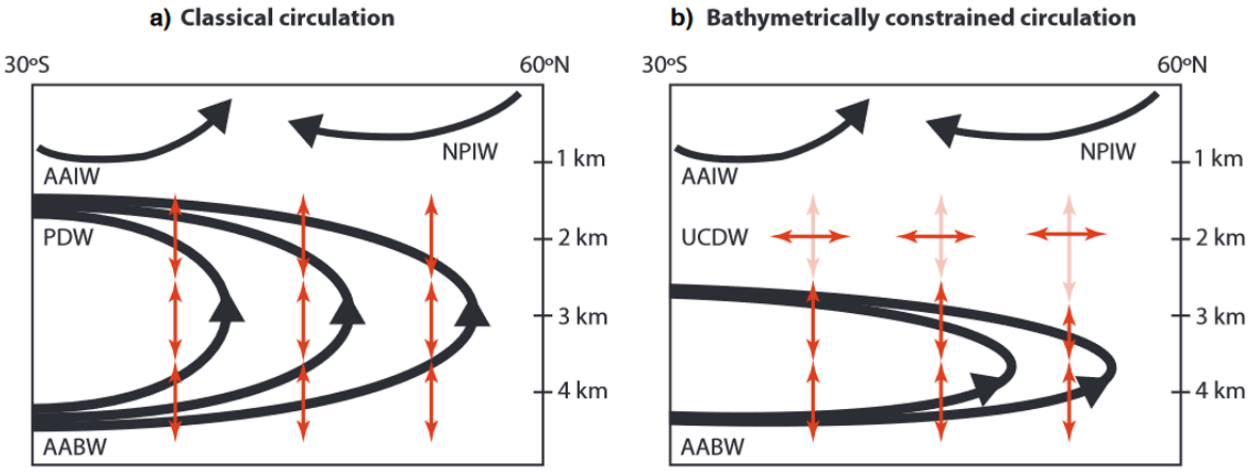

Figure 1: Deux visions distinctes de la circulation profonde actuelle du Pacifique, adaptées de Holzer et al. (2021). La circulation de retournement classique est illustrée en (a), et la circulation contrainte par la bathymétrie en (b). Les courbes noires épaisses représentent les principales branches de la circulation de retournement. Les flèches rouges verticales et horizontales à double tête illustrent respectivement le mélange diapycnal et le mélange isopycnal. Les masses d'eau importantes sont étiquetées : Eau de Fond Antarctique (AABW), Eau Profonde du Pacifique (PDW), Eau Profonde Circumpolaire Supérieure (UCDW), Eau Intermédiaire Antarctique (AAIW) et Eau Intermédiaire du Pacifique Nord (NPIW).

Afin d'apporter des contraintes sur la ventilation océanique, l'utilisation de traceurs conservatifs se révèle particulièrement astucieuse. En effet, ces traceurs ne peuvent être modifiés par la biologie. Ainsi, leurs variations sont directement dues au mélange et transport des différentes masses d'eaux. Les observations de ces traceurs permettent donc de directement contraindre la ventilation océanique. Dans cette thèse nous utiliserons l'abondance realtive de l'isotope ^{18}O de l'oxygène, pour contraindre la ventilation de l'océan moderne et glaciaire. Des mesures de l'abondance relative de cet isotope dans l'eau de mer ($\delta^{18}O_{sw}$) permettent d'apporter des contraintes sur l'océan moderne. Pour l'analyse de la ventilation du dernier maximum glaciaire, des mesures de l'eau de mer ne peuvent être directement effectuées et nous utilisons les coquilles des foraminifères benthiques. Ces organismes vivent au fond des océans et enregistrent des informations sur leur environnement, au moment de la formation de leurs coquille. L'analyse du ratio de l'abondance relative de l'oxygène-18 dans leurs coquilles ($\delta^{18}O_{CaCO_3}$) permet de reconstruire la ventilation océanique passée.

Cette thèse vise à répondre aux questions suivantes:

1. Quels sont les mécanismes responsables de la ventilation profonde du Pacifique, et quelles voies les eaux empruntent-elles ?
2. Que peut-on déduire des mesures des rapport isotopiques de l'oxygène pour la ventilation moderne ($\delta^{18}O_{sw}$) et glaciaire ($\delta^{18}O_{CaCO_3}$) ?
3. Dans quelle mesure la ventilation de l'océan moderne est-elle réaliste dans les modèles numériques d'océans? Que manque t'il actuellement dans les paramétrisations de ces modèles pour représenter avec précision la ventilation de l'océan Pacifique profond ?

Contributions

La réponse à ces questions a mené à la publication d'un article, et à la préparation de deux autres:

- Millet, B., Gray, W.R., de Lavergne, C. et al. Oxygen isotope constraints on the ventilation of the modern and glacial Pacific. Clim Dyn 62, 649–664 (2024). https://doi.org/10.1007/s00382-023-06910-8
- Bruno Millet, Casimir de Lavergne, William R. Gray, Christian Ethé, Gurvan Madec, Mark Holzer, Geoffrey Gebbie, and Didier M. Roche. Global ocean ventilation: a comparison between a general circulation model and data-constrained inverse models. *Journal of Advances in Modeling Earth Systems*.
- Bruno Millet, William R. Gray, Casimir de Lavergne, Claire Waelbroeck et al. The oxygen isotope ratio of seawater in the modern deep ocean: a clear marker of water origin?

Les travaux développés dans cette thèse ont également menés à des collaborations au sein d'autres projets:

- Saurabh Rathore, Casimir de Lavergne, Gurvan Madec, Jean-Baptiste Sallée, Christian Ethé, Antoine Nasser, Bruno Millet, Martin Vancoppenolle. Effects of improved tidal mixing in NEMO one-degree global ocean model (2024). *Journal of Advances in Modeling Earth Systems*.

- Contribution to the LOCEAN-CISE database, which compiles measurements of the oxygen and hydrogen isotope ratios in seawater made at the LOCEAN laboratory.
- Contribution to the upcoming second version of the World Atlas of late Quaternary Foraminiferal Oxygen and Carbon Isotope Ratios (Mulitza et al., 2022).

Réponses à la question 1

La diffusion isopycnale joue un rôle majeur dans la ventilation des profondeurs moyennes de l'océan Pacifique. Dans les plaines abyssales, les eaux AABW se propagent vers le nord avant de remonter après transformation par mélange diapycnal et chauffage géothermique et retournent vers l'océan Austral. Le Chapitre I a mis en évidence une remontée de traceurs abyssaux le long de la topographie dans le Pacifique subarctique. La remontée des eaux profondes semble être le processus dominant pour la ventilation des profondeurs moyennes, au nord de 35°N. Les candidats probables pour expliquer cette remontée de traceurs sont le mélange diapycnal et la remontée causée par le pompage d'Ekman. Aucune réponse claire n'est ressortie de notre étude sur leurs rôles respectif et des travaux futurs sont nécessaires pour approfondir cet aspect.

Dans le Chapitre I, nous avons émis l'hypothèse que l'emplacement du minimum de radiocarbone dans le Pacifique, qui correspond aux eaux les plus anciennes de l'océan mondial, était déterminé par l'influence combinée de (1) la ventilation par diffusion isopycnale depuis le sud, à mi-profondeur, et (2) la ventilation par la remontée des traceurs abyssaux le long de la topographie au nord du Pacifique. Les différentes paramétrisations de mélange utilisées dans NEMO au Chapitre II ont confirmé que la localisation du maximum d'âge dépend à la fois de la diffusion isopycnale et diapycnale. Les eaux de mi-profondeur du Pacifique sont donc ventilées par un équilibre entre diffusion isopycnale (venant du sud) et diapycnale (venant d'eaux plus profondes).

Les distributions modernes des traceurs conservatifs sont quasi-uniformes dans le Pacifique. Ceci s'explique par la faible variabilité de ceux-ci dans le Pacifique Sud. Cependant, le potentiel de la diffusion isopycnale pour établir une forte variabilité de traceurs à mi-profondeur dans le Pacifique est démontré à travers l'utilisation d'un traceur passif. En effet, dans le Chapitre II, le traceur passif représentant les eaux provenant de l'Atlantique Nord, possède un maximum à mi-profondeur, qui persiste au travers du Pacifique. Précisément, ces différences de traceurs pourraient s'être produites au cours du LGM, puisqu'un maximum marqué de $\delta^{18}O_{CaCO_3}$ est observé dans le Pacifique Nord. Les preuves géochimiques glaciaires suggèrent une plus forte stratification des eaux au cours du LGM, avec une moindre connexion entre les abysses et les profondeurs moyennes. Il est intéressant de noter qu'un relativement léger biais de densité dans les eaux provenant de l'Atlantique Nord dans nos simulations NEMO résulte en un océan plus stratifié, et suggère une possible déconnexion entre les cellules de retournement de l'Atlantique et de l'Antarctique. Ce résultat indique le potentiel de la diffusion isopycnale pour contrôler la majeure partie de la ventilation à mi-profondeur dans des états climatiques différents, et notamment le LGM.

Réponses à la question 2

Le rapport isotopique de l'oxygène de l'eau de mer ($\delta^{18}O_{sw}$) présente de fortes différences entre les deux principales masses d'eaux contribuant à la ventilation de l'océan profond : AABW et NADW. La différence dans leur signature isotopique permet de simples reconstructions pour quantifier leurs contributions relatives à la ventilation de l'océan Austral. Un maximum dans le $\delta^{18}O_{sw}$ est observé dans une gamme de densités correspondant aux eaux denses formées dans l'Atlantique Nord tout autour de l'Océan Austral. De plus, je montre qu'un échantillonnage plus systématique dans les bassins indien et pacifique pourrait aider à contraindre le mélange des différentes masses d'eaux dans l'océan Austral et lorsque celles-ci s'écoulent et/ou diffusent dans les autres bassins. Le rôle que ce traceur pourrait jouer pour mesurer la pénétration des eaux de faible densité dans l'océan n'a pas été entièrement exploré, mais pourrait être d'un intérêt majeur. Des campagnes d'échantillonnage ciblées, zonales dans l'océan austral et méridiennes dans le Pacifique et l'océan Indien, pourraient contribuer à préciser les schémas et les mécanismes de ventilation de l'océan.

L'existence d'un gradient de $\delta^{18}O_{CaCO_3}$ entre les deux masses d'eau profonde au LGM reste incertaine. Initialement, le maximum de $\delta^{18}O_{CaCO_3}$ observé à mi-profondeur dans le Pacifique Nord plaidait en faveur d'une différence significative entre les masses d'eau dans le Pacifique Sud. Les reconstitutions des températures de l'eau de fond, à l'aide d'éléments traces, confirment que le signal observé est principalement lié à un changement dans le profil de $\delta^{18}O_{sw}$. Cependant, grâce à une recherche systématique dans différentes bases de données et à l'analyse de carottes de sédiments pertinentes, nous n'obtenons pas de preuves claires d'une diffusion du maximum de $\delta^{18}O_{sw}$ à mi-profondeur au LGM qui aurait finalement entraîné le maximum de $\delta^{18}O_{CaCO_3}$ observé dans le Pacifique Nord.

En outre, l'analyse de carottes de sédiments idéalement choisies montre qu'il n'existe peut-être pas de différences significatives dans le $\delta^{18}O_{CaCO_3}$ glaciaire des deux masses d'eau profonde. Les incertitudes associées aux fractions glaciaires à l'emplacement des carottes de sédiments, en plus des incertitudes expérimentales, d'échantillonnage et d'analyse, limitent de plus cette étude. J'aimerais insister sur le fait que la création de méthodes permettant d'utiliser les nouvelles base de données paléocéanographiques de manière systématique pourrait être le seul moyen de surmonter ces biais inhérents. Dans le Chapitre V, nous utilisons une compilation de carottes de sédiments de l'Atlantique pour montrer que le changement de $\delta^{18}O_{CaCO_3}$ entre l'Holocène et le LGM montre également des informations intéressantes et indique soit un changement dans le gradient de température glaciaire par rapport au présent, soit que la masse d'eau glaciaire NADW était moins profonde qu'aujourd'hui, et centrée à 2 km de profondeur. En outre, le fort signal de $\delta^{18}O_{sw}$ aux profondeurs intermédiaires dans le Pacifique Nord glaciaire plaide en faveur d'une expansion glaciaire des eaux NPIW. Trouver des carottes de sédiments appropriées pour étudier la portée et l'étendue de cette masse d'eau glaciaire pourrait être essentiel pour déduire les changements dans le cycle biogéochimique glaciaire.

Réponses à la question 3

Dans le Chapitre II, j'ai comparé une configuration globale du modèle de circulation océanique NEMO à deux modèles inverses contraints par les données. Cette comparaison a utilisé principalement les volumes ventilées par 5 régions de surface ainsi que les vitesses de ventilation des eaux, à l'équilibre. Ceux-ci partagent plusieurs caractéristiques importantes, mais des différences majeures entre les modèles révèlent également d'importants biais et inconnues :

- Les âges des eaux sont systématiquement plus élevés dans les simulations NEMO que dans les états du modèle inverse. Les paramétrisations de mélange isopycnal et diapycnal les plus récentes donnent un âge maximum dans le Pacifique plus de deux fois supérieur à celui des estimations des modèles inverse. Une sous-estimation généralisée des taux de mélange isopycnal et diapycnal dans l'océan profond est jugée probable.

- Les expériences NEMO présentent une stratification plus forte des colorants numériques que les modèles inverses. Plusieurs facteurs peuvent expliquer cette différence : (i) la surestimation de la diffusion diapycnale par les modèles inverses (ii) la production de NADW dans une plage de densité neutre trop étroite (27,8-27,9 kg m^{-3}) dans NEMO ; et (iii) la sous-estimation du mélange diapycnal à l'intérieur de l'océan dans NEMO.

Dans l'ensemble, les simulations NEMO actuelles sont plus à même de représenter les volumes de ventilation que les vitesses de ventilation. Ces biais liés à l'âge sont préoccupants lorsqu'il s'agit de modéliser la réponse du système terrestre aux changements anthropiques : ils affectent non seulement la réponse à long terme de l'océan, mais aussi l'état de base simulé de la biogéochimie marine, qui dépend étroitement des taux de ventilation de l'océan profond. En d'autres termes, des biais importants dans l'âge affecteront l'étalonnage des modèles biogéochimiques et, par conséquent, la réponse transitoire simulée des écosystèmes marins et du cycle du carbone.

Les températures des 2 km supérieurs sont également mal représentées dans le Pacifique Nord subarctique; ce bias est étudié dans le Chapitre III. Le courant limite de Kuroshio semble être mal représenté. Celui-ci est combiné à un schéma de mélange isopycnal inadéquat qui résulte en ce biais de température. Il en résulte une mauvaise représentation de la densité et de la pénétration des eaux NPIW, qui est essentielle pour le cycle biogéochimique de l'océan Pacifique Nord.

Contents

LIST OF ACRONYMS AND SYMBOLS

AABW	Antarctic Bottom Waters
NADW	North Atlantic Deep Waters
AAIW	Antarctic intermediate Waters
NPIW	North Pacific intermediate Waters
UCDW	Upper-circumpolar Deep Waters
PDW	Pacific Deep Waters
CDW	Circumpolar Deep Waters
OGCM	Ocean General Circulation Model
NEMO	Nucleus for European Modelling of the Ocean
ACC	Antarctic circumpolar Current
$\delta^{18}O_{sw}$	the oxygen-18 isotope ratio of seawater
$\delta^{18}O_{CaCO_3}$	the oxygen-18 isotope ratio in the shells of benthic foraminifera
LGM	Last Glacial Maximum

"Entre l'Australia et la South America, dans l'Océan South Pacific, l'atoll de Pom Pom Galli"

INTRODUCTION

Over the past two million years Earth's climate has cycled through a succession of glacial (cold) and interglacial (warm) periods, accompanied by variations in atmospheric CO_2 of up to 90 ppmv. The reason behind the apparition of these cycles remains debated, but is thought to principally depends on how the carbon cycle, cryosphere, and ocean circulation interact in their response to changes in orbital forcings (Paillard, 2015). While the periodicity of these cycles is controlled by orbital forcings (Imbrie et al., 1984), the magnitude of the Earth's climate system response (or global temperature change) cannot be explained by orbital forcings alone (which only affect the season and latitude of incoming solar radiation) (Brook and Buizert, 2018). As such, feedbacks within the climate system are required to explain the CO_2 variations (Sigman and Boyle, 2000) and global temperature changes. Certain feedbacks, such as ice-albedo or water vapor, are well understood. However, the deep-ocean carbon cycle processes thought to underpin the glacial-interglacial variations in atmospheric CO_2 are much more poorly constrained. These variations present a challenge to our understanding of the climate as a system. Increasing our knowledge of the different feedback mechanisms operating within the climate system is crucial to better understand both past and future climates.

The Earth's climate system consists of several components: the atmosphere, the ocean, the cryosphere, continental surfaces (vegetation and rivers), and the oceanic and continental crust, that store and exchange CO_2 between one another over very different timescales (Sigman and Boyle, 2000). The only viable candidate to explain the associated atmospheric CO_2 changes over glacial-interglacial cycles is the deep ocean, because of its reservoir size and response time (Broecker, 1982). Many mechanisms have been proposed to explain these CO_2 variations, among which changes in ocean circulation (Ferrari et al., 2014; Kwon et al., 2012; Toggweiler et al., 2006), changes in the mixed-layer environment (Abelmann et al., 2015; Stephens and Keeling, 2000), or even changes in the nutrient inventory processes (Shoenfelt et al., 2018; Wallmann et al., 2016). The real challenge now is not to find additional mechanisms that could explain a CO_2 change but rather understand the contribution arising from each mechanism (Galbraith and Skinner, 2020).

The role of the ocean in regulating atmospheric CO_2 starts at its interface with the atmosphere: the surface ocean. Here it either takes up or releases CO_2 to the atmosphere, depending on the difference in the CO_2 partial pressure between the surface ocean and atmosphere. The eventual drawdown of atmospheric CO_2 during glacial periods is made possible by the existence of the "biological pump" which exports CO_2 from the surface ocean to the deep ocean and sediment interface (Knox and McElroy, 1984). It consists of different marine organisms that incorporate nutrients such as CO_2, nitrate, and phosphate into organic matter. Some of this organic matter is consumed by the marine food chain, while some, following death or excretion, sink into the deep ocean and sea bed in particulate form. This process ultimately removes CO_2 from the surface ocean and consequently, from the atmosphere.

Most of the CO_2 exported from the surface ocean is not buried in the sediments, and is instead converted back into its inorganic constituents by other marine organisms (Guidi et al., 2015). This process, referred to as remineralization, slowly loads deep waters with inorganic carbon as they circulate through the deep ocean. Those waters eventually reach the surface, charged with 'remineralized' nutrients, which leads to CO_2 outgassing. The upwelling of those waters to the surface is mainly driven by the winds in the tropics and in the Southern Ocean; as part of a larger dynamic, oceanic circulation.

Global ocean circulation, dominated in its vertical dimension by the Meridional Overturning Circulation (MOC), is a complex system of currents that intertwine through all of the world's basins (Talley, 2013).

In order to describe its structure, the oceanographic community has often defined different 'water masses' that represent bodies of water with coherent salinity, temperature and other biochemical properties. A water mass inherits its properties directly from the area where it forms (via heat and freshwater exchanges), usually near the surface. Those newly formed waters flow in the ocean and progressively lose their core properties under the influence of turbulent mixing. The distributions of tracers in the ocean are shaped by both large-scale currents and turbulent mixing (Holzer and Primeau, 2006; Naveira Garabato et al., 2017); the combination of those two tracer transport processes is referred here-on as ocean ventilation.

The difficulty associated to direct observations of large-scale currents and turbulent mixing led oceanographers to mainly rely on tracer distributions to constrain the contribution of different water masses to the ventilation of the ocean. However, describing ocean ventilation from a single tracer distribution is hazardous and can lead to different conclusions (e.g. use of $\delta^{13}C$ to infer glacial circulation, Curry and Oppo, 2005; Gebbie, 2014; Kwon et al., 2012). In this exercise, the use of tracers that are only altered by ocean circulation and turbulent mixing, referred to as conservative tracers, proves particularly judicious.

In this thesis, I will use the oxygen-18 isotopic abundance ratio of seawater, which is conservative, to constrain modern ocean ventilation. Interestingly, this tracer is incorporated in the shells of calcifying ocean organisms that eventually deposit on the seafloor in sediments. As such, analysis of these organisms may in turn help us constrain ocean ventilation in the past.

The Last Glacial Maximum (LGM) corresponds to the last period of glaciation marked by a relatively stable climate which lasted from 23,000 to 19,000 years ago. The global average surface air temperature was on the order of 5°C colder than the pre-industrial equivalent (Annan et al., 2022; Bereiter et al., 2018). It is probably the most studied past period for ocean ventilation; due to its relative temporal proximity, we have an abundance of proxy data. Uncertainties associated to reconstruction of the climate state are relatively low, and multiple community efforts have been put into running and assessing climate models under LGM forcings (e.g. Kageyama et al., 2021). Yet representing ocean ventilation during the LGM has revealed itself to be harder than first anticipated, as models and observations give different answers on the structure of the ocean circulation (Kageyama et al., 2021; Muglia and Schmittner, 2015). Efforts have been made to reconcile proxies and ocean models (Gebbie, 2014; Kwon et al., 2012), but our inability to convincingly represent ocean ventilation for the Last Glacial Maximum (the most recent period with a stable climate state very different to today) gives us a sense of the uncertainty surrounding our understanding of ocean ventilation.

Correctly representing ocean ventilation in climate models is essential because our knowledge of the Earth's response to anthropogenic forcing is largely derived from climate models. Climate models are divided in different sub-models representing the different media of the climate system: ice sheets, atmosphere, land, and ocean (together with sea ice). Those sub-models are coupled and interact with one another, resulting in costly simulations. Fortunately, as they can be run separately, the study of the ocean ventilation under constant forcing can be made without running those comprehensive simulations, using only the dynamic part of the ocean model. Indeed, the representation of the ocean is often separated in two, one responsible for the biology, and another one modelling the physics of the ocean, which is called Ocean General Circulation Model (OGCM). Finding adequate parameterizations to correctly model the different processes impacting ocean ventilation in OGCMs is an enduring challenge (McWilliams, 1996). Yet assessment of an OGCM's ability to correctly represent ocean ventilation is seldom made, despite being key to model correct tracer distributions in the ocean. The method of modelling ocean dynamics to obtain tracer distributions can

be reversed to start from tracer distributions and deduce ocean dynamics. Models that use the latter are called inverse models and will be used in this thesis to assess the accuracy of OGCMs in representing ocean ventilation.

The deep Pacific Ocean is often thought as the terminus of global ocean ventilation, because it is located the furthest away from the various deep-water sources, and is home to the oldest waters in the world (Key et al., 2004). The MOC in this basin is relatively weak, particularly at mid-depths (1 to 3 km below the surface) where most of the ventilation occurs via diffusion (Holzer et al., 2021). The deep ventilation of the Pacific has received little attention compared to its Atlantic counterpart, both in the modern and under past climate states. The main reasons for this likely include the absence of deepwater formation at high-latitudes in the north of the basin today (Ferreira et al., 2018; Warren, 1983), and the poor preservation of calcifying organisms in the Pacific (Broecker, 1982), which makes past paleo-tracer reconstruction more difficult. Yet the Pacific represents about 50% of the global ocean volume and understanding how it is ventilated both at present and in the past, is key to understanding how carbon is cycled through the ocean, and how this may have varied over glacial-interglacial cycles.

This thesis investigates deep ocean ventilation, with a special focus on the Pacific Ocean, in both modern and glacial states, using both data and models. Figure 1 offers a general overview of the thesis structure and motivation. In the following pages of introduction I will explain the key concepts underpinning the PhD work, and expose the questions I am trying to address.

In Chapter I, we use tracer distributions of the modern and glacial Pacific Ocean to constrain its ventilation. We find that in both modern and glacial states the mid-depths of the Pacific are largely ventilated by diffusion from the south. Additionally, we find a return path for nutrients in the modern subarctic Pacific that may have reduced during the LGM.

In Chapter II, the comparison between an OGCM and two inverse models leads to estimates of ventilation volumes, pathways, and rates from the surface to the deep ocean. Mixing parameterizations and their influence for the ventilation of the Pacific as simulated by an OGCM are also discussed. We find that the OGCM systematically underestimates ventilation rates in the deep North Pacific, perhaps due to misrepresentation of near-boundary dynamics in the subarctic Pacific.

We directly investigate this in Chapter III as a special focus is made to diagnose the origin of the temperature bias in the subarctic Pacific in our OGCM simulations.

Chapter IV uses seawater oxygen isotope data, that we both compiled and generated, to show the potential of this proxy to constrain the modern ocean circulation. We also propose a new product that should correctly represent the structure of seawater oxygen isotopes in the deep ocean.

In the same vein, Chapter V investigates the potential of the isotopic ratio of benthic foraminifera shells in reconstructing past ocean ventilation. We show that although being hard to interpret, this proxy can give constraints on ocean ventilation, and could provide additional important information if treated in a systematic way.

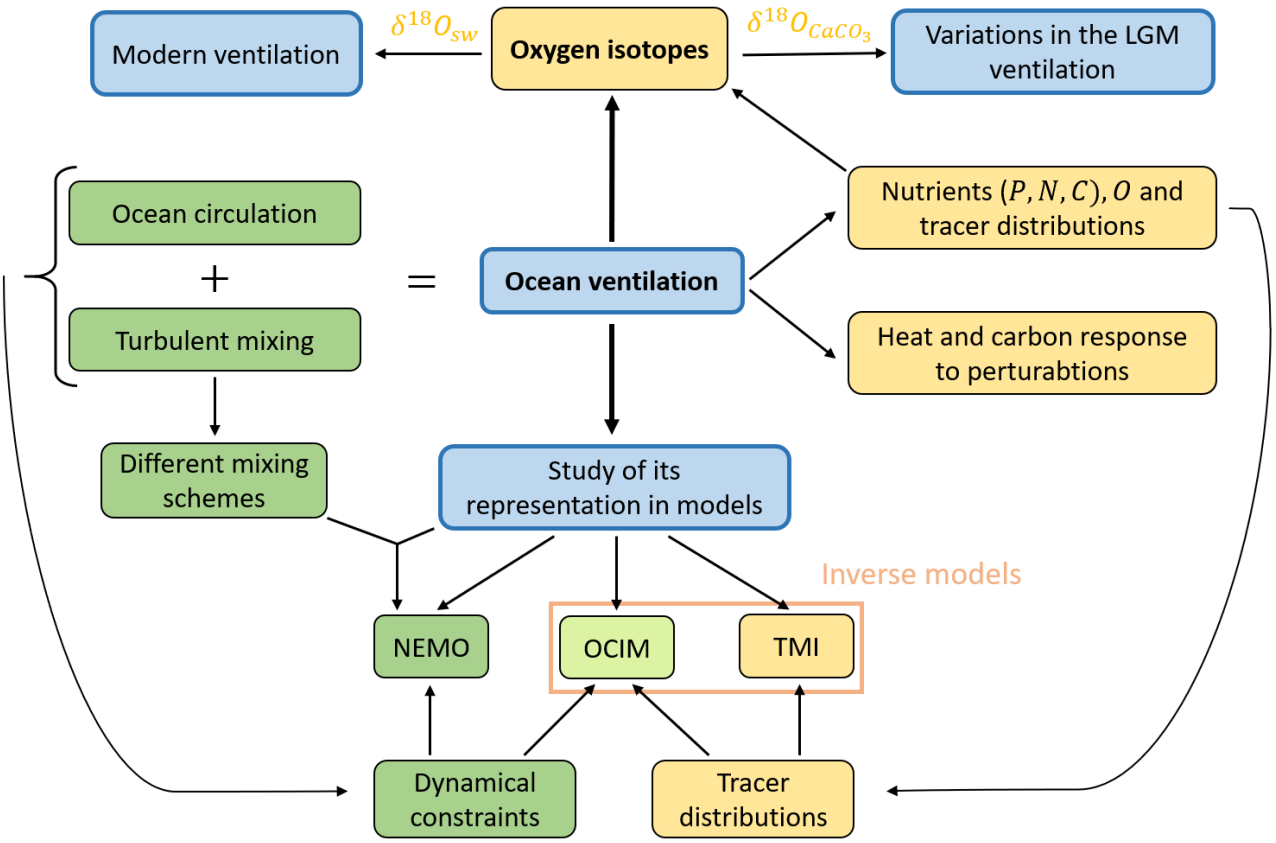

Figure 1: Diagram showing the main aspects of the thesis: at the center of this thesis is the study of the ocean ventilation. The key points studied in this thesis are represented by blue rectangles. Green rectangles indicate a relation to dynamics, and yellow rectangles indicate a relation to tracers. The Nucleus for European Modelling of the Ocean (NEMO) is the OGCM that we will employ in the thesis. The Ocean Circulation Inverse Model (OCIM) has a light green rectangle, because it incorporates both dynamical and tracer constraints. The Total Matrix Intercomparison (TMI) inverse model only incorporates tracer constraints.

1 . Ocean Ventilation

Ocean ventilation sets the tracer distributions within its interior. It is driven by currents, also referred to as 'circulation' or 'advection', and by turbulent mixing, also referred to as 'diffusion'. Mixing aims at erasing tracers gradients, and occurs without any net mass transport. After, I first describe the recent evolution of our knowledge regarding circulation, before addressing the impact of turbulent mixing on ocean ventilation, with a focus on the Pacific.

1.1 . The Meridional Overturning Circulation (MOC)

Our view on deep ocean circulation has greatly varied across time. The "great ocean conveyor" was first illustrated by Wallace Broecker (1987), who originally designed it as a simplified version for a non-oceanographic community (Figure 2). It depicts the formation of North Atlantic Deep Waters (NADW) as the central point of the oceanic circulation, with a return path by upwelling in the Indian and Pacific Oceans; it shows how the different basins are intertwined. The influence of the dense waters formed near Antarctica, called Antarctic Bottom Water (AABW), was also known despite its absence in the schematic. Mixing along the Southern Ocean of NADW and AABW was highlighted using the preformed phosphate tracer (Broecker et al., 1985). At this point, the great ocean conveyor was also referred to as thermohaline circulation, because buoyancy fluxes (temperature and salinity gain or loss) were thought to be the primary driver of this circulation. Since then, it has been established that surface buoyancy fluxes are not the sole driver of the thermohaline circulation: wind stress forcing and tidal forces play essential roles (Kuhlbrodt et al., 2007; Munk and Wunsch, 1998).

Oceanographers have often resorted to defining different water masses to characterize ocean circulation. A water mass represents a body of water with coherent salinity, temperature and other biochemical properties. Water masses are often defined by a neutral density (γ) range, and a formation region. Neutral density

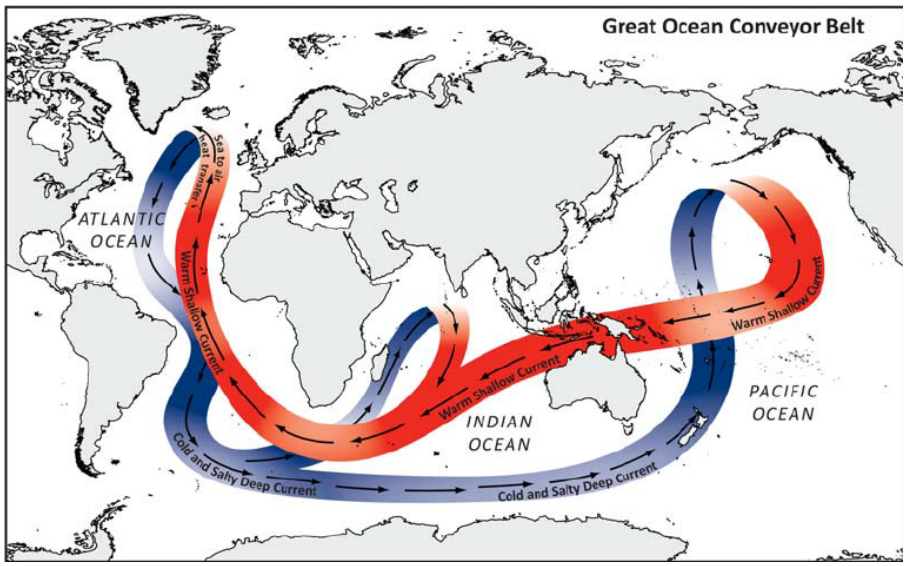

Figure 2: The "Great Ocean Conveyor", as proposed by Broecker, 1987.

is a globally consistent measure of density in the ocean, with compressibility effects removed (Jackett and McDougall, 1997). Water masses tend to follow isopycnals (surfaces of constant neutral density) as they journey away from their formation sites; their signature in tracers can extend over thousands of kilometers from the formation site. Nonetheless, during its journey the core properties of a water mass gradually erode, under the action of turbulent mixing with other water masses. We will first present the key water masses influencing the deep Pacific, before discussing the drivers of the MOC.

1.2 . Water Masses

1.2.1 . Relevant water masses for the ventilation of the Pacific

In winter at high-latitudes, lack of insolation and cold atmospheric temperatures contribute to form dense water. In two main regions, waters become dense enough to sink to the seafloor and spread across the blue planet: in the North Atlantic, and along the Antarctic margin. The two thus-formed water masses, NADW and AABW, fill most of the deep ocean, but have different hydrographic properties.

Tropical surface waters flow northward in the Atlantic Ocean and undergo substantial evaporation along their path. The evaporation raises their salinity and in combination with winter-time cooling at high latitudes they become dense enough to sink. Two locations host the formation of deep waters in the North Atlantic: the Labrador Sea where the lighter part of the NADW forms through open ocean convection, and the Greenland and Norwegian Seas, where denser NADW forms (Lozier et al., 2019; Petit et al., 2020). These denser waters overflow the ridges connecting Greenland, Iceland and Scotland to fill the abyss of the North Atlantic basin (Dickson and Brown, 1994). These two water masses constitute NADW and span the neutral density range $27.8 \leq \gamma \leq 28.1$.

In the Southern Hemisphere, AABW fills most of the abyss. AABW is the densest global-scale water mass, and is both fresher and colder than NADW. AABW originates at four different sites on the Antarctic continental shelf: in the Weddell Sea, the Ross Sea, near the Adélie Coast and near Pridz Bay (Silvano et al., 2023). A similar key formation mechanism is observed in those regions: intense sea ice formation at the coast which elevates the seawater salinity through brine rejection, creating dense shelf water. Interactions with floating glaciers within sub-ice-shelf cavities can further cool and freshen dense shelf waters. The dense waters then cascade down the continental slope and mix with nearby warmer waters. AABW is thus a mixture of high-salinity shelf waters, ice-shelf waters, and warmer circumpolar deep waters. In the Southern Ocean, AABW is often defined as waters with neutral density $\gamma > 28.27$. On a global scale, AABW is often taken as deep waters colder than 0°C.

AABW is not the only water mass formed in the Southern Ocean: within 60-40°S intermediate-density water masses are formed: Antarctic Intermediate Water (AAIW) and Subantarctic Mode Water (SAMW), with an approximate neutral density range of $27.2 \leq \gamma \leq 27.5$. These cool subantarctic water masses mainly ventilate the depth range from 0.5 to 1.5 km, but their influence may propagate deeper. Indeed, the underlying mid-depth waters, known as Upper Circumpolar Deep Water in the Southern Ocean, Indian Deep Water in the Indian Ocean and Pacific Deep Water in the Pacific, do not fall on the NADW-AABW mixing line in temperature-salinity space (Worthington, 1981), implicating the influence of intermediate waters such as AAIW and SAMW.

Another relevant intermediate water mass for the Pacific ventilation is the one forming at mid to high latitudes in the North Pacific, called North Pacific Intermediate Water (NPIW). This water mass is defined as the salinity minimum in the North Pacific at depths of 300-700 m, with a density range of $26.7 \leq \gamma \leq 26.9$

(Talley, 1993). NPIW forms at the boundary between the Oyashio and Kuroshio currents where water coming from the subtropical gyre mix with waters ventilated in the Okhotsk Sea. It has ultimate surface origins beneath sea ice in the Okhotsk Sea (Kitani, 1973) and it is influenced by vertical diffusion in the western subarctic gyre (Talley, 1988). Unlike the North Atlantic, no deep waters are formed in the North Pacific because the balance between evaporation and precipitation does not allow surface waters to become salty enough, such that even if brought to freezing point, surface waters of the subpolar gyre would remain too fresh and light to sink to the deep ocean (Ferreira et al., 2018; Warren, 1983).

1.2.2 . Fractions and end-members

During this thesis, I will often resort to a simple representation of ventilation in the ocean: we assume that water at a given place is a mixture of a few discrete water masses called end-members. The contribution of each end-member i to a local water volume is quantified by its local fraction f_i. By definition, $\sum_i f_i = 1$ at every location. Each end-member has a set of tracer values. If these tracers are conservative, tracer values X can be reconstructed at any location using the following equation:

$$X = \sum_i f_i * X_i \tag{1}$$

where X_i represents the tracer values of the end-members.

1.3 . Drivers of ocean ventilation

1.3.1 . Wind driven advection in the ocean

At this point, one can wonder what governs the ocean circulation? Talley (2013) gives a good summary of our representation of oceanic deep circulation. She states that both wind-driven upwelling in the Southern Ocean and diapycnal mixing in the Indian and Pacific basins are key to explain the modern circulation. By estimating the ocean heat budget, Talley (2013) infers that most of the ocean cooling leading to NADW and AABW formation is compensated by deep diffusive heating in the Indian and Pacific Oceans.

The upper ocean circulation is mainly driven by the winds (Munk, 1950). In the upper layer of the ocean, wind stress (force exerted by the wind on the ocean surface) causes water to move at an angle to the direction of the wind. Due to the Coriolis effect, the net movement of water averaged over the Ekman layer is 90° to the right of the wind direction in the Northern Hemisphere and 90° to the left in the Southern Hemisphere; this net movement is called Ekman transport. The wind stress patterns over the ocean surface can be summarized as:

- Trade winds that blow from east to west between the equator and approximately 30 degrees latitude in both hemispheres.
- Westerlies which prevail between approximately 30 and 60 degrees latitude in both hemispheres, blowing from west to east.
- Polar Easterlies that are blowing, near the poles from east to west.

Those wind stress patterns combined with the induced Ekman transports largely control gyre circulations, which consist of subtropical gyres in the mid-latitudes and subpolar gyres in the high-latitudes of both hemispheres.

Gyre circulations also exist in some deep ocean basins and can be influenced by surface wind stress. The strongest direct impact of wind stress on deep ocean circulation takes place in the Southern Ocean (Marshall and Speer, 2012). First, the westerlies blowing over the Southern Ocean (between 40 and 60°S) are an essential driver of the Antarctic Circumpolar Current (ACC) (Munday et al., 2011). Additionally, the westerlies tend to displace surface waters toward the north, which results in a divergence at southern high latitudes and consequent upwelling of deep waters (Toggweiler and Samuels, 1995). Winds are thus a primary cause of advection in the deep ocean, and variations in the winds have often been invoked to explain changes of the MOC in the past (Gray et al., 2023; Gray et al., 2020; Toggweiler et al., 2006). However, surface buoyancy forcing and mixing in the ocean interior also play important roles in deep ocean circulation and ventilation (de Lavergne et al., 2022).

1.3.2 . Mixing

Mixing in the ocean interior acts to erase tracer variance that is generated by boundary fluxes (Zika et al., 2015). Mixing (or ocean turbulence) can be divided into two main regimes: geostrophic turbulence and small-scale three-dimensional turbulence. Geostrophic turbulence consists of mesoscale eddies which are circular or spiral movements of water in the ocean with a typical diameter of 10-100 km. They are formed by baroclinic instability of the large-scale flow environment (Charney, 1947; McWilliams and Chow, 1981), typically when a current flows past an obstacle or interacts with other currents. This turbulence contributes ultimately to reduce large-scale tracer variance along isopycnals (McDougall et al., 2014), and is thus considered to drive isopycnal mixing. By contrast, small-scale turbulence is isotropic and therefore causes isotropic mixing. Nonetheless, because mixing rates induced by small-scale turbulence are typically seven orders of magnitude lower than isopycnal mixing rates, small-scale turbulence is considered to drive diapycnal mixing, i.e., mixing across isopycnals (McDougall et al., 2014). In the ocean interior diapycnal mixing is mainly sustained by the breaking of internal waves (de Lavergne et al., 2020). Diapycnal mixing is strongest near the ocean boundaries, within the surface and bottom boundary layers.

Mixing affects the ventilation of the ocean in a variety of ways. Firstly, it gradually erodes water masses as they move away from their formation region. For example, AABW is already a mixture of waters originating from around Antarctica and waters coming from the ACC, even before it flows north in the major ocean basins (Orsi et al., 1999). Bottom waters further transform in the Atlantic, Pacific and Indian basins as they are mixed with other water masses and made lighter. Secondly, isopycnal mixing is important to complement or counteract tracer transport by the large-scale ocean currents (Naveira Garabato et al., 2017), and notably for the ventilation of waters that are excluded from these currents such as in the mid-depth Pacific (Holzer et al., 2021). Diapycnal mixing in the deep ocean is bottom-intensified, and thus has a paramount role for tracer transports near topography. Less than 10% of the World Ocean seafloor area lies between 0.5 and 2.5 km depth, reducing the role of diapycnal mixing in establishing ventilation there (de Lavergne et al., 2017).

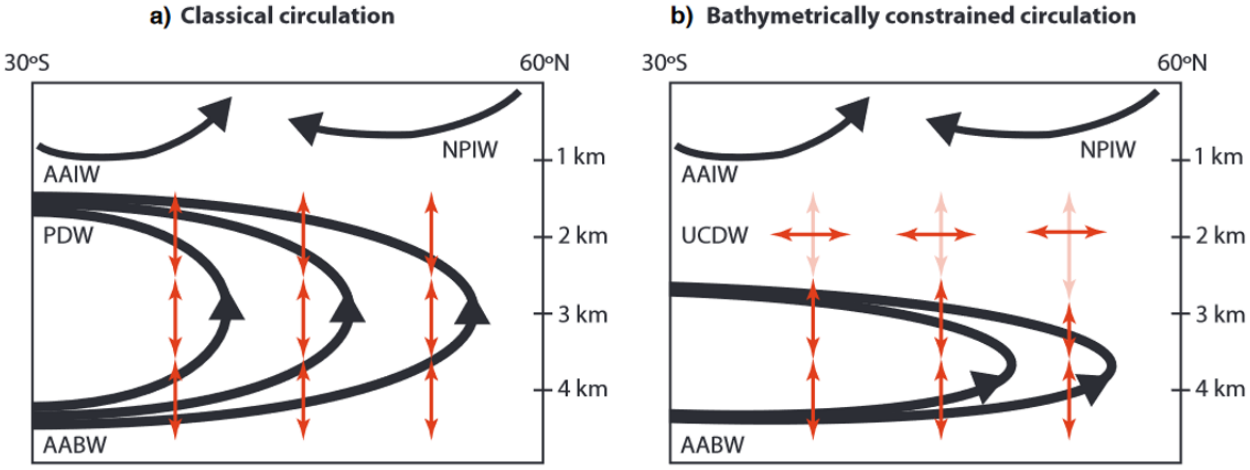

Figure 3: Two distinct views of the modern Pacific deep circulation, adapted from Holzer et al. (2021). The classical overturning circulation is sketched in (a), the bathymetrically constrained circulation in (b). Thick black curves illustrate major branches of the overturning circulation. Double-headed vertical and horizontal red arrows illustrate respectively vertical mixing and isopycnal mixing. Prominent water masses are labeled: Antarctic Bottom Water (AABW), Pacific Deep Water (PDW), Upper Circumpolar Deep Water (UCDW), Antarctic Intermediate Water (AAIW) and North Pacific Intermediate Water (NPIW)

1.4 . Ventilation of the deep Pacific

The ventilation of the modern Pacific is currently debated: two views of the Pacific ventilation are represented in Figure 3. The classical view sees AABW flowing northward before upwelling diffusively up to 1.5 km depth across the basin and flowing southward back to the Southern Ocean (Talley, 2013). An alternative 'bathymetrically constrained' view (de Lavergne et al., 2017) contends that the bulk of diffusive upwelling is confined to abyssal depths where the seafloor is abundant, leaving a mid-depth layer that is excluded from the overturning and weakly ventilated by diffusion and recirculation.

Figure 3b introduces an important water mass: Upper Circumpolar Deep Water (UCDW). This water mass differs from other water masses discussed so far in that it does not have a surface formation region: it is a mixture of different water masses. Little net meridional advection exists in the density range of UCDW ($27.5 \leq \gamma \leq 28$) in the Pacific (de Lavergne et al., 2017): this layer is located above the bulk of the seafloor (mostly between 1.5 and 2.5 km depth) and is thus postulated to be mainly influenced by isopycnal diffusion (Figure 3b). Meridional tracer transport in this layer occurs with little net mass transport and can be both south to north (e.g., oxygen) or north to south (e.g., silicate) depending on the prevailing large-scale isopycnal gradient. Quantifying the influence of isopycnal diffusion relative to the overturning circulation and diapycnal diffusion in the Pacific is a central aspect of this thesis.

2 . Oxygen Isotopes

Oxygen has three naturally occurring isotopes: ^{16}O (99.76%), ^{17}O (0.04%), and ^{18}O (0.2%). These isotopes have been especially useful in understanding changes in global ice volume, Earth's mean global temperature, and sea level through different geological periods. In this thesis we use only the ratio $^{18}O/^{16}O$ to define $\delta^{18}O$:

$$\delta^{18}O = \left(\frac{\left(\frac{^{18}O}{^{16}O}\right)_{sample}}{\left(\frac{^{18}O}{^{16}O}\right)_{standard}} - 1 \right) * 1000 \quad (2)$$

$\delta^{18}O$ is unitless, usually expressed in per mil (‰), and its value is obtained relative to a reference value $\left(\frac{^{18}O}{^{16}O}\right)_{standard}$. For the oxygen-18 isotopic ratio of seawater, $\delta^{18}O_{sw}$, we use the Vienna Standard Mean Ocean Water (VSMOW) scale, and for the oxygen-18 isotopic ratio of the calcite shells of benthic foraminifera, $\delta^{18}O_{CaCO_3}$, the Vienna Peedee Belemnite (VPDB) scale.

2.1 . Oxygen isotopes in seawater

Variations in the relative concentrations of the isotopes are linked to their respective weights: ^{18}O is heavier than ^{16}O. As a consequence, the ^{18}O will be less likely to evaporate (respectively more likely to precipitate) than ^{16}O. This favoured precipitation, referred as Rayleigh fractionation, will decrease the $\delta^{18}O$ of the water vapor remaining after precipitation (Dansgaard, 1964). Hence, when a cloud is formed and starts to rain, the $\delta^{18}O$ of the water vapor in the cloud decreases. Additionally, the colder the temperature, the more condensation will favour ^{16}O to precipitate. These two effects lead to very depleted $\delta^{18}O$ values in ice and snow. Furthermore, they create a latitudinal gradient in $\delta^{18}O$ at the sea surface (LeGrande and Schmidt, 2006), and in precipitation on land (see Figure 5 Lachniet, 2009).

The $\delta^{18}O_{sw}$ of the ocean surface waters is closely linked to the evaporation-precipitation balance. Empirical relationships show a clear correlation between $\delta^{18}O_{sw}$ and salinity within the ocean since freshwater fluxes, including evaporation and precipitation affect both. Using distinct regions to define different salinity-$\delta^{18}O_{sw}$ relationships, LeGrande and Schmidt (2006) constructed a global ocean $\delta^{18}O_{sw}$ gridded product. Figure 4 shows two transects from this product, one at 200°E in the Pacific, and a second one at 25°W in the Atlantic. The different water masses previously mentioned in section 1.2 are clearly identified on those transects. NADW is heavy and AAIW and AABW are relatively depleted in $\delta^{18}O_{sw}$. The Pacific transect exhibits a rather uniform deep structure and a slight mid-depth maximum in $\delta^{18}O_{sw}$ (Figure 4a), an observation which helped motivate this thesis. Indeed, this maximum cannot originate by mixing between water masses above and below, and thus must originate by lateral transport from the Southern Ocean, suggesting an important role for isopycnal diffusion in the ventilation of the mid-depth Pacific. Additionally, the magnitude of this mid-depth maximum suggests a role for NADW in ventilating this Pacific ocean layer.

However, the abrupt transitions visible in the transects and the relatively small magnitude of the mid-depth maximum make these inferences uncertain. The slight mid-depth enrichment is indeed in range of measurements error (~ 0.1‰). Furthermore, the product of LeGrande and Schmidt (2006) does not represent well some key deviations from empirical $\delta^{18}O_{sw}$-salinity relationships such as localized ice-shelf melting or brine rejection which are important in the formation of AABW (Section 1.2).

Brine rejection is the mechanism that occurs when sea ice forms in polar regions: as seawater freezes, it excludes the salt, which results in a salinity increase of the underlying water. If no ^{18}O fractionation

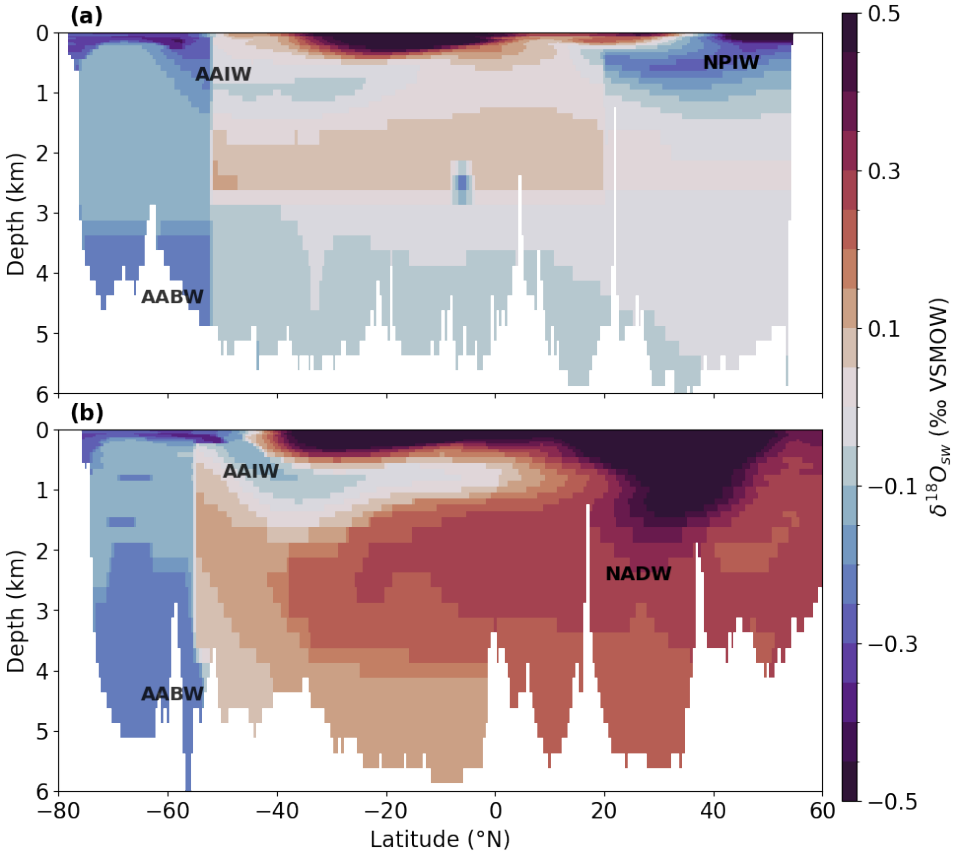

Figure 4: Transects at 200°E **(a)** and 25°W **(b)** of the $\delta^{18}O_{sw}$ from the product of LeGrande and Schmidt (2006).

occurred during this process (i.e. the same $\delta^{18}O$ ratio between sea-ice and the newly rejected waters), then the waters formed would already be more $\delta^{18}O_{sw}$ depleted in regard to other waters with similar salinity, as this salinity increase would not be associated to a $\delta^{18}O_{sw}$ increase (as is the case with evaporation). But studies showed that sea ice is slightly enriched in $\delta^{18}O$ (Biddle et al., 2019; Melling and Moore, 1995; Price et al., 2008; Östlund and Hut, 1984), further increasing the $\delta^{18}O_{sw}$-salinity difference due to brine rejection. Furthermore, the addition of a small amount of ice-shelf meltwater can substantially decrease the $\delta^{18}O_{sw}$ of the waters formed near the coast of Antarctica as these ice-shelf waters have $\delta^{18}O_{sw}$ values of about -30‰(Schlosser et al., 1990; Weiss et al., 1979; Weppernig et al., 1996).

Hence, the deep structure in the LeGrande and Schmidt (2006) $\delta^{18}O_{sw}$ product is rather uncertain. Nonetheless the observed gradient between the different water masses holds promises. This thesis will aim to add new constraints on the variability of $\delta^{18}O_{sw}$ in the deep Pacific, and explore its relevance for understanding ocean ventilation.

2.2 . Reconstructing past $\delta^{18}O_{sw}$ from benthic foraminifera

The $\delta^{18}O_{sw}$ can be studied in past climates using pore water measurements or calcifying organisms. However, due to the temperature dependent fractionation of ^{18}O during calcification, calcifying organisms record a combination of the $\delta^{18}O_{sw}$ and the temperature of the seawater when the shells are forming. Untangling the influence of each of these two tracers from the $\delta^{18}O_{CaCO_3}$ has been a puzzle that paleoceanographers have tried to solve for a long time. Yet without necessarily untangling those separate effects, the $\delta^{18}O_{CaCO_3}$ is a quasi-conservative tracer, which may be used to constrain ventilation (Lund et al., 2011).

Of all calcifying organisms, the most used for past climate reconstruction are the foraminifera. Many different species have been studied and can be divided into two groups: planktic foraminifera, which float in the surface ocean, and benthic foraminifera, living at the ocean-sediment interface. Benthic foraminifera record past information on the deep ocean and clearly record changes in both the timing and intensity of glacial-interglacial cycles over the last 800,000 years. Figure 5 represents a stack of the deep ocean benthic $\delta^{18}O_{CaCO_3}$ over the last two million years, extracted from Lisiecki and Raymo (2005). Glacial periods are characterized by $\delta^{18}O_{CaCO_3}$ maxima and interglacial periods with minima. The magnitude and periodicity of the cycles is not constant which poses interesting questions regarding the mechanisms driving them.

Many empirical relationships link the $\delta^{18}O_{CaCO_3}$ of the different foraminifera species to temperature and $\delta^{18}O_{sw}$ (Daëron and Gray, 2023), although the temperature sensitivity of ^{18}O fractionation into foraminiferal calcite is identical to that observed between dissolved bicarbonate/carbonate and water (Beck et al., 2005). During the LGM, sea level decreased by around 120 m relative to modern day; the associated water was moved to the different ice sheets, which have an isotopic signature ranging from -16 to -60‰, thus increasing the overall $\delta^{18}O_{sw}$ of the ocean. Duplessy et al. (2002) highlighted the difficulties in reconstructing the isotopic signatures of different ice sheets, but pore water estimates indicate a whole ocean glacial increase of 1.05±0.20‰ in $\delta^{18}O_{sw}$. No mechanism other than sea level change is thought to drive large changes in whole ocean $\delta^{18}O_{sw}$ during glacial periods such that temperature is thought to drive the rest of the $\delta^{18}O_{CaCO_3}$ change.

$\delta^{18}O_{CaCO_3}$ has typically been used as a stratigraphic tool more often than a water mass tracer (following the methodology of Lisiecki and Raymo, 2005), despite its conservative nature. Indeed, vital effects between the different benthic foraminiferal species can introduce uncertainty into reconstructing $\delta^{18}O_{sw}$, which

complicates the comparison of absolute values. The different species are often considered to have a constant offset from 'equilibrium' with seawater, but some benthic records show abnormal variations (*Uvigerina* in McCave et al., 2008; Schmiedl and Mackensen, 2006). In order to minimise potential vital effects across different species, this thesis will only use a single species to constrain ocean ventilation: *Cibicidoides wüellerstorfi*. This species lives at the sediment-water interface and is thought to calcify in equilibrium with the seawater. Using this specific species, we will try to constrain changes in deep ocean ventilation between the present day and the LGM.

Key questions of the thesis

The thesis aims at answering the following questions:

1. What are the processes and pathways of Pacific deep ventilation?
2. What do oxygen isotope observations tell about ventilation of the modern ocean ($\delta^{18}O_{sw}$) and ventilation of the LGM ocean ($\delta^{18}O_{CaCO_3}$)?
3. How well is the modern ocean ventilation represented in OGCMs? Which aspects of OGCMs need to be improved to accurately model the deep Pacific Ocean ventilation?

In Chapter I, we address the first two questions focusing on the ventilation of the Pacific alone, and we describe the ventilation pathways within the basin in both modern and glacial states. We study the modern global ocean ventilation in Chapter II, with special attention given to the Pacific Ocean and to the evaluation of OGCMs. We explore the representation of subarctic Pacific dynamics in NEMO in Chapter III. Chapter IV explores in more depth the utility of the $\delta^{18}O_{sw}$ to constrain ventilation of the modern ocean, and how it may help quantify mixing of the different water masses in the Pacific. Finally, past changes in ventilation, comparing the LGM to the present-day, are further explored in Chapter V using $\delta^{18}O_{CaCO_3}$.

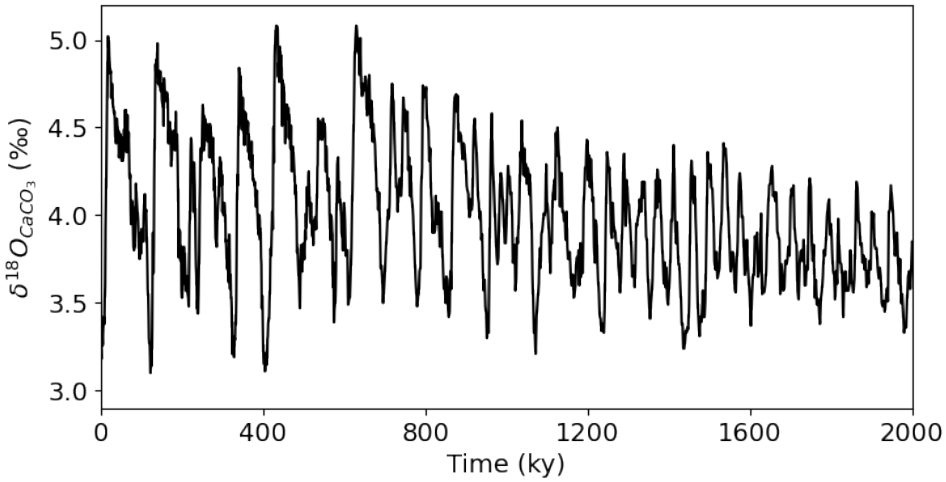

Figure 5: LR04 stack from Lisiecki and Raymo (2005) representing the $\delta^{18}O_{CaCO_3}$ of deep sea benthic foraminifera over the Pleistocene.

References

Abelmann, A., Gersonde, R., Knorr, G., Zhang, X., Chapligin, B., Maier, E., Esper, O., Friedrichsen, H., Lohmann, G., Meyer, H., & Tiedemann, R. (2015). The seasonal sea-ice zone in the glacial southern ocean as a carbon sink. *Nature Communications*, *6*(1), 8136. https://doi.org/10.1038/ncomms9136

Annan, J. D., Hargreaves, J. C., & Mauritsen, T. (2022). A new global surface temperature reconstruction for the last glacial maximum. *Climate of the Past*, *18*(8), 1883–1896. https://doi.org/10.5194/cp-18-1883-2022

Beck, W. C., Grossman, E. L., & Morse, J. W. (2005). Experimental studies of oxygen isotope fractionation in the carbonic acid system at 15°, 25°, and 40°c. *Geochimica et Cosmochimica Acta*, *69*(14), 3493–3503. https://doi.org/10.1016/j.gca.2005.02.003

Bereiter, B., Shackleton, S., Baggenstos, D., Kawamura, K., & Severinghaus, J. (2018). Mean global ocean temperatures during the last glacial transition. *Nature*, *553*(7686), 39–44. https://doi.org/10.1038/nature25152

Biddle, L. C., Loose, B., & Heywood, K. J. (2019). Upper ocean distribution of glacial meltwater in the amundsen sea, antarctica. *Journal of Geophysical Research: Oceans*, *124*(10), 6854–6870. https://doi.org/10.1029/2019JC015133

Broecker, W. S. (1982). Glacial to interglacial changes in ocean chemistry. *Progress in Oceanography*, *11*(2), 151–197. https://doi.org/10.1016/0079-6611(82)90007-6

Broecker, W. S. (1987). Unpleasant surprises in the greenhouse? *Nature*, *328*(6126), 123–126. https://doi.org/10.1038/328123a0

Broecker, W. S., Takahashi, T., & Takahashi, T. (1985). Sources and flow patterns of deep-ocean waters as deduced from potential temperature, salinity, and initial phosphate concentration. *Journal of Geophysical Research: Oceans*, *90*(C4), 6925–6939. https://doi.org/10.1029/JC090iC04p06925

Brook, E. J., & Buizert, C. (2018). Antarctic and global climate history viewed from ice cores. *Nature*, *558*(7709), 200–208. https://doi.org/10.1038/s41586-018-0172-5

Charney, J. G. (1947). The dynamics of long waves in a baroclinic westerly current. *Journal of Atmospheric Sciences*, *4*(5), 136–162. https://doi.org/10.1175/1520-0469(1947)004<0136:TDOLWI>2.0.CO;2

Curry, W. B., & Oppo, D. W. (2005). Glacial water mass geometry and the distribution of δ13c of Σco2 in the western atlantic ocean. *Paleoceanography*, *20*(1). https://doi.org/https://doi.org/10.1029/2004PA001021

Dansgaard, W. (1964). Stable isotopes in precipitation. *Tellus*, *16*(4), 436–468. https://doi.org/10.1111/j.2153-3490.1964.tb00181.x

Daëron, M., & Gray, W. R. (2023). Revisiting oxygen-18 and clumped isotopes in planktic and benthic foraminifera. *Paleoceanography and Paleoclimatology*, *38*(10), e2023PA004660. https://doi.org/10.1029/2023PA004660

de Lavergne, C., Madec, G., Roquet, F., Holmes, R., & McDougall, T. (2017). Abyssal ocean overturning shaped by seafloor distribution. *Nature*, *551*(7679), 181–186. https://doi.org/10.1038/nature24472

de Lavergne, C., Vic, C., Madec, G., Roquet, F., Waterhouse, A., Whalen, C., Cuypers, Y., Bouruet-Aubertot, P., Ferron, B., & Hibiya, T. (2020). A parameterization of local and remote tidal mixing [e2020MS002065 10.1029/2020MS002065]. *Journal of Advances in Modeling Earth Systems*, *12*(5), e2020MS002065. https://doi.org/10.1029/2020MS002065

de Lavergne, C., Groeskamp, S., Zika, J., & Johnson, H. L. Chapter 3 - the role of mixing in the large-scale ocean circulation (M. Meredith & A. Naveira Garabato, Eds.). In: *Ocean mixing* (M. Meredith & A. Naveira Garabato, Eds.). Ed. by Meredith, M., & Naveira Garabato, A. Elsevier, 2022, pp. 35–63. isbn: 978-0-12-821512-8. https://doi.org/10.1016/B978-0-12-821512-8.00010-4

Dickson, R. R., & Brown, J. (1994). The production of north atlantic deep water: Sources, rates, and pathways. *Journal of Geophysical Research: Oceans*, *99*(C6), 12319–12341. https://doi.org/10.1029/94JC00530

Duplessy, J.-C., Labeyrie, L., & Waelbroeck, C. (2002). Constraints on the ocean oxygen isotopic enrichment between the last glacial maximum and the holocene: Paleoceanographic implications [EPILOG]. *Quaternary Science Reviews*, *21*(1), 315–330. https://doi.org/10.1016/S0277-3791(01)00107-X

Ferrari, R., Jansen, M. F., Adkins, J. F., Burke, A., Stewart, A. L., & Thompson, A. F. (2014). Antarctic sea ice control on ocean circulation in present and glacial climates. *Proceedings of the National Academy of Sciences*, *111*(24), 8753–8758. https://doi.org/10.1073/pnas.1323922111

Ferreira, D., Cessi, P., Coxall, H. K., de Boer, A., Dijkstra, H. A., Drijfhout, S. S., Eldevik, T., Harnik, N., McManus, J. F., Marshall, D. P., Nilsson, J., Roquet, F., Schneider, T., & Wills, R. C. (2018). Atlantic-pacific asymmetry in deep water formation. *Annual Review of Earth and Planetary Sciences*, *46*(Volume 46, 2018), 327–352. https://doi.org/10.1146/annurev-earth-082517-010045

Galbraith, E. D., & Skinner, L. C. (2020). The biological pump during the last glacial maximum. *Annual Review of Marine Science*, *12*(Volume 12, 2020), 559–586. https://doi.org/10.1146/annurev-marine-010419-010906

Gebbie, G. (2014). How much did glacial north atlantic water shoal? *Paleoceanography*, *29*(3), 190–209. https://doi.org/10.1002/2013PA002557

Gray, de Lavergne, C., Jnglin Wills, R. C., Menviel, L., Spence, P., Holzer, M., Kageyama, M., & Michel, E. (2023). Poleward shift in the southern hemisphere westerly winds synchronous with the deglacial rise in co2 [e2023PA004666 2023PA004666]. *Paleoceanography and Paleoclimatology*, *38*(7), e2023PA004666. https://doi.org/10.1029/2023PA004666

Gray, W., Wills, R., Rae, J., Burke, A., Ivanovic, R., Roberts, W., Ferreira, D., & Valdes, P. (2020). Wind-driven evolution of the north pacific subpolar gyre over the last deglaciation [e2019GL086328 2019GL086328]. *Geophysical Research Letters*, *47*(6). https://doi.org/10.1029/2019GL086328

Guidi, L., Legendre, L., Reygondeau, G., Uitz, J., Stemmann, L., & Henson, S. A. (2015). A new look at ocean carbon remineralization for estimating deepwater sequestration. *Global Biogeochemical Cycles*, *29*(7), 1044–1059. https://doi.org/10.1002/2014GB005063

Holzer, M., DeVries, T., & de Lavergne, C. (2021). Diffusion controls the ventilation of a pacific shadow zone above abyssal overturning. *Nature Communications*, *12*(1), 4348. https://doi.org/10.1038/s41467-021-24648-x

Holzer, M., & Primeau, F. (2006). The diffusive ocean conveyor. *Geophysical Research Letters*, *33*(14). https://doi.org/10.1029/2006GL026232

Imbrie, J., Hays, J. D., Martinson, D. G., McIntyre, A., Mix, A. C., Morley, J. J., Pisias, N. G., Prell, W. L., & Shackleton, N. J. (1984). The orbital theory of Pleistocene climate : support from a revised chronology of the marine δ^{18} O record, 269.

Jackett, D. R., & McDougall, T. J. (1997). A neutral density variable for the world's oceans. *Journal of Physical Oceanography*, *27*(2), 237 –263. https://doi.org/10.1175/1520-0485(1997)027<0237:ANDVFT>2.0.CO;2

Kageyama, M., Harrison, S. P., Kapsch, M.-L., Lofverstrom, M., Lora, J. M., Mikolajewicz, U., Sherriff-Tadano, S., Vadsaria, T., Abe-Ouchi, A., Bouttes, N., Chandan, D., Gregoire, L. J., Ivanovic, R. F., Izumi, K., LeGrande, A. N., Lhardy, F., Lohmann, G., Morozova, P. A., Ohgaito, R., … Zhu, J. (2021). The pmip4 last glacial maximum experiments: Preliminary results and comparison with the pmip3 simulations. *Climate of the Past*, *17*(3), 1065–1089. https://doi.org/10.5194/cp-17-1065-2021

Key, R. M., Kozyr, A., Sabine, C., Lee, K., Wanninkhof, R., Bullister, J., Feely, R., Milero, F., Mordy, C., & Peng, T.-H. (2004). A global ocean carbon climatology: Results from global data analysis project (glodap). *Global Biogeochemical Cycles*, *18*(4), GB4031. https://doi.org/10.1029/2004GB002247

Kitani, K. (1973). An oceanographic study of the okhotsk sea-particularly in regard to cold waters. *Bull. Far. Seas. Fish. Res.*, *9*, 45–77.

Knox, F., & McElroy, M. B. (1984). Changes in atmospheric co2: Influence of the marine biota at high latitude. *Journal of Geophysical Research: Atmospheres*, *89*(D3), 4629–4637. https://doi.org/10.1029/JD089iD03p04629

Kuhlbrodt, T., Griesel, A., Montoya, M., Levermann, A., Hofmann, M., & Rahmstorf, S. (2007). On the driving processes of the atlantic meridional overturning circulation. *Reviews of Geophysics*, *45*(2). https://doi.org/10.1029/2004RG000166

Kwon, E. Y., Hain, M. P., Sigman, D. M., Galbraith, E. D., Sarmiento, J. L., & Toggweiler, J. R. (2012). North atlantic ventilation of "southern-sourced" deep water in the glacial ocean. *Paleoceanography*, *27*(2). https://doi.org/10.1029/2011PA002211

Lachniet, M. (2009). Climatic and environmental controls on speleothem oxygen-isotope values. *Quaternary Science Reviews*, *28*, 412–432. https://doi.org/10.1016/j.quascirev.2008.10.021

LeGrande, A. N., & Schmidt. (2006). Global gridded data set of the oxygen isotopic composition in seawater. *Geophysical Research Letters*, *33*(12). https://doi.org/10.1029/2006GL026011

Lisiecki, L. E., & Raymo, M. E. (2005). A pliocene-pleistocene stack of 57 globally distributed benthic δ180 records. *Paleoceanography*, *20*(1). https://doi.org/10.1029/2004PA001071

Lozier, M. S., Li, F., Bacon, S., Bahr, F., Bower, A. S., Cunningham, S. A., de Jong, M. F., de Steur, L., deYoung, B., Fischer, J., Gary, S. F., Greenan, B. J. W., Holliday, N. P., Houk, A.,

Houpert, L., Inall, M. E., Johns, W. E., Johnson, H. L., Johnson, C., … Zhao, J. (2019). A sea change in our view of overturning in the subpolar north atlantic. *Science*, *363*(6426), 516–521. https://doi.org/10.1126/science.aau6592

Lund, D. C., Adkins, J. F., & Ferrari, R. (2011). Abyssal atlantic circulation during the last glacial maximum: Constraining the ratio between transport and vertical mixing. *Paleoceanography*, *26*(1). https://doi.org/10.1029/2010PA001938

Marshall, J., & Speer, K. (2012). Closure of the meridional overturning circulation through southern ocean upwelling. *Nature Geoscience*, *5*(3), 171–180. https://doi.org/10.1038/ngeo1391

McCave, I., Carter, L., & Hall, I. (2008). Glacial–interglacial changes in water mass structure and flow in the sw pacific ocean. *Quaternary Science Reviews*, *27*(19), 1886–1908. https://doi.org/10.1016/j.quascirev.2008.07.010

McDougall, T., Groeskamp, S., & Griffies, S. (2014). On geometrical aspects of interior ocean mixing. *Journal of Physical Oceanography*, *44*(8), 2164–2175. https://doi.org/10.1175/JPO-D-13-0270.1

McWilliams, J., & Chow, J. (1981). Equilibrium geostrophic turbulence i: A reference solution in a β-plane channel. *Journal of Physical Oceanography*, *11*(7), 921–949. https://doi.org/10.1175/1520-0485(1981)011<0921:EGTIAR>2.0.CO;2

McWilliams, J. C. (1996). Modeling the oceanic general circulation. *Annual Review of Fluid Mechanics*, *28*(Volume 28, 1996), 215–248. https://doi.org/https://doi.org/10.1146/annurev.fl.28.010196.001243

Melling, H., & Moore, R. M. (1995). Modification of halocline source waters during freezing on the beaufort sea shelf: Evidence from oxygen isotopes and dissolved nutrients. *Continental Shelf Research*, *15*(1), 89–113. https://doi.org/https://doi.org/10.1016/0278-4343(94)P1814-R

Muglia, J., & Schmittner, A. (2015). Glacial atlantic overturning increased by wind stress in climate models. *Geophysical Research Letters*, *42*(22), 9862–9868. https://doi.org/10.1002/2015GL064583

Munday, D. R., Allison, L. C., Johnson, H. L., & Marshall, D. P. (2011). Remote forcing of the antarctic circumpolar current by diapycnal mixing. *Geophysical Research Letters*, *38*(8). https://doi.org/10.1029/2011GL046849

Munk, W. (1950). On the wind-driven ocean circulation. *Journal of Atmospheric Sciences*, *7*(2), 80–93. https://doi.org/10.1175/1520-0469(1950)007<0080:OTWDOC>2.0.CO;2

Munk, W., & Wunsch, C. (1998). Abyssal recipes ii: Energetics of tidal and wind mixing. *Deep Sea Research Part I: Oceanographic Research Papers*, *45*(12), 1977–2010. https://doi.org/10.1016/S0967-0637(98)00070-3

Naveira Garabato, A. C., MacGilchrist, G. A., Brown, P. J., Evans, D. G., Meijers, A. J. S., & Zika, J. D. (2017). High-latitude ocean ventilation and its role in earth's climate transitions. *Philos Trans A Math Phys Eng Sci*, *375*(2102). https://doi.org/10.1098/rsta.2016.0324

Orsi, A., Johnson, G., & Bullister, J. (1999). Circulation, mixing, and production of antarctic bottom water. *Progress in Oceanography*, *43*(1), 55–109. https://doi.org/10.1016/S0079-6611(99)00004-X

Paillard, D. (2015). Quaternary glaciations: From observations to theories. *Quaternary Science Reviews*, *107*, 11–24. https://doi.org/10.1016/j.quascirev.2014.10.002

Petit, T., Lozier, M. S., Josey, S. A., & Cunningham, S. A. (2020). Atlantic deep water formation occurs primarily in the iceland basin and irminger sea by local buoyancy forcing [e2020GL091028 2020GL091028]. *Geophysical Research Letters*, *47*(22), e2020GL091028. https://doi.org/10.1029/2020GL091028

Price, M. R., Heywood, K. J., & Nicholls, K. W. (2008). Ice-shelf-dash; ocean interactions at fimbul ice shelf, antarctica from oxygen isotope ratio measurements. *Ocean Science*, *4*(1), 89–98. https://doi.org/10.5194/os-4-89-2008

Schlosser, P., Bayer, R., Foldvik, A., Gammelsrød, T., Rohardt, G., & Münnich, K. O. (1990). Oxygen 18 and helium as tracers of ice shelf water and water/ice interaction in the weddell sea. *J Geophys Res C3*, *95*, 3253–3263.

Schmiedl, G., & Mackensen, A. (2006). Multispecies stable isotopes of benthic foraminifers reveal past changes of organic matter decomposition and deepwater oxygenation in the arabian sea. *Paleoceanography*, *21*(4). https://doi.org/10.1029/2006PA001284

Shoenfelt, E. M., Winckler, G., Lamy, F., Anderson, R. F., & Bostick, B. C. (2018). Highly bioavailable dust-borne iron delivered to the southern ocean during glacial periods. *Proceedings of the National Academy of Sciences*, *115*(44), 11180–11185. https://doi.org/10.1073/pnas.1809755115

Sigman, D. M., & Boyle, E. A. (2000). Glacial/interglacial variations in atmospheric carbon dioxide. *Nature*, *407*(6806), 859–869. https://doi.org/10.1038/35038000

Silvano, A., Purkey, S., Gordon, A. L., Castagno, P., Stewart, A. L., Rintoul, S. R., Foppert, A., Gunn, K. L., Herraiz-Borreguero, L., Aoki, S., Nakayama, Y., Naveira Garabato, A. C., Spingys, C., Akhoudas, C. H., Sallée, J.-B., de Lavergne, C., Abrahamsen, E. P., Meijers, A. J. S., Meredith, M. P., … Lee, W. S. (2023). Observing antarctic bottom water in the southern ocean. *Frontiers in Marine Science*, *10*. https://doi.org/10.3389/fmars.2023.1221701

Stephens, B. B., & Keeling, R. F. (2000). The influence of antarctic sea ice on glacial–interglacial co2 variations. *Nature*, *404*(6774), 171–174. https://doi.org/10.1038/35004556

Talley, L. D. (1988). Potential vorticity distribution in the north pacific. *Journal of Physical Oceanography*, *18*(1), 89–106. https://doi.org/10.1175/1520-0485(1988)018<0089:PVDITN>2.0.CO;2

Talley, L. D. (1993). Distribution and formation of north pacific intermediate water. *Journal of Physical Oceanography*, *23*(3), 517 –537. https://doi.org/10.1175/1520-0485(1993)023<0517:DAFONP>2.0.CO;2

Talley, L. D. (2013). Closure of the global overturning circulation through the indian, pacific, and southern oceans: Schematics and transports. *Oceanography*, *26*(1), 80–97.

Toggweiler, J., Russell, J. L., & Carson, S. (2006). Midlatitude westerlies, atmospheric co2, and climate change during the ice ages. *Paleoceanography*, *21*(2). https://doi.org/10.1029/2005PA001154

Toggweiler, J., & Samuels, B. (1995). Effect of drake passage on the global thermohaline circulation. *Deep Sea Research Part I: Oceanographic Research Papers*, *42*(4), 477–500. https://doi.org/10.1016/0967-0637(95)00012-U

Wallmann, K., Schneider, B., & Sarnthein, M. (2016). Effects of eustatic sea-level change, ocean dynamics, and nutrient utilization on atmospheric pco_2 and seawater composition over the last 130 000 years: A model study. *Climate of the Past*, *12*(2), 339–375. https://doi.org/10.5194/cp-12-339-2016

Warren, B. A. (1983). Why is no deep water formed in the north pacific? *Journals of Marine Research*, *41*, 327–347. https://doi.org/10.1357/002224083788520207

Weiss, R., Östlund, H., & Craig, H. (1979). Geochemical studies of the weddell sea. *Deep Sea Research Part A. Oceanographic Research Papers*, *26*(10), 1093–1120. https://doi.org/10.1016/0198-0149(79)90059-1

Weppernig, R., Schlosser, P., Khatiwala, S., & Fairbanks, R. G. (1996). Isotope data from ice station weddell: Implications for deep water formation in the weddell sea. *Journal of Geophysical Research: Oceans*, *101*(C11), 25723–25739. https://doi.org/https://doi.org/10.1029/96JC01895

Worthington, L. (1981). The water masses of the world ocean: Some results of a fine-scale census. *Evolution of Physical Oceanography, Scientific Surveys in Honor of Henry Stommel*, 42–60. https://ocw.mit.edu/ans7870/textbooks/Wunsch/Edited/Chapter2.pdf

Zika, J. D., Skliris, N., Nurser, A. J. G., Josey, S. A., Mudryk, L., Laliberté, F., & Marsh, R. (2015). Maintenance and broadening of the ocean's salinity distribution by the water cycle. *Journal of Climate*, *28*(24), 9550 –9560. https://doi.org/10.1175/JCLI-D-15-0273.1

Östlund, H. G., & Hut, G. (1984). Arctic ocean water mass balance from isotope data. *Journal of Geophysical Research: Oceans*, *89*(C4), 6373–6381. https://doi.org/10.1029/JC089iC04p06373

CHAPTER I

OXYGEN ISOTOPE CONSTRAINTS ON THE VENTILATION OF THE MODERN AND GLACIAL PACIFIC

Climate Dynamics
https://doi.org/10.1007/s00382-023-06910-8

Oxygen isotope constraints on the ventilation of the modern and glacial Pacific

Bruno Millet[1] · **William R. Gray**[1] · **Casimir de Lavergne**[2] · **Didier M. Roche**[1,3]

Received: 9 May 2023 / Accepted: 29 July 2023

Abstract
Changes in Pacific tracer reservoirs and transports are thought to be central to the regulation of atmospheric CO_2 on glacial–interglacial timescales. However, there are currently two contrasting views of the circulation of the modern Pacific; the classical view sees southern sourced abyssal waters upwelling to about 1.5 km depth before flowing southward, whereas the bathymetrically constrained view sees the mid-depths (1–2.5 km) largely isolated from the global overturning circulation and predominantly ventilated by diffusion. Furthermore, changes in the circulation of the Pacific under differing climate states remain poorly understood. Through both a modern and a Last Glacial Maximum (LGM) analysis focusing on oxygen isotopes in seawater and benthic foraminifera as conservative tracers, we show that isopycnal diffusion strongly influences the mid-depths of the Pacific. Diapycnal diffusion is most prominent in the subarctic Pacific, where an important return path of abyssal tracers to the surface is identified in the modern state. At the LGM we infer an expansion of North Pacific Intermediate Water, as well as increased layering of the deeper North Pacific which would weaken the return path of abyssal tracers. These proposed changes imply a likely increase in ocean carbon storage within the deep Pacific during the LGM relative to the Holocene.

Keywords Pacific Ocean · Ocean circulation · Ventilation · Oxygen isotopes · Last Glacial Maximum

1 Introduction

Atmospheric CO_2 varied by up to 100 ppm over glacial–interglacial cycles and is closely linked to changes in global temperature (Augustin et al. 2004). Understanding the mechanisms underpinning these variations in atmospheric CO_2 may help us to understand key carbon cycle feedbacks within the climate system relevant for future climate change. Because of its size and the timescale at which it can interact with the atmosphere, the deep ocean is the most likely candidate to store and release carbon over glacial–interglacial cycles (Sigman and Boyle 2000; Adkins 2013). The Pacific represents about 50% of the global ocean volume and contains the oldest and most carbon-rich waters in the global ocean (Key 2004). Yet, despite being fundamental to our understanding of the carbon cycle, the circulation of the Pacific in the modern climate—and, by extension, in past climates—remains poorly understood (e.g. Stewart 2017; Hautala 2018; Kawasaki et al. 2021). The role of the Pacific ocean in the global carbon cycle, and inferred glacial–interglacial changes in Pacific upper-ocean circulation (Keigwin 1998; Matsumoto et al. 2002; Okazaki et al. 2010; Rae et al. 2014, 2020; Struve et al. 2022), motivate further inquiry into Pacific tracer distributions.

The global overturning circulation ventilates the deep ocean through the formation and sinking of dense waters at high latitudes of the North Atlantic and Southern Ocean.

✉ Bruno Millet
bruno.millet@lsce.ipsl.fr

William R. Gray
william.gray@lsce.ipsl.fr

Casimir de Lavergne
casimir.delavergne@locean.ipsl.fr

Didier M. Roche
didier.roche@lsce.ipsl.fr

[1] Laboratoire des Sciences du Climat et de l'Environnement, LSCE/IPSL, CEA-CNRS-UVSQ, Université Paris-Saclay, Orme des Merisiers, 91191 Gif-sur-Yvette, France

[2] LOCEAN Laboratory, Sorbonne Université-CNRS-IRD-MNHN, 4 place Jussieu, 75005 Paris, France

[3] Faculty of Science, Department of Earth Sciences, Vrije Universiteit Amsterdam, Amsterdam, The Netherlands

Published online: 31 August 2023

The newly formed waters progressively replace older deep waters and thereby flush carbon sequestered by the biological pump back to the upper ocean and atmosphere. As the North Pacific is remote from the main sources of deep water formation, its waters deeper than 1 km are very old, depleted in oxygen and enriched in carbon (Key 2004). Characterizing the mechanisms by which the North Pacific is slowly ventilated is therefore crucial to our understanding of oceanic carbon storage.

In the modern Pacific below the main thermocline, ventilation is thought to occur via three main circulation branches (Fig. 1). At intermediate depths, down to about 1 km, Antarctic Intermediate Water (AAIW) formed in the Southern Ocean dominates ventilation of the South Pacific, while North Pacific Intermediate Water (NPIW) formed in the northwest end of the basin dominates ventilation of the North Pacific. In deeper layers, ventilation relies exclusively on waters coming from the Southern Ocean, since there is no formation of deep water in the North Pacific (Warren 1983). The drivers and pathways of this deep ventilation remain debated (Holzer et al. 2021). Indeed, there are two contrasting views of the deep Pacific circulation, illustrated in Fig. 1, that disagree on the ventilation of the mid-depths. Talley (2013) described dense Antarctic waters (AABW) flowing northward deeper than about 3.5 km, before they upwell diffusively up to about 1.5 km depth, and return southward as Pacific Deep Water (PDW) to the Southern Ocean surface. An alternative view (de Lavergne et al. 2017) contends that the bulk of diffusive upwelling is confined to abyssal depths where the seafloor is abundant, leaving a mid-depth layer that is excluded from the overturning and weakly ventilated by diffusion and recirculation. This latter 'bathymetrically constrained' circulation is supported by estimates of water mass transformation by tidal mixing and geothermal heating (de Lavergne et al. 2022; Kawasaki et al. 2021), and is qualitatively consistent with observed silicate and radiocarbon distributions (de Lavergne et al. 2017) as well as inverse modelling of multiple geochemical tracers (Holzer et al. 2021).

Multiple lines of evidence indicate changes in deep ocean circulation between the LGM and Holocene. Although still subject of debate, proposed alterations at LGM relative to today include a shallower northern component of deep water formed in the North Atlantic (Curry and Oppo 2005; Ferrari et al. 2014), an enhanced NPIW source (e.g. Keigwin 1998; Matsumoto et al. 2002; Rae et al. 2020), and a colder and saltier global ocean, with enhanced deep stratification due to salinity rather than temperature (Adkins et al. 2002). On the other hand, the abyssal overturning cell could be expected to have a broadly unaltered structure, set by deep topography (Toggweiler and Samuels 1995a; de Lavergne et al. 2017).

In order to shed light on both modern and past physical ocean states, we use conservative tracers. We first explore ventilation pathways in the modern Pacific by using temperature, salinity, the oxygen isotopic ratio of seawater and preformed phosphate. Then, we investigate changes in ventilation during the LGM with the oxygen isotopic ratio within $CaCO_3$ shells of benthic foraminifera *Cibicidoides mundulus*, *Cibicidoides wüellerstorfi* and *Planulina spp.* Those three genus are closely related and equally reliable; their isotopic ratio acts as a quasi-conservative tracer (Lund et al. 2011). We find that the mid-depths of both the modern and LGM Pacific host tracer extrema that cannot result from a mixture of waters above and below. This pattern is consistent with a vertically compressed abyssal overturning and a prominent influence of isopycnal diffusion on

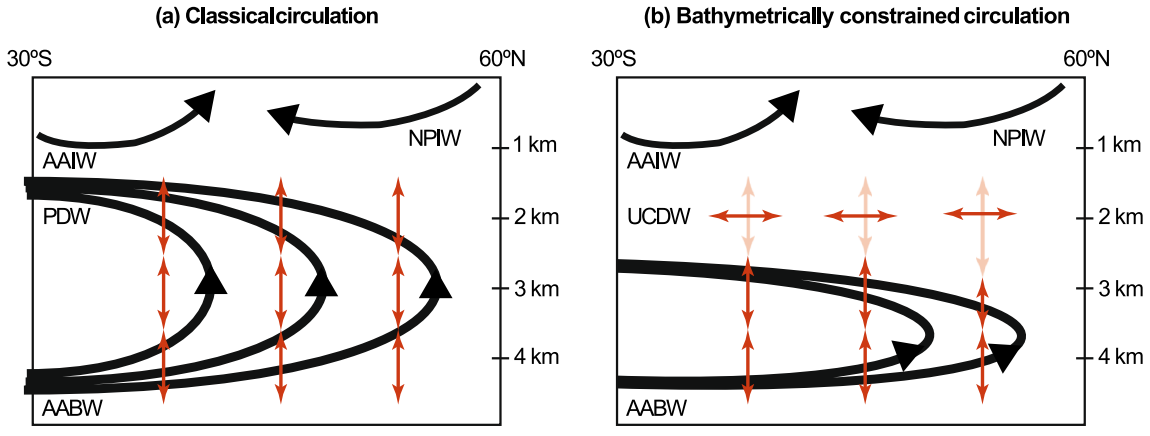

Fig. 1 Two distinct views of the modern Pacific deep circulation, adapted from Holzer et al. (2021). The classical overturning circulation is sketched in (**a**), the bathymetrically constrained circulation in (**b**). Thick black curves illustrate major branches of the overturning circulation. Double-headed vertical and horizontal red arrows illustrate respectively vertical mixing and isopycnal mixing. Prominent water masses are labeled: Antarctic Bottom Water (AABW), Pacific Deep Water (PDW), Upper Circumpolar Deep Water (UCDW), Antarctic Intermediate Water (AAIW) and North Pacific Intermediate Water (NPIW)

Pacific mid-depth waters. However we also find evidence of upwelling of abyssal tracers in the modern subarctic Pacific. At the LGM, this upwelling may have been suppressed, while NPIW formation was enhanced.

2 Least-squares method

In order to characterise ventilation patterns in the modern Pacific, we developed a least-squares method to estimate the fractional contribution of four end-members (corresponding to the water masses labeled in Fig. 1) to local water volumes. The resultant distributions of water fractions give a simple integrated view of circulation and mixing (see e.g. Johnson 2008; Rae and Broecker 2018). We describe in turn the tracers that we use in our modern study, the least-squares calculation and the definition of the end-members.

2.1 Conservative tracers for the modern ocean

In this study, we focus on conservative tracers, that is, tracers that have no sources and sinks away from ocean boundaries. In the ocean interior, such tracers only change due to advection and diffusion, so that their distributions bear direct information on ocean circulation and mixing. The four chosen tracers are shown as a zonal average over the main Pacific basin in Fig. 2. Note that the 'main Pacific' (see Fig. 2a) refers to the Pacific excluding semi-enclosed seas and waters east of the East Pacific Rise, following de Lavergne et al. (2017).

First, we calculated conservative temperature (Θ) and preformed salinity (S) using the Gibbs SeaWater toolbox of McDougall and Barker (201) and the WOCE global hydrographic climatology of Gouretski and Koltermann (2004), an annual mean climatology constructed using along-isopycnal interpolation. Preformed salinity is closely related to absolute salinity but excludes biological contributions to salinity, and in particular excludes the contribution of silicate which is significant in the deep Pacific (McDougall et al. 2012).

Next, we attempted to remove the impact of geothermal heating on temperatures of the deep Pacific, since this heat source along the seafloor could bias our estimates of water fractions which assume strict tracer conservation throughout the deep Pacific north of 30°S. We decided to approximate and remove the geothermal heating effect using a simple linear function of depth which increases from 0 °C at 1 km to 0.5 °C at 6 km depth, which we subtract from the three-dimensional conservative temperature field. This linear vertical profile finds justification in the model analysis of Emile-Geay and Madec (2009) (see their Figure 6c). We note that this correction has little impact on our results: it changes the estimated AABW fractions in the abyss by at most a few percent, while reducing the overall error of the method (see Sect. 2.4).

Preformed phosphate, PO_4^*, defined by Broecker et al. (1985), was calculated from the GLODAPv2 product (Olsen et al. 2016), using a phosphate to oxygen ratio of 1:175 following Rae and Broecker (2018). This tracer is approximately conserved in the deep ocean, because the oxygen consumed in the remineralization of organic matter is broadly constant in the deep ocean (Anderson and Sarmiento 1994). Like conservative temperature and preformed salinity, PO_4^* displays a clear vertical gradient between the abyss and the mid-depths, with higher PO_4^* values in the abyss (Fig. 2b). While latitudinal variations in the C:P ratio of organic matter (Moreno et al. 2022) may lead to non-conservative spatial bias in PO_4^*, these deviations from Redfield stoichiometry cannot explain the depth structure we observe.

The seawater oxygen isotope ($\delta^{18}O_{sw}$) climatology used is the gridded product of LeGrande and Schmidt (2006). The zonal average of $\delta^{18}O_{sw}$ in the main Pacific exhibits a mid-depth maximum throughout the basin (Fig. 2c). It must be emphasized that seawater $\delta^{18}O$ measurements contributing to the climatology are extremely scarce in the deep Pacific. However, the mid-depth maximum appears to be a robust feature, not an artefact of the mapping, as it is present in several individual datasets (e.g. Herguera et al. 1992; Keigwin 1998; McCave et al. 2008). This maximum cannot be explained by vertical mixing and upwelling of AABW: it must originate from lateral (diffusive and/or advective) transport from the Southern Ocean. Although $\delta^{18}O_{sw}$ is conservative, a clear discontinuity is observable around 20°N in Fig. 2c; this artefact stems from the region-by-region gridding procedure of LeGrande and Schmidt (2006). The employed climatology of $\delta^{18}O_{sw}$ is thus imperfect, and increasing the spatial coverage and inter-calibration of $\delta^{18}O_{sw}$ data in the Pacific will help to further constrain ventilation patterns.

The spatial structure of $\delta^{18}O_{sw}$ suggests a dominant south-to-north transport of this tracer at mid-depths in the Pacific, which would support the circulation regime presented in Fig. 1b.

In order to quantitatively assess the constraints on Pacific ventilation contained in our four tracer distributions, we develop a least-squares algorithm that quantifies the volume contributions of each water mass in the Pacific, using AABW, AAIW, NPIW and either PDW [as a representation of the classical circulation] or Upper Circumpolar Deep Water (UCDW) [as a representation of the bathymetrically constrained circulation] as our end-members. We will show that the calculation is most accurate when the fourth end-member is defined as 30°S UCDW (see Sect. 3).

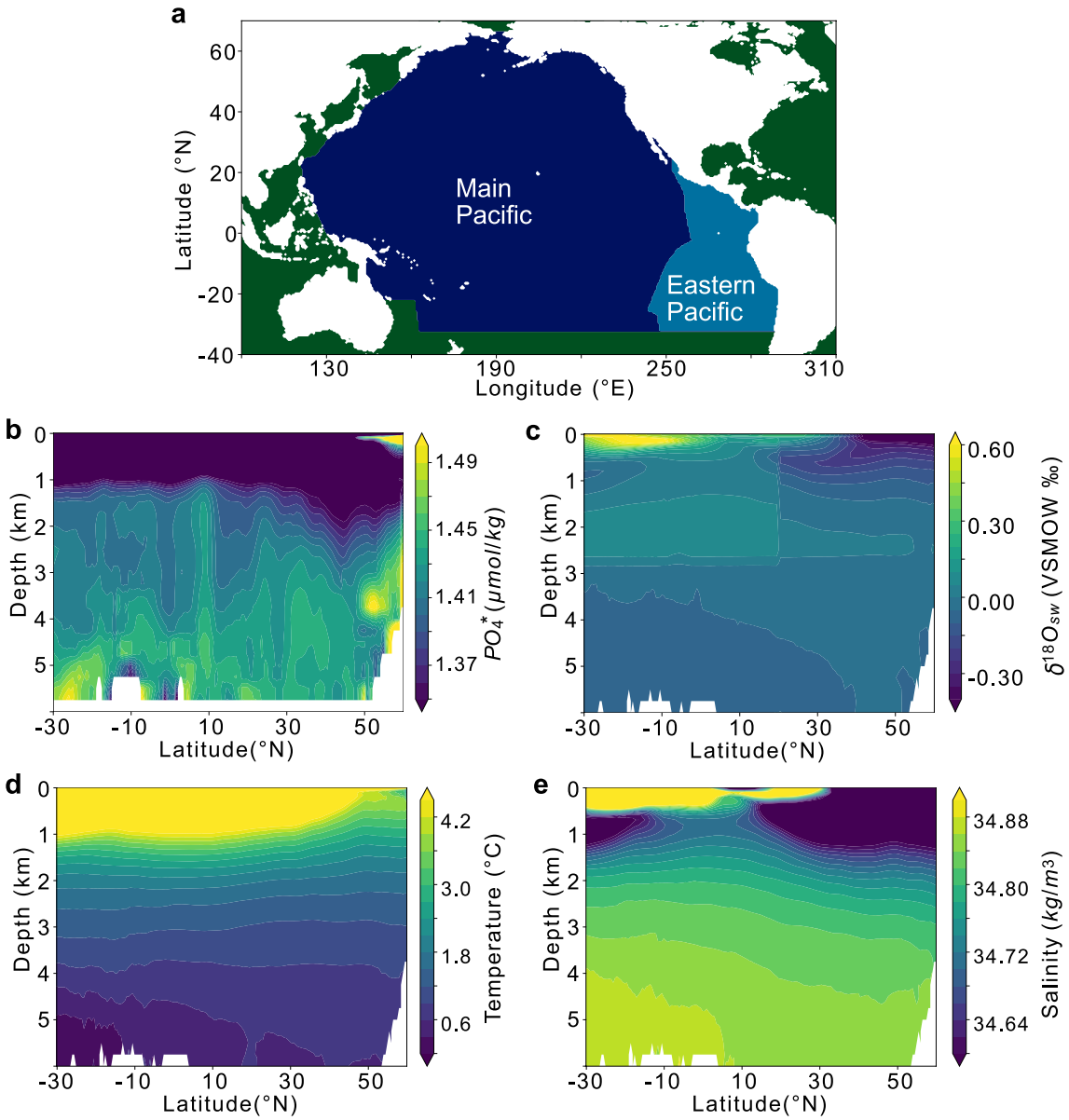

Fig. 2 (**a**) Shows the mask that defines the 'main Pacific' domain, which excludes the semi-enclosed seas and waters east of the East Pacific Rise, following de Lavergne et al. (2017). Zonal averages over the 'main Pacific' of the four tracers used in the least-squares method are plotted in (**b**–**e**). Preformed phosphate (**b**) is defined following Rae and Broecker (2018) and computed using GLODAPv2 gridded fields (Olsen et al. 2016). The oxygen isotopic ratio of seawater (**c**) is based on the gridded field of LeGrande and Schmidt (2006). Conservative temperature corrected from geothermal heating (**d**), and preformed salinity (**e**), are based on the WOCE global hydrographic climatology (Gouretski and Koltermann 2004)

2.2 Water fractions algorithm

The water-fraction algorithm is an optimization problem based on four conservative tracers: Θ, S, $\delta^{18}O_{sw}$ and PO_4^*. The optimization problem uses a linear least squares method to approximate, at each point of our grid (45 depth levels, $0.5° \times 0.5°$ horizontal resolution), the four water fractions. These fractions represent the contribution of each end-member to the volume (hence tracer content) of each grid cell. The water fractions are obtained by minimizing the resultant r based on the following equation:

$$\|M.f - d\|^2 = r^2 \tag{1}$$

Our optimization variable is a (1, 4) vector, f, representing the fractions of our four end-members, d is a (1, 5) vector containing the physical and biochemical properties of the ocean at this grid-point. M is a (5, 4) matrix that contains

the values of the end-member for each tracer divided by the typical range of the tracer in the deep Pacific. Dividing the tracer values by their typical variation is necessary when we sum and compare each tracer error in order to minimize the total error of the method. Typical variations are defined as follows: we average horizontally each tracer over the whole deep ($\geq$ 1 km) Pacific, and take the largest difference in the resulting vertical profile. The obtained values are referenced in Table 1. The fifth parameter entering the minimization, corresponding to the fifth row in the left-hand-side of Eq. (1), ensures that the sum of our fractions is very close to 1. Furthermore, a constraint is placed on the fractions such that they are comprised between 0 and 1. Our problem is thus over-constrained and we could add new end-members should we desire to.

Although all conservative, our tracers are not equally reliable. Thus we associate weights to control the relative influence of each tracer in our optimization problem, therefore in M and d. Following Johnson (2008), we decided to put the relative weight of temperature at one-fourth the weight of salinity. Subjectively, we set the weight of $\delta^{18}O_{sw}$ at a quarter of that of temperature because the data for the deep Pacific is very scarce, and because of artefacts in the interpolation. The weight of PO_4^* is chosen to be one-half the weight of temperature because this tracer is reconstructed from two biochemical tracers that are less well observed than temperature and salinity and because of the required assumptions in the Redfield stoichiometry. Although the exact choice of weights is subjective, we found that changing them over reasonable ranges did not alter the broad structure that we identify.

2.3 Definition of the end-members

The AAIW, UCDW and AABW end-members are defined at 30°S by averaging over specific neutral density (γ^n) (see Jackett and McDougall 1997) ranges, that are characteristic of each water mass according to previous studies and our inspection of 30°S tracer distributions. The UCDW end-member tracer values are averages between 27.7 and 27.95 neutral density surfaces. Although UCDW is usually defined as the 27.5–28 neutral density range in the Southern Ocean, we reduced the range to minimise overlap with AAIW in the South Pacific. Indeed, the AAIW end-member is defined as the water between the 27.2 and 27.5 neutral density surfaces, at 30°S. The AABW end-member is taken to be the water below the 28.11 neutral density surface at 30°S (Ganachaud and Wunsch 2000; de Lavergne et al. 2017). For the NPIW end-member, we choose a specific location in the North Pacific to determine the NPIW, following Johnson (2008): 37°N, 159.5°E and 400 m depth. The neutral density there is 26.8, well within the typical density range of NPIW ($\sim$ 26.7–26.9) (Talley 1993). The four end-member values for each tracer are reported in Table 1.

Table 1 This table lists the tracer values of each end-member used for our water fractions algorithm

	Θ (°C)	S (kg m^{-3})	$\delta^{18}O_{sw}$ (‰)	PO_4^* (μ mol kg^{-1})
AABW	0.435	34.868	– 0.0572	1.435
UCDW	2.342	34.746	0.0515	1.417
AAIW	4.771	34.511	– 0.0527	1.283
NPIW	6.438	34.130	– 0.227	0.872
Typical variations	3.456	0.229	0.114	0.102
Weight	1	4	0.25	0.5
Error max	1.728	0.0287	0.227	0.102

The typical range, weight and maximum tolerated error of each tracer are also given

The definition of PDW is somewhat more ambiguous, as PDW is usually interpreted as the product of distributed upwelling and transformation of AABW, enabled by vertical mixing. The large degree of transformation, apparent in the observed vertical tracer gradients between 5 and 1.5 km in Fig. 2, motivates the inclusion of a PDW end-member distinct from AABW. For a fair comparison to the 30°S UCDW end-member scenario, we try multiple definitions of the PDW end-member: tracer values are averaged over the main Pacific basin for a neutral density of $\gamma_n = 27.8$ kg m^{-3} (as defined by Talley 2013) at different latitudes: 20°S, 0°N, 20°N or 40°N, giving four different scenarios. In a fifth scenario the PDW end-member tracer values are volume averaged at the same density and over the 20°S-40°N range within the main Pacific basin.

2.4 Error discrimination

This model aims to broadly represent deep ventilation patterns, and we cannot expect it to capture all features of the Pacific hydrography. In particular the model will fail in low-latitude upper-ocean waters since it lacks appropriate end-members there. We therefore introduce an error threshold beyond which we mask out the output of our optimization problem. Specifically, the water fractions estimated by the algorithm allow to reconstruct local tracer values from the end-member values. If the difference between the reconstructed and actual tracer values is too large then we determine that our model is unable to explain how the ocean is ventilated at this specific location.

The error is calculated as the norm of our resultant r, representing the deviations between our predictions and the actual values of the tracers. We define a threshold above which the results will be considered erroneous. This threshold implies a maximum tolerated error for each tracer, given in Table 1. Note that this maximum is never reached because

errors beyond the threshold are due to several tracers rather than a single one.

3 Water fraction estimates in the modern Pacific

We first compare six simulations with different choices for the fourth end-member (Table 2). We define the total error of a simulation as the sum of resultants over all grid points of the main Pacific at depths greater than 500 m. This error is a measure of the ability of obtained water fractions to reconstruct three-dimensional tracer distributions across the considered Pacific domain. We find that the error decreases as the PDW end-member is moved toward the south, and is smallest using the 30°S UCDW end-member (Table 2). Hence, the optimization works best when the mid-depth end-member is defined at the southern boundary of the domain, rather than inside the domain. This result, not obvious since one could expect a more central end-member to yield a better average match with tracer observations, suggests that the preferential ventilation pathway of Pacific mid-depths is south-to-north. Interestingly, the simulation in which the PDW end-member is defined at 40°N creates a very local water mass (see Supplementary Figure S1), suggesting that the water at this location is a fairly stagnant and unique mixture of the surrounding sources.

Table 2 This table reports a measure of total error for each simulation, where the error is normalized by that of our reference simulation (using the UCDW end-member defined at 30°S)

PDW ($\gamma_n = 27.8$)	− 20°N	0°N	20°N	40°N	− 20 to 40°N
Error normalized to UCDW	1.02	1.04	1.16	1.45	1.08

Only the fourth end-member (UCDW or PDW) definition changes across simulations, and the error associated to each simulation is shown (with the error associated to the UCDW being 1)

In all the following, we only retain the scenario with the UCDW end-member, and we will use the phrase 'dominating fraction' when a fraction is superior to the sum of the other three. The results are illustrated in Fig. 3, where zonally averaged fractions are shaded and the characteristic isopycnals of each water mass are drawn in red.

The fractions indicate that the mid-depths (1–3 km) of the Pacific, up to 35°N, exhibit tracer distributions that are compatible with ventilation dominantly through isopycnal diffusion from the south. The zonal mean UCDW fraction is above 0.7 between 1.5 and 2.5 km depth up to 20°N (Fig. 3c). The UCDW mid-depth tongue erodes further north, until it is no longer the dominating fraction, around 35°N.

The AABW end-member dominates below 3 km depth, and almost throughout the water column of the subarctic Pacific, north of 45°N, as shown by Fig. 3d. The latter feature suggests the upwelling of abyssal tracers there. Diffusive (and possibly advective) upwelling in the subarctic Pacific was identified in radiocarbon observations (Toggweiler et al.

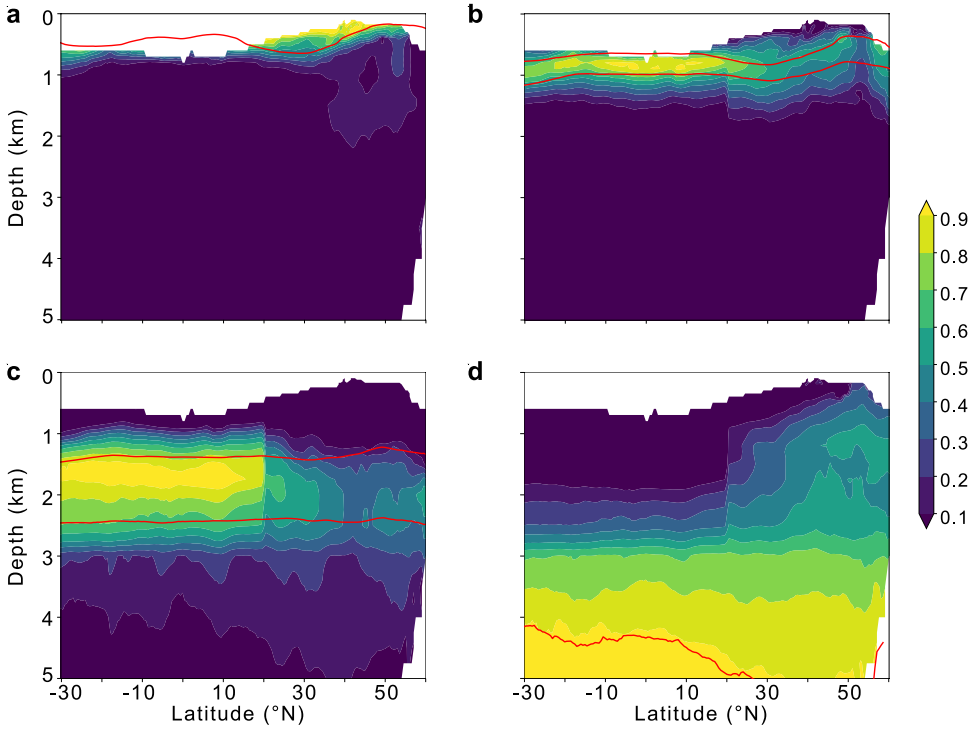

Fig. 3 This figure illustrates water fractions from our reference simulation (using UCDW as the fourth end-member). Each fraction is zonally averaged over the main Pacific basin, as defined in Fig. 2a. Characteristic isopycnals of each end-member are overlain in red. The NPIW fraction (**a**) is mainly situated above the 26.9 neutral density surface, and confined to the North Pacific. The AAIW (**b**) and UCDW (**c**) fractions are mainly enclosed by their end-member density range, respectively 27.2–27.5 and 27.7–27.95. The AABW fraction (**d**) is at its highest below the 28.11 neutral density surface, and is dominant in the major part of the Pacific ocean below 3 km

2019) and a data-constrained inverse model of ocean circulation (Holzer et al. 2021). Additionally, advective upwelling of deep water is deemed necessary in the formation of the modern NPIW (Warren 1983). Whether advective or diffusive, the upwelling probably occurs along topography in the northernmost Pacific, with its signature spreading southward (to about 30°N, Fig. 3d) through isopycnal diffusion and recirculation.

The NPIW fraction is mainly confined to the intermediate depths of the North Pacific, dominating within 200–800 m and 10–50°N (Fig. 3a). NPIW fractions above 0.1 are found down to about 2 km depth north of 30°N, suggesting weak downward diffusion of NPIW tracers to that depth. In accord with Sarmiento et al. (2004), the NPIW core underlies the entire North Pacific subtropical gyre. Finally, the AAIW fraction dominates near 1 km depth in both the South and North Pacific (Fig. 3b). The upward shift north of 30°N follows the sloping isopycnals of the North Pacific subpolar gyre.

The abrupt transition at 20°N in the values of UCDW and AABW fractions that we obtain is due to the discontinuity in the $\delta^{18}O_{sw}$ product. However the transition also reflects a real (smoother) feature because the UCDW fraction remains relatively high up to 35°N and only there becomes outmatched by AABW. In addition, a simulation with only temperature and salinity tracers and only three end-members (removing either AAIW or NPIW) yields about the same result (Supplementary Figure S2). This shows that the northward reduction in the UCDW fraction at mid-depths is not an artifact of the $\delta^{18}O_{sw}$ discontinuity but a real feature.

4 Glacial profile of $\delta^{18}O_{CaCO_3}$ and its implications for circulation

4.1 Changes in $\delta^{18}O_{CaCO_3}$ between the LGM and Holocene

In order to investigate changes in circulation at the LGM we use the $\delta^{18}O_{CaCO_3}$ (δ_c) of *Cibicidoides* & *Planulina*. δ_c is a function of $\delta^{18}O_{sw}$ and in-situ temperature, hence it is approximately conservative (Lund et al. 2011). The only non-conservative variations of δ_c arise due to the moderate increase of in-situ temperature with pressure; an effect that can be estimated and corrected for (Marchitto et al. 2014).

We compiled the sediment core data from three different studies (Keigwin 1998; Matsumoto et al. 2002; Herguera et al. 2010) (see Fig. 4a) that provide water column profiles of δ_c from the North Pacific. These datasets provide a sparse sampling of the basin from 20°N up to 55°N, and from the coast of Japan to that of Baja California. The Holocene and LGM δ_c measurements from these cores are shown as a function of depth in Fig. 4c. In order to help identify the trends with depth, we fit both the Holocene and LGM data with a generalised additive model (GAM) (Wood 2011), with the smoothing term determined by restricted maximum likelihood (REML) (Wood et al. 2016). The resultant Holocene δ_c profile is relatively uniform below 2 km depth, consistent with the near-uniform distributions of temperature and $\delta^{18}O_{sw}$ at these depths of the modern North Pacific (Fig. 2c,d). By contrast, the glacial δ_c profile exhibits a maximum centred near 2.5–3 km depth. The maximum is visible in both of the individual datasets that span this depth range (Keigwin 1998; Matsumoto et al. 2002), indicating that it is a robust feature in the data and not an artifact of inter-laboratory offsets. This maximum cannot be explained by the pressure dependence of in-situ temperature, which could account for a decrease of only 0.025 per mil in δ_c between 4 and 3 km depth (0.1 °C). The maximum can neither come from vertical advective-diffusive transport of AABW or NPIW, since both water masses have lower δ_c. Instead, we hypothesize that this maximum stems from isopycnal diffusion of higher δ_c coming from Southern Ocean mid-depths.

The δ_c gradient between intermediate and mid-depths is also stronger in the glacial profile than in the Holocene profile (Fig. 4b). This difference may be explained by a glacial expansion of NPIW, whose influence likely reached deeper down than today (e.g. Keigwin 1998; Matsumoto et al. 2002; Rae et al. 2020).

Next, we assess whether these two major changes in the δ_c profile between the LGM and the Holocene can be explained by a change in the end-member tracer values, or whether they imply a change in water fractions (i.e., a change in circulation and mixing).

4.2 Attributing profile changes

Before discussing potential drivers of the change in δ_c profile, we first consider the differences in the spatial sampling of tracer fields between modern and LGM states; whereas 3-D gridded tracer climatologies are available to us in the modern, we rely on sparse observations at the LGM ($n = 59$ cores). To test if the spatial sampling of the sediment cores can be considered representative of the wider North Pacific we sample the 3-D fields of modern tracers and water fractions at the sediment core locations, and compare the resulting profiles to the basin (20–55°N) averages (Supplementary Figures S3 and S4). This comparison indicates that our compilation can indeed represent the broad-scale hydrographic features of the North Pacific deeper than 1.7 km. At shallower depths, tracers contain more pronounced horizontal variability: for example, relatively cold waters occupy the

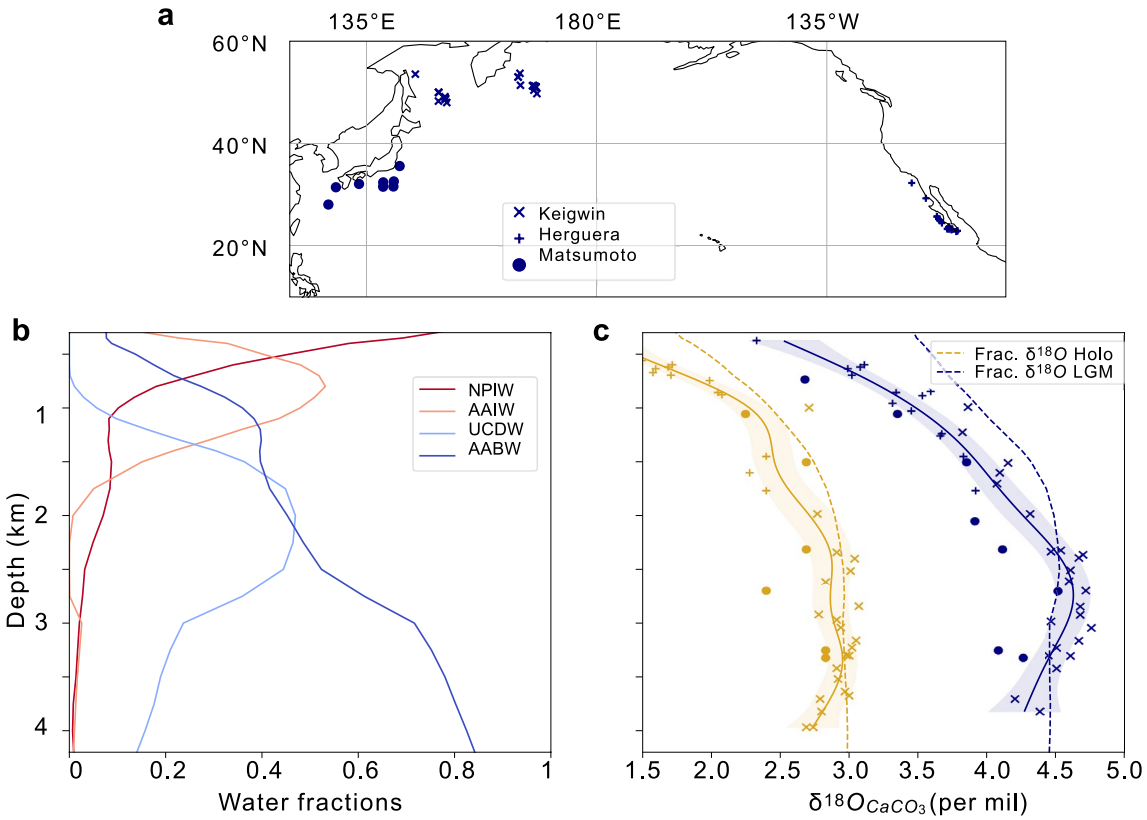

Fig. 4 (**a**) Displays the spatial distribution of our compilation of sediment cores. (**b**) Shows water fractions horizontally averaged between 20°N and 55°N, as estimated here for the modern North Pacific. Red is NPIW, orange is AAIW, light blue is UCDW and navy blue is AABW. (**c**) Shows the North Pacific δ_c data from our compilation of benthic foraminifera as a function of water depth. Time slices for the Late Holocene (yellow) and the LGM (navy blue) were extracted from the different studies. Sediment cores published by Keigwin (1998) are represented by crosses; the ones from Matsumoto et al. (2002), represented by circles; and the ones from Herguera et al. (2010), represented by plus signs. Both modern and glacial data have been fitted with a GAM (solid curves; 95% confidence interval is shaded). The ice volume effect was not subtracted from the glacial data. Reconstructed δ_c profiles from the fractions and appropriate end-member values (see Table 3) are also plotted as dashed curves in (**c**)

highest latitudes and relatively salty waters run along the eastern boundary. As a result, the intermediate-depth sites of Keigwin (1998) are biased toward AABW whereas those of Herguera et al. (2010) are biased toward AAIW and UCDW (Supplementary Figures S3 and S4). These sampling biases should be borne in mind when interpreting the Holocene data; at LGM, however, intermediate-depth data suggest coherent properties throughout the basin (Fig. 4b), likely due to expanded NPIW influence.

We now assess whether we can reconstruct the modern and glacial δ_c profiles with our horizontally-averaged modern water fractions over the North Pacific (Fig. 4b) and appropriate end-member values. This reconstruction thus assumes unchanged water fractions at the LGM relative to today. We denote by f_i the modern fractions averaged over the North Pacific and by $\delta_{c,i}$ the value of δ_c for each end-member. The reconstructed profile ($\delta_{c,r}$) is then determined at each depth using $\delta_{c,r} = \sum_i f_i * \delta_{c,i}$.

The reconstruction requires end-member values for the LGM, and consistently defined values for the Holocene (Table 3). For the UCDW and AAIW end-members we choose cores around 45°S east of New Zealand (Supplementary Figure S5), an ideal location to capture flow into the Pacific basin (Warren 1973). Finding a core to represent the AABW end-member is difficult because of carbonate dissolution in the deep Pacific and of the scarcity of sufficiently deep cores. Nonetheless, a core near Tasmania exists at a location where the modern neutral density is 28.18 and where modern temperature and salinity are about the same as the AABW end-member values of Table 1; this core is thus chosen for the AABW $\delta_{c,i}$. The determination of NPIW $\delta_{c,i}$ is most ambiguous because we do not know precisely how this water mass evolved during the LGM. We choose to compute the modern NPIW $\delta_{c,i}$ using the equation from Marchitto et al. (2014) that relates δ_c to temperature and $\delta^{18}O_{sw}$. For its glacial counterpart, we exploit our GAM fit to the glacial data (shown

Table 3 Table summarizing the chosen sediment cores and corresponding δ_c end-member values employed to reconstruct the North Pacific δ_c profile in the modern and glacial states

Water mass	Core	Modern γ_n	Modern $\delta^{18}O_{CaCO_3}$	LGM $\delta^{18}O_{CaCO_3}$
AABW	RS147-GC34	28.18	3.01	4.35
UCDW	SO213_2_82-1	27.9	3.00	4.73
NPIW	Computed	26.80	1.55	3.36
AAIW	SO136-003	27.32	2.13	3.91

The modern neutral density (γ_n) at each site is also given. Only the NPIW end-member values were computed and not deduced from one core, because of the complexity of selecting a representative core for this water mass. The *RS147-GC34* core (147.742°E, 45.1°S, 4002 m deep) δ_c values were taken from Moy et al. (2006) while *SO213_2_82-1* (176.602°E, − 45.778°S, 2066 m deep) and *SO136-003* (169.878°E, 42.296°S, 944 m deep) values come from Ronge et al. (2015)

in Fig. 4c) and take the value at 900 m depth, where glacial NPIW is expected to dominate. The $\delta_{c,i}$ values selected are referenced in Table 3.

It is noteworthy that the glacial UCDW δ_c is higher than its AABW and AAIW counterparts, whereas the Holocene end-member values of AABW and UCDW are almost identical (Table 3). These patterns may be understood by considering the two factors affecting δ_c: $\delta^{18}O_{sw}$ and temperature. UCDW is largely ventilated by waters coming from the North Atlantic (Tamsitt et al. 2017; Holzer et al. 2021), and $\delta^{18}O_{sw}$ is higher in deep waters sourced in the North Atlantic than in those formed around Antarctica. Indeed North Atlantic surface waters undergo substantial evaporation as they travel north to their sinking sites (e.g. Worthington 1970), whereas AABW derives its elevated salinity from brine rejection, a process that causes little fractionation of seawater oxygen isotopes (Weiss et al. 1979). Furthermore, the glacial meltwater input at the Antarctic margins lowers the $\delta^{18}O_{sw}$ of AABW (Toggweiler and Samuels 1995b), increasing the $\delta^{18}O_{sw}$ contrast between AABW and NADW. In the present day, North Atlantic deep waters are also warmer than AABW and the deep vertical temperature gradient offsets the impact of the $\delta^{18}O_{sw}$ difference on δ_c, leading to relatively uniform deep ocean δ_c. In contrast during the LGM, deep temperatures may have been more uniform (Adkins et al. 2002) likely allowing a δ_c maximum to emerge at mid-depths.

The reconstructed profiles employing the modern North Pacific fractions (Fig. 4b) and the chosen end-members (Table 3) are shown as dashed lines in Fig. 4c.

We find that the reconstructed profile for the Holocene matches the deep data reasonably well; the mismatches at intermediate depths can largely be explained by the tendency of the Herguera et al. (2010) dataset to over-sample (with respect to the basin mean) AAIW and UCDW at these depths (Supplementary Figures S3 and S4) and the influence of the subtropical gyre at the shallowest sites. We may similarly expect these spatial sampling biases to persist at the LGM, however removing the data from sites below 800 m [below which we expect the influence of the subtropical gyre to be minimal] results in an identical δ_c profile, indicating the steep δ_c gradient in the intermediate depths at the LGM persists once the influence of the subtropical gyre is removed. By contrast, the reconstructed LGM profile fails to reconstruct the glacial data and capture the mid-depth maximum and associated vertical gradients. Modifying the glacial δ_c end-member values over reasonable ranges [by up to 5 times the observed difference] yields the same conclusion: using the modern water fractions, it is not possible to reproduce the shape of the glacial δ_c profile. This implies that a change in water fractions (i.e., a change in circulation and mixing) is required to explain the glacial δ_c observations.

To showcase a possible change in water fractions that would be compatible with observations, we construct idealized profiles of water fractions for the North Pacific at LGM (Fig. 5a). These idealized profiles are guided by four hypotheses. First, we presume that NPIW was expanded and overwhelmingly dominant at intermediate depths, influencing ocean properties down to about 2 km (Rae et al. 2020; Matsumoto et al. 2002; Keigwin 1998; Herguera et al. 2010; Struve et al. 2022). Second, we expect that glacial AAIW was shallower than today (Ronge et al. 2015) and therefore largely absent from the deep North Pacific. Consistent with this expectation, the LGM δ_c of core *SO213_84_2-1* at 972 m depth in the South Pacific, corresponding to glacial AAIW (Ronge et al. 2015), is around 0.25 ‰heavier than the mean δ_c at the same depth in our LGM North Pacific compilation. We thus discard the AAIW end-member for this analysis (i.e. we set the AAIW fraction to zero). Third, we hypothesize that the peak UCDW fractions were situated about 400 m (minus LGM sea level change) deeper than today. This downward shift is suggested by the glacial δ_c observations overlain on the estimated modern UCDW fraction (Fig. 6). Finally, guided by observations (Fig. 4c) and theory (Ferrari et al. 2014), we presume the deep Pacific Ocean to be strongly layered at LGM, such that each water mass occupies virtually all the North Pacific volume within its core depth range.

Combined with the end-member values of Table 3, the idealized profiles of water fractions in Fig. 5a yield a reconstructed glacial δ_c profile that is roughly consistent with the observations deeper than 1 km (Fig. 5b). The slight overestimation of the mid-depth maximum is consistent with overestimation of the peak UCDW fraction, which was set to 1 over 2.2–3 km depth, an unrealistically high value given erosion by vertical mixing of the UCDW signature as it spreads northward. Still, much

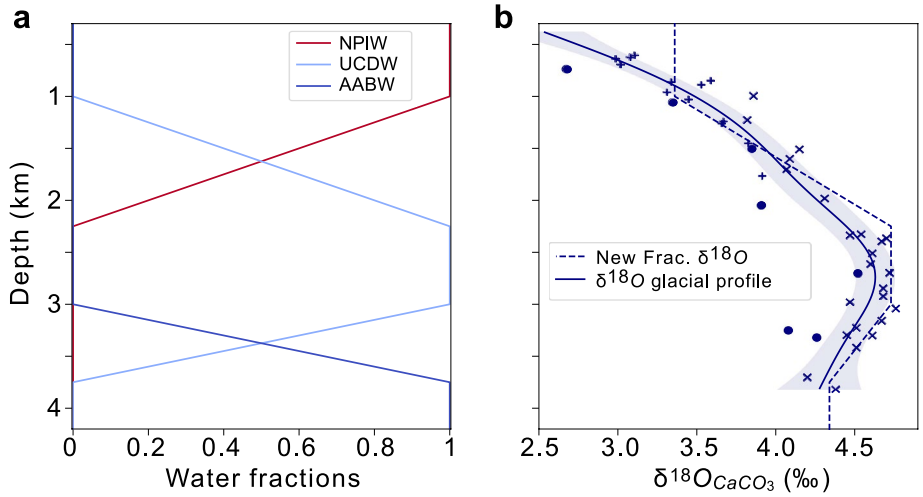

Fig. 5 (**a**) shows idealized fractions for the glacial North Pacific (20–55°N) as a function of depth. Red is NPIW, light blue is UCDW and navy blue is AABW. In (**b**), we show the glacial δ_c data and GAM fit (solid line and 95% confidence interval shaded) as presented in Fig. 4c, together with the reconstructed profile using the idealized water fractions (dashed line). Sediment cores published by Keigwin (1998) are represented by crosses; the ones from Matsumoto et al. (2002), represented by circles; and the ones from Herguera et al. (2010), represented by plus signs

larger mid-depth UCDW fractions than the modern estimates (see Fig. 6) are necessary to reproduce the observed mid-depth bulge in glacial δ_c—unless our end-member values grossly underestimate the source water-mass contrasts. This analysis thus bolsters the hypothesis of a stronger water-mass layering in the glacial deep North Pacific than today, presumably caused by reduced vertical diffusion or increased isopycnal diffusion or both.

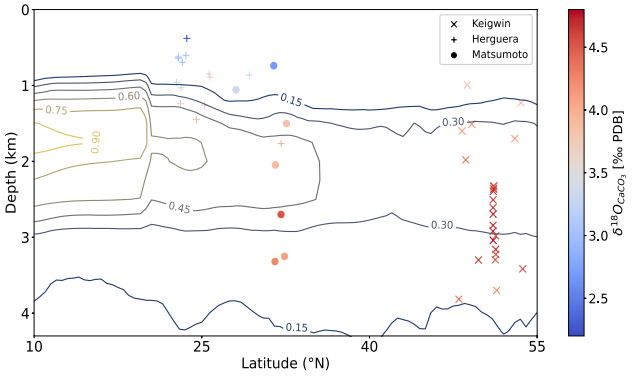

Fig. 6 The δ_c glacial data from our compilation is shown by shaded symbols, as a function of the latitude and water depth of each core. Crosses denote data from Keigwin (1998), plus signs data from Herguera et al. (2010) and circles data from Matsumoto et al. (2002). Contours show the zonally averaged UCDW fraction as estimated for the modern state

4.3 Geothermal heat hypothesis

We asserted that the mid-depth maximum in δ_c apparent in the LGM North Pacific data is too large to be explained by pressure-driven increase of in-situ temperature. However, the ~ 0.3‰difference we observe between 3 and 4 km depth (Figs. 4c and 6) could be driven, in theory (Marchitto et al. 2014), by a ~ 1.5 °C temperature increase from 3 to 4 km depth. If the abyssal Pacific was strongly stratified in salinity, such a temperature inversion could have existed without destabilizing the water column. The difference in absolute salinity between 4 and 3 km depth would need to exceed 0.33 g/kg (taking absolute salinity and conservative temperature at 4 km to be near 36 g/kg and 0.5 °C, respectively), about 17 times the present-day difference. Given that dense waters formed around Antarctica and in the high-latitude Atlantic were close to freezing point at LGM (Adkins et al. 2002), geothermal heating is the only possible source of this hypothetical abyssal heat reservoir (see Adkins et al. 2005).

Several considerations cast doubt on the ability of geothermal heating to explain, alone, the observed mid-depth maximum in glacial δ_c. First, a 1.5 °C temperature excess at 4 km relative to 3 km requires a substantial (at least threefold) increase in the residence time of Pacific bottom waters (deeper than 4 km) compared to today, and an even larger increase in the vertical geothermal heat gradient. Indeed it is estimated that present-day geothermal heating drives less than 0.5 °C warming in North Pacific waters deeper than 4 km, and about half this warming at 3 km depth (Adcroft et al. 2001; Emile-Geay and Madec 2009). Proxy estimates of Pacific abyssal flows (McCave et al. 2008) and

radiocarbon estimates (Rafter et al. 2022) do not suggest such a large residence time of the glacial Pacific bottom waters. In addition, the mid-depth maximum in δ_c appears to be larger in the southwestern Pacific (Table 3) than in the North Pacific (4c), whereas geothermal heating is expected to cause abyssal warming that increases from south to north (Adcroft et al. 2001; Emile-Geay and Madec 2009). Hence, we consider it highly unlikely that geothermal heating can be the primary cause of the increase in abyssal to mid-depth δ_c. Nonetheless, we cannot exclude that the imprint of geothermal heating on Pacific abyssal temperatures was larger than today, and that it contributes to increase the apparent influence of isopycnal diffusion from the south in the mid-depths.

5 Discussion

5.1 Vertical and lateral influences on Pacific mid-depths

Our analysis of modern tracer distributions, especially $\delta^{18}O_{sw}$ from LeGrande and Schmidt (2006), and sediment archives of LGM δ_c (Keigwin 1998; Matsumoto et al. 2002; Herguera et al. 2010), indicates that mid-depth (1.5–3 km) Pacific waters are not merely a mixture of waters lying below and above. A sizeable influence from Southern Ocean UCDW on Pacific mid-depths is inferred. This south-to-north isopycnal ventilation pathway is theoretically compatible with net southward volume transport at these depths (Fig. 1a), since strong isopycnal diffusion could overwhelm the influence of the overturning (Naveira Garabato et al. 2017). However, the estimated percentage influence of UCDW on the mid-depth North Pacific in the modern (Fig. 3c) and glacial (Fig. 5a) states advocates for weak vertical diffusion and overturning in this layer (Fig. 1b). We thus propose that relatively weak overturning allows isopycnal diffusion and recirculation to emerge as the primary communication pathway between Pacific mid-depths and surrounding oceans, in accord with a recent inverse model analysis (Holzer et al. 2021).

Beyond these common characteristics, the glacial and modern states appear to differ in important ways. In particular, the deep North Pacific may have been more strongly layered at LGM than it is today. Increased layering could arise from one or a combination of the following: (i) larger contrasts in source (end-member) water masses, (ii) increased isopycnal diffusion at mid-depths, and (iii) reduced vertical diffusion. More efficient isopycnal communication between Southern Ocean and North Pacific mid-depths in the glacial state could have contributed to maintain a more distinct water-mass signature at these depths. However it is not clear why isopycnal diffusion rates should have been much larger at LGM; this scenario would imply a widespread increase in mesoscale eddy energy or decrease in mixing suppression by mean flows (Groeskamp et al. 2020; Abernathey et al. 2022). On the other hand, an increase in water-mass and density contrasts, together with reduced vertical mixing, appear to be plausible. Indeed, large LGM Antarctic sea ice seasonality (Crosta et al. 2022) is expected to strengthen the salinity contrast between bottom and intermediate waters (Ferrari et al. 2014; Haumann et al. 2016; Galbraith and de Lavergne 2019), potentially contributing to strong salinity-based stratification in the deep North Pacific (Adkins et al. 2002). In turn, increased stratification could have reduced vertical mixing rates, since vertical diffusivity is inversely proportional to vertical density gradient for a given power input to mixing (Osborn 1980).

5.2 Evidence from carbon isotopes

Carbon isotope observations provide some independent support for our interpretations of modern and glacial Pacific ventilation. In Fig. 7, we show the dominating end-member (as diagnosed in Sect. 3) and the zonally averaged radiocarbon distribution ($\Delta^{14}C$, from de Lavergne et al. (2017)) overlain with contours of the UCDW fraction, within the modern main Pacific. The $\Delta^{14}C$ minimum is located at mid-depths between 30 and 45°N (Fig. 7b). The fact that this minimum is not located further north (i.e., further away from the southern sources of ventilation) concurs with the inferred upwelling of abyssal tracers in the subarctic Pacific. The latitudinal position of the $\Delta^{14}C$ minimum appears to lie at the junction between the declining influence of UCDW towards the north, and the rising influence of AABW in the subarctic Pacific, as illustrated by the dominant water-mass distribution shown in Fig. 7a. What causes the rise of the AABW fraction and associated upwelling of tracers in the subarctic Pacific remains unknown, however. Potential causes include high vertical mixing, low isopycnal mixing and wind-driven uplifting (Toggweiler et al. 2019; Sigman et al. 2021).

In the cores that we used for the analysis of oxygen isotopes, the carbon isotopic ratio $\delta^{13}C$ of benthic foraminifera was also measured. Although $\delta^{13}C$ is not conservative since remineralization of organic matter lowers the ratio (Duplessy et al. 1988), it provides a source of information complementary to δ_c. In Fig. 8, we show both the modern and glacial $\delta^{13}C$ from the same cores that we used in Sect. 4. In the modern ocean, $\delta^{13}C$ increases from 2.5 to 4 km depth, suggesting an older water mass at mid-depths than in the abyss. In the glacial ocean, $\delta^{13}C$ exhibits a very different shape, with a minimum centred near 2.5 km depth, similar to the depth of the δ_c maximum (Figs. 4c and 5b). This shape is qualitatively consistent with a relatively isolated mid-depth layer, sandwiched between younger AABW and expanded NPIW. Additionnally, the differences in glacial $\delta^{13}C$ between the dataset from the

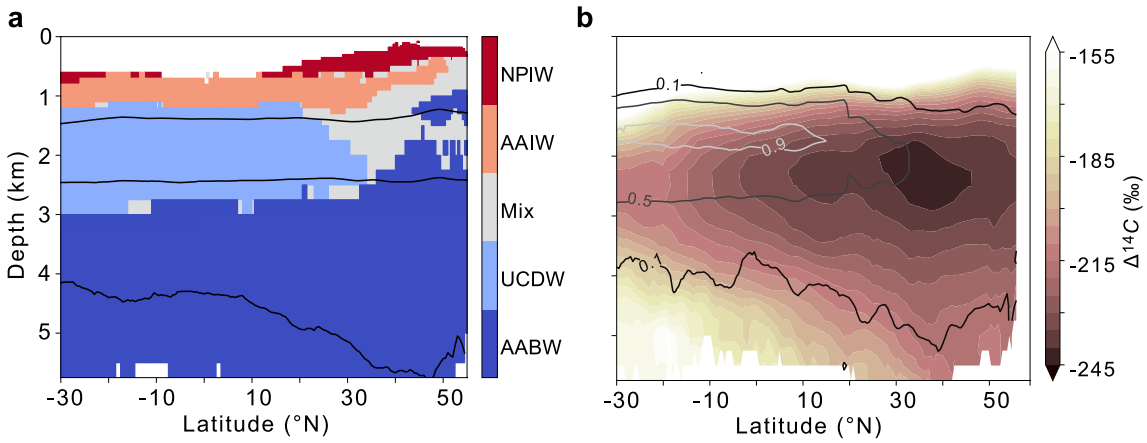

Fig. 7 The dominating zonally averaged water fraction in the main Pacific is shaded in (**a**). A fraction is defined as dominant when superior to the sum of the other three. Grey shading indicates Where no fraction dominates ("Mix" zone). The characteristic isopycnals of the UCDW and AABW end-members are shown as black curves. In (**b**), the zonal mean modern $\Delta^{14}C$ distribution is shaded, and the zonal mean UCDW fraction is contoured. This figure illustrates that the radiocarbon minimum is located at the end of the UCDW tongue, near the "Mix" zone, where ventilation by isopycnal diffusion and diapycnal diffusion appears to be weakest

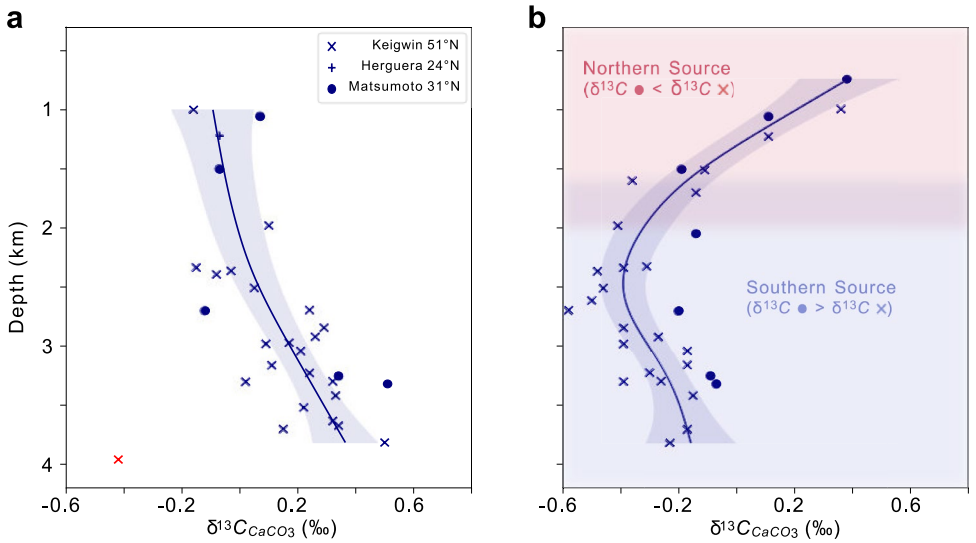

Fig. 8 (**a**) Shows the modern $\delta^{13}C$ values from our North Pacific compilation as a function of water depth. (**b**) Shows the equivalent for the LGM. In both panels, the data have been fitted with a GAM (dashed curves; 95% confidence interval is shaded). In (**a**), the deepest core (*Vinogr GGC-17_2*, in red) was left out of the GAM calculation because of the large anomaly relative to the other modern values. In (**b**), light blue shading indicates a southern ventilation source, while red shading indicates a northern source, as deduced from the geographical $\delta^{13}C$ gradients (i.e. the differences between datasets of Keigwin (1998) and Matsumoto et al. (2002)). Data from Keigwin (1998) are marked with crosses, from Matsumoto et al. (2002) with circles, and from Herguera et al. (2010) with plus signs (only one $\delta^{13}C$ value is available from the latter study, in (**a**)). In (**a**), the latitude indicated next to the name of the authors corresponds to the average latitude of each study's cores

coast of Japan (Matsumoto et al. 2002) and that near the Bering Strait (Keigwin 1998) (see Fig. 5a) corroborate the notion that ventilation was dominantly south-to-north deeper than 1.5–2 km, and dominantly north-to-south at intermediate depths (see shading in Fig. 8b). Indeed, when moving toward the north (from circles to crosses in Fig. 8b), $\delta^{13}C$ becomes lighter (respectively heavier) in the deeper (respectively shallower) part of the water column. Furthermore, the vertical gradient between mid-depths (2–3 km) and deeper waters also appears to increase toward the north; although uncertain, this pattern

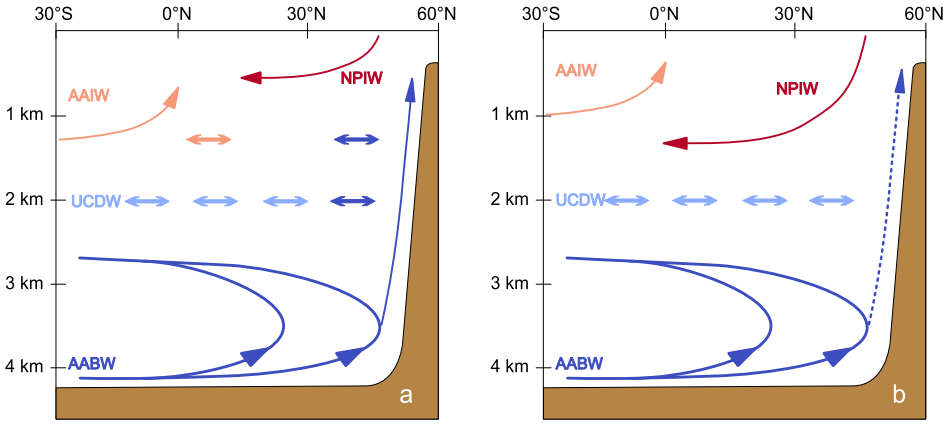

Fig. 9 Proposed modern (**a**) and glacial (**b**) Pacific ocean circulation regimes. Curved arrows denote major circulation branches while double-headed straight arrows denote isopycnal diffusion and recirculation. In the glacial state, an expansion of NPIW to the detriment of AAIW may have taken place at intermediate depths, while stronger stratification in deeper layers may have decreased the upwelling of abyssal tracers in the subarctic Pacific leading to an increased northward penetration of UCDW. Note that the inferred slight deepening of the UCDW influence at LGM is not represented on the schematic for simplicity; this deepening probably results from the other circulation changes

would suggest that strong layering extended into the glacial subarctic Pacific.

5.3 Implications for glacial carbon storage

Together, oxygen and carbon isotopes thus suggest increased layering of the different water masses in the North Pacific at the LGM relative to present. An increase in deep stratification probably reduced the upwelling of abyssal tracers, leading to the increased layering observed in the deep Pacific. This was possibly associated with stronger NPIW influence in the upper 1.5 km. The combined NPIW expansion and reduced AABW influence in the mid-depths of the subarctic Pacific would have resulted in a stronger and slightly deeper UCDW influence at mid-depths. These circulation changes are summarized in Fig. 9. Modern upwelling of abyssal tracers in the subarctic Pacific influences the tracer distributions at mid and intermediate depths, acting as an important return pathway for nutrients (Sarmiento et al. 2004; Holzer et al. 2021). A reduction in the upwelling of abyssal tracers at LGM would limit the return path of remineralized nutrients through the mid-depths which would thus reduce CO_2 outgassing from the surface. A host of biogeochemical tracers suggest a reduction in the supply of nutrients and carbon to the surface of the subarctic Pacific during the LGM (Jaccard et al. 2009; Ren et al. 2015; Gray et al. 2018), despite climate models indicating a substantial increase in wind-driven upwelling within the region under glacial boundary conditions (Gray et al. 2018, 2020). This can be explained by the reduced influence of AABW and increased influence of NPIW at intermediate depths (Fig. 9), which would have lowered the nutrient concentrations of the upwelling waters (Rae et al. 2020). Furthermore, the expansion of NPIW provides a new-source of low-preformed nutrient water in the global ocean, providing a mechanism to lower atmospheric CO_2 (Rae et al. 2020). These changes are complementary and would work together to increase the efficiency of the biological pump: the expansion of NPIW lowers the ocean's preformed nutrient inventory, while reduced vertical mixing in the deep ocean would trap remineralised nutrient in the abyss. The proposed changes in ventilation thus likely imply an increase in oceanic carbon storage during glacial times relative to present.

Over deglaciation, upwelling from the abyssal subarctic Pacific appears to have increased around the onset of the Bolling-Allerod, roughly coeval with onset of modern rates of NADW formation (Galbraith et al. 2007), bringing carbon-rich deepwaters to the surface in the subarctic Pacific and outgassing CO_2 to the atmosphere (Gray et al. 2018).

6 Conclusion

We analysed the distribution of quasi-conservative tracers, including oxygen isotopes in seawater and benthic foraminifera, to constrain ventilation patterns in the modern and glacial Pacific Ocean. The analysis supports a crucial role for isopycnal diffusion in the ventilation of Pacific mid-depths (1.5–3 km). However, substantial vertical tracer transport from the abyss to the upper ocean appears to overwhelm this isopycnal influence in the modern subarctic Pacific (north of about 40°N). Isotopes of benthic foraminifera ($\delta^{18}O$ and $\delta^{13}C$) from the North Pacific suggest a stronger layering of the deep ocean during the LGM than at present, including a possible suppression of the subarctic bottom-to-surface tracer upwelling. A reduction in vertical mixing linked to increased

stratification in the deep North Pacific, and an expansion of NPIW, may have contributed to these differences. Overall, the inferred changes in ventilation would imply that North Pacific deep waters were more isolated and more carbon rich at LGM than they are today. Further work is required to better understand the drivers of subarctic Pacific upwelling, and to better constrain the LGM North Pacific water-mass structure and its implications for deep ocean carbon storage.

6.1 Supplementary information

This article has five figures in supplementary materials and a csv file containing the North Pacific compilation data. The water fractions and associated error datasets are accessible at: https://doi.org/10.5281/zenodo.8183224.

Supplementary Information The online version contains supplementary material available at https://doi.org/10.1007/s00382-023-06910-8.

Acknowledgements We thank Claire Waelbroeck, Elisabeth Michel, Nathaëlle Bouttes, James Rae and Kazuyo Tachikawa for helpful discussions. We are grateful to two anonymous reviewers for their thoughtful and constructive comments. DMR is supported by CNRS and VU Amsterdam.

Funding Financial support was provided by a thesis grant from the French Alternative Energies and Atomic Energy Commission (CEA), the French national LEFE programme through the ROOF project, and ANR grant CARBCOMP.

Data availability The water fractions and associated error datasets are accessible at https://doi.org/10.5281/zenodo.8183224.

Declarations

Conflict of interest The authors have no competing interests to declare that are relevant to the content of this article.

References

Abernathey R, Gnanadesikan A, Pradal MA et al (2022) Chapter 9—isopycnal mixing. In: Meredith M, Naveira Garabato A (eds) Ocean mixing. Elsevier, Amsterdam, pp 215–256. https://doi.org/10.1016/B978-0-12-821512-8.00016-5

Adcroft A, Scott JR, Marotzke J (2001) Impact of geothermal heating on the global ocean circulation. Geophys Res Lett 28(9):1735–1738. https://doi.org/10.1029/2000GL012182

Adkins JF (2013) The role of deep ocean circulation in setting glacial climates. Paleoceanography 28(3):539–561. https://doi.org/10.1002/palo.20046

Adkins JF, McIntyre K, Schrag DP (2002) The salinity, temperature, and $\delta^{18}O$ of the glacial deep ocean. Science 298(5599):1769–1773. https://doi.org/10.1126/science.1076252

Adkins JF, Ingersoll AP, Pasquero C (2005) Rapid climate change and conditional instability of the glacial deep ocean from the thermobaric effect and geothermal heating. Quatern Sci Rev 24(5):581–594. https://doi.org/10.1016/j.quascirev.2004.11.005

Anderson LA, Sarmiento JL (1994) Redfield ratios of remineralization determined by nutrient data analysis. Global Biogeochem Cycles 8(1):65–80. https://doi.org/10.1029/93GB03318

Augustin L, Barbante C, Barnes PRF et al (2004) Eight glacial cycles from an antarctic ice core. Nature 429(6992):623–628. https://doi.org/10.1038/nature02599

Broecker WS, Takahashi T, Takahashi T (1985) Sources and flow patterns of deep-ocean waters as deduced from potential temperature, salinity, and initial phosphate concentration. J Geophys Res Oceans 90(C4):6925–6939. https://doi.org/10.1029/JC090iC04p06925

Crosta X, Kohfeld KE, Bostock HC et al (2022) Antarctic sea ice over the past 130 000 years—part 1: a review of what proxy records tell us. Climate Past 18(8):1729–1756. https://doi.org/10.5194/cp-18-1729-2022

Curry W, Oppo D (2005) Glacial water mass geometry and the distribution of δ 13c of ΣCO_2 in the western atlantic ocean. Paleoceanography 20:859–869. https://doi.org/10.1029/2004PA001021

de Lavergne C, Madec G, Roquet F et al (2017) Abyssal ocean overturning shaped by seafloor distribution. Nature 551(7679):181–186. https://doi.org/10.1038/nature24472

de Lavergne C, Groeskamp S, Zika J et al (2022) Chapter 3—the role of mixing in the large-scale ocean circulation. In: Meredith M, Naveira Garabato A (eds) Ocean Mixing. Elsevier, Amsterdam, pp 35–63. https://doi.org/10.1016/B978-0-12-821512-8.00010-4

Duplessy JC, Shackleton NJ, Fairbanks RG et al (1988) Deep water source variations during the last climatic cycle and their impact on the global deep water circulation. Paleoceanography 3(3):343–360. https://doi.org/10.1029/PA003i003p00343

Emile-Geay J, Madec G (2009) Geothermal heating, diapycnal mixing and the abyssal circulation. Ocean Sci 5(2):203–217. https://doi.org/10.5194/os-5-203-2009

Ferrari R, Jansen MF, Adkins JF et al (2014) Antarctic sea ice control on ocean circulation in present and glacial climates. Proc Natl Acad Sci 111(24):8753–8758. https://doi.org/10.1073/pnas.1323922111

Galbraith E, de Lavergne C (2019) Response of a comprehensive climate model to a broad range of external forcings: relevance for deep ocean ventilation and the development of late cenozoic ice ages. Clim Dyn 52(1):653–679. https://doi.org/10.1007/s00382-018-4157-8

Galbraith ED, Jaccard SL, Pedersen TF et al (2007) Carbon dioxide release from the north pacific abyss during the last deglaciation. Nature 449(7164):890–893. https://doi.org/10.1038/nature06227

Ganachaud A, Wunsch C (2000) Improved estimates of global ocean circulation, heat transport and mixing from hydrographic data. Nature 408(6811):453–457. https://doi.org/10.1038/35044048

Gouretski V, Koltermann KP (2004) Woce global hydrographic climatology. Berichte des BSH 35:1–52

Gray WR, Rae JWB, Wills RCJ et al (2018) Deglacial upwelling, productivity and CO_2 outgassing in the north pacific ocean. Nat Geosci 11(5):340–344. https://doi.org/10.1038/s41561-018-0108-6

Gray WR, Wills RCJ, Rae JWB et al (2020) Wind-driven evolution of the north pacific subpolar gyre over the last deglaciation. Geophys Res Lett 47(6):e2019GL086328. https://doi.org/10.1029/2019GL086328

Groeskamp S, LaCasce JH, McDougall TJ et al (2020) Full-depth global estimates of ocean mesoscale eddy mixing from observations and theory. Geophys Res Lett 47(18):e2020GL089,425. https://doi.org/10.1029/2020GL089425

Haumann FA, Gruber N, Münnich M et al (2016) Sea-ice transport driving southern ocean salinity and its recent trends. Nature 537(7618):89–92. https://doi.org/10.1038/nature19101

Hautala SL (2018) The abyssal and deep circulation of the northeast pacific basin. Prog Oceanogr 160:68–82. https://doi.org/10.1016/j.pocean.2017.11.011

Herguera J, Herbert T, Kashgarian M et al (2010) Intermediate and deep water mass distribution in the pacific during the last glacial maximum inferred from oxygen and carbon stable isotopes. Quatern Sci Rev 29(9):1228–1245. https://doi.org/10.1016/j.quascirev.2010.02.009

Herguera JC, Jansen E, Berger WH (1992) Evidence for a bathyal front at 2000-m depth in the glacial pacific, based on a depth transect on Ontong Java plateau. Paleoceanography 7(3):273–288. https://doi.org/10.1029/92PA00869

Holzer M, DeVries T, de Lavergne C (2021) Diffusion controls the ventilation of a pacific shadow zone above abyssal overturning. Nat Commun 12(1):4348. https://doi.org/10.1038/s41467-021-24648-x

Jaccard S, Galbraith E, Sigman D et al (2009) Subarctic pacific evidence for a glacial deepening of the oceanic respired carbon pool. Earth Planet Sci Lett 277(1):156–165. https://doi.org/10.1016/j.epsl.2008.10.017

Jackett DR, McDougall TJ (1997) A neutral density variable for the world's oceans. J Phys Oceanogr 27(2):237–263. https://doi.org/10.1175/1520-0485(1997)027<0237:ANDVFT>2.0.CO;2

Johnson GC (2008) Quantifying Antarctic bottom water and North Atlantic deep water volumes. J Geophys Res Oceans. https://doi.org/10.1029/2007JC004477

Kawasaki T, Hasumi H, Tanaka Y (2021) Role of tide-induced vertical mixing in the deep pacific ocean circulation. J Oceanogr 77(2):173–184. https://doi.org/10.1007/s10872-020-00584-0

Keigwin LD (1998) Glacial-age hydrography of the far northwest pacific ocean. Paleoceanography 13(4):323–339. https://doi.org/10.1029/98PA00874

Key RM (2004) A global ocean carbon climatology: results from global data analysis project (GLODAP). Global Biogeochem Cycles 18(4):GB4031. https://doi.org/10.1029/2004GB002247

LeGrande AN, Schmidt GA (2006) Global gridded data set of the oxygen isotopic composition in seawater. Geophys Res Lett. https://doi.org/10.1029/2006GL026011

Lund DC, Adkins JF, Ferrari R (2011) Abyssal Atlantic circulation during the last glacial maximum: constraining the ratio between transport and vertical mixing. Paleoceanography. https://doi.org/10.1029/2010PA001938

Marchitto T, Curry W, Lynch-Stieglitz J et al (2014) Improved oxygen isotope temperature calibrations for cosmopolitan benthic foraminifera. Geochim Cosmochim Acta 130:1–11. https://doi.org/10.1016/j.gca.2013.12.034

Matsumoto K, Oba T, Lynch-Stieglitz J et al (2002) Interior hydrography and circulation of the glacial pacific ocean. Quatern Sci Rev 21(14):1693–1704. https://doi.org/10.1016/S0277-3791(01)00142-1

McCave I, Carter L, Hall I (2008) Glacial–interglacial changes in water mass structure and flow in the SW Pacific Ocean. Quatern Sci Rev 27(19):1886–1908. https://doi.org/10.1016/j.quascirev.2008.07.010

McDougall TJ, Barker PM (2011) Getting started with teos—10 and the gibbs seawater (gsw) oceanographic toolbox. SCOR/IAPSO WG127, ISBN 978-0-646-55621-5

McDougall TJ, Jackett DR, Millero FJ et al (2012) A global algorithm for estimating absolute salinity. Ocean Sci 8(6):1123–1134. https://doi.org/10.5194/os-8-1123-2012

Moreno AR, Larkin AA, Lee JA et al (2022) Regulation of the respiration quotient across ocean basins. AGU Adv. https://doi.org/10.1029/2022AV000679

Moy AD, Howard WR, Gagan MK (2006) Late quaternary palaeoceanography of the circumpolar deep water from the south Tasman rise. J Quarten Sci 21:763–777. https://doi.org/10.1002/jqs.1067

Naveira Garabato AC, MacGilchrist GA, Brown PJ et al (2017) High-latitude ocean ventilation and its role in Earth's climate transitions. Philos Trans R Soc A Math Phys Eng Sci 375(2102):20160,324. https://doi.org/10.1098/rsta.2016.0324

Okazaki Y, Timmermann A, Menviel L et al (2010) Deepwater formation in the North Pacific during the last glacial termination. Science 329(5988):200–204. https://doi.org/10.1126/science.1190612

Olsen A, Key RM, van Heuven S et al (2016) The global ocean data analysis project version 2 (GLODAPV2)—an internally consistent data product for the world ocean. Earth Syst Sci Data 8(2):297–323. https://doi.org/10.5194/essd-8-297-2016

Osborn TR (1980) Estimates of the local rate of vertical diffusion from dissipation measurements. J Phys Oceanogr 10(1):83–89. https://doi.org/10.1175/1520-0485(1980)010<0083:EOTLRO>2.0.CO;2

Rae JWB, Broecker W (2018) What fraction of the Pacific and Indian oceans' deep water is formed in the southern ocean? Biogeosciences 15(12):3779–3794. https://doi.org/10.5194/bg-15-3779-2018

Rae JWB, Sarnthein M, Foster GL et al (2014) Deep water formation in the north Pacific and deglacial CO_2 rise. Paleoceanography 29(6):645–667. https://doi.org/10.1002/2013PA002570

Rae JWB, Gray WR, Wills RCJ et al (2020) Overturning circulation, nutrient limitation, and warming in the glacial North Pacific. Sci Adv 6(50):eabd1654. https://doi.org/10.1126/sciadv.abd1654

Rafter PA, Gray WR, Hines SK et al (2022) Global reorganization of deep-sea circulation and carbon storage after the last ice age. Sci Adv. https://doi.org/10.1126/sciadv.abq5434

Ren H, Studer AS, Serno S et al (2015) Glacial-to-interglacial changes in nitrate supply and consumption in the Subarctic North Pacific from microfossil-bound n isotopes at two trophic levels. Paleoceanography 30(9):1217–1232. https://doi.org/10.1002/2014PA002765

Ronge TA, Steph S, Tiedemann R et al (2015) Pushing the boundaries: glacial/interglacial variability of intermediate and deep waters in the Southwest Pacific over the last 350,000 years. Paleoceanography 30(2):23–38. https://doi.org/10.1002/2014PA002727

Sarmiento JL, Gruber N, Brzezinski MA et al (2004) High-latitude controls of thermocline nutrients and low latitude biological productivity. Nature 427(6969):56–60. https://doi.org/10.1038/nature02127

Sigman DM, Boyle EA (2000) Glacial/interglacial variations in atmospheric carbon dioxide. Nature 407(6806):859–869. https://doi.org/10.1038/35038000

Sigman DM, Fripiat F, Studer AS et al (2021) The southern ocean during the ice ages: a review of the antarctic surface isolation hypothesis, with comparison to the North Pacific. Quatern Sci Rev 254(106):732. https://doi.org/10.1016/j.quascirev.2020.106732

Stewart AL (2017) Mixed up at the sea floor. Nature 551(7679):178–179. https://doi.org/10.1038/551178b

Struve T, Wilson DJ, Hines SKV et al (2022) A deep Tasman outflow of Pacific waters during the last glacial period. Nat Commun 13(1):3763. https://doi.org/10.1038/s41467-022-31116-7

Talley LD (1993) Distribution and formation of North Pacific intermediate water. J Phys Oceanogr 23(3):517–537. https://doi.org/10.1175/1520-0485(1993)023<0517:DAFONP>2.0.CO;2

Talley LD (2013) Closure of the global overturning circulation through the Indian, Pacific, and southern oceans: schematics and transports. Oceanography 26(1):80–97

Tamsitt V, Drake HF, Morrison AK et al (2017) Spiraling pathways of global deep waters to the surface of the southern ocean. Nat Commun 8(1):172. https://doi.org/10.1038/s41467-017-00197-0

Toggweiler J, Samuels B (1995) Effect of drake passage on the global thermohaline circulation. Deep Sea Res I 42(4):477–500. https://doi.org/10.1016/0967-0637(95)00012-U

Toggweiler JR, Samuels B (1995) Effect of sea ice on the salinity of Antarctic bottom waters. J Phys Oceanogr 25(9):1980–1997. https://doi.org/10.1175/1520-0485(1995)025<1980:EOSIOT>2.0.CO;2

Toggweiler JR, Druffel ERM, Key RM et al (2019) Upwelling in the ocean basins north of the ACC: 1. On the upwelling exposed by the surface distribution of Δ14c. J Geophys Res Oceans 124(4):2591–2608. https://doi.org/10.1029/2018JC014794

Warren BA (1973) Transpacific hydrographic sections at lats. 43°s and 28°s: the scorpio expedition—II. Deep water. Deep-Sea Res Oceanogr Abstr 20(1):9–38. https://doi.org/10.1016/0011-7471(73)90040-5

Warren BA (1983) Why is no deep water formed in the North Pacific? J Mar Res 41:327–347. https://doi.org/10.1357/002224083788520207

Weiss R, Östlund H, Craig H (1979) Geochemical studies of the Weddell sea. Deep Sea Res Part A Oceanogr Res Pap 26(10):1093–1120. https://doi.org/10.1016/0198-0149(79)90059-1

Wood SN (2011) Fast stable restricted maximum likelihood and marginal likelihood estimation of semiparametric generalized linear models. J R Stat Soc Ser B (Stat Methodol) 73(1):3–36. https://doi.org/10.1111/j.1467-9868.2010.00749.x

Wood SN, Pya N, Säfken B (2016) Smoothing parameter and model selection for general smooth models. J Am Stat Assoc 111(516):1548–1563. https://doi.org/10.1080/01621459.2016.1180986

Worthington L (1970) The Norwegian sea as a Mediterranean basin. Deep-Sea Res Oceanogr Abstr 17(1):77–84. https://doi.org/10.1016/0011-7471(70)90088-4

Supplementary materials for “Oxygen isotope constraints on the circulation of the modern and Glacial Pacific”

Bruno Millet[1], William Gray[1], Casimir de Lavergne[2], Didier Roche[1,3].

[1]Laboratoire des Sciences du Climat et de l’Environnement, LSCE/IPSL, CEA-CNRS-UVSQ, Université Paris-Saclay, Orme des Merisiers, Gif-sur-Yvette, 91191, France.

[2]LOCEAN Laboratory, Sorbonne Université-CNRS-IRD-MNHN, 4 place Jussieu, Paris, 75005, France.

[3]Faculty of Science, Department of Earth Sciences, Vrije Universiteit Amsterdam, Amsterdam, The Netherlands.

Corresponding author: Bruno Millet, Bruno.millet@lsce.ipsl.fr

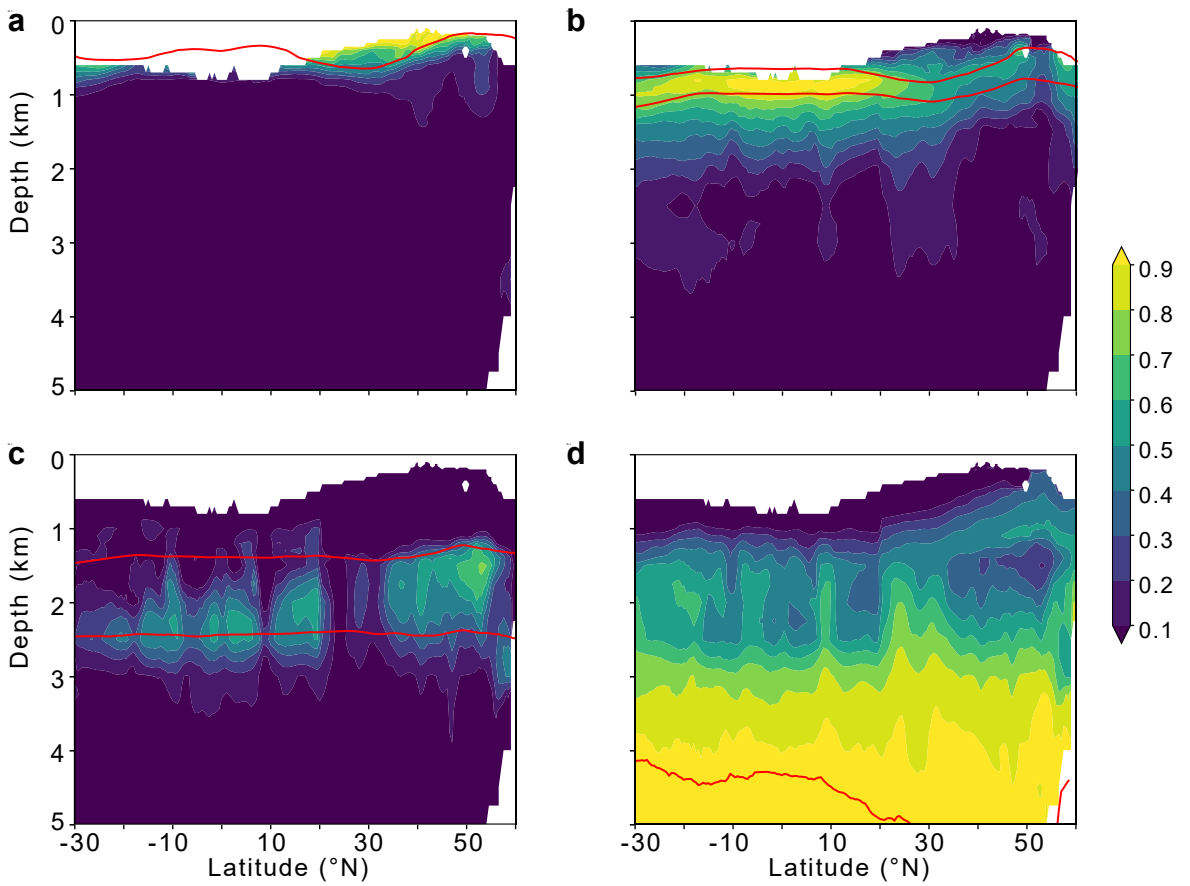

Figure S1. Zonally averaged water fractions over the main Pacific obtained with the following four end-members: NPIW (**a**), AAIW (**b**), PDW averaged at a neutral density $\gamma_n = 27.8\ kg.m^{-3}$ and 40°N (**c**), and AABW (**d**). Red curves delineate the characteristic isopycnals (described in the main text) of each end-member. The PDW fraction suggests that this water mass, as presently defined, does not have a clear circulation pathway and instead embodies a relatively stagnant mixture of surrounding water masses.

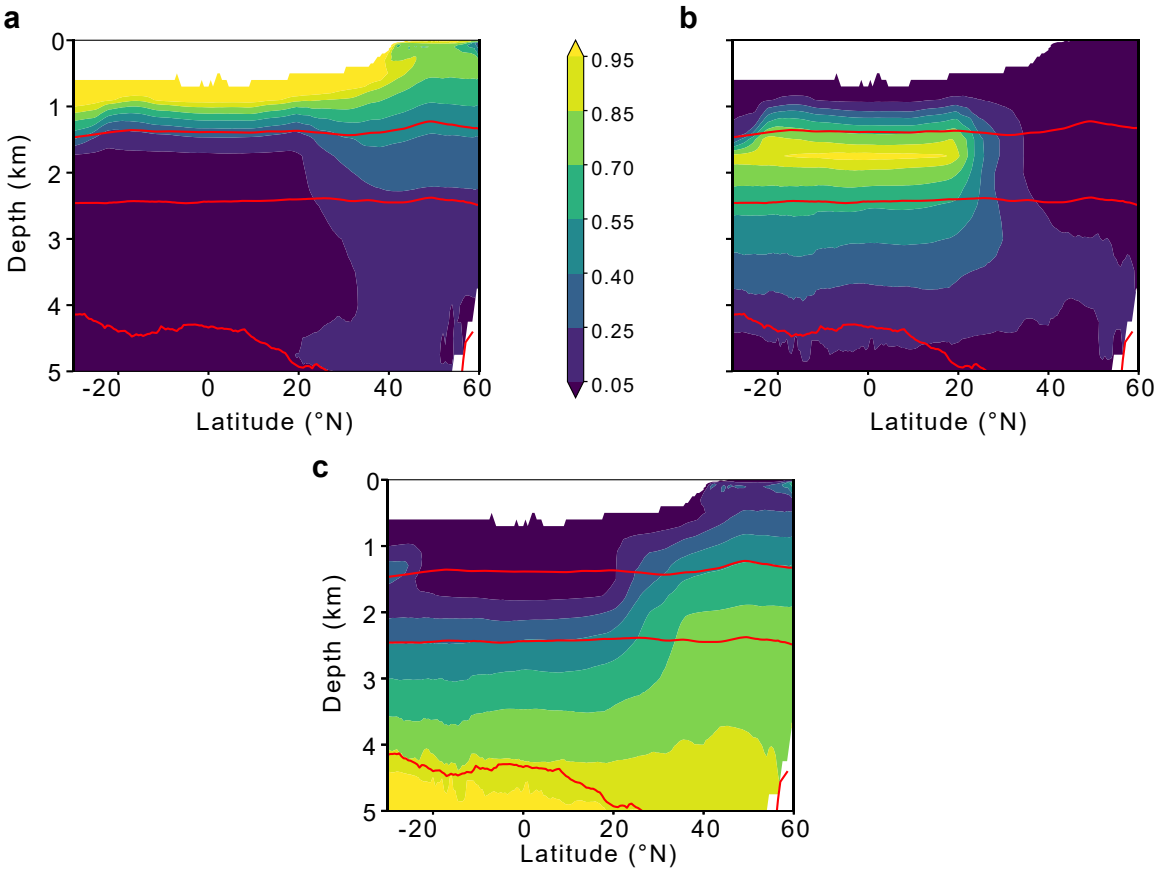

Figure S2. Zonally averaged water fractions over the main Pacific obtained with the following three end-members: AAIW (**a**), UCDW (**b**) and AABW (**c**). In this solution, only two tracers, conservative temperature and preformed salinity, are used to constrain the water fractions. Red curves delineate the characteristic isopycnals of UCDW and AABW, as described in the main text. The UCDW fraction dominates at mid-depth from 30°S to about 30°N; it decreases sharply with latitude near 25°N. This shows that the steep decrease of the UCDW fraction between 20°N and 30°N obtained in the reference solution (Fig. 3 of the article) is not merely driven by patterns of the $\delta^{18}O_{sw}$ product.

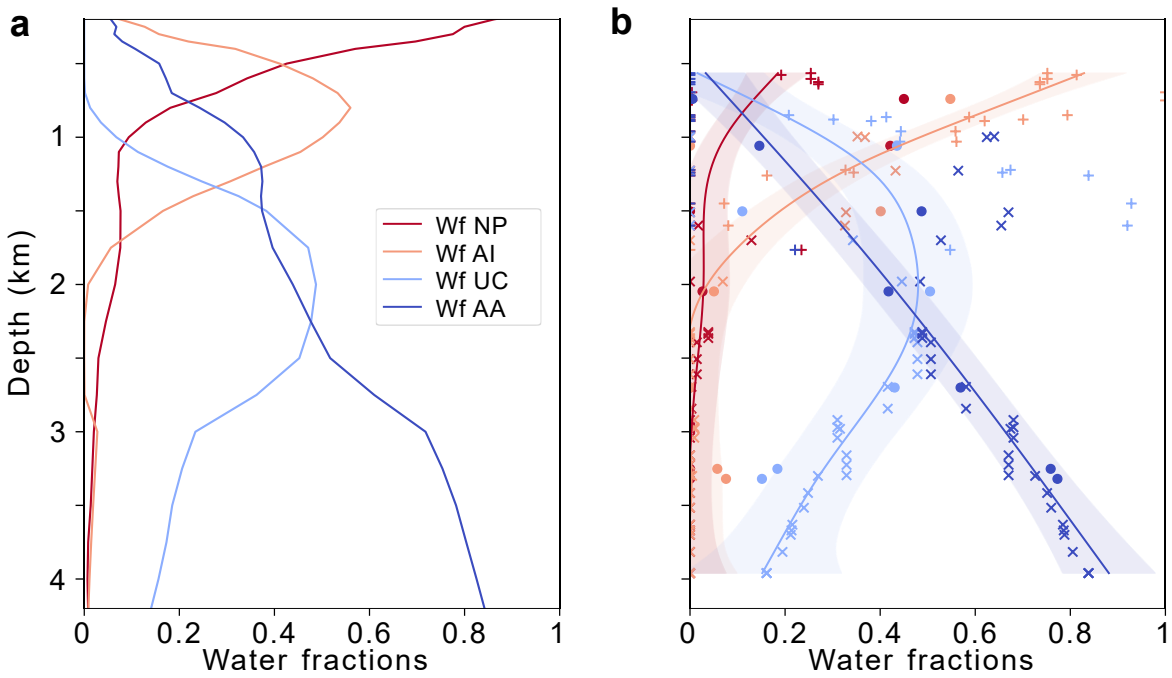

Figure S3. Water fractions horizontally averaged over the North Pacific within 20ºN-55ºN are shown in panel (**a)**. In panel (**b)**, we show the same water fractions sampled at the (longitude, latitude, depth) locations of each sediment core, as a function of depth. When unavailable at the core locations, the water fractions were retrieved from the closest location where the model converged. Core sites from (Keigwin 1998) are marked with crosses, those from (Matsumoto, et al. 2002) with circles and those from (Herguera, et al. 2010) with plus signs. Solid curves are GAM fits through each water fraction scatter, with 95% confidence intervals shown by grey shading. In both panels, colors correspond to the different end-members: red for NPIW, orange for AAIW, light blue for UCDW and navy blue for AABW.

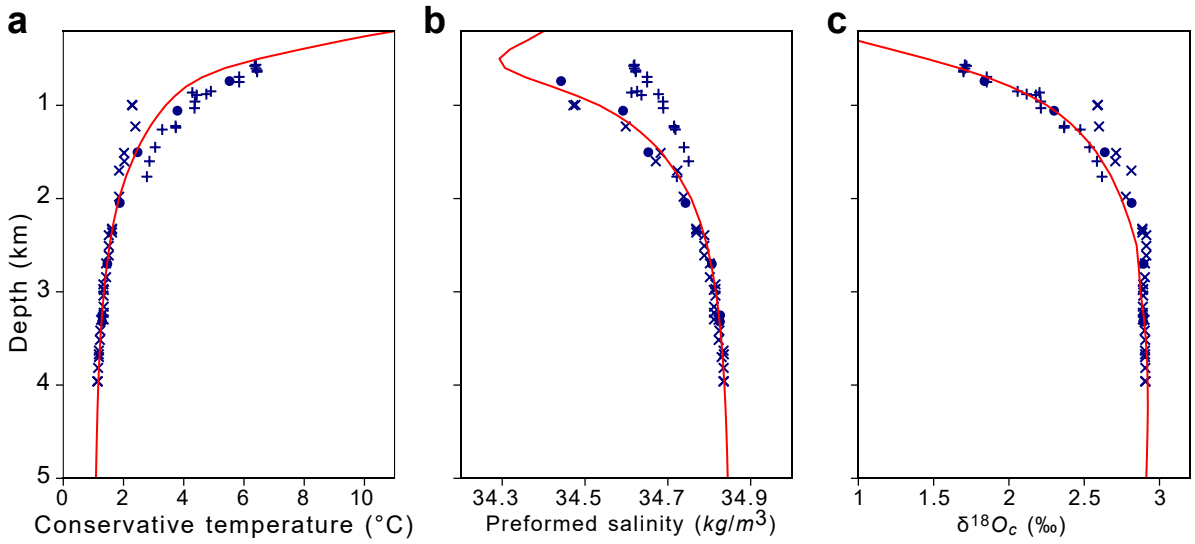

Figure S4. Profiles of conservative temperature (**a**), preformed salinity (**b**) and $\delta^{18}O_{CaCO_3}$ (**c**), averaged over the North Pacific within 20ºN-55ºN (red curves) and sampled at the core locations (blue symbols) the method for Figure S3. Core sites from Keigwin (1998) are marked with crosses, those from Matsumoto et al. (2002) with circles and those from Herguera et al. (2010) with plus signs. The oxygen isotopic ratio of calcite was calculated using the equation of Marchitto et al. (2014) combined with 3D fields of in-situ temperature and $\delta^{18}O_{sw}$.

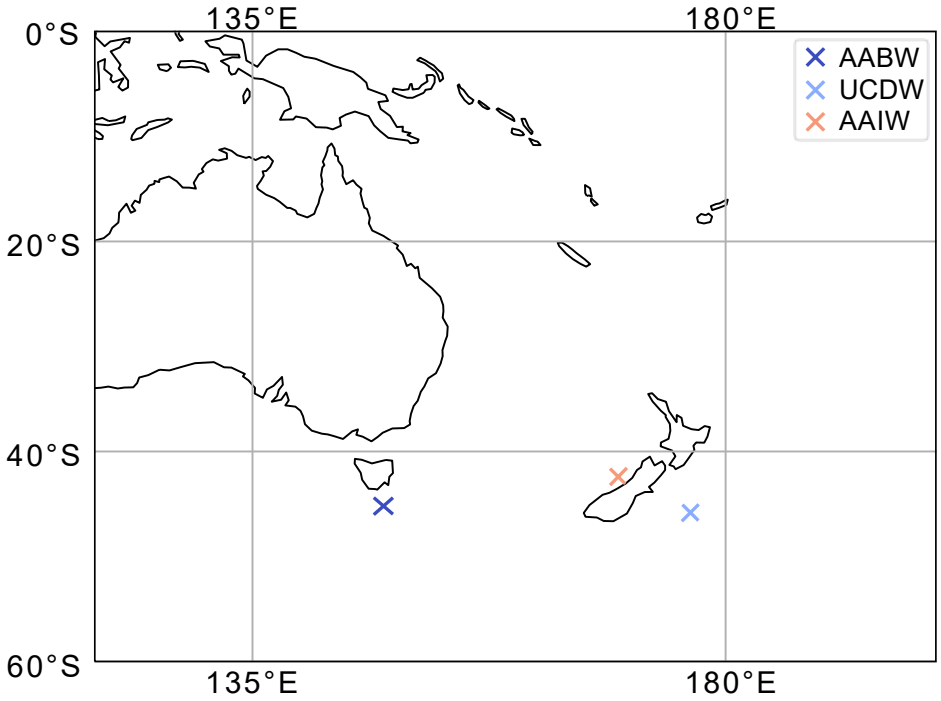

Figure S5. Locations of the sediment cores that have been used to define $\delta^{18}O_{CaCO_3}$ values for our three southern end-members: AABW (navy blue), UCDW (light blue) and AAIW (orange).

References

Herguera, J.C., T. Herbert, M. Kashgarian, et C. Charles. «Intermediate and deep water mass distribution in the Pacific during the Last Glacial Maximum inferred from oxygen and carbon stable isotopes.» *Quaternary Science Reviews* 29, n° 9 (2010): 1228-1245.

Keigwin, LD. «Glacial-age hydrography of the far northwest pacific ocean.» *Paleoceanography* 13, n° 4 (1998): 323–33.

Marchitto, T.M., W.B. Curry, J. Lynch-Stieglitz, S.P. Bryan, K.M. Cobb, et D.C. Lund. «Improved oxygen isotope temperature calibrations for cosmopolitan benthic foraminifera.» *Geochimica et Cosmochimica Acta* 130 (2014): 1-11.

Matsumoto, Katsumi, Tadamichi Oba, Jean Lynch-Stieglitz, et Hirofumi Yamamoto. «Interior hydrography and circulation of the glacial Pacific Ocean.» *Quaternary Science Reviews* 21, n° 14 (2002): 1693-1704.

CHAPTER II

GLOBAL OCEAN VENTILATION: A COMPARISON BETWEEN A GENERAL CIRCULATION MODEL AND DATA-CONSTRAINED INVERSE MODELS

In Chapter I, we have proposed that the mid-depths of the Pacific are largely ventilated through isopycnal diffusion from the south. The end-members we used to highlight this diffusion were defined at 30°S in the Pacific, rather than at the surface, so that ventilation pathways upstream of the 30°S vertical section could not be discussed. Nonetheless, we suggested that the modern $\delta^{18}O_{sw}$ structure in the Pacific could plausibly be explained by a relatively strong presence of waters of North Atlantic origin at mid-depth in the Pacific.

In this chapter, we propose to test these hypotheses by propagating six regional dyes whose source regions pave the whole ocean surface in an OGCM: the Nucleus for European Modelling of the Ocean (NEMO). The NEMO simulations we explore here originate from another study in which I am co-author: "Effects of improved tidal mixing in NEMO one-degree global ocean model", referred to in the text as Rathore et al., (2024), soon to be submitted and attached here in Supplementary Information. In addition, we track the same regional dyes in two data-constrained inverse models, the Ocean Circulation Inverse Model (OCIM) and the Total Matrix Intercomparison (TMI), to evaluate NEMO and to gain deeper insights in steady state ventilation patterns and rates. Ventilation volumes, rates and routes from the six surface regions are thus compared across the three models. We will also resort to different mixing parameterizations in NEMO to assess the impact of isopycnal and diapycnal mixing on tracer distributions in the Pacific Ocean. This work will soon be submitted to the Journal of Advances in Modeling Earth Systems:

- Millet, B., de Lavergne, C., Gray, W.R., Ethé C., Madec, G., Holzer, M., Gebbie, G., and Roche D. M., *in prep*. Global ocean ventilation: a comparison between an ocean general circulation model and data-constrained inverse models.

Abstract

Ocean ventilation, or the transfer of tracers from the surface boundary layer into the ocean interior, is a critical process in biogeochemical cycles and the climate system. Here, we assess steady-state ventilation patterns and rates in three models of ocean transports: a 1° global configuration of the Nucleus for European Modelling of the Ocean (NEMO), a recent 2° solution of the Ocean Circulation Inverse Model (OCIM), and a 2° solution of the Total Matrix Intercomparison (TMI). We release artificial dyes in six surface regions of each model and compare equilibrium dye distributions as well as ideal age distributions. It takes about twice as long as the maximum ideal age to fill 99% of the ocean, and thus for dyes to reach quasi-equilibrium. We find good qualitative agreement in large-scale dye distributions across the three models. However, the distributions indicate that TMI is more diffusive than OCIM, itself more diffusive than NEMO. NEMO simulates a sharp separation between antarctic and subantarctic ventilation zones in the Southern Ocean, leading to a weaker influence of the latter zone on the abyssal ocean. A shallow bias of North Atlantic ventilation in NEMO contributes to a stronger presence of the North Atlantic dye in the mid-depth Southern Ocean and Pacific. This isopycnal communication between the North Atlantic surface and the mid-depth Pacific is very slow, however, and NEMO simulates a maximum age in the North Pacific about 900 years higher than the data-constrained models. Possible causes of this age bias are interrogated with NEMO sensitivity experiments. Implementation of a state-of-the-art observation-based 3D map of isopycnal diffusivity augments the maximum age, due to weaker isopycnal diffusion at depths. Tripling of diapycnal mixing by subinertial internal tides in the North Pacific improves the spatial pattern of ideal age, yet only reduces the age bias by about 150 years. Overly slow ventilation of the Pacific thus persists across experiments encompassing our current best knowledge of diapycnal and isopycnal mixing. We suggest that the dynamics of subarctic Pacific upwelling and ventilation are misrepresented in NEMO, and may be key missing pieces in the representation of global ocean ventilation in general circulation models.

1 . Introduction

Global ocean circulation is often pictured as a gigantic conveyor belt moving tracers across basins, latitudes and layers (Broecker, 1991; Gordon, 1986). Accordingly, large-scale tracer distributions are commonly interpreted to result from transport and sources or sinks along the conveyor belt. In fact, the circuit of the conveyor belt is itself largely deduced from observed tracer distributions (Richardson, 2008; Talley, 2013). This simple paradigm has proven powerful to describe some of the ocean's roles in climate and biogeochemical cycles (Broecker, 1991). However it has been challenged by the observation that the ocean is fundamentally chaotic (Gregg, 1987; Lozier, 2010) and the ensuing demonstration that tracer distributions are shaped by turbulent mixing as much as they are by large-scale currents (Holzer and Primeau, 2006; Naveira Garabato et al., 2017).

The chaotic nature of the ocean represents a formidable challenge for models of ocean tracer transports: such models need to represent mixing along and across density surfaces in addition to capturing the large-scale flows of mass. For example, prognostic Ocean General Circulation Models (OGCMs) employ uncertain parameterizations of isopycnal and diapycnal mixing, which have a prominent influence on simulated tracer distributions and transports (Jones and Abernathey, 2019; Oka and Niwa, 2013) and ultimately on the

climate simulated by coupled ocean-atmosphere GCMs (Hieronymus et al., 2019; Pradal and Gnanadesikan, 2014). Similarly, inverse models that infer ocean transports from observed tracer distributions often resort to a priori constraints and adjustable mixing parameters to reconstruct plausible three-dimensional transport pathways (Hernández-Guerra and Talley, 2016; Holzer et al., 2021). The chosen constraints are partly subjective and can have a substantial impact on the obtained solutions (Groeskamp et al., 2017).

These difficulties in mapping and modelling tracer transports limit our comprehension of global ocean ventilation. Ocean ventilation signifies broadly the transport of tracers from the surface boundary layer to deeper layers. Here we distinguish 'ventilation' from 'subduction' and 'circulation', the latter two terms traditionally referring to mass transports. Tracer transports result both from circulation (or advection) and turbulent mixing (or diffusion). Ocean ventilation is an essential process in the climate system because it affects the baseline climate state and controls the response of ocean heat and carbon reservoirs to perturbations (Gregory et al., 2024; Kwon et al., 2011; Ödalen et al., 2018). In addition, ventilation shapes the distributions of dissolved oxygen, nutrients and other biochemical substances in the ocean interior that are critical to the functioning of marine ecosystems (Davila et al., 2023; Gupta et al., 2022). In spite of these implications, there have been few comprehensive assessments of ventilation patterns and rates in the modern ocean.

It is established that the deeper half of the ocean (below about 2 km depth) is ventilated primarily from localized sources located in the subpolar North Atlantic and on Antarctic shelves (Orsi et al., 2001). Yet the percentage volume filled from each source remains uncertain: studies estimate that the Antarctic source represents between $\sim$ 70% and 300% of its North Atlantic counterpart (DeVries and Primeau, 2011; Gebbie and Huybers, 2010; Holzer et al., 2021; Johnson, 2008). The composition of the voluminous mid-depth (1-3 km) Pacific is most uncertain because these waters do not fall on the mixing line (in temperature-salinity space) between waters of Antarctic origin and North Atlantic origin (Worthington, 1981), nor do they lie on the circuit of the global conveyor belt (de Lavergne et al., 2017; Holzer et al., 2021).

Relatedly, the pathways that connect the surface North Atlantic to the deep Pacific remain debated. Talley (2013) proposed that the vast majority of dense waters formed in the subpolar North Atlantic (collectively referred to as North Atlantic Deep Water, NADW) upwell near Antarctica, where they are converted into colder Antarctic Bottom Water (AABW) which subsequently spreads northward in the abyssal Pacific. A Lagrangian analysis (Rousselet et al., 2021) indicates a more direct route skipping upwelling at high southern latitudes, whereby NADW advects eastward and gains density along the northern flank of the Antarctic Circumpolar Current before moving north in the abyssal Pacific. Recent tracer-based studies highlight two routes and suggest that denser varieties of NADW are incorporated in AABW at southern high latitudes whereas lighter varieties spread diffusively at mid-depths (Holzer et al., 2021; Millet et al., 2023). Such contrasting paradigms for the connectivity between the surface North Atlantic and deep Pacific carry large implications for nutrient and carbon inventories and sensitivities in the global deep ocean (Baker et al., 2023; Kwon et al., 2012).

In the upper half of the ocean (above about 2 km depth), ventilation has been traced primarily to the production and subduction of mode and intermediate waters at latitudes between 30° and 60° (Gebbie and Huybers, 2011; Samelson and Vallis, 1997). Yet the spreading processes and pathways of these water masses in the ocean interior are poorly characterized (Sloyan and Rintoul, 2001; Toggweiler et al., 2019; You, 2003). For example, the degree to which Subantarctic Mode Water and Antarctic Intermediate Water spread into Northern Hemisphere oceans or into the abyssal ocean is largely unknown. The role of mixing

in controlling ventilation by mode and intermediate waters in northern and southern basins is also subject to debate (Fu et al., 2020; Urakawa and Hasumi, 2012).

Counter-intuitively, ventilation rates are often better known than ventilation routes and volumes. Indeed, whereas estimating ventilation patterns generally requires combining numerous tracer distributions, ventilation rates can be constrained more directly using radiocarbon (Gebbie and Huybers, 2012; Holzer et al., 2010) or chlorofluorocarbon (Orsi et al., 2001) measurements. Ventilation rate is usually quantified by the ideal age of seawater, which is the time elapsed since this water was last at the surface. Because a given interior water volume can be fed by different surface-to-interior trajectories of different duration, care must be taken when estimating and interpreting the ideal age of a water volume, which is an effective average across trajectories (England, 1995; Wunsch, 2002). Nuclear bomb radiocarbon (Broecker and Olson, 1960), the Suess effect (Friedli et al., 1986), measurement limitations and temporal variability further complicate ideal age reconstructions. Nevertheless, combining chlorofluorocarbon and radiocarbon measurements provides strong constraints on upper-ocean and deep-ocean ventilation rates (Schlitzer, 2007). Generally, studies indicate rapid ventilation in the deep Atlantic, slower ventilation of the deep North Pacific, reaching a maximum age circa 1,500 years, with the deep Indian Ocean falling in between (DeVries and Primeau, 2011).

Despite the availability of observation-based climatologies of radiocarbon, chlorofluorocarbon and ideal age (Cimoli et al., 2023; de Lavergne et al., 2017; Gebbie and Huybers, 2012; Key et al., 2004), these observations are seldom employed to evaluate OGCM-simulated ventilation rates (Dutay et al., 2002). Indeed, although ideal age is frequently included in OGCM simulations, integration times are generally too short to simulate steady ideal ages (e.g., Adcroft et al., 2019). Evaluation of climate-scale OGCM experiments generally focuses on temperature and salinity distributions, mixed layer depths, and meridional overturning circulation. Given the climatic implications of ocean ventilation and the influence of mixing on ventilation, in-depth evaluation of ventilation patterns and rates that goes beyond overturning streamfunctions is desirable (Dutay et al., 2002; England, 1995).

Here, we evaluate steady-state ventilation patterns and rates simulated by a global NEMO configuration whose nominal horizontal resolution is 1° (Rathore et al., 2024). This simulation includes an ideal age tracer and regional dye tracers that track ventilation emanating from six distinct ocean regions. The evaluation is performed by comparing equivalent tracer distributions in two data-constrained inverse models: a recent 2° solution of OCIM (Holzer et al., 2021), and a 2° solution of TMI (Gebbie and Huybers, 2010; Gebbie and Huybers, 2012). The three models are state-of-the-art but structurally different: in essence, NEMO is dynamically constrained, TMI is observationally constrained, while OCIM is both observationally and dynamically constrained. The employed models and tracers are described in more detail in the next section. In section 3, we examine steady-state ventilation volumes, pathways and rates predicted by the three models. Section 4 further explores salient questions raised by the comparison, namely (i) NADW pathways to the deep Pacific, (ii) sensitivity of the maximum ideal age to mixing parameterizations, (iii) dynamics of the subarctic Pacific and (iv) implications for the glacial ocean. We summarize our findings in section 5.

2 . Methods

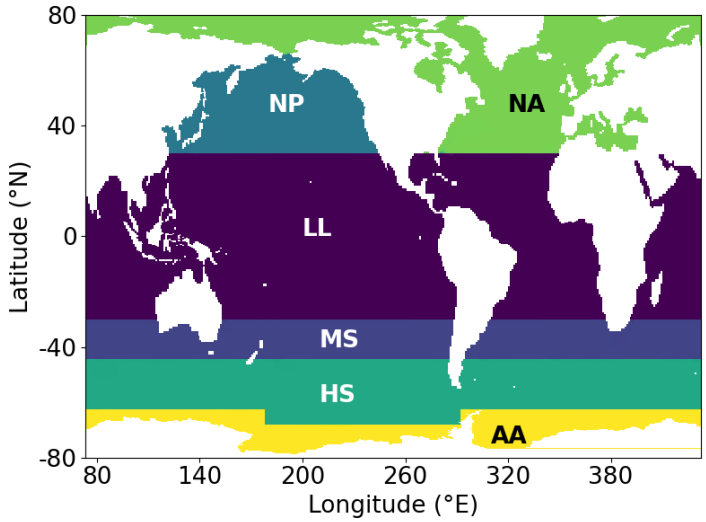

Figure 2.1: Surface regions used to define the six regional dye tracers. From south to north, these regions cover Antarctic polar seas (AA), high southern latitudes (HS), mid southern latitudes (MS), low latitudes (LL), the northern North Pacific (NP), and the northern North Atlantic and Arctic (NA). Region boundaries mostly track longitude circles at 30°N, 30°S, 45°S and 63°S or 68°S.

2.1 . NEMO general circulation model

We employ a global configuration of NEMO that has a nominal horizontal resolution of 1° and 75 layers in the vertical. We build upon the work of Rathore et al. (2024), who performed and evaluated three thousand-year-long experiments with this configuration under climatological COREv2 forcing (Large and Yeager, 2009). They showed that the simulated stratification and circulation are quasi-steady by model year 1,000. In this study, we focus on their experiment 'TRA', which contains the most comprehensive representation of diapycnal mixing by breaking internal tides (Rathore et al., 2024). We run this experiment for an additional year with output at five-day frequency, and then use this output to propagate passive tracers in offline mode. The offline mode implies that velocities, diffusivities and stratification parameters are not computed again but instead read and time-interpolated from five-day output files (corresponding here to model year 1,001), so as to evolve only the passive tracers. The numerical scheme for advection of passive tracers is the same as that used in the online simulation: a second-order Flux Corrected Transport scheme, which is computationally expensive but generates relatively low levels of spurious numerical mixing.

Seven passive tracers are included in the offline simulation: an ideal age tracer and six regional dye tracers released in different regions covering the whole ocean surface (Figure 2.1). The ideal age tracer is restored to zero in the top 10 m, and increases at a rate of 1 year per year deeper than 10 m. This tracer was included in the online simulation and is thus extended offline for another 6,000 years. The regional dye tracers are restored to 1 in the top 10 m within their source region, and restored to zero elsewhere in the top 10 m. Deeper than 10 m, they are conservative, that is, they are only affected by advection and diffusion. The initial state for these dye tracers is zero at every grid point. Like the ideal age tracer, dye tracers are evolved for 6,000 years in our reference offline simulation, which we call REF hereafter.

In order to study the impact of different mixing scenarios on global ocean ventilation, we perform four

Simulation name	K_z includes subinertial contrib.	K_i depends on			Simulated time (years)
		latitude	longitude	depth	
REF	Yes	Yes	Yes	No	6000
DIALOW	No	Yes	Yes	No	3000
DIAHIGH	Yes, tripled in NP	Yes	Yes	No	3000
ISOCST	Yes	Yes	No	No	3000
ISO3D	Yes	Yes	Yes	Yes	3000

Table 1: Summary of NEMO sensitivity experiments. Diapycnal mixing does not change across experiments except for the representation of mixing by subinertial internal tides.

additional offline simulations of 3,000-year duration, as summarized in Table 1. The reference (REF) offline simulation follows the experiment 'TRA' of Rathore et al. (2024): it has an isopycnal diffusivity that is independent of depth but varies with latitude and longitude according to the simulated stratification and flow (Figure 2.2b). Two simulations, ISOCST and ISO3D, are used to assess the influence of isopycnal mixing parameterization on ventilation. In the ISOCST experiment, isopycnal diffusivity varies only with latitude (Figure 2.2a). In the ISO3D experiment, isopycnal diffusivity is set by the static three-dimensional map of Groeskamp et al. (2020), based on observations and theory (Figure 2.2c,d). Note that ISO3D and ISOCST share the same stratification, velocities and diapycnal diffusivities as REF: isopycnal diffusion was not changed during the online simulations. Two more simulations, DIALOW and DIAHIGH, aim to assess the impact of different diapycnal mixing parameterizations. These additional simulations were run online for 1,000 years, then offline for 3,000 years; hence the impact of vertical mixing on stratification and circulation is accounted for. The DIALOW experiment is identical to REF except that it excludes the mixing contribution of subinertial internal tides (corresponding to experiment 'NEW' of Rathore et al., 2024). The DIAHIGH experiment is identical to REF except that the power input to subinertial internal tides in the North Pacific is tripled. Subinertial internal tides are bottom-trapped internal waves generated by tide-topography interactions at latitudes where the tidal frequency is lower than the Coriolis frequency (Chapman, 1989). They exist only poleward of 30° and their contribution to mixing is most significant in subpolar and polar oceans (Müller, 2013).

Most of the forthcoming analysis will focus on the REF simulation, which shares the same isopycnal mixing (K_i) or the same diapycnal mixing (K_z) scheme with other simulations. The different parameterizations will be discussed only in section 4. Hence, unless otherwise stated, all statements about NEMO refer to experiment REF.

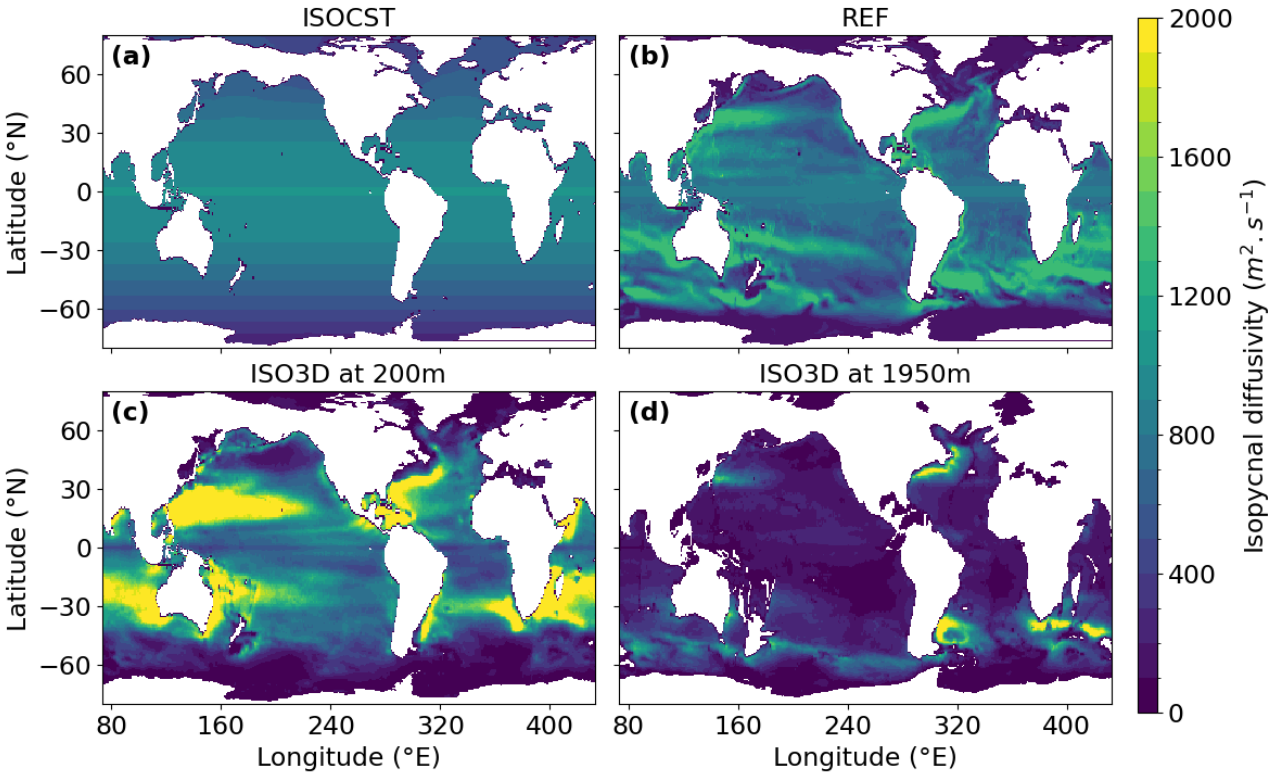

Figure 2.2: Maps of the isopycnal diffusivity used in NEMO sensitivity experiments called ISOCST **(a)**, REF **(b)** and ISO3D **(c,d)**. The diffusivity is independent of depth in both ISOCST and REF. In ISO3D, it varies with depth and is shown here at depths of 200 m **(c)** and 1950 m **(d)**.

2.2 . Inverse models

We use two inverse models, TMI and OCIM, to assess global ocean ventilation and its representation in our NEMO experiments. TMI was developed by Gebbie and Huybers (2010). It connects every point of the ocean interior to every surface point by inverting six tracers: potential temperature, salinity, phosphate, nitrate, oxygen and the oxygen-18 isotopic ratio of seawater. The method relies on the notion that any grid box in the ocean interior exchanges volume with its six neighbours. Assuming steady transports in the ocean, and using volume conservation, volume exchanges can then be deduced from gridded fields of at least five independent tracers. This approach reconstructs connectivity across the global ocean but not ventilation rates. Transport rates were later estimated by Gebbie and Huybers (2012) using the gridded natural radiocarbon climatology of Key et al. (2004). We use the code available at https://github.com/ggebbie/TMI.mat to simulate ideal age and regional dye tracers for 6,000 years. The simulated fields are defined on a regular longitude-latitude grid of uniform 2° resolution, with 33 layers in the vertical. An alternative TMI solution at 4° resolution was also explored but deemed less realistic; we thus restrict our analysis to the 2° solution.

OCIM integrates both dynamical and observational constraints to estimate the mean state of the ocean circulation (DeVries and Primeau, 2011). It uses a linearized dynamical ocean circulation model, with adjustable forcing terms in the horizontal momentum equation determined through minimization of a cost function (DeVries and Primeau, 2011). The density distribution is prescribed following the World Ocean Atlas 2013 climatology (Locarnini et al., 2013; Zweng et al., 2013). In its most recent iteration (Holzer et al., 2021), OCIM deduces isopycnal diffusivities as part of the optimization whereas it prescribes diapycnal diffusivities using the three-dimensional map of de Lavergne et al. (2020). The cost function includes differences between modelled and observed tracer concentrations. Six tracers are assimilated: potential temperature, salinity, natural radiocarbon (Δ^{14}C), chlorofluorocarbon-11, chlorofluorocarbon-12 and helium-3 (δ^3He). Chlorofluorocarbon concentrations help to better constrain the injection of tracers into the thermocline (DeVries, 2014) while δ^3He helps to constrain the abyssal circulation (DeVries and Holzer, 2019). The resolution of the OCIM solution used here (Holzer et al., 2021) is 2° in longitude and latitude and 48 levels in the vertical. As for TMI and NEMO, OCIM-derived transports are used to simulate ideal age and six regional dye tracers for 6,000 years. The analysis of the three models will focus on steady-state distributions, hence on final model years.

2.3 . Equilibration times

Dye tracers can be used to estimate the volume of the ocean filled as a function of model time. We define the total dye as the sum of the six regional dyes. This total dye is uniformly equal to zero in the initial state. From the first time step onward, it is restored to 1 everywhere at the ocean surface, and thus gradually fills the ocean until its concentration reaches 1 in every grid cell. The total dye concentration in a grid cell thus represents the fraction of the cell's volume which has been filled or ventilated. Integrating the total dye concentration over the global ocean volume yields the global volume filled. Steady state is reached when this filled volume equals the model's global ocean volume.

The evolution of the filled volume in TMI, OCIM and the reference (REF) NEMO experiment is shown in Figure 2.3a. It takes almost 6,000 years to fill over 99% of the global ocean volume in REF, compared to only about 3,000 years in TMI and 4,000 years in OCIM. The differences in filled volume across the three models are relatively small during the first 500 years, then the difference between REF and inverse models

increases markedly. This indicates that REF predicts slower ventilation of the weakly ventilated oceanic realms. Indeed, we find that the discrepancy comes largely from the mid-depth Pacific shadow zone, where the mean meridional advection is very weak (de Lavergne et al., 2017; Holzer et al., 2021). The phrase 'shadow zone' refers here to an oceanic domain largely excluded from the meridional overturning circulation (de Lavergne et al., 2017); it is analogous but distinct from upper-ocean shadow zones excluded from the horizontal gyre circulation (Luyten et al., 1983). In REF, the core of this shadow zone, between 1.5 and 3 km in the North Pacific, resists complete ventilation for about 6,000 years (Figure 2.3b). Strikingly, this filling time (taken as the time when the percentage volume filled surpasses 99%) is much larger than the maximum zonal mean Pacific ideal age simulated by REF of about 2,500 years. Similarly, in TMI, the filling time of the shadow zone is about 3,000 years whereas the maximum zonal mean Pacific ideal age is close to 1,600 years. OCIM produces a similar shadow zone as in REF (Holzer et al., 2021), albeit with a reduced filling time of about 4,000 years. This filling time again far exceeds the maximum zonal mean ideal age in OCIM's shadow zone, which is close to 1,600 years.

The difference between filling time and ideal age can be understood as follows: ideal age equilibration requires the uniform interior source to be balanced by transport from the surface sink, whereas dye tracer equilibration requires unbroken transport from surface source to surface sink via the ocean interior. Hence, dye tracer equilibration time is more akin to residence time, which is the sum of time since last surface contact (ideal age) and time to next surface contact (resurfacing time). The large filling times found in the three models, exceeding 3,000 years, underline the need for multi-millennial climate simulations to achieve climate states without artificial deep ocean drift (Gebbie and Huybers, 2019; Jansen et al., 2018).

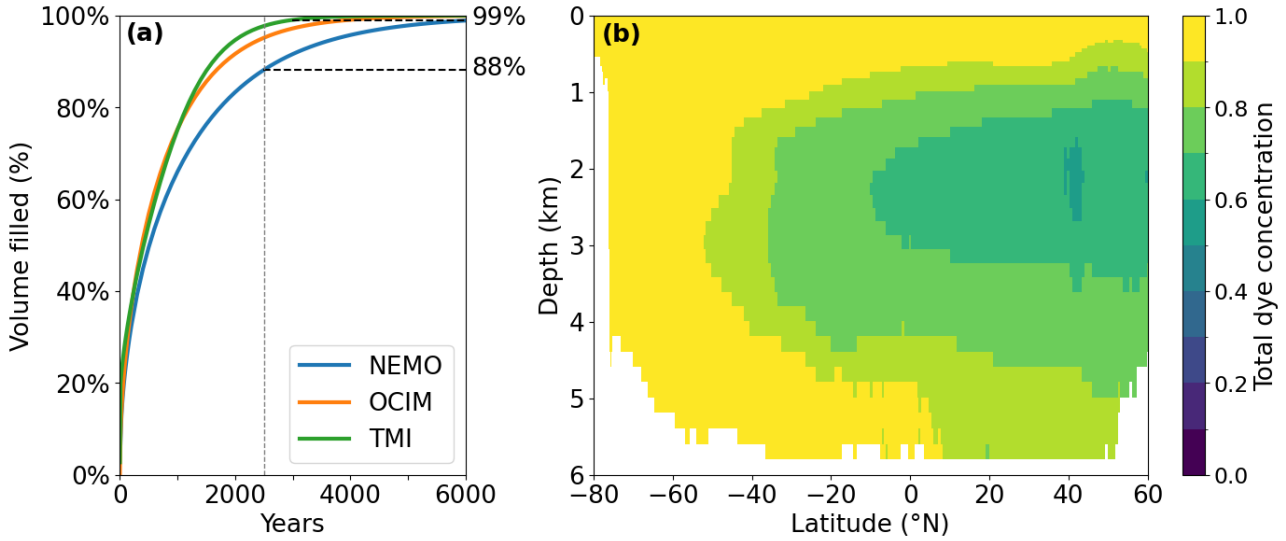

Figure 2.3: Panel **(a)** shows the percentage of the global ocean volume which has been filled as a function of model time, in the reference (REF) NEMO experiment (blue), in OCIM (orange) and in TMI (green). The vertical dashed line marks year 2,500. Panel **(b)** shows the Pacific zonal mean total dye concentration at year 2,500 of the REF simulation. Even though the maximum zonal mean ideal age is about 2,500 years in REF, the core of the shadow zone is only 60% filled by year 2,500.

Despite near-complete filling of the global ocean by year 6,000 in REF, the total dye concentration is

not exactly equal to 1 in all grid cells. To estimate steady-state dye concentrations, we divide each dye concentration by the total dye concentration in every grid cell. This correction assumes that dye proportions at year 6,000 are representative of the steady state; an excellent approximation given the attained near-complete equilibration.

Other NEMO experiments were not carried for 6,000 years and instead stopped at 3,000 years (Table 1). The different mixing parameterizations alter the rates of ventilation of the ocean: for the same year at the same grid cell, the filled volume will vary across the different simulations. In order to compare the different experiments, we first estimate steady-state dye concentrations for each experiment. By year 3,000, about 90% of the ocean has been filled (Figure 2.3a) and dye concentrations evolve quasi linearly in time (Fig. S2.1), so that extrapolation is feasible. We thus estimate the equilibrium concentration $d_i(eq)$ of a dye sourced in region i as a function local dye concentrations at model years 2,900 and 3,000:

$$d_i(eq) = d_i(3000) + \frac{d_i(3000) - d_i(2900)}{\sum_j [d_j(3000) - d_j(2900)]} \times \left(1 - \sum_j d_j(3000)\right) \tag{II.1}$$

The equilibrium dye concentration is thus the concentration at year 3,000 plus the product of the centennial variation from year 2,900 to 3,000 and the corresponding number of centuries to equilibrium; the latter number being estimated as the ratio of the volume fraction yet to be filled to the centennial variation of the total dye. This extrapolation ensures that the equilibrium total dye concentration, $\sum_j d_j(eq)$, is equal to 1. We assess the accuracy of this extrapolation by applying it to REF, for which we know (to a very good approximation) the true equilibrium concentrations. We find differences between true and extrapolated equilibrium dye concentrations of less than half a percent in the Pacific zonal mean (Fig. S2.2). This demonstrates the predictive accuracy of equation (1).

As with the dye concentrations, the ideal age tracer is not fully equilibrated after 3,000 years of simulation. A similar extrapolation can be performed to estimate the steady-state ideal age $A(eq)$ in NEMO sensitivity experiments:

$$A(eq) = A(3000) + \frac{A(3000) - A(2900)}{\sum_j [d_j(3000) - d_j(2900)]} \times \left(1 - \sum_j d_j(3000)\right) \tag{II.2}$$

Again, we validate this extrapolation by applying it to the REF experiment which was extended to 6,000 years. We find differences of less than 2.5% between extrapolated and true equilibrium ideal ages (S2.3).

3 . Results

We now compare the steady-state dye and ideal age distributions in REF, OCIM and TMI.

3.1 . Dye volumes and distributions

The contributions of each surface source region to the volume of the global, Atlantic and Pacific oceans are shown in Figure 2.4. In this and following figures, Atlantic and Pacific oceans are extended to Antarctica: boundaries south of 32°S are 68°W, 25°E for the Atlantic and 150°E, 68°W for the Pacific. There is good agreement overall in the ventilated volumes across the three models. The northern North Atlantic (NA) and Antarctic (AA) regions contribute each about a third of the global ocean volume, while high southern latitudes (HS) contribute about a fifth (Figure 2.4a). In the Atlantic, almost 60% of the volume is ventilated from NA, about two times more than from AA (Figure 2.4b). Conversely, in the Pacific, about 60% of the volume is ventilated south of 45°S (AA and HS), and only about 25% from the NA region (Figure 2.4c). The 45°S-30°N latitude band (LL and MS) ventilates about 10% of the Pacific, Atlantic and global ocean volumes. The northern North Pacific (NP) ventilates about 5% of the Pacific volume, and virtually none of the Atlantic.

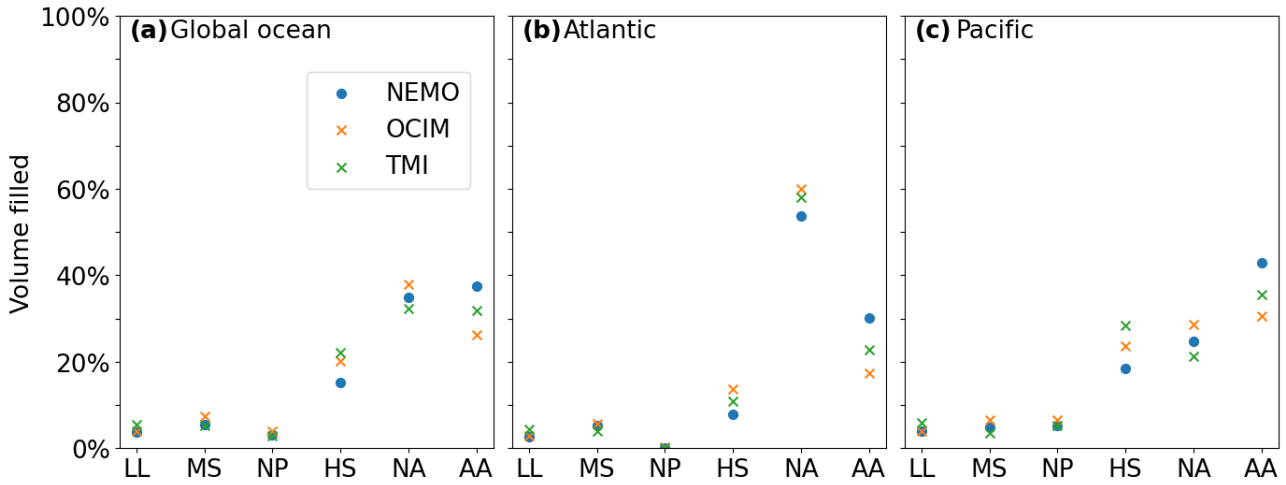

Figure 2.4: Percentage volume ventilated from each surface region. The contributions of Antarctic (AA), high southern (HS), mid southern (MS), low latitude (LL), North Atlantic (NA) and North Pacific (NP) surface regions—as defined in Figure 1—to the global **(a)**, Atlantic **(b)** and Pacific **(c)** ocean volumes are given. The blue circle corresponds to the REF experiment of NEMO, the orange cross to OCIM and the green cross to TMI. Atlantic and Pacific basins are extended to Antarctica, thus spanning the 80°S-65°N latitude range.

Differences between REF and either OCIM or TMI are of the same order of magnitude as differences between the two data-constrained models (Figure 2.4). REF tends to have more water of Antarctic origin: the AA global volume fraction of REF is 0.04 and 0.11 higher than its TMI and OCIM counterparts, respectively. At global scale, this excess is mostly compensated by a smaller volume contribution of the neighbouring HS region. However, in the Atlantic, compensation occurs mostly through a deficit of NA water. The most noticeable difference between the two inverse models is the larger contribution of NA in OCIM, which manifests mostly outside of the Atlantic and goes with a weaker influence of HS and AA regions.

Similarity in ventilation volumes does not warrant similarity in ventilation patterns. Ventilation patterns

in the Atlantic are illustrated in Figure 2.5. In all three models, a clear layering is apparent: the top two hundred meters equatorward of 30° are ventilated by the low latitude region (LL), thermocline waters immediately beneath (0.2-0.5 km) largely originate from 45°S-30°S (MS), HS dominates the ventilation of intermediate layers around 0.5-1.5 km depth, NA ventilates the bulk of the deep Atlantic between 1.5 and 3.5 km depth, and AA takes over in densest layers. The two data-constrained models display strong resemblance of their dye distributions, despite weaker vertical gradients in TMI compared to OCIM. REF shows the strongest layering, including a sharp separation between NA and AA dyes near 3.5 km depth. This stronger layering in REF is associated with overly pure and abundant AA dye in the abyssal Atlantic, and overly pure and abundant NA dye in the overlying mid-depths. This bias likely stems from the lack of dense varieties of NADW overflowing from the Nordic seas (Rathore et al., 2024), a common deficiency of OGCM simulations (Danabasoglu et al., 2014). It should be noted that REF has little bias in the overall density stratification of the water column (Rathore et al., 2024); hence biases cannot be attributed to overly dense AABW and overestimated deep stratification.

In the Pacific, zonal mean dye concentrations also show broad qualitative similarity between the three models (Figure 2.6). The AA dye decreases from the bottom upward and dominates throughout much of the deep Pacific, up to about 2 km depth. The HS dye is predominant between 0.5 and 2 km depth between 60°S and 30°N; it is also important in deeper layers within TMI. This indicates that ventilation from the subantarctic zone spreads well into the Northern Hemisphere. By contrast, the NP dye is largely confined to the Northern Hemisphere and depths shallower than 1.5 km. The NA dye has a strong but relatively uniform influence throughout depths greater than 1.5 km. Finally the LL and MS dyes fill mostly the top 500 m of the low-latitude Pacific.

Major differences in Pacific ventilation patterns are also apparent. In TMI, the HS dye spreads downward into the abyssal ocean, such that it plays a major role for the deep South Pacific ventilation (Figure 2.6j). Such vertical penetration is less pronounced in OCIM and even less so in REF (Figure 2.6k,l). In the North Pacific, the NP dye spreads deeper in the inverse models than it does in REF (Figure 2.6g-i), suggesting that NEMO simulates vertical transports that are too weak within this region. REF also stands out for its distinct mid-depth maximum of the NA dye up to about 20°N (Figure 2.6o). This mid-depth maximum is visible in the Southern Ocean of OCIM but altogether absent in TMI (Figure 2.6m,n). A mid-depth maximum of the NA dye exists in all three models in the Atlantic sector of the Southern Ocean (Figure 2.5m-o); however in REF this maximum is higher and less rapidly eroded in the Antarctic Circumpolar Current (Fig. S2.4). The northward penetration of this mid-depth tongue of NA dye in the Pacific is due to isopycnal diffusion rather than circulation (Millet et al., 2023).

A recurring feature in the analyzed dye distributions is the lower contribution of the HS surface region to deep ocean ventilation in REF compared to OCIM and especially to TMI. Both TMI and OCIM predict the HS dye to spread into the abyssal ocean, whereas REF does not. This difference may stem from differing levels of deep diapycnal mixing and/or from differing degrees of entrainment of the HS dye in the lower branch of the overturning (see Figures 2.5j-l and 2.6j-l). To shed light on these possibilities, we show in Figure 2.7 the total dye concentration (minus the NA dye concentration) at depths of 300 m and 1 km in the Southern Ocean, after only 100 years of simulation.

A ventilation minimum is visible in TMI, OCIM and REF at 300 m depth between the Polar Front and the Antarctic continental slope (Figure 2.7a,c,e). We interpret this ventilation desert as the signature of advective upwelling, which is focused in this area of the Southern Ocean (Gray et al., 2023; Styles et al.,

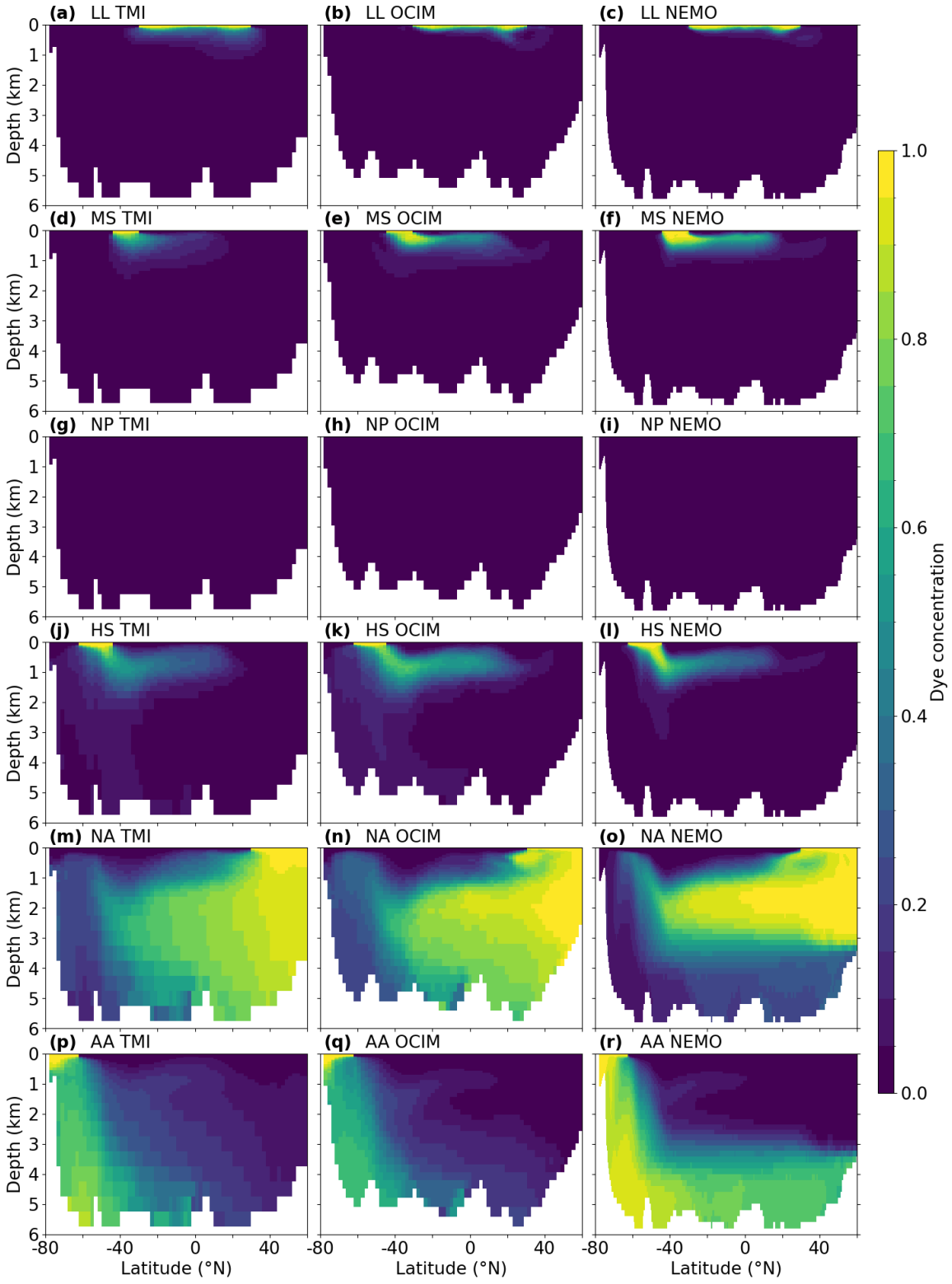

Figure 2.5: Zonal means of the LL **(a-c)**, MS **(d-f)**, NP **(g-i)**, HS **(j-l)**, NA **(m-o)** and AA **(p-r)** dye concentrations over the Atlantic basin for TMI (left column), OCIM (middle column) and the REF NEMO experiment (right column).

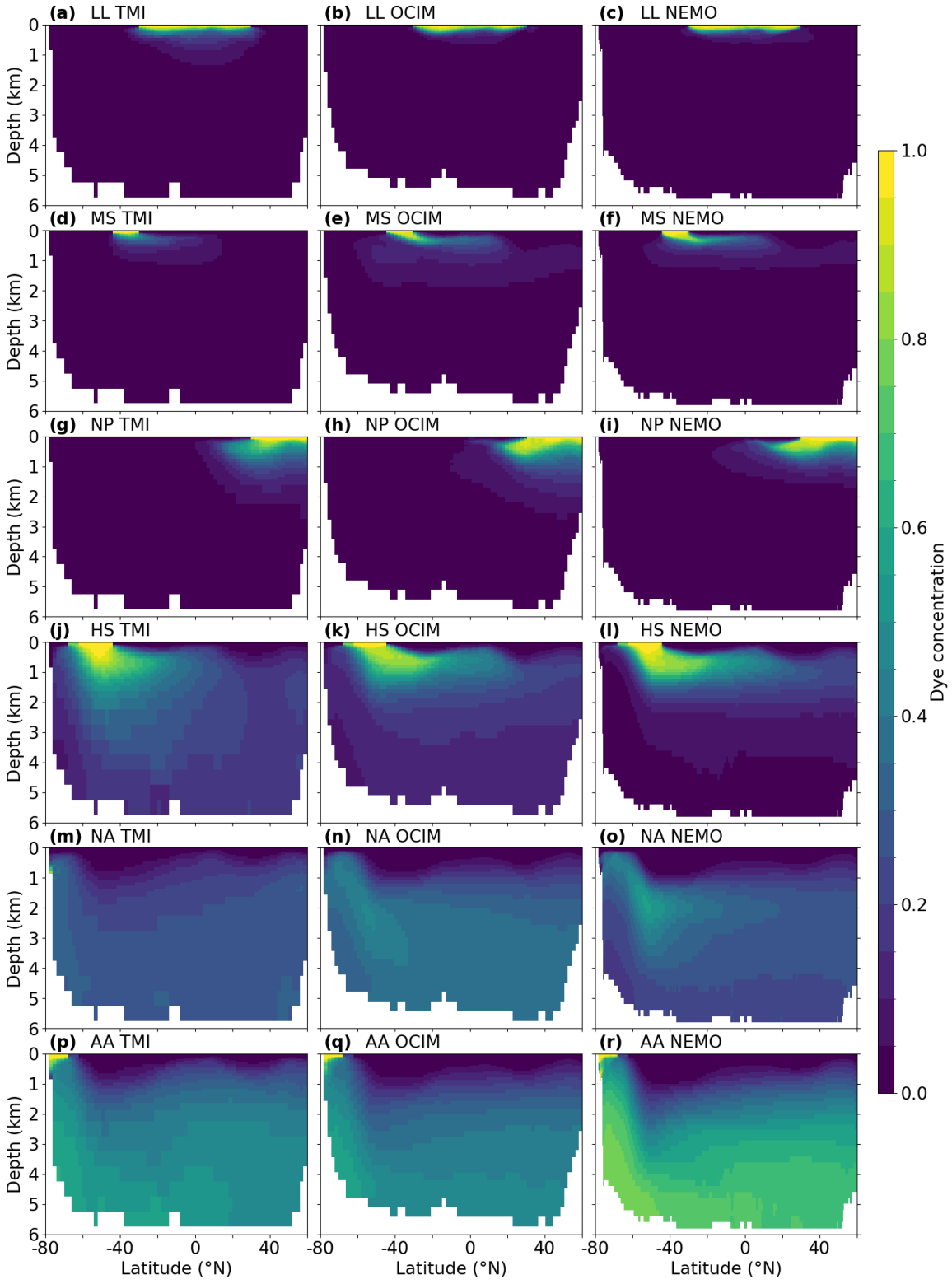

Figure 2.6: Zonal means of the LL **(a-c)**, MS **(d-f)**, NP **(g-i)**, HS **(j-l)**, NA **(m-o)** and AA **(p-r)** dye concentrations over the Pacific basin for OCIM (left column), TMI (middle column) and the REF NEMO experiment (right column).

2024). The separation between the HS and AA regions (red line in Figure 2.7) largely tracks the ventilation minimum, providing justification to the choice of boundary. Beyond these shared patterns, the ventilation desert is evidently more pronounced in REF, such that AA and HS dyes barely mix in the subsurface Southern Ocean, each following a distinct physical ventilation route. By contrast, ventilation is more geographically diffuse in OCIM, and still more in TMI, such that AA and HS dyes intertwine at depth and partly share antarctic and subantarctic ventilation routes. Furthermore, the surface released dye propagates faster and deeper in the Antarctic Circumpolar Current in both inverse models (Figure 2.7b,d,f), suggesting higher effective mixing there.

3.2 . Quantifying water-mass mixing

The foregoing qualitative analysis of dye distributions suggests that REF predicts stronger layering and reduced mixing of the different dyes than do both inverse models. Here we quantify the degree to which dyes mix with other dyes (Figure 2.8a) or mix across density surfaces (Figure 2.8b) in the three models. The first measure of 'diffusiveness' does not distinguish between isopycnal and diapycnal mixing: it is simply the average dye concentration weighted by dye volume. Each dye (i) occupies a global total volume V_i. At every grid cell n, we know the volume of the cell $V(n)$, the dye concentration $C_i(n)$, and thus the volume occupied by the dye $V_i(n) = V(n) \times C_i(n)$. We can thus compute the average dye concentration weighted by the volume it occupies, $C_{i,avg}$, as follows:

$$C_{i,avg} = \frac{\sum_n C_i(n) \times V_i(n)}{V_i} \tag{II.3}$$

If this weighted average concentration is close to one, it implies that the dye is extremely pure on average; in other words, it remains largely separated from other dyes. If instead the weighted average concentration of a dye is close to the global volume fraction it fills (cf Figure 2.4a), dilution is maximum. We find that REF is least diffusive in that its dyes tend to have higher weighted average concentrations (Figure 2.8a). The difference is largest for the LL, MS and AA dyes, hence for the lightest and densest water masses, which are much less diluted in REF than in OCIM or TMI. For the HS, NP and NA dyes, differences across the three models are less pronounced.

The hierarchy between the three models and the different dyes is more obvious when only mixing across density surfaces is considered. To quantify degrees of diapycnal diffusion, we first bin the ocean volume as a function of annual mean σ_2 (the potential density referenced to 2,000 dbars) in each of the three models. We then repeat this calculation for each dye, that is, we bin dye volumes as a function of σ_2. We thus obtain the density distribution of total water volume, and the density distribution of dye volume, for each dye and each model. Should a dye be completely mixed across the global ocean, its concentration would be uniform and its distribution as a function of σ_2 would mirror the distribution of total water volume. To measure the degree of mixing, we thus normalize all distributions and calculate the Euclidean distance (E_i) between the volume distribution for a given dye ($V_i(\sigma_2)$) and the distribution for total water volume ($V(\sigma_2)$):

$$E_i = \| V(\sigma_2) - V_i(\sigma_2) \| \tag{II.4}$$

The larger the distance, the lower the bulk diapycnal mixing. We find that this distance is systematically larger for REF than for TMI and OCIM (Figure 2.8b). Differences between TMI and OCIM vary across dyes: LL, MS and NP dyes spread more across isopycnals in OCIM, whereas HS, NA and AA dyes show

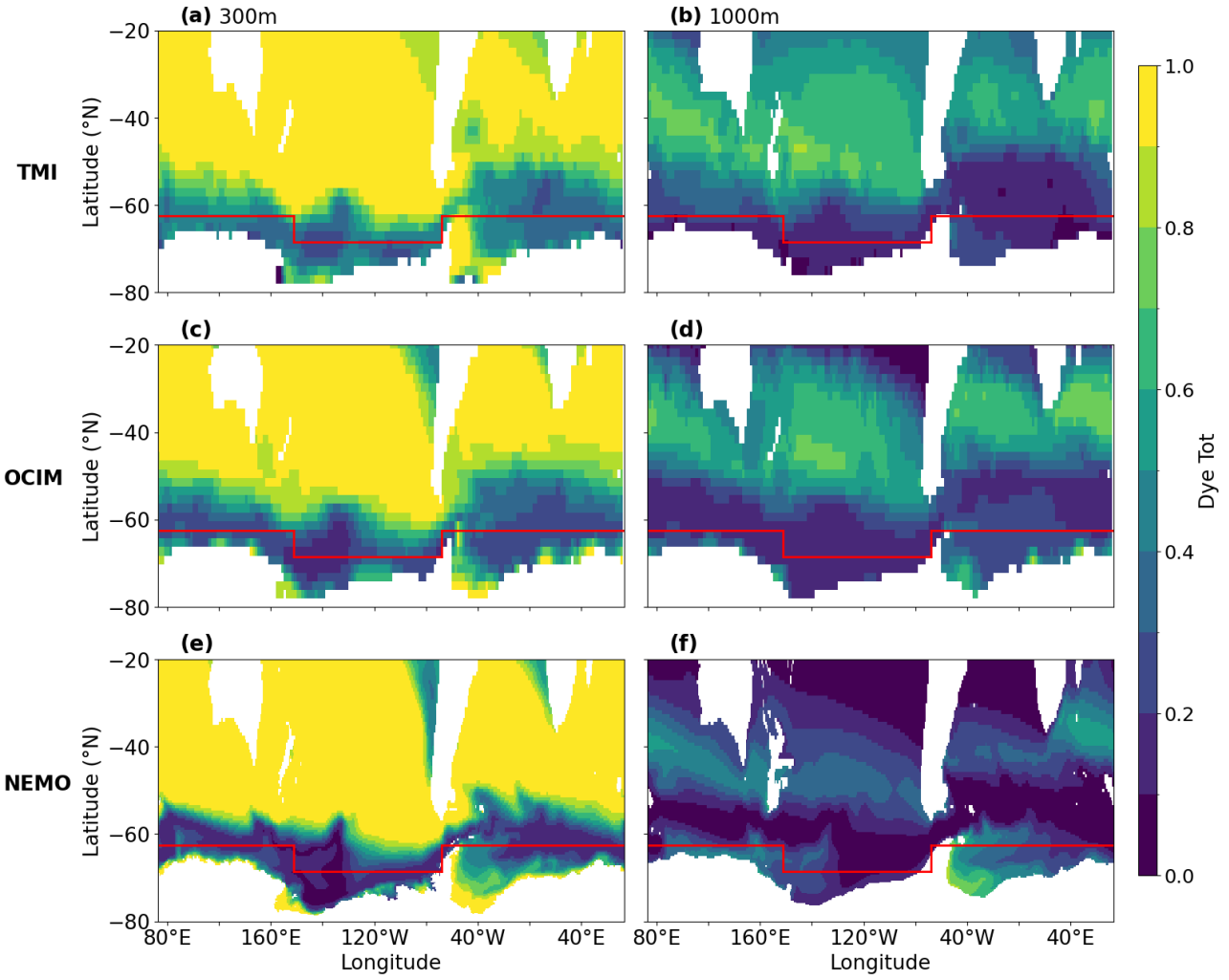

Figure 2.7: Transient Southern Ocean ventilation in TMI **(a,b)**, OCIM **(c,d)** and the REF NEMO experiment **(e,f)**. Shading shows the total dye concentration minus the NA dye concentration, at model year 100 and at depths of 300 m **(a,c,e)** and 1 km **(b,d,f)**. The red line corresponds to the separation between AA and HS source regions.

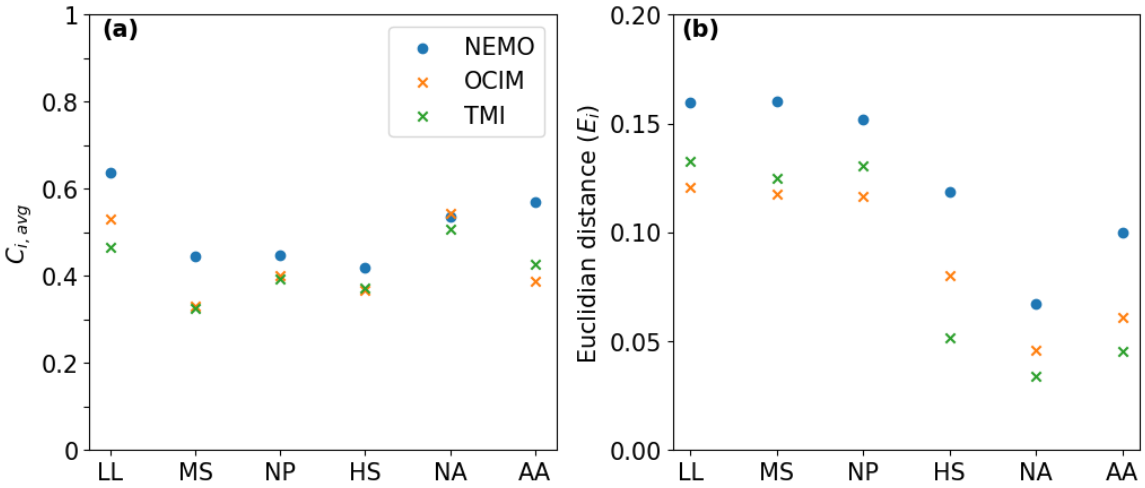

Figure 2.8: Intercomparison of diffusiveness across the three models. Panel **(a)** represents the average dye concentration weighted by dye volume, and panel **(b)** displays the Euclidean distance between the density distribution of water volume and the density distribution of dye volume. Both metrics are shown for each dye (x-axis) and each model (symbols). Blue circles correspond to the REF NEMO experiment, orange crosses to OCIM and green crosses to TMI. The distributions have been normalized prior to calculating the Euclidean distance, so that this distance only measures differences in the shapes of distributions. Density is measured with σ_2, the potential density referenced to 2,000 dbars.

stronger diapycnal spreading in TMI. These contrasted differences are consistent with qualitative patterns visible in Figures 2.5 and 2.6. Our quantification demonstrates notably that the HS dye features the largest discrepancies in diapycnal spreading across models (Figure 2.8b), indicating that ventilation from the subantarctic zone remains poorly modelled and constrained. In addition, we find a consistent hierarchy across dyes: the NA dye is the most well-mixed in the global ocean, whereas LL, MS and NP dyes are the least well-mixed, as might be expected from their more regional realms.

Overall, these diagnostics demonstrate that NEMO is less diffusive than OCIM, itself less diffusive than TMI. Since the density stratification is very similar in NEMO and inverse models (Fig. S2.5), this difference suggests that diapycnal mixing is underestimated in our NEMO configuration. Importantly, it implies that spurious numerical mixing by the model's discrete advection schemes (Burchard and Rennau, 2008; Holmes et al., 2021) is relatively weak (weaker than diapycnal mixing of the real ocean), making the addition of physical sources of mixing beneficial. Sources of deep ocean mixing unaccounted for in REF include wind-induced low-mode near-inertial waves (Alford, 2020) and interactions between geostrophic currents and topography (Evans et al., 2022; Garabato et al., 2019; Yang et al., 2021). Efforts to faithfully parameterize these processes in NEMO may contribute to more realistic simulation of ventilation rates and pathways.

	NEMO	OCIM	TMI
500 m	1492	902	878
2,000 m	2519	1640	1535
4,000 m	2022	1386	1527

Table 2: Maximum age in the North Pacific (north of the equator, excluding marginal seas) for the three models, at 500 m depth, 2 km depth and along the seafloor.

3.3 . Ideal age

Steady-state dye distributions illustrate ventilation patterns of the global ocean but do not provide information on ventilation rates. We now examine steady-state distributions of the ideal age tracer in the three models. The ideal age predicted by TMI, OCIM and REF at 500 m depth, 2 km depth and the seafloor is shown in Figure 2.9. The models share principal large-scale patterns. Waters are younger than 300 years at 500 m depth except in upwelling zones such as the equatorial Pacific and polar Southern Ocean (Figure 2.9a,d,g). The maximum age at 500 m is actually located in the northwest corner of the Pacific, signalling the upwelling of particularly old deep waters in this region (Millet et al., 2023; Sarmiento et al., 2004; Toggweiler et al., 2019). A strong inter-basin contrast at 2 km depth features centenarian waters in the Atlantic and thousand-year-old waters in the Pacific, with the Indian Ocean lying in between these extremes (Figure 2.9b,e,h). Ideal age increases northward in the deep Indian and Pacific basins, consistent with ventilation from the south (Figure 2.9b,c,e,f,h,i). In the Atlantic, age increases with depth below 2 km, due to slower ventilation by AABW relative to NADW; the reverse is true in the deep Pacific and eastern Indian oceans, where northward-flowing bottom waters are the youngest water mass (Figure 2.9b,c,e,f,h,i).

Major differences between models are also apparent. Most conspicuously, the REF experiment has generally higher ages than inverse models (Figure 2.9). The largest difference is in the mid-depth Pacific shadow zone, where ideal age peaks at about 2,500 years in REF, compared to about 1,600 years in TMI and OCIM (Table 2). The location of the maximum age is also different: it lies at the northeast end of the Pacific in REF, but near 35°N in inverse models (Figure 2.9b,e,h) like the minimum in measured radiocarbon (Key et al., 2004). The overly sluggish ventilation of the shadow zone in REF contributes to higher ages at shallower depths in upwelling zones, especially in the subarctic Pacific (Figure 2.9g). In the Atlantic, differences are less pronounced except at abyssal depths, where REF has higher ages associated with a deficit of ventilation from the North Atlantic (see section 3.1).

Figure 2.10 shows the zonal mean ideal age in the Pacific for the three models. The range of values in TMI and OCIM is similar, but the depth structure is not the same: TMI has a much weaker depth dependence of age in the deep Pacific (Figure 2.10a,b). We attribute this difference to the radiocarbon data used: TMI uses the GLODAP gridded product of bomb-corrected radiocarbon (Key et al., 2004), whereas OCIM assimilates only local radiocarbon measurements from GLODAPv2 (Olsen et al., 2016) that have no anthropogenic imprint (based on absence of chlorofluorocarbons). The latter method incorporates additional measurements, avoids their interpolation and obviates the correction for bomb-produced ^{14}C, which appears to introduce biases in the deep ocean (Burke et al., 2015; de Lavergne et al., 2017). Thus, we posit that (i) both inverse models predict realistic age maxima in the Pacific shadow zone, where natural ^{14}C is directly measured; and (ii) the spatial structure of age is more accurate in OCIM.

In the REF NEMO experiment, zonal mean Pacific ideal age has a similar structure to OCIM, but the

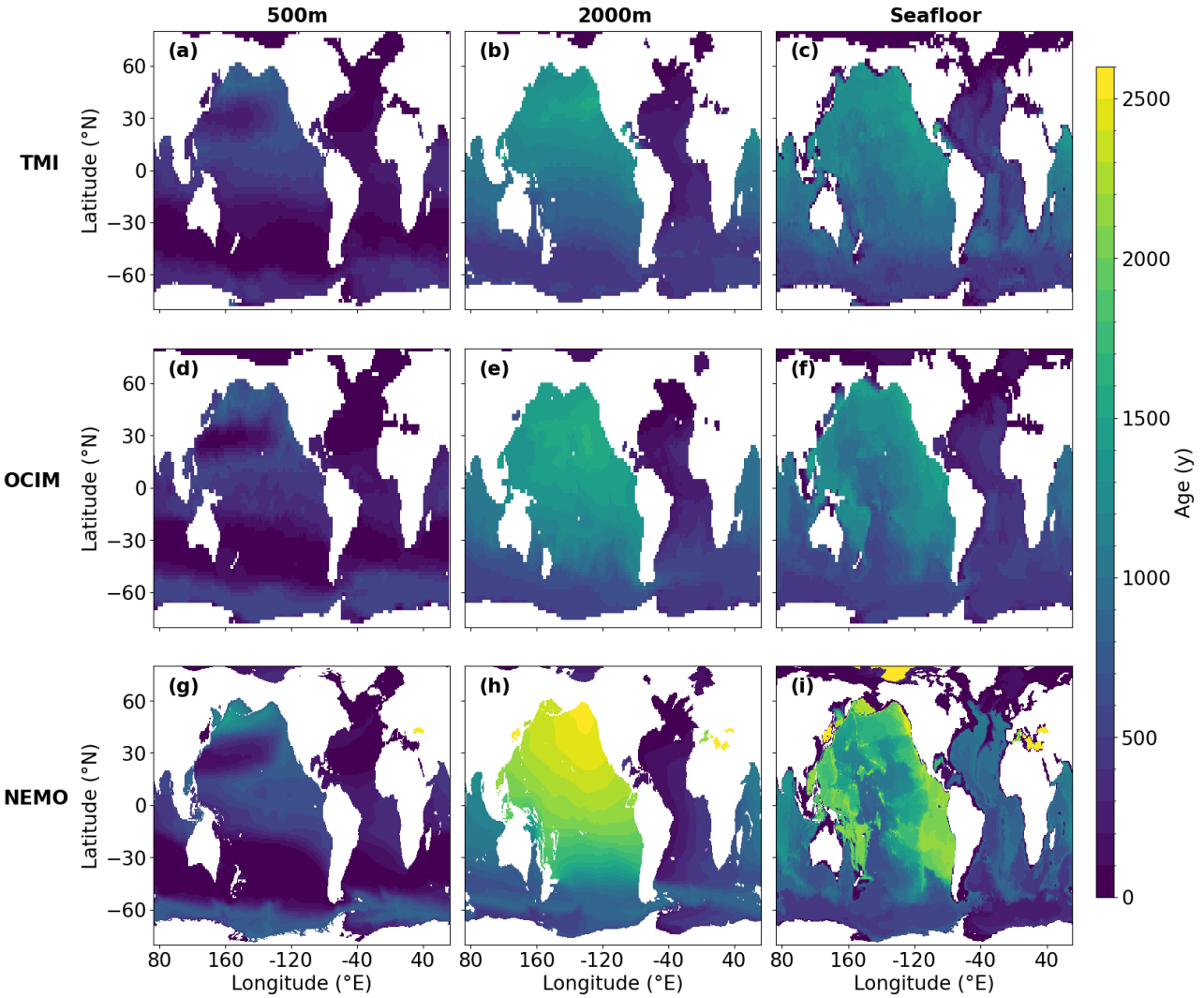

Figure 2.9: Steady-state ideal age at 500 m depth **(a,d,g)**, 2 km depth **(b,e,h)** and at the seafloor **(c,f,i)** in TMI **(a-c)**, OCIM **(d-f)** and the REF NEMO experiment **(g-i).**

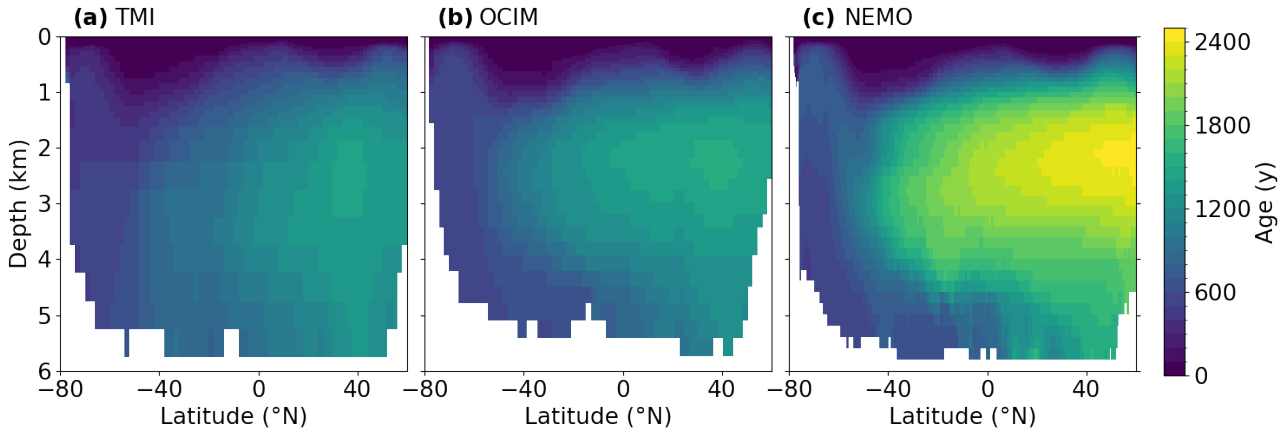

Figure 2.10: Pacific zonal mean ideal age in TMI **(a)**, OCIM **(b)** and the REF NEMO experiment **(c)**. Marginal seas are excluded from the zonal average.

age exceeds that of OCIM across most of the basin (Figure 2.10b,c). Bottom waters entering and filling the South Pacific abyss display the same age in OCIM and REF, thus the higher mid-depth ages in REF do not stem from waters that are already too old when they enter the Pacific but rather from excess aging within the Pacific. Note that the Pacific density stratification is not overestimated in REF (Fig. S2.5); however, the Pacific abyssal overturning is slower in REF than in OCIM (Fig. S2.6; Rathore et al., 2024). As we discuss in section 4, a lack of diffusive and/or advective upwelling in the subarctic Pacific of REF is plausibly an important contributor to the age bias. The widespread overestimation of age apparent in Figure 2.9 further suggests that systematic underestimation of isopycnal and/or diapycnal diffusion in REF is likely. We explore hereafter the sensitivity of simulated age and dye distributions to mixing parameterizations in NEMO.

4 . Discussion

Comparisons detailed above highlighted three distinctive features of the Pacific Ocean simulated by the REF NEMO experiment: (i) a mid-depth maximum of the North Atlantic dye concentration that pervades the basin; (ii) excessive isolation of mid-depth waters; and (iii) an age maximum located in the northeast corner of the basin, rather than further south as suggested by radiocarbon observations and inverse models. We now explore ventilation processes underpinning these features and their sensitivity to mixing parameters, resorting to NEMO experiments described in Table 1.

4.1 . From the North Atlantic surface to the deep Pacific

Steady-state dye distributions do not always allow a clear identification of ventilation pathways. To aid interpretation, we show in Figure 2.11 the transient spreading of the NA dye in the Pacific, at year 800 of the REF simulation. Two pathways are clearly apparent: an abyssal pathway that tracks the circulation of AABW, and a mid-depth pathway that transports the NA dye horizontally from its core in the Antarctic Circumpolar Current (ACC) toward the north. The weakness of simulated overturning flows in this mid-depth zone (Fig. S2.6) and the large latitudinal gradient in the NA dye suggest that isopycnal diffusion is the main driver of this mid-depth propagation, consistent with recent proposals (Holzer et al., 2021; Millet et al., 2023). Importantly, the northward propagation of the NA dye at mid-depths is at odds with the common view that tracers move towards the south (along the conveyor) in this layer (Talley, 2013). We argue that tracers can move either northward or southward in the mid-depth Pacific shadow zone, depending on their large-scale isopycnal concentration gradient.

The role of isopycnal diffusion in the mid-depth spreading of the NA dye is further evidenced by analysis of NEMO sensitivity experiments (Figure 2.12). We focus on steady-state distributions of the zonal mean NA dye concentration in the Pacific. In ISO3D, which has substantially weaker isopycnal diffusivities than REF in the deep ocean (Figure 2.2b,d), a mid-depth maximum of the NA dye is present but only south of 5°N (Figure 2.12b). By contrast, ISOCST has a slightly stronger mid-depth tongue of NA dye than REF, extending to 40°N, consistent with higher average isopycnal diffusivities across the basin (Figure 2.2a,b). Differences in isopycnal diffusivity outside the deep Pacific can also explain some of the differences in dye distributions. In particular, ISO3D has smaller mean isopycnal diffusivities south of 45°S (Figure 2.2); this leads to weaker resurfacing and removal of the NA dye at the Southern Ocean surface, and thereby to an overall increase in NA dye content within the ACC and across the global deep ocean (Figure 2.12b,c, Fig. S2.4). Thus, changes in isopycnal mixing alone can modify the balance between northern and southern ventilation of the deep ocean (Jones and Abernathey, 2019).

Diapycnal mixing also influences the northward spreading of the NA dye in the Pacific. Removing the contribution of subinertial internal tides to diapycnal mixing (as in DIALOW) enhances the mid-depth maximum of NA dye concentration, which then spreads to the northern boundary of the Pacific (Figure 2.12e). This is due to weaker diapycnal diffusion south of 30°S, which reduces removal of NA dye in the polar Southern Ocean, and to weaker diapycnal diffusion in the Pacific north of 30°N, which reduces local erosion of the mid-depth maximum. Tripling mixing by subinertial tides in the North Pacific (as in DIAHIGH) does not significantly alter the NA dye distribution, because of weak vertical gradients already present in REF north of 30°N (Figure 2.12a,c).

Overall, the presence of a marked mid-depth maximum of NA dye in the Pacific sector of the ACC which spreads northward in the basin near 2 km depth is a robust feature of our NEMO sensitivity experiments (Figure 2.12). This maximum is stronger and shallower than that found in the ACC of OCIM (Figure 2.6n,o). The light and shallow bias of NADW in our NEMO configuration (Rathore et al., 2024) may largely explain this difference. Specifically, the lack of NADW in the abyssal Atlantic in NEMO may favour the mid-depth pathway over the abyssal pathway connecting the surface North Atlantic to the deep Pacific (Figure 2.11).

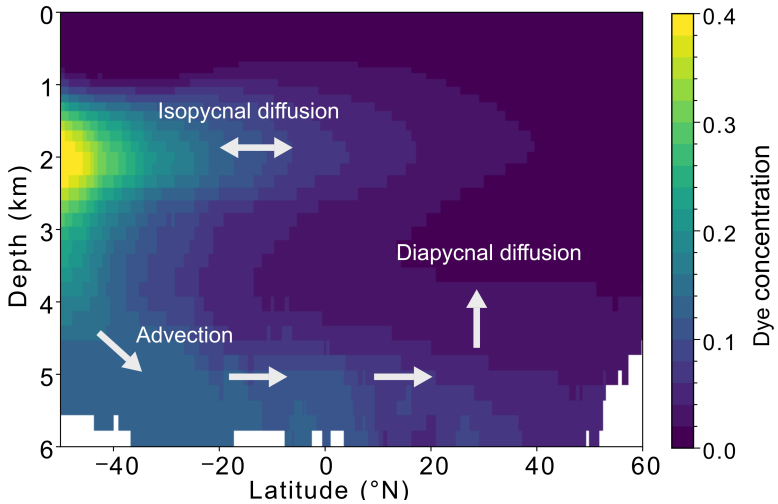

Figure 2.11: Pacific zonal mean NA dye concentration in the REF NEMO experiment after 800 years of simulation. White arrows are a simplified depiction of the two pathways of NA dye spreading: in the abyss along the abyssal overturning cell, and at mid-depth via isopycnal diffusion. Note the dye concentration scale is different than in other figures, for improved visualization.

4.2 . The maximum age of the deep Pacific

Pacific ventilation rates display stronger sensitivity to mixing parameterizations than do ventilation patterns. Figure 2.13 compares Pacific zonal mean ideal ages at steady state in the five NEMO experiments and in OCIM. The broad structure is similar across all simulations, with a peak zonal mean age located near 2 km depth in the North Pacific. However the magnitude of this peak age varies between 2,300 years (DIAHIGH) and 3,000 years (ISO3D) in NEMO, compared to only about 1,600 years in OCIM. Hence all NEMO experiments simulate an overly isolated Pacific shadow zone. The degree of isolation decreases as bulk isopycnal diffusivity in the deep Pacific increases (from ISO3D via REF to ISOCST) and as bulk diapycnal diffusivity increases (from DIALOW via REF to DIAHIGH). Puzzlingly, simulation ISO3D, which includes state-of-the-art maps of diapycnal (Rathore et al., 2024) and isopycnal diffusivity (Groeskamp et al., 2020), possesses the largest age bias. A more realistic three-dimensional structure of isopycnal diffusivity, including a decrease of diffusivity with depth, thus reinforces the regional deficit of ventilation.

This result could imply that diapycnal diffusivity is substantially underestimated in the deep North Pacific. However, tripling the mixing power of subinertial internal tides in the North Pacific reduces the peak age by only about 150 years (compare DIAHIGH and REF, Figures 2.13a,e and 2.14h). This reduction is less than that obtained by adding the mixing contribution of subinertial internal tides in the first place (compare REF and DIALOW, Figures 2.13a,b and 2.14g). The increase in shadow zone ventilation rate from DIALOW to REF is mostly due to regionally increased mixing in the Pacific north of 30°N, since age differences at the southern entry of the Pacific are relatively small (Figures 2.13a,b and 2.14g). Hence, increasing regional diapycnal mixing further than tested in DIAHIGH may not achieve much further reduction in peak age, unless the increase in diapycnal mixing is unrealistically strong or widely spread. We hypothesize that our NEMO experiments misrepresent vertical mass transports in the subarctic Pacific (see section 4.3), and thereby systematically overestimate deep Pacific age.

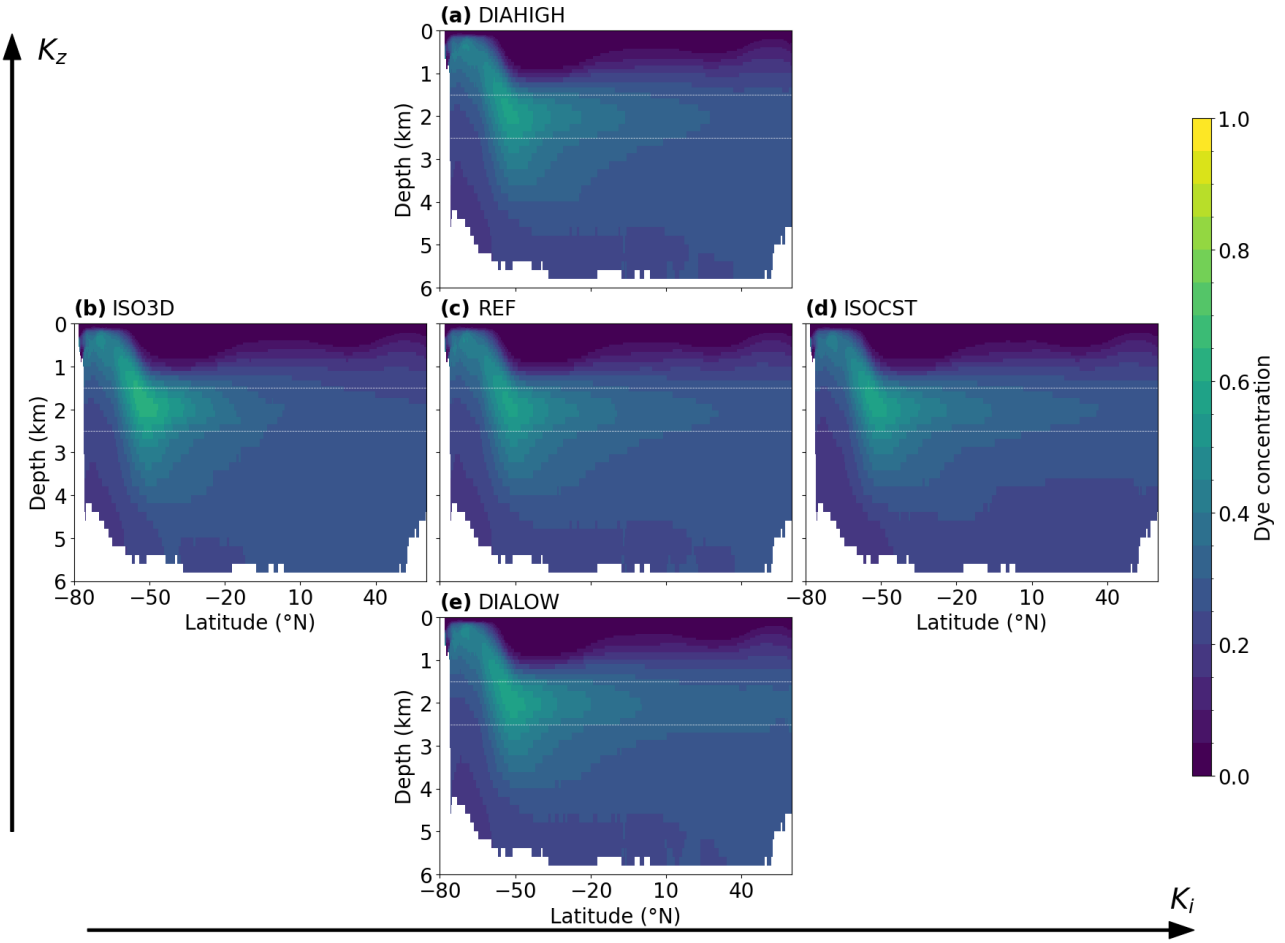

Figure 2.12: Pacific zonal mean NA dye concentration at steady state, for each NEMO experiment. White lines mark depths of 1.5 and 2.5 km. Panels have been organized so that isopycnal diffusion in the deep Pacific increases toward the right, from ISO3D **(b)** via REF **(c)** to ISOCST **(d)**, while diapycnal diffusion increases toward the top, from DIALOW **(e)** via REF **(c)** to DIAHIGH **(a)**.

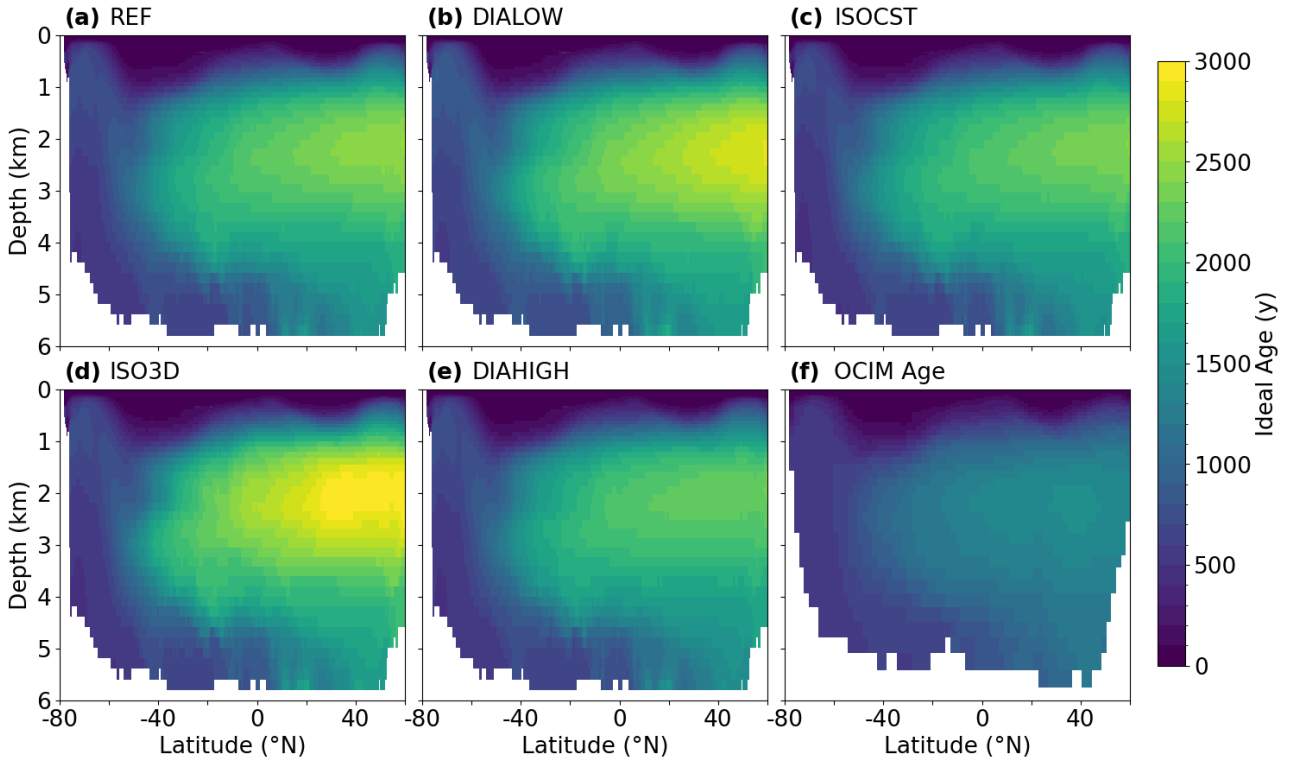

Figure 2.13: Pacific zonal mean ideal age at steady state in the different NEMO experiments: REF **(a)**, DIALOW **(b)**, ISOCST **(c)**, ISO3D **(d)** and DIAHIGH **(e)**. The equivalent in OCIM is shown in panel **(f)**.

Analysis of the spatial pattern of ideal age at 2 km depth corroborates some of these inferences. In REF, DIALOW and ISOCST, the maximum age is found in the northeastern corner of the basin, near 140°W, 55°N (Figure 2.14a-c). By contrast, it is situated about 20° further south in ISO3D, DIAHIGH and OCIM (Figure 2.14d-f), in accord with radiocarbon observations (de Lavergne et al., 2017). The addition of mixing by subinertial internal tides, which is particularly strong along the Aleutian arc and in the Kuril Straits (Müller, 2013), contributes to shift the peak age away from the northern rim of the basin and away from the Bering Sea (Figure 2.14g,h). Reduced isopycnal diffusivity in the deep North Pacific, with lowest values in the eastern half of the subpolar gyre (Figure 2.2c,d) as predicted by Groeskamp et al. (2020), also favours the emergence of peak ages at middle latitudes offshore of North America (Figure 2.14i). Lower isopycnal diffusivities enhance the footprint of large-scale circulation and diapycnal mixing patterns on the age distribution, leading to a more complex and less meridional age distribution. Overall, the magnitude and pattern of age biases across NEMO experiments suggest that REF overestimates large-scale isopycnal homogenization rates but underestimates vertical communication rates, notably in the subarctic Pacific.

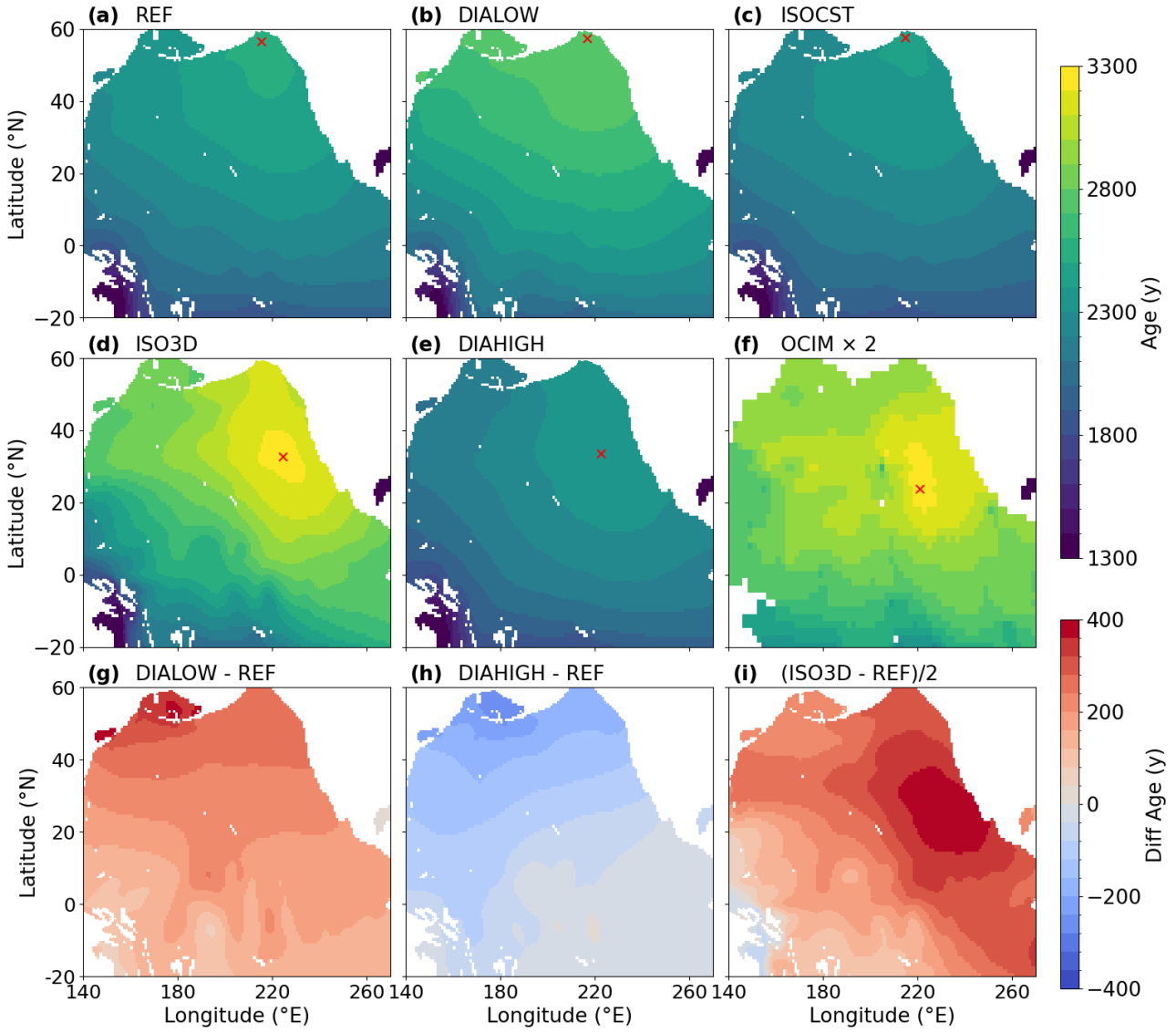

Figure 2.14: Ideal age at 2 km depth in the North Pacific simulated by REF **(a)**, DIALOW **(b)**, ISOCST **(c)**, ISO3D **(d)**, DIAHIGH **(e)** and OCIM **(f)**. Red crosses indicate the location of the maximum value of age in each simulation. The difference in age between DIALOW and REF **(g)**, DIAHIGH and REF **(h)**, and ISO3D and REF **(i)** is also shown. Note that the ideal age of OCIM is multiplied by 2 in panel **(f)** to share the range of other panels. For the same reason the difference between ISO3D and REF is divided by 2 in panel **(i)**.

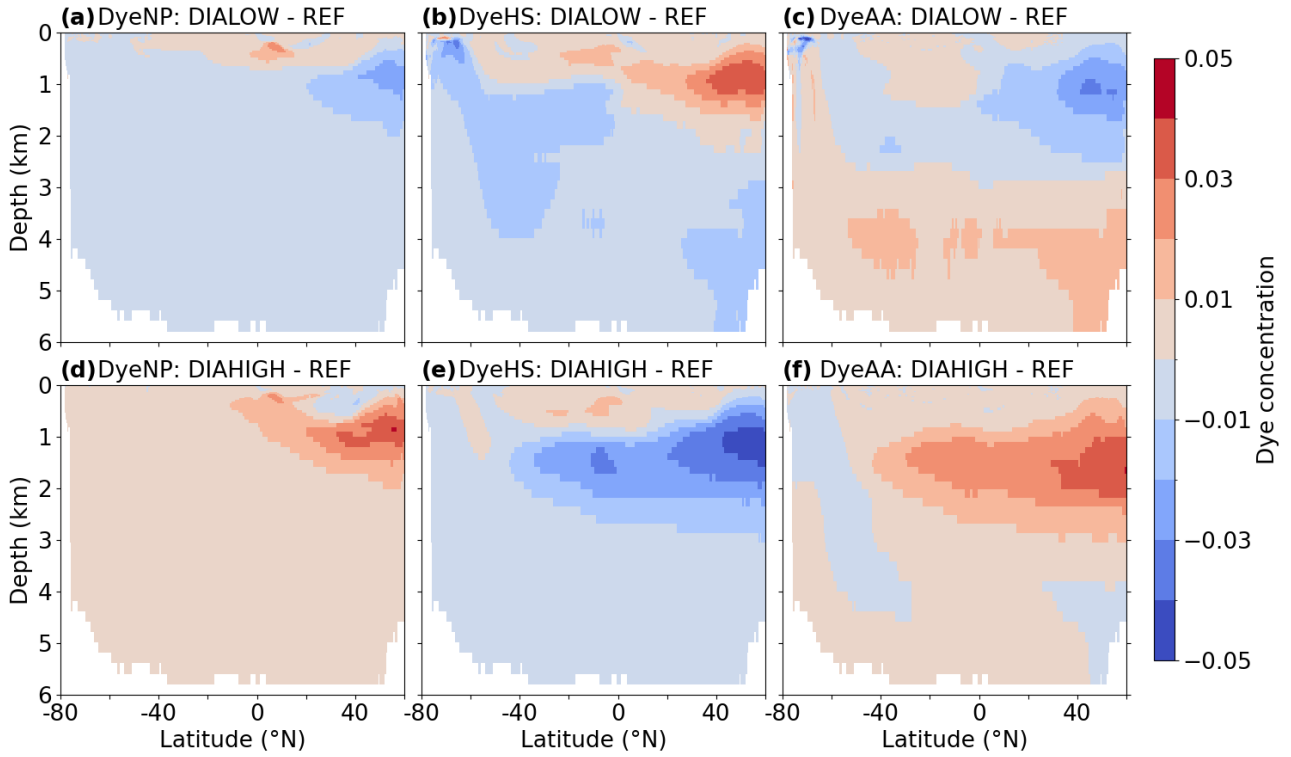

Figure 2.15: Difference in NP **(a,d)**, HS **(b,e)** and AA **(c,f)** dye concentrations between DIALOW and REF **(a-c)** and between DIAHIGH and REF **(d-f)**.

4.3 . Upwelling in the subarctic Pacific

Maps of ideal age at 500 m depth in TMI, OCIM and REF suggest localized upwelling of old deep waters in subarctic Pacific (Figure 2.9a,d,g). The presence of such upwelling has been inferred previously from in situ observations and regional tracer budgets (Holzer et al., 2021; Millet et al., 2023; Sarmiento et al., 2004; Toggweiler et al., 2019; Warren, 1983). However it remains unclear what is the driver of tracer upwelling from abyssal depths to the surface in this understudied region. Candidates include tidal mixing (Sarmiento et al., 2004) and wind-driven upwelling (Toggweiler et al., 2019).

Internal tide-driven mixing in the subarctic Pacific is dominated by subinertial internal tides (Rathore et al., 2024; Müller, 2013; Tanaka, 2023). Comparison of DIALOW, REF and DIAHIGH experiments may thus shed light on the role of tidal mixing on vertical tracer transports in the northern North Pacific. Figure 2.15 shows zonal mean differences in dye concentrations across the three experiments. Sensitivity of dye concentrations peaks north of 40°N between 300 m and 2 km depth. Zonal mean concentrations of the Antarctic (AA) dye tracer in this depth range increase by up to 0.03 from DIALOW to REF, and by a similar amount from REF to DIAHIGH (Figure 2.15c,f). The increased upward spreading of the AA dye is accompanied by increased downward spreading of the NP dye; both increases are compensated by a drop of the HS dye (Figure 2.15a,b,d,e). This demonstrates that mixing by subinertial internal tides contributes to vertical transports across the mid-depth shadow zone, and in particular to the upwelling of tracers from the abyss to the near-surface in the subarctic Pacific. Nevertheless, the effect on dye distributions is limited: it

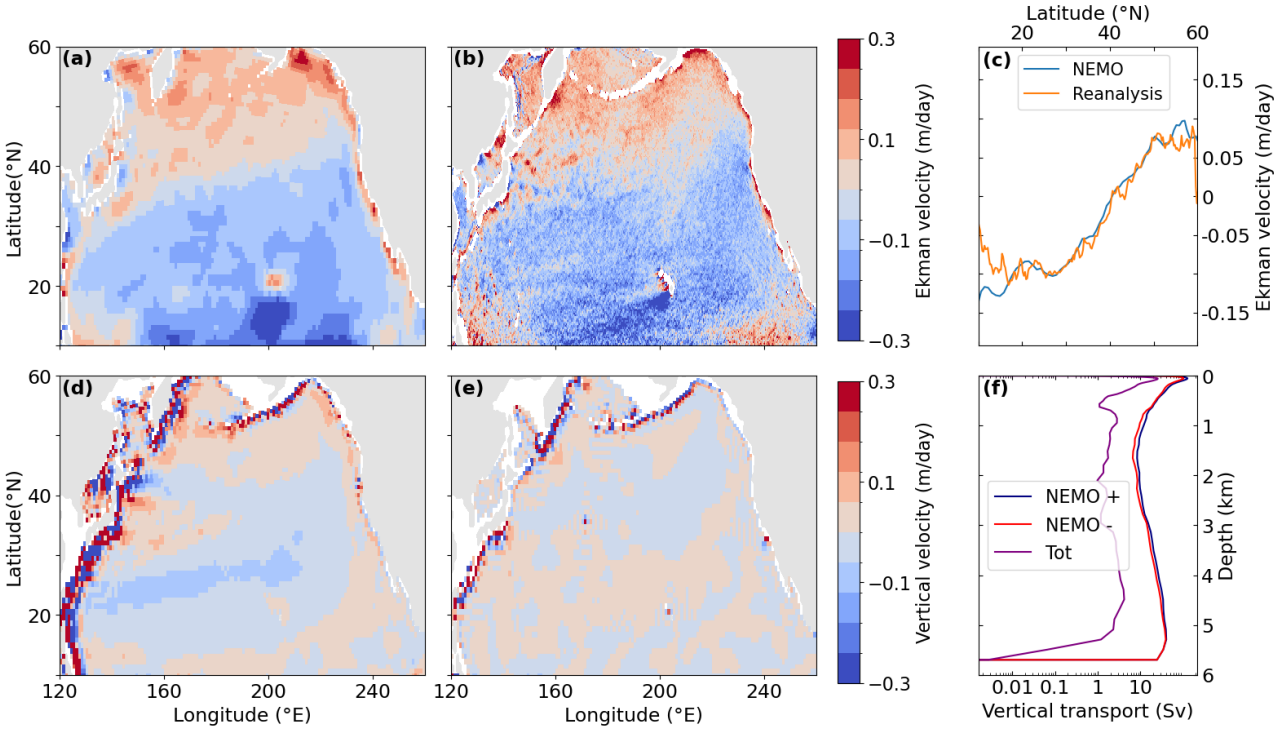

Figure 2.16: Annual mean Ekman pumping velocity in REF **(a)** and the Mercator Ocean reanalysis **(b)** in the North Pacific. The zonally averaged Ekman velocity in both REF and the reanalysis is shown in panel **(c)**. This average was taken over the main Pacific basin, excluding marginal seas. Vertical velocity at 300 m depth **(d)** and 1000 m depth **(e)** in REF. In panel **(f)**, we plot the horizontally integrated vertical velocity in the Pacific north of 0°N (purple), and the same integral for negative-only (red) and positive-only (blue) vertical velocities. The x-axis of panel **(f)** uses a logarithmic scale.

changes the overall balance of ventilation (Figure 2.6) by a few percent only.

Radiocarbon observations (Toggweiler et al., 2019) and the simulated age pattern at 500 m depth (Figure 2.9a,d,g) point to the area just east of the Kamchatka peninsula as the primary upwelling zone. This location does not coincide with the strongest rates of tidal mixing, suggesting that other—likely advective—processes are at play. To probe the representation of vertical flows in our NEMO experiments, we map the annual mean Ekman pumping velocities implied by the wind stress forcing of REF (Figure 2.16a) and the equivalent in a high-resolution ocean reanalysis (Figure 2.16b; extracted from https://doi.org/10.48670/moi-00185). Both REF and the reanalysis feature Ekman upwelling across most of the subpolar gyre, including regionally enhanced upwelling in the northeastern corner of the basin and off the Kamchatka peninsula. Averaged zonally over the main Pacific basin, the annual mean Ekman pumping in REF is comparable to that of the reanalysis (Figure 2.16c). Hence wind stress forcing in our experiments (which is based on the COREv2 normal year dataset; Large and Yeager, 2009) does not appear to underestimate Ekman suction in the northern North Pacific.

However, the actual vertical velocities in REF do not simply reflect Ekman dynamics: while upwelling dominates at 300 m in the cyclonic subpolar gyre, large vertical velocities of both signs are simulated along

the boundary (Figure 2.16d). Note that vertical velocities include a parameterized eddy-driven component (Gent and McWilliams, 1990) in addition to the resolved component; however we find the parameterized component to be one order of magnitude smaller than the resolved component in this region (not shown). Near-boundary vertical velocities vary substantially (and frequently change sign) from one grid cell to the next, pointing to numerical artifacts (Figure 2.16d). The same is true at 1000 m depth (Figure 2.16e). Vertical tracer communication in the subarctic Pacific in REF could thus be dominated by these large opposing velocities. Horizontal integration of the vertical velocity across the basin north of 0°N shows that the net upwelling varies between 1 and 2 Sverdrups (Sv; 1 Sv $\equiv 10^6$ m^3 s^{-1}) between 0.5 and 5 km depth, but is the residual of much larger upward and downward volume transports (Figure 2.16f). All in all, this analysis suggests that our NEMO experiments do not faithfully simulate vertical flows along the northern rim of the Pacific, and thus do not adequately represent the observationally inferred upwelling in the subarctic Pacific.

4.4 . Perspectives on Pacific glacial ocean ventilation

While focusing on the present-day ocean, this study offers insights of potential relevance to understanding ventilation of the glacial ocean. During the Last Glacial Maximum (LGM) about 21,000 years ago, the salinity difference between bottom and intermediate waters is thought to have been larger than today (Ferrari et al., 2014; Galbraith and de Lavergne, 2019), leading to a stronger deep ocean stratification (Adkins et al., 2002) and a greater disconnect between NADW and AABW realms (Ferrari et al., 2014; Gebbie, 2014). To draw apart AABW and NADW, models generally require a large increase in salt stratification, typically achieved via enhanced brine rejection in the Southern Ocean (Bouttes et al., 2010; Jansen, 2017). Here, our NEMO experiments simulate a rather strict separation between NADW and AABW (as measured by the NA and AA dye tracers), especially in the Atlantic and Southern Oceans (Figure 2.5), despite having a density stratification close to present day. This suggests that sharp separation between northern- and southern-sourced water can potentially be achieved without a major change in density stratification. In the modern climate, formation of slightly lighter NADW than currently observed, as is the case in our NEMO experiments (Rathore et al., 2024), may indeed suffice to largely separate dense waters of North Atlantic and Antarctic origins.

Millet et al. (2023) analyzed the oxygen-18 isotopic ratio of calcite within shells of benthic foraminifera in sediment cores of the North Pacifc. They found a stronger mid-depth maximum of this quasi-conservative tracer at LGM relative to the Holocene, suggesting increased layering of the deep ($>$ 2 km) North Pacific at LGM. This stronger mid-depth maximum could come from increased influence of isopycnal diffusion relative to vertical transports in the region's ventilation (Millet et al., 2023). The NA dye tracer distributions simulated in present NEMO experiments corroborate these arguments: they demonstrate that a North Pacific mid-depth maximum in conservative tracers can exist via isopycnal diffusion from the south, notably via isopycnal spreading of tracers contained in mid-depth waters of North Atlantic origin. In addition, they show that the strength of the mid-depth maximum is sensitive to the balance of isopycnal and diapycnal diffusion in the deep Pacific. We hypothesize that reduced density of NADW relative to AABW, together with reduced vertical transports in the deep North Pacific, may underpin the LGM ventilation patterns inferred by Millet et al. (2023).

Finally, we have shown that the filling time of the ocean far exceeds the maximum ideal age of the ocean (by a factor of about two), and varies strongly between basins. In the modern state, assuming steady

circulation and mixing, we estimate that near complete (99%) renewal of the mid-depth (1-3 km) Pacific requires between 3,000 and 4,000 years (Figure 2.3). Under changing boundary conditions, such as during the last deglaciation (about 20,000 to 10,000 years ago), the mid-depth Pacific would be expected to adjust with multi-millennial lag and to feature persistent disequilibrium with respect to the surface climate (Gebbie and Huybers, 2019; Wunsch and Heimbach, 2014). Interpretation of proxy records of past climate changes thus needs to account for spatially varying lags between deep sea states and global surface climate (Skinner and Shackleton, 2005). The very notion of climatic equilibrium or steady state is questionable given the presently inferred adjustment time of the mid-depth Pacific.

5 . Conclusion

In this study we compared a global configuration of the NEMO general circulation model to two data-constrained inverse models, focusing on steady-state ventilation patterns and rates. More precisely, we examined the volumes ventilated by different surface regions and the ideal age distribution of the three model oceans. The three models share several important features. First, we find that the time needed to fill (or renew) 99% of the ocean volume is roughly twice the maximum ideal age. The mid-depth Pacific hosts the maximum age and takes the longest to fill. Given a steady modern circulation state as reconstructed by the inverse models, over 3,000 years are needed to entirely renew the mid-depth Pacific. Second, global volumetric contributions of each source region are fairly similar across the three models. The North Atlantic (north of 30°N) and Antarctic marginal seas each ventilate approximately one-third of the global ocean volume (Figure 2.4a). About one-fifth of the ocean volume originates from the subantarctic zone where Antarctic Intermediate Water and Subantarctic Mode Water are formed (Figure 2.4a).

Major differences between the models also reveal important biases and unknowns. First, ideal ages are consistently higher in the NEMO simulations than in the inverse model states. When state-of-the-art maps of isopycnal (Groeskamp et al., 2020) and diapycnal (de Lavergne et al., 2020, Rathore et al., 2024) mixing are implemented in NEMO (experiment ISO3D), the maximum ideal age in the Pacific reaches 3,300 years, twice the inverse estimates of about 1,600 years constrained by radiocarbon data. This difference occurs despite realistic representation in NEMO of the density stratification in the Pacific. A widespread underestimate of both isopycnal and diapycnal mixing rates in the deep ocean of experiment ISO3D is deemed likely. Nonetheless, sensitivity experiments suggest that plausible increases of diapycnal mixing are unlikely to eliminate the age bias. In point of fact, NEMO appears to misrepresent vertical flows along the northern rim of the Pacific, when these flows seem to play a key role in North Pacific tracer budgets and ventilation rates (Millet et al., 2023; Sarmiento et al., 2004; Toggweiler et al., 2019). The drivers and pathways of ventilation in the subarctic Pacific deserve further scrutiny. Second, NEMO experiments exhibit stronger layering of the numerical dyes than the inverse models do. Several factors may underpin this difference: (i) overestimation of diapycnal diffusion by the inverse models, especially by TMI; (ii) production of NADW in a too narrow neutral density range (27.8-27.9 kg m^{-3}) in NEMO; and (iii) underestimated diapycnal mixing in the ocean interior of NEMO. The latter factor suggests that numerical mixing (that is, spurious mixing due to the discretisation of advection) is sufficiently weak in our NEMO experiments that parameterizing additional (non tidal) sources of deep diapycnal mixing would be beneficial.

Overall, present NEMO experiments, benchmarked against the two observationally constrained inverse

model solutions, show more skill in the representation of ventilation patterns than ventilation rates. Indeed, whereas dye volumes and distributions compare well across the models on basin scales, ideal ages appear to be substantially overestimated in slowly renewed pools of the global ocean in NEMO. Such age biases are of concern when modelling the Earth system's response to anthropogenic change: they affect not only the long-term response of the ocean but also the simulated base state of marine biogeochemistry, which is tightly dependent on deep-ocean ventilation rates (Eggleston and Galbraith, 2018; Ödalen et al., 2018). In other words, large biases in ideal age will affect the calibration of biogeochemical models and thereby the simulated transient response of marine ecosystems and carbon cycling. Our sensitivity analysis suggests that energetically plausible changes in mixing parameterizations may not completely overcome age biases in this NEMO configuration, pointing to biases in resolved dynamics. More broadly, the present study outlines a methodology to thoroughly assess ocean ventilation simulated by general circulation models. Since ventilation of the ocean interior is a paramount climatic process, systematic assessments akin to the present study may prove helpful for the calibration and evaluation of Earth system models.

References

Adcroft, A., Anderson, W., Balaji, V., Blanton, C., Bushuk, M., Dufour, C. O., Dunne, J. P., Griffies, S. M., Hallberg, R., Harrison, M. J., Held, I. M., Jansen, M. F., John, J. G., Krasting, J. P., Langenhorst, A. R., Legg, S., Liang, Z., McHugh, C., Radhakrishnan, A., … Zhang, R. (2019). The gfdl global ocean and sea ice model om4.0: Model description and simulation features. *Journal of Advances in Modeling Earth Systems*, *11*(10), 3167–3211. https://doi.org/10.1029/2019MS001726

Adkins, J. F., McIntyre, K., & Schrag, D. P. (2002). The salinity, temperature, and $\delta^{18}O$ of the glacial deep ocean. *Science*, *298*(5599), 1769–1773. https://doi.org/10.1126/science.1076252

Alford, M. H. (2020). Global calculations of local and remote near-inertial-wave dissipation. *Journal of Physical Oceanography*, *50*(11), 3157 –3164. https://doi.org/10.1175/JPO-D-20-0106.1

Baker, J. A., Bell, M. J., Jackson, L. C., Renshaw, R., Vallis, G. K., Watson, A. J., & Wood, R. A. (2023). Overturning pathways control amoc weakening in cmip6 models. *Geophysical Research Letters*, *50*(14), e2023GL103381. https://doi.org/10.1029/2023GL103381

Bouttes, N., Paillard, D, & Roche, D. M. (2010). Impact of brine-induced stratification on the glacial carbon cycle. *Climate of the Past*, *6*(5), 575–589.

Broecker, W. S. (1991). The great ocean conveyor. *Oceanography*, *4*. https://doi.org/10.5670/oceanog.1991.07

Broecker, W. S., & Olson, E. A. (1960). Radiocarbon from nuclear tests, ii. *Science*, *132*(3429), 712–721. Retrieved December 12, 2023, from http://www.jstor.org/stable/1705791

Burchard, H., & Rennau, H. (2008). Comparative quantification of physically and numerically induced mixing in ocean models. *Ocean Modelling*, *20*(3), 293–311. https://doi.org/10.1016/j.ocemod.2007.10.003

Burke, A., Stewart, A. L., Adkins, J. F., Ferrari, R., Jansen, M. F., & Thompson, A. F. (2015). The glacial mid-depth radiocarbon bulge and its implications for the overturning circulation. *Paleoceanography*, *30*(7), 1021–1039. https://doi.org/10.1002/2015PA002778

Chapman, D. C. (1989). Enhanced subinertial diurnal tides over isolated topographic features. *Deep Sea Research Part A. Oceanographic Research Papers*, *36*(6), 815–824. https://doi.org/10.1016/0198-0149(89)90030-7

Cimoli, L., Gebbie, G., Purkey, S. G., & Smethie, W. M. (2023). Annually resolved propagation of cfcs and sf6 in the global ocean over eight decades. *Journal of Geophysical Research: Oceans*, *128*(3), e2022JC019337. https://doi.org/10.1029/2022JC019337

Danabasoglu, G., Yeager, S. G., Bailey, D., Behrens, E., Bentsen, M., Bi, D., Biastoch, A., Böning, C., Bozec, A., Canuto, V. M., Cassou, C., Chassignet, E., Coward, A. C., Danilov, S., Diansky, N., Drange, H., Farneti, R., Fernandez, E., Fogli, P. G., … Wang, Q. (2014). North atlantic simulations in coordinated ocean-ice reference experiments phase ii (core-ii). part i: Mean states. *Ocean Modelling*, *73*, 76–107. https://doi.org/10.1016/j.ocemod.2013.10.005

Davila, X., Olsen, A., Lauvset, S. K., McDonagh, E. L., Brakstad, A., & Gebbie, G. (2023). On the origins of open ocean oxygen minimum zones. *Journal of Geophysical Research: Oceans*, *128*(8). https://doi.org/10.1029/2023JC019677

de Lavergne, C., Madec, G., Roquet, F., Holmes, R., & McDougall, T. (2017). Abyssal ocean overturning shaped by seafloor distribution. *Nature*, *551*(7679), 181–186. https://doi.org/10.1038/nature24472

de Lavergne, C., Vic, C., Madec, G., Roquet, F., Waterhouse, A., Whalen, C., Cuypers, Y., Bouruet-Aubertot, P., Ferron, B., & Hibiya, T. (2020). A parameterization of local and remote tidal mixing [e2020MS002065 10.1029/2020MS002065]. *Journal of Advances in Modeling Earth Systems*, *12*(5), e2020MS002065. https://doi.org/10.1029/2020MS002065

DeVries, T. (2014). The oceanic anthropogenic co2 sink: Storage, air-sea fluxes, and transports over the industrial era. *Global Biogeochemical Cycles*, *28*(7), 631–647. https://doi.org/10.1002/2013GB004739

DeVries, T., & Holzer, M. (2019). Radiocarbon and helium isotope constraints on deep ocean ventilation and mantle-3he sources. *Journal of Geophysical Research: Oceans*, *124*(5), 3036–3057. https://doi.org/10.1029/2018JC014716

DeVries, T., & Primeau, F. (2011). Dynamically and observationally constrained estimates of water-mass distributions and ages in the global ocean. *Journal of Physical Oceanography*, *41*(12), 2381 –2401. https://doi.org/https://doi.org/10.1175/JPO-D-10-05011.1

Dutay, J.-C, Bullister, J., Doney, S., Orr, J., Najjar, R, Caldeira, K, Campin, J.-M, Drange, H, Follows, M, Gao, Y, Gruber, N, Hecht, M., Ishida, A, Joos, F, Lindsay, K, Madec, G, Maier-Reimer, E, Marshall, J., Matear, R., … Yool, A. (2002). Evaluation of ocean model ventilation with cfc-11: Comparison of 13 global ocean models. *Ocean Modelling*, *4*(2), 89–120. https://doi.org/10.1016/S1463-5003(01)00013-0

Eggleston, S., & Galbraith, E. D. (2018). The devil's in the disequilibrium: Multi-component analysis of dissolved carbon and oxygen changes under a broad range of forcings in a general circulation model. *Biogeosciences*, *15*(12), 3761–3777. https://doi.org/10.5194/bg-15-3761-2018

England, M. H. (1995). The age of water and ventilation timescales in a global ocean model. *Journal of Physical Oceanography*, *25*(11), 2756–2777. https://doi.org/10.1175/1520-0485(1995)025<2756:TAOWAV>2.0.CO;2

Evans, D. G., Frajka-Williams, E., & Naveira Garabato, A. C. (2022). Dissipation of mesoscale eddies at a western boundary via a direct energy cascade. *Scientific Reports*, *12*(1), 887. https://doi.org/10.1038/s41598-022-05002-7

Ferrari, R., Jansen, M. F., Adkins, J. F., Burke, A., Stewart, A. L., & Thompson, A. F. (2014). Antarctic sea ice control on ocean circulation in present and glacial climates. *Proceedings of the National Academy of Sciences*, *111*(24), 8753–8758. https://doi.org/10.1073/pnas.1323922111

Friedli, H., Lötscher, H., Oeschger, H., Siegenthaler, U., & Stauffer, B. (1986). Ice core record of the 13c/12c ratio of atmospheric co2 in the past two centuries. *Nature*, *324*(6094), 237–238. https://doi.org/10.1038/324237a0

Fu, Y., Li, F., Karstensen, J., & Wang, C. (2020). A stable atlantic meridional overturning circulation in a changing north atlantic ocean since the 1990s. *Science Advances*, *6*(48), eabc7836. https://doi.org/10.1126/sciadv.abc7836

Galbraith, E., & de Lavergne, C. (2019). Response of a comprehensive climate model to a broad range of external forcings: Relevance for deep ocean ventilation and the development of late cenozoic ice ages. *Climate Dynamics*, *52*(1), 653–679. https://doi.org/10.1007/s00382-018-4157-8

Garabato, A. C. N., Frajka-Williams, E. E., Spingys, C. P., Legg, S., Polzin, K. L., Forryan, A., Abrahamsen, E. P., Buckingham, C. E., Griffies, S. M., McPhail, S. D., Nicholls, K. W., Thomas, L. N., & Meredith, M. P. (2019). Rapid mixing and exchange of deep-ocean waters in an abyssal boundary current. *Proceedings of the National Academy of Sciences*, *116*(27), 13233–13238. https://doi.org/10.1073/pnas.1904087116

Gebbie, G., & Huybers, P. (2019). The little ice age and 20th-century deep pacific cooling. *Science*, *363*(6422), 70–74. https://doi.org/10.1126/science.aar8413

Gebbie, G. (2014). How much did glacial north atlantic water shoal? *Paleoceanography*, *29*(3), 190–209. https://doi.org/10.1002/2013PA002557

Gebbie, G., & Huybers, P. (2010). Total matrix intercomparison: A method for determining the geometry of water-mass pathways. *Journal of Physical Oceanography*, *40*(8), 1710 –1728. https://doi.org/10.1175/2010JPO4272.1

Gebbie, G., & Huybers, P. (2011). How is the ocean filled? *Geophysical Research Letters*, *38*(6). https://doi.org/https://doi.org/10.1029/2011GL046769

Gebbie, G., & Huybers, P. (2012). The mean age of ocean waters inferred from radiocarbon observations: Sensitivity to surface sources and accounting for mixing histories. *Journal of Physical Oceanography*, *42*(2), 291 –305. https://doi.org/10.1175/JPO-D-11-043.1

Gent, P., & McWilliams, J. (1990). Isopycnal mixing in ocean circulation models. *Journal of Physical Oceanography*, *20*(1), 150–155. https://doi.org/10.1175/1520-0485(1990)020<0150:IMIOCM>2.0.CO;2

Gordon, A. L. (1986). Interocean exchange of thermocline water. *Journal of Geophysical Research: Oceans*, *91*(C4), 5037–5046. https://doi.org/10.1029/JC091iC04p05037

Gray, de Lavergne, C., Jnglin Wills, R. C., Menviel, L., Spence, P., Holzer, M., Kageyama, M., & Michel, E. (2023). Poleward shift in the southern hemisphere westerly winds synchronous with the deglacial rise in co2 [e2023PA004666 2023PA004666]. *Paleoceanography and Paleoclimatology*, *38*(7), e2023PA004666. https://doi.org/10.1029/2023PA004666

Gregg, M. C. (1987). Diapycnal mixing in the thermocline: A review. *Journal of Geophysical Research: Oceans*, *92*(C5), 5249–5286. https://doi.org/10.1029/JC092iC05p05249

Gregory, J. M., Bloch-Johnson, J., Couldrey, M. P., Exarchou, E., Griffies, S. M., Kuhlbrodt, T., Newsom, E., Saenko, O. A., Suzuki, T., Wu, Q., Urakawa, S., & Zanna, L. (2024). A new conceptual model of global ocean heat uptake. *Climate Dynamics*, *62*(3), 1669–1713. https://doi.org/10.1007/s00382-023-06989-z

Groeskamp, S., LaCasce, J., McDougall, T., & Roge, M. (2020). Full-depth global estimates of ocean mesoscale eddy mixing from observations and theory. *Geophysical Research Letters*, *47*(18). https://doi.org/10.1029/2020GL089425

Groeskamp, S., Sloyan, B. M., D., Z. J., & McDougall, T. J. (2017). Mixing inferred from an ocean climatology and surface fluxes. *Journal of Physical Oceanography*, *47*(3), 667 –687. https://doi.org/10.1175/JPO-D-16-0125.1

Gupta, M., Williams, R. G., Lauderdale, J. M., Jahn, O., Hill, C., Dutkiewicz, S., & Follows, M. J. (2022). A nutrient relay sustains subtropical ocean productivity. *Proceedings of the National Academy of Sciences*, *119*(41). https://doi.org/10.1073/pnas.2206504119

Hernández-Guerra, A., & Talley, L. D. (2016). Meridional overturning transports at 30°s in the indian and pacific oceans in 2002–2003 and 2009. *Progress in Oceanography*, *146*, 89–120. https://doi.org/10.1016/j.pocean.2016.06.005

Hieronymus, M., Nycander, J., Nilsson, J., Döös, K., & Hallberg, R. (2019). Oceanic overturning and heat transport: The role of background diffusivity. *Journal of Climate*, *32*(3), 701 –716. https://doi.org/10.1175/JCLI-D-18-0438.1

Holmes, R. M., Zika, J. D., Griffies, S. M., Hogg, A. M., Kiss, A. E., & England, M. H. (2021). The geography of numerical mixing in a suite of global ocean models [e2020MS002333 2020MS002333]. *Journal of Advances in Modeling Earth Systems*, *13*(7), e2020MS002333. https://doi.org/10.1029/2020MS002333

Holzer, M., Primeau, F., W., S., & Khatiwala, S. (2010). Where and how long ago was water in the western north atlantic ventilated? maximum entropy inversions of bottle data from woce line a20. *Journal of Geophysical Research: Oceans*, *115*(C7). https://doi.org/10.1029/2009JC005750

Holzer, M., DeVries, T., & de Lavergne, C. (2021). Diffusion controls the ventilation of a pacific shadow zone above abyssal overturning. *Nature Communications*, *12*(1), 4348. https://doi.org/10.1038/s41467-021-24648-x

Holzer, M., & Primeau, F. (2006). The diffusive ocean conveyor. *Geophysical Research Letters*, *33*(14). https://doi.org/10.1029/2006GL026232

Jansen, M. F. (2017). Glacial ocean circulation and stratification explained by reduced atmospheric temperature. *Proceedings of the National Academy of Sciences*, *114*(1), 45–50. https://doi.org/10.1073/pnas.1610438113

Jansen, M. F., Nadeau, L.-P., & Merlis, T. M. (2018). Transient versus equilibrium response of the ocean's overturning circulation to warming. *Journal of Climate*, *31*(13), 5147 –5163. https://doi.org/10.1175/JCLI-D-17-0797.1

Johnson, G. C. (2008). Quantifying antarctic bottom water and north atlantic deep water volumes. *Journal of Geophysical Research: Oceans*, *113*(C5). https://doi.org/10.1029/2007JC004477

Jones, C. S., & Abernathey, R. P. (2019). Isopycnal mixing controls deep ocean ventilation. *Geophysical Research Letters*, *46*(22), 13144–13151. https://doi.org/10.1029/2019GL085208

Key, R. M., Kozyr, A., Sabine, C., Lee, K., Wanninkhof, R., Bullister, J., Feely, R., Milero, F., Mordy, C., & Peng, T.-H. (2004). A global ocean carbon climatology: Results from global data analysis project (glodap). *Global Biogeochemical Cycles*, *18*(4), GB4031. https://doi.org/10.1029/2004GB002247

Kwon, E. Y., Sarmiento, J. L., Toggweiler, J. R., & DeVries, T. (2011). The control of atmospheric pco2 by ocean ventilation change: The effect of the oceanic storage of biogenic carbon. *Global Biogeochemical Cycles*, *25*(3). https://doi.org/10.1029/2011GB004059

Kwon, E. Y., Hain, M. P., Sigman, D. M., Galbraith, E. D., Sarmiento, J. L., & Toggweiler, J. R. (2012). North atlantic ventilation of "southern-sourced" deep water in the glacial ocean. *Paleoceanography*, *27*(2). https://doi.org/10.1029/2011PA002211

Large, W. G., & Yeager, S. G. (2009). The global climatology of an interannually varying air–sea flux data set. *Climate Dynamics*, *33*(2), 341–364. https://doi.org/10.1007/s00382-008-0441-3

Locarnini, R. A., Mishonov, A. V., Antonov, J. I., Boyer, T. P., Garcia, H. E., Baranova, O. K., Zweng, M. M., Paver, C. R., Reagan, J. R., Johnson, D. R., Hamilton, M., & Seidov, D. (2013). World ocean atlas 2013, volume 1: Temperature (S. Levitus & A. Mishonov, Eds.). *73*, 40.

Lozier, M. S. (2010). Deconstructing the conveyor belt. *Science*, *328*(5985), 1507–1511. https://doi.org/10.1126/science.1189250

Luyten, J. R., Pedlosky, J., & Stommel, H. (1983). The ventilated thermocline. *Journal of Physical Oceanography*, *13*(2), 292 –309. https://doi.org/10.1175/1520-0485(1983)013<0292:TVT>2.0.CO;2

Millet, B., Gray, W. R., de Lavergne, C., & Roche, D. M. (2023). Oxygen isotope constraints on the ventilation of the modern and glacial pacific. *Climate Dynamics*. https://doi.org/10.1007/s00382-023-06910-8

Müller, M. (2013). On the space- and time-dependence of barotropic-to-baroclinic tidal energy conversion. *Ocean Modelling*, *72*, 242–252. https://doi.org/10.1016/j.ocemod.2013.09.007

Naveira Garabato, A. C., MacGilchrist, G. A., Brown, P. J., Evans, D. G., Meijers, A. J. S., & Zika, J. D. (2017). High-latitude ocean ventilation and its role in earth's climate transitions. *Philos Trans A Math Phys Eng Sci*, *375*(2102). https://doi.org/10.1098/rsta.2016.0324

Ödalen, M., Nycander, J., Oliver, K. I. C., Brodeau, L., & Ridgwell, A. (2018). The influence of the ocean circulation state on ocean carbon storage and co_2 drawdown potential in an earth system model. *Biogeosciences*, *15*(5), 1367–1393. https://doi.org/10.5194/bg-15-1367-2018

Oka, A., & Niwa, Y. (2013). Pacific deep circulation and ventilation controlled by tidal mixing away from the sea bottom. *Nature Communications*, *4*(1), 2419. https://doi.org/10.1038/ncomms3419

Olsen, A., Key, R. M., van Heuven, S., Lauvset, S. K., Velo, A., Lin, X., Schirnick, C., Kozyr, A., Tanhua, T., Hoppema, M., Jutterström, S., Steinfeldt, R., Jeansson, E., Ishii, M., Pérez, F. F., & Suzuki, T. (2016). The global ocean data analysis project version 2 (glodapv2) – an internally consistent data product for the world ocean. *Earth System Science Data*, *8*(2), 297–323. https://doi.org/10.5194/essd-8-297-2016

Orsi, A. H., Jacobs, S. S., Gordon, A. L., & Visbeck, M. (2001). Cooling and ventilating the abyssal ocean. *Geophysical Research Letters*, *28*(15), 2923–2926. https://doi.org/10.1029/2001GL012830

Pradal, M.-A., & Gnanadesikan, A. (2014). How does the redi parameter for mesoscale mixing impact global climate in an earth system model? *Journal of Advances in Modeling Earth Systems*, *6*(3), 586–601. https://doi.org/10.1002/2013MS000273

Richardson, P. L. (2008). On the history of meridional overturning circulation schematic diagrams. *Progress in Oceanography*, *76*(4), 466–486. https://doi.org/10.1016/j.pocean.2008.01.005

Rousselet, L., Cessi, P., & Forget, G. (2021). Coupling of the mid-depth and abyssal components of the global overturning circulation according to a state estimate. *Science Advances*, *7*(21), eabf5478. https://doi.org/10.1126/sciadv.abf5478

Samelson, R., & Vallis, G. K. (1997). Large-scale circulation with small diapycnal diffusion: The two-thermocline limit. *Journal of Marine Research*, *55*(2), 223–275.

Sarmiento, J. L., Gruber, N., Brzezinski, M. A., & Dunne, J. P. (2004). High-latitude controls of thermocline nutrients and low latitude biological productivity. *Nature*, *427*(6969), 56–60. https://doi.org/10.1038/nature02127

Schlitzer, R. (2007). Assimilation of radiocarbon and chlorofluorocarbon data to constrain deep and bottom water transports in the world ocean. *Journal of Physical Oceanography*, *37*(2), 259 –276. https://doi.org/10.1175/JPO3011.1

Skinner, L., & Shackleton, N. (2005). An atlantic lead over pacific deep-water change across termination i: Implications for the application of the marine isotope stage stratigraphy. *Quaternary Science Reviews*, *24*(5), 571–580. https://doi.org/10.1016/j.quascirev.2004.11.008

Sloyan, B. M., & Rintoul, S. R. (2001). The southern ocean limb of the global deep overturning circulation. *Journal of Physical Oceanography*, *31*(1), 143 –173. https://doi.org/10.1175/1520-0485(2001)031<0143:TSOLOT>2.0.CO;2

Styles, A. F., MacGilchrist, G. A., Bell, M. J., & Marshall, D. P. (2024). Spatial and temporal patterns of southern ocean ventilation [e2023GL106716 2023GL106716]. *Geophysical Research Letters*, *51*(4), e2023GL106716. https://doi.org/10.1029/2023GL106716

Talley, L. D. (2013). Closure of the global overturning circulation through the indian, pacific, and southern oceans: Schematics and transports. *Oceanography*, *26*(1), 80–97.

Tanaka, Y. (2023). Energy conversion rate from subinertial surface tides to internal tides. *Journal of Physical Oceanography*, *53*(5), 1355 –1374. https://doi.org/10.1175/JPO-D-22-0201.1

Toggweiler, J., Druffel, E. R., Key, R., & Galbraith, E. D. (2019). Upwelling in the ocean basins north of the acc: 1. on the upwelling exposed by the surface distribution of Δ14c. *Journal of Geophysical Research: Oceans*, *124*(4), 2591–2608. https://doi.org/10.1029/2018JC014794

Urakawa, L. S., & Hasumi, H. (2012). Eddy-resolving model estimate of the cabbeling effect on the water mass transformation in the southern ocean. *Journal of Physical Oceanography*, *42*(8), 1288 –1302. https://doi.org/10.1175/JPO-D-11-0173.1

Warren, B. A. (1983). Why is no deep water formed in the north pacific? *Journals of Marine Research*, *41*, 327–347. https://doi.org/10.1357/002224083788520207

Worthington, L. (1981). The water masses of the world ocean: Some results of a fine-scale census. *Evolution of Physical Oceanography, Scientific Surveys in Honor of Henry Stommel*, 42–60. https://ocw.mit.edu/ans7870/textbooks/Wunsch/Edited/Chapter2.pdf

Wunsch, C. (2002). Oceanic age and transient tracers: Analytical and numerical solutions. *Journal of Geophysical Research: Oceans*, *107*(C6), 1–18. https://doi.org/10.1029/2001JC000797

Wunsch, C., & Heimbach, P. (2014). Bidecadal thermal changes in the abyssal ocean. *Journal of Physical Oceanography*, *44*(8), 2013 –2030. https://doi.org/10.1175/JPO-D-13-096.1

Yang, L., Nikurashin, M., Hogg, A. M., & Sloyan, B. M. (2021). The impact of lee waves on the southern ocean circulation. *Journal of Physical Oceanography*, *51*(9), 2933 –2950. https://doi.org/10.1175/JPO-D-20-0263.1

You, Y. (2003). The pathway and circulation of north pacific intermediate water. *Geophysical Research Letters*, *30*(24). https://doi.org/https://doi.org/10.1029/2003GL018561

Zweng, M. M., Reagan, J. R., Antonov, J. I., Locarnini, R. A., Mishonov, A. V., Boyer, T. P., Garcia, H. E., Baranova, O. K., Johnson, D. R., Seidov, D., & Biddle, M. M. (2013). World ocean atlas 2013, volume 2: Salinity (S. Levitus & A. Mishonov, Eds.). *74*, 39.

Supplementary Information

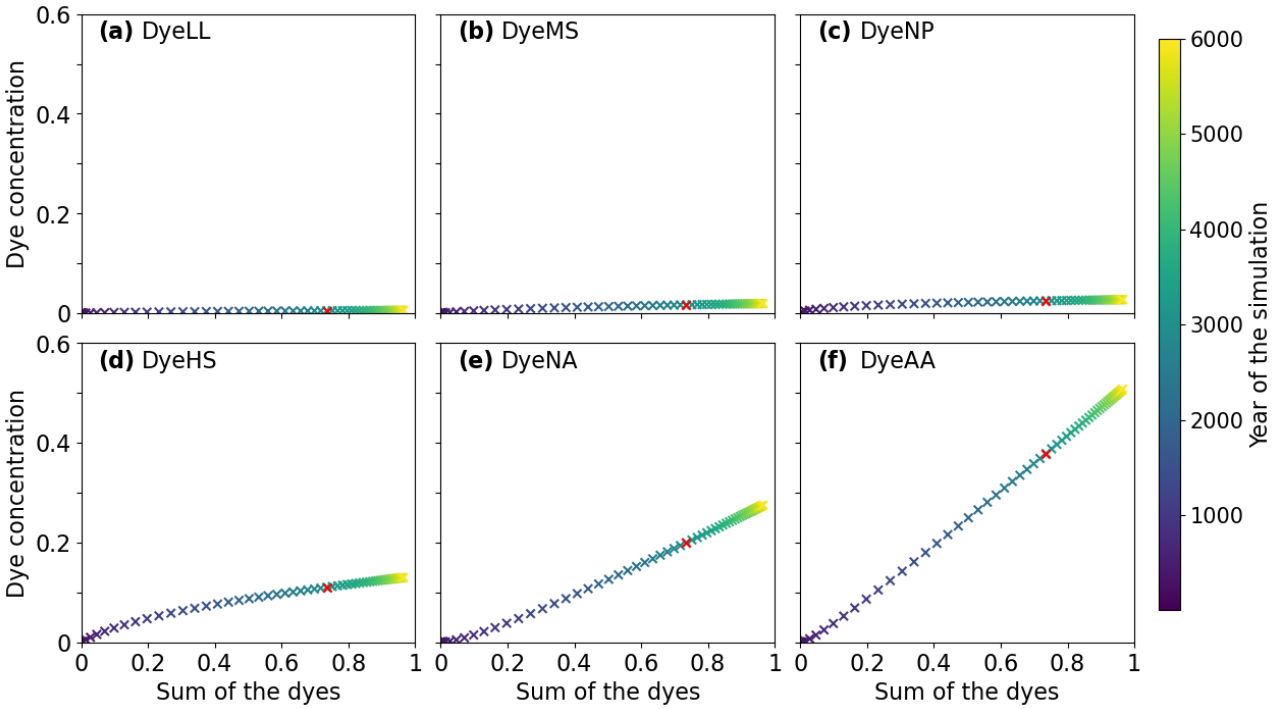

Figure S2.1: Figure showing the evolution of the zonal mean of each dye in the Pacific Shadow Zone (PSZ) as a function of the sum of the dyes, in the REF experiment. The colouring represents the year of the simulation to show the resistance to filling of the PSZ. The red cross in each panel marks the mean dye concentration at year 3,000. The PSZ is defined as the volume within 30-60°N, 150°E-120°W, and 1.5-3 km depth.

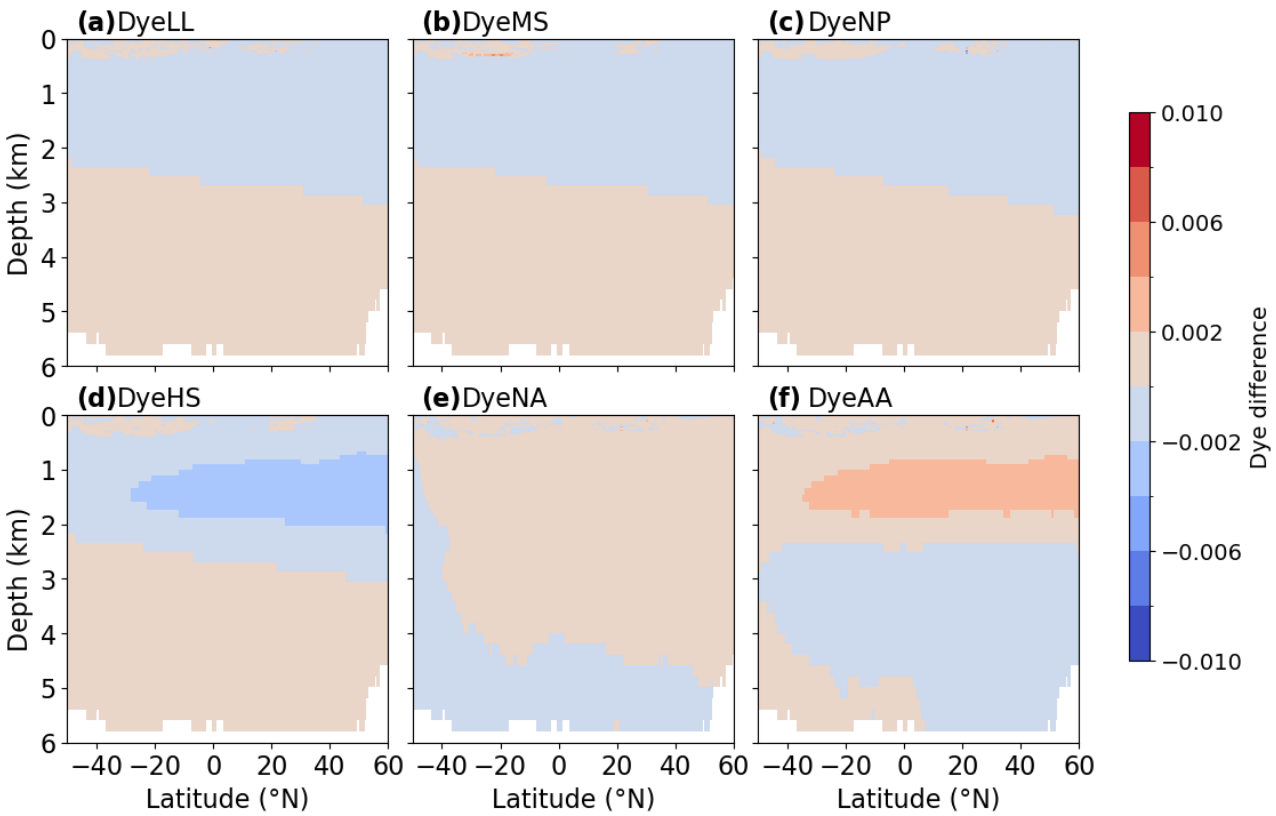

Figure S2.2: Zonal mean difference between dye concentrations extrapolated to equilibrium from year 3,000 and from year 6,000 in experiment REF. Note that simulated dye concentrations at year 6,000 and extrapolated concentration from year 6,000 are extremely close.

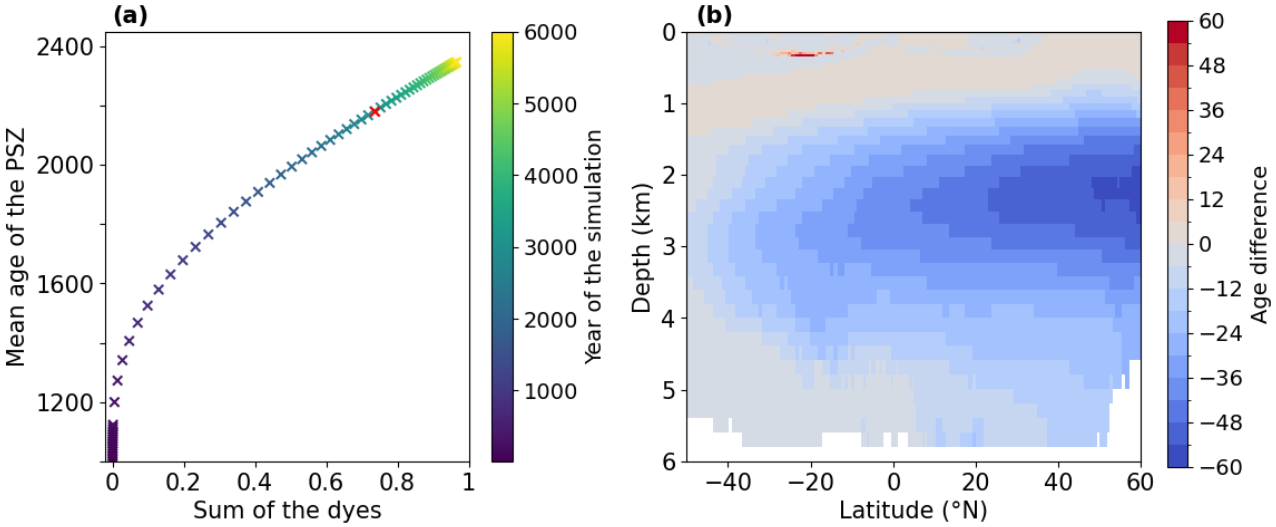

Figure S2.3: Panel **(a)** represents the mean age of the Pacific Shadow Zone (PSZ) as a function of the mean total dye concentration in the PSZ, in the REF experiment. The colouring represents the year of the simulation and the red cross marks year 3,000. Panel **(b)** shows the difference between the age extrapolated to equilibrium from year 3,000 and the simulated age at year 6,000, divided by the sum of the dyes. The PSZ is defined as the volume within 30-60°N, 150°E-120°W, and 1.5-3 km depth.

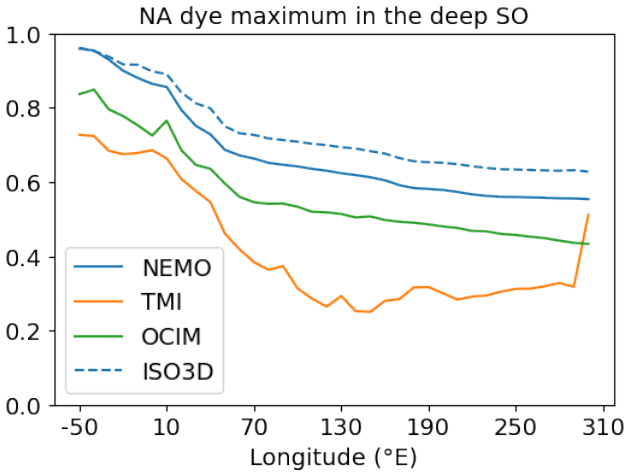

Figure S2.4: The maximum of the NA dye concentration within 30-60°S below 1 km depth is shown as a function of longitude, for REF (blue), TMI (orange) and OCIM (green). Another NEMO simulation, ISO3D, is also represented as a dashed blue curve to show the impact of a different isopycnal mixing scheme.

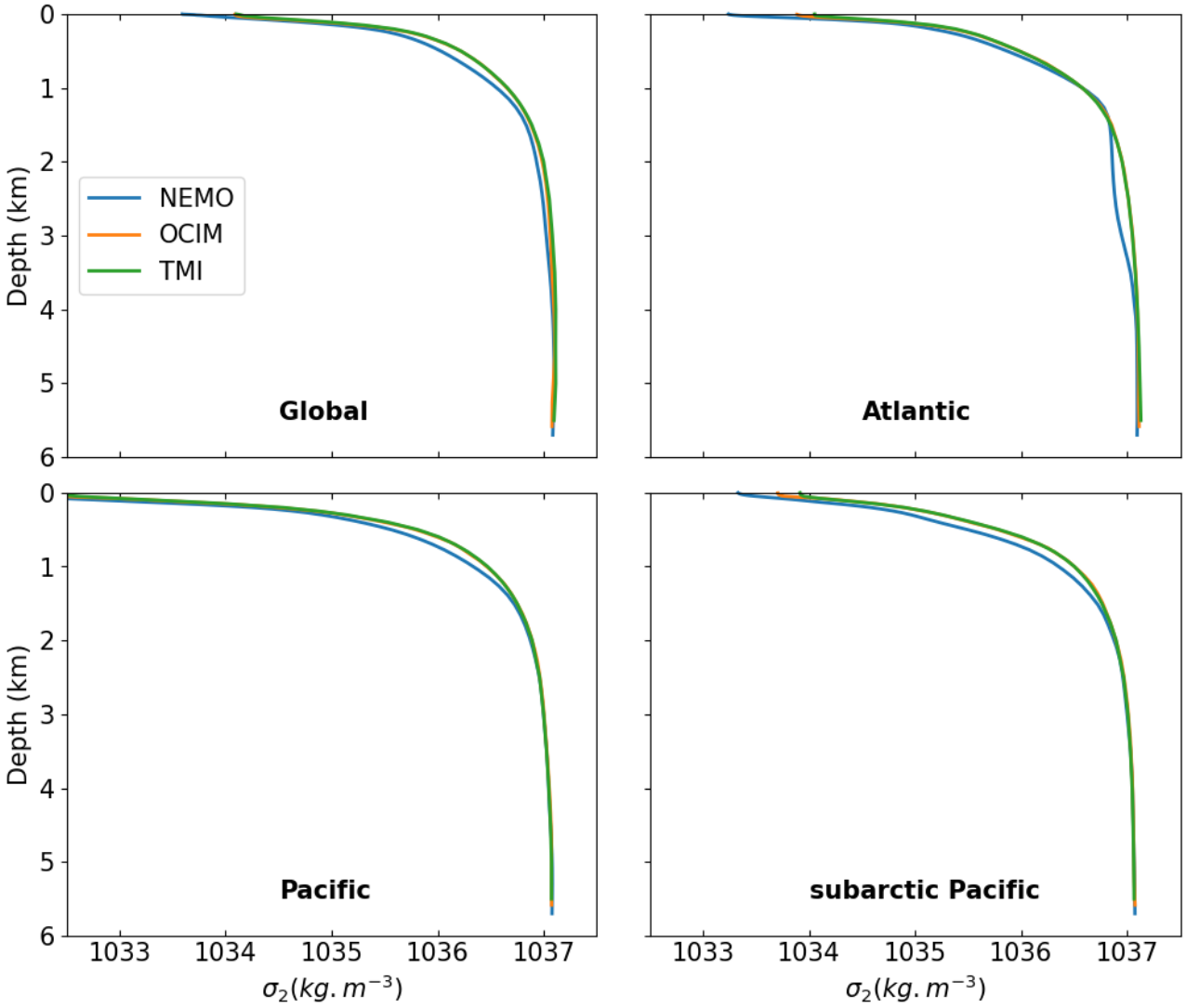

Figure S2.5: A comparison of the stratification for the REF simulation in NEMO and the inverse models OCIM and TMI, for the global ocean (top left), Pacific (bottom left), Atlantic (top right) and subarctic Pacific (bottom right). The southern boundary of the Pacific and Atlantic for this figure is 30°S. The southern boundary of the subarctic Pacific is 30°N.

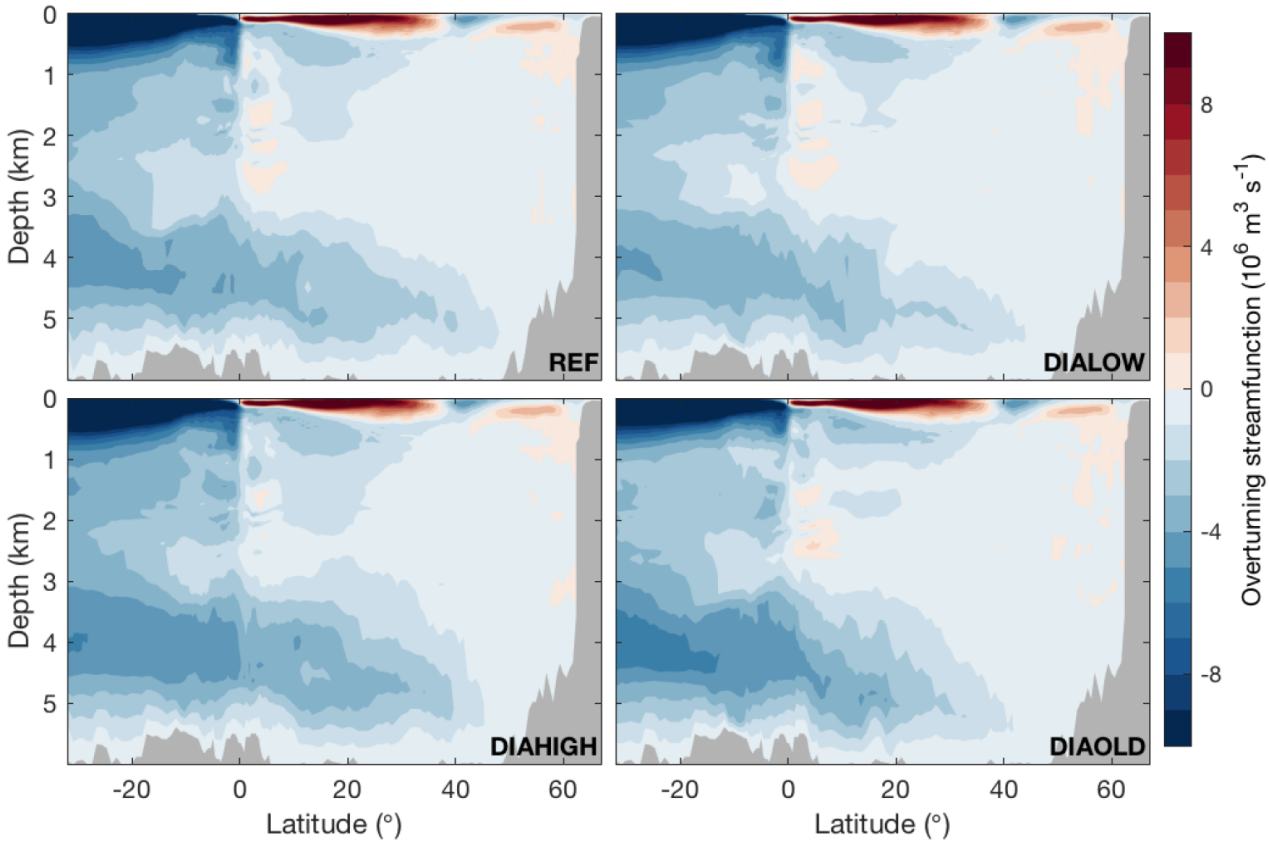

Figure S2.6: The overturning streamfunction in the different online NEMO simulations (representing different diapycnal mixing parameterizations) used in this study, at the year 1000. DIAOLD was not used in this study and represent the simulation 'OLD' in Rathore et al. (2024).

Rathore et al. (2024)

Effects of improved tidal mixing in NEMO one-degree global ocean model

Saurabh Rathore[1,2], Casimir de Lavergne[1], Gurvan Madec[1,3], Jean-Baptiste Sallée[1], Christian Ethé[1], Antoine Nasser[1,3], Bruno Millet[4], Martin Vancoppenolle[1]

1 LOCEAN Laboratory, Sorbonne University-CNRS-IRD-MNHN, Paris, France
2 Indian Institute of Technology, Delhi, India
3 Université Grenoble Alpes, Inria, CNRS, Grenoble INP, LJK, Grenoble, France
4 Laboratoire des Sciences du Climat et de l'Environnement, CEA-CNRS-UVSQ, Université Paris-Saclay, Gif-sur-Yvette, France

Correspondence: Saurabh Rathore (srathore@iitd.ac.in)

Abstract: Diapycnal mixing in the ocean interior has diverse numerical representations in extant global ocean models. These representations affect the simulated transport and storage of oceanic tracers in ways that remain little studied. Here we present the impacts of three different tidal mixing schemes in thousand-year-long simulations with the NEMO global ocean model at one-degree resolution. The first scheme includes local bottom-intensified mixing at internal tide generation sites and a constant background diffusivity. The second explicitly includes both local and remote tidal mixing, with no background diffusivity. The third scheme is identical to the second but has the added contribution of bottom-trapped (subinertial) internal tides, known to be important in polar regions. The three simulations show broadly similar circulation and stratification but important regional differences. Explicit representation of remote tidal mixing strengthens the Atlantic Meridional Overturning Circulation by up to 1.5 x 10^6 m^3 s^{-1}. Inclusion of bottom-trapped internal tides reduces heat reaching Antarctica by eroding Circumpolar Deep Water at southern high latitudes, and reduces the mean age of the global deep (> 2 km) ocean by 10%. The results call for more observational constraints on polar ocean mixing, and point to multi-faceted climatic repercussions of tidal mixing representations.

1. Introduction

The ocean can be viewed as a stack of density layers that exchange slowly with their neighbors. Cross-layer exchanges of heat and matter occur at ocean boundaries via surface and geothermal fluxes, and in the interior via mixing of ocean tracers at molecular scale (Walin 1982, Iudicone et al. 2008). This irreversible mixing of tracers is catalyzed by small-scale turbulence, which effectively controls the rate at which layers communicate with each other in the ocean interior (Gregg 1987). By transferring mass and tracers across density layers, small-scale turbulence thus shapes the physical ocean state and regulates the transport and storage of climatically important tracers, such as nutrients, carbon and heat (Tuerena et al. 2019, de Lavergne et al. 2022, Melet et al. 2022).

Global ocean models do not resolve small-scale turbulence and must therefore resort to parameterizations of its effects. The common approach is to provide a vertical (or diapycnal) diffusivity that mixes tracers and momentum across the model layers. However, methods to determine the diapycnal diffusivity distribution vary widely across models. In the strongly mixing surface boundary layer, energetic considerations and/or classical turbulence theory are generally invoked to obtain a set of equations relating diffusivity to surface forcing, velocity shear and density stratification (Gaspar et al. 1990, Large et al. 1994, Reichl and Hallberg 2018). In the deeper ocean, diffusivity is locally enhanced when the resolved shear or stratification is unstable. But this falls short of capturing the effects of unresolved instabilities energized by winds and tides. To account for the latter, most models combine a static background diffusivity (Jochum 2009) with a representation of bottom-enhanced tidal mixing (Simmons et al. 2004). Even so, the choice of background diffusivity and the imposed tidal mixing distribution vary across modelling centers and across model configurations (e.g., Adcroft et al. 2019, Kiss et al. 2020).

Consequences of varying the oceanic background diffusivity or the tidal mixing energy distribution have been recently explored using climate model simulations (Melet et al. 2016, Tatebe et al. 2018, Hieronymus et al. 2019). These studies highlight important changes in the heat balance and overturning circulation of the global ocean, motivating the need to better constrain diapycnal mixing in the ocean interior and to refine its representation in climate models. Studies also emphasized the need to develop energy constrained parameterizations, where diffusivity is not static but instead deduced from a three-dimensional distribution of turbulence production (Huang 1998, Eden et al. 2014). This requires tracking energy routes from forcing to small-scale turbulence production.

The main such energy route involves the generation, propagation and breaking of internal tides—that is, internal waves of tidal frequency sparked by interaction of barotropic tidal currents with sloping topography (Egbert and Ray 2000, Vic et al. 2019, de Lavergne et al. 2019). The traditional parameterization strategy is to estimate the rate of internal tide generation at the bottom, and assume that a third of this power dissipates in the local water column according to an exponential decay from the seafloor upwards (St Laurent et al. 2002, Simmons et al. 2004). However, it has become clear that the remaining two-thirds of power, which correspond to large-scale (or low-mode) internal tides able to propagate far from generation sites, also require explicit parameterization (Eden and Olbers 2014, MacKinnon et al. 2017, de Lavergne et al. 2019). Indeed, low-mode internal tides explain the bulk of observed dissipation patterns in the upper ocean beneath the mixed layer, and cannot be reliably represented by a constant background diffusivity (Pollmann et al. 2017, de Lavergne et al. 2020).

Two schemes have been developed to track the propagation and dissipation of internal tide energy, including that of low-mode internal tides. The scheme of Eden and Olbers (2014) prescribes two-dimensional maps of internal wave generation, split between a high-mode and a low-mode compartment, and uses internal wave theory to redistribute this power horizontally and vertically within the simulated stratification. An alternative scheme (de Lavergne et al. 2020) prescribes four two-dimensional maps of internal tide dissipation,

whose power is then distributed vertically within the simulated stratification according to a process-dependent vertical structure. The latter scheme thus neglects interactivity of the low-mode internal tide energy propagation, but allows for a realistic three-dimensional distribution of mixing energy at low computational cost (de Lavergne et al. 2020).

Neither scheme includes subinertial internal tides, that is, internal tides whose frequency is lower than the local Coriolis frequency. Such internal tides, which occur poleward of 74.5° for the dominant M_2 semidiurnal tide and poleward of 30° for the K_1 diurnal tide, are trapped at the bottom and ultimately break to cause mixing near the seafloor (Chapman 1989, Tanaka et al. 2013, Falahat and Nycander 2014, Tanaka 2023). They are thought to play an important role in mixing the polar oceans (Rippeth et al. 2015, Fer et al. 2020), where they dominate over their freely propagating counterparts (Müller 2013). Yet the potential global-scale impacts of mixing by bottom-trapped internal tides remain unexplored.

Here, we implement the parameterization of local and remote tidal mixing proposed by de Lavergne et al. (2020) in the Nucleus for European Modelling of the Ocean (NEMO), and document its behavior in a long integration of a global ocean configuration with 1° nominal horizontal resolution. We also examine differences with two twin experiments: one which includes the additional – hitherto neglected – contribution of subinertial internal tides, and another which follows the traditional choice (Simmons et al. 2004) of a constant background diffusivity and local bottom-intensified tidal mixing. The configuration and mixing parameterizations are presented in detail in the next section. In section 3, we document the main characteristics and sensitivities of our simulations. We conclude with a summary and discussion of results (section 4).

2. Methods

2.1 Configuration overview and forcing

Our configuration uses version 4.2 of NEMO (NEMO System Team 2022), which solves the primitive equations in Boussinesq approximation. The ocean model component is coupled to the SI^3 dynamic-thermodynamic sea ice model (Rousset et al. 2015, Vancoppenolle et al. 2023). We employ a global Mercator grid of 1° nominal horizontal resolution, referred to as ORCA1. The meridional resolution is refined at high latitudes so that the meridional grid spacing matches the reducing zonal spacing, and refined within 15° of the equator to better resolve equatorial dynamics. As a result, the average area-weighted horizontal resolution is 0.69° or 83 km over the global ocean; in the Southern Ocean south of 40°S, it is 0.57° or 45 km. In the vertical, the model includes 75 layers that follow geopotential surfaces, except for time-dependent stretching or squeezing of layers to accompany changes in sea surface height. The vertical grid spacing varies from about 1 m near the surface to 200 m in the abyssal ocean. Partial cells at the bottom allow for a better representation of the observed bathymetry. The domain covers depths of up to 6000 m.

The model is ran for 1,000 years with a time step of 45 minutes. Initial hydrographic conditions are Conservative Temperature and preformed salinity fields calculated from the observational climatology of Gourestki (2019) using the Gibbs SeaWater Toolbox (McDougall and Barker 2011). Preformed salinity is used instead of Absolute Salinity because the model, while employing the TEOS-10 equation of state (IOC, SCOR and IAPSO 2010), does not represent biological (non conservative) sources of salt included in Absolute Salinity. For brevity, Conservative Temperature and preformed salinity will be referred to as temperature and salinity in all the following. At the simulation start, velocities are zero and sea ice is present where the initial sea surface temperature is within 0.5 °C of the freezing point.

At the bottom, the model is forced by geothermal heat fluxes mapped by Lucazeau (2019) (Supplementary Figure S1). At the surface, atmospheric conditions are prescribed following version 2 of the Coordinated Ocean-ice Reference Experiments (COREv2) normal year forcing (Large and Yeager 2009), which represents a typical year of the instrumental period (mostly between 1979 and 2006). This forcing includes 6-hourly fields of zonal and meridional wind at 10 m and of air temperature and humidity at 10 m. In addition, it includes daily mean radiation and monthly mean precipitation (rain and snow) reaching the surface. Freshwater forcing also includes river runoff, iceberg melt released in the surface layer following the spatial pattern estimated by Merino et al. (2016), and basal melt from Antarctic ice-shelf cavities released at depth over the mouth of cavities (Mathiot et al. 2017). Basal melt fluxes from each cavity and the total magnitude of Antarctic iceberg melt are prescribed according to estimates of Depoorter et al. (2013); they are not interactive and the cavities are closed.

Surface fluxes including evaporation are computed using bulk formulae, as a function of the simulated sea surface temperature and sea ice cover. To compensate for missing atmospheric feedbacks, restoring to the observed seasonally varying sea surface salinity (as mapped by Gouretski (2019)) is activated, with a timescale of 230 days per 50 m of seawater. To ensure that the freshwater balance is globally closed and avoid drift in sea level, the global mean freshwater flux entering the ocean is calculated at each time step and subtracted from evaporative-precipitative fluxes of every surface ocean grid cell. This uniform adjustment adds 0.13 m of sea level every year on average in our simulations, a magnitude that can be compared to the 1.11 m added by precipitation every year. Closure of the freshwater balance in forced-ocean experiments is a delicate issue: our experience shows that the required adjustment can grow large in the absence of careful calibration. In addition, this adjustment introduces a non-physical global interdependence of freshwater fluxes that should be borne in mind when interpreting temporal variability or sensitivity to forcing and physics.

2.2 Representation of advection and diffusion

The vector-invariant form of equations is chosen. Advection of momentum uses a second-order centered scheme, and an energy and enstrophy conserving scheme for the relative and planetary vorticity terms (Sadourny 1975). These choices allow for reduced sensitivity of the simulated circulation to artificial indentation of model isobaths (Nasser et al. 2023).

Momentum diffusion is accomplished by a Laplacian operator and a prescribed horizontal viscosity of 20,000 $m^2 s^{-1}$, reduced to 1,000 $m^2 s^{-1}$ around the equator. The lateral boundary condition is free slip. To aid downslope flow of dense water along the staircase-like topography, the advective scheme of Campin and Goosse (1999) is activated. A quadratic bottom drag with coefficient 1.0×10^{-3} is included.

Restratification by baroclinic mesoscale eddies is parameterized by downgradient diffusion of isopycnal layer thickness, following the approach of Gent and McWilliams (1990). The associated thickness diffusivity varies horizontally with the simulated stratification (Supplementary Figure S2): it is proportional to the square of the Rossby radius and to the Eady growth rate (Held and Larichev 1996, Visbeck et al. 1997), and tapered equatorward of 20° to account for the increasing sparsity of baroclinic mesoscale eddies there (Chelton et al. 2011). Restratification of the surface mixed layer by submesoscale eddies is parameterized following Fox-Kemper et al. (2008).

Advection of all tracers is performed with a second-order Flux Corrected Transport scheme. Diffusion of tracers along isopycnals by mesoscale and smaller scale turbulence (Redi 1982, Abernathey et al. 2022) is parameterized with a diffusivity that varies geographically with the local Rossby radius and Eady growth rate (Supplementary Figure S2), like the thickness diffusivity.

Vertical diffusion of momentum and tracers is parameterized by three components: a Turbulent Kinetic Energy (TKE) closure, a convection scheme, and a tidal mixing scheme. The TKE closure is order 1.5: it includes a prognostic equation for TKE and diagnostic equations relating mixing parameters and TKE (Gaspar et al. 1990, Blanke and Delecluse 1993). This scheme produces enhanced vertical mixing when the Richardson number of the resolved flow falls below a critical value of 0.22. Mixing is further enhanced near the base of the mixed layer to account for the effects of unresolved Langmuir cells (Axell 2002) and near-inertial oscillations. Near-inertial oscillations of the mixed layer, generated by high-frequency winds, fuel intense mixing at the base of the mixed layer and relatively weak mixing in the deeper ocean (Plueddemann and Farrar 2006, Alford 2020, von Storch and Lüschow 2023). In the TKE scheme of NEMO their contribution to upper-ocean mixing is represented by adding a vertical profile of TKE that decays exponentially with depth and that peaks at a small fraction of the surface TKE. Here we choose the fraction to be 8%, and the decay scale to vary from 1 m at the equator to 30 m at high latitudes. The advantages of this scheme are its simplicity and interactivity: the induced mixing depends on the surface TKE hence on the instantaneous wind forcing. The drawbacks are the ad hoc vertical profile and the absence of constraint on the power consumed by this mixing.

The convective scheme simply consists in enhancing the vertical diffusivity to 10 $m^2 s^{-1}$ when stratification is statically unstable. No parameterization of double diffusive mixing is included here. Hence, in our experiments, vertical mixing in the ocean interior (away from the surface boundary layer) relies almost exclusively on the tidal mixing parameterization, which is detailed next.

2.3 Tidal mixing parameterization and sensitivity experiments

The tidal mixing scheme employs four static maps of depth-integrated internal tide energy dissipation (de Lavergne et al. 2020), which have been remapped onto the ORCA1 grid using an energy-conserving interpolation. Each map is associated with a distinct dissipation mechanism and a corresponding vertical structure of turbulence production, which depends on the simulated stratification. Hence, at each time step, the power available in each water column is distributed in the vertical, yielding a global three-dimensional distribution of turbulence production $\varepsilon(x,y,z)$. The vertical diffusivity K_ρ is then deduced from turbulence production using a zero-order closure, $K_\rho = R_f \, \varepsilon \, N^{-2}$, where N is the buoyancy frequency and R_f is the mixing efficiency (Osborn 1980). Mixing efficiency is known to vary depending on local flow and turbulence characteristics (e.g., Mashayek and Peltier 2013, Bouffard and Boegman 2013, Vladoiu et al. 2019). However there is no consensus about, nor comprehensive model of, mixing efficiency variations in the ocean, so that the traditional assumption of a constant $R_f = 1/6$ remains the standard choice (Gregg et al. 2018). For simplicity, we take $R_f = 1/6$ in all three experiments. 500-year simulations performed with a coarser (2°) resolution global ocean configuration showed only weak sensitivity of ocean circulation to mixing efficiency variations when parameterized following de Lavergne et al. (2016). An upper bound of 10^{-2} m^2 s^{-1} is imposed on the tidal vertical diffusivity. The lower bound is 1.4×10^{-7} m^2 s^{-1} for tracers and 1.4×10^{-6} m^2 s^{-1} for momentum, corresponding to molecular heat diffusivity and molecular viscosity, respectively. No differential mixing between temperature and salinity is implemented.

The mapping of internal tide energy dissipation performed by de Lavergne et al. (2019, 2020) uses analytical estimates of internal tide generation that are valid only at seafloor depths greater than 400 m and equatorward of the turning latitude of each tidal constituent, due to assumptions in the analytical theory (Bell 1975, Falahat et al. 2014). To remedy these two limitations, we turn to an alternative estimate of internal tide generation, obtained with a high-resolution ocean general circulation model (Müller 2013). This model estimate agrees broadly with the analytical calculation of Falahat et al. (2014) within overlapping validity regions, while also including internal tides generated over shallow (< 400 m) topography and poleward of their turning latitude. Müller (2013) provides four two-dimensional power fields (available at https://www.wdc-climate.de/ui/entry?acronym=DKRZ_lta_510), corresponding to the four tidal constituents (M_2, S_2, K_1 and O_1) included in the simulation. These fields have positive and realistic global integrals (Table 1) yet contain frequent negative values, like the analytical estimates of Falahat et al. (2014). We correct for these negative values following de Lavergne et al. (2019): we first set negative values to zero, then multiply the resulting fields by a depth-dependent factor that preserves the original depth-profile of internal tide generation. This procedure is ad hoc but yields plausible distributions (de Lavergne et al. 2019; Fig.1). Within each of the four corrected fields, we select regions where the tidal frequency exceeds the Coriolis frequency to obtain the generation rate of *trapped internal tides* (E_{tra}). In the remainder of the ocean, we select grid cells where bathymetry is less than 400 m to obtain the generation rate of *shallow internal tides* (E_{sha}). The total power available from each of the two components and each of the four tidal constituents is given in Table 1.

To implement these two components in the tidal mixing parameterization, we sum over the four tidal constituents, using scaling factors (see Table 1) to account for missing constituents, following de Lavergne et al. (2019). We then remap the total fields, E_{tra} and E_{sha}, onto our model grid (Fig.1). The two fields correspond to generation rates, not dissipation rates, hence they are not direct estimates of turbulence production integrated over the water column. However, we expect the dissipation to be near local in both cases, because subinertial internal tides are bottom-trapped (Albrecht et al. 2006, Tanaka et al. 2013, Musgrave et al. 2016), and because the decay time of internal tides implied by wave-wave interactions is very short in shallow seas (de Lavergne et al. 2019). We thus assume local dissipation at the 1° resolution of our configuration. Subinertial internal tides are expected and observed to cause mixing intensified near the seafloor (Tanaka et al. 2013, Rippeth et al. 2015, Musgrave et al. 2017): we choose the same vertical structure as that attributed to dissipation at critical topography, i.e. an exponential decay from the bottom upwards with a decay scale determined by local topographic slopes (de Lavergne et al. 2020). Shallow internal tides are expected to dissipate primarily via wave-wave interactions: we thus distribute their power in the vertical as proportional to the square of the simulated buoyancy frequency (Gregg 1989, D'Asaro and Lien 2000).

To investigate the sensitivity of the ocean state to the representation of tidal mixing, we performed three experiments. Experiment NEW includes explicit and comprehensive treatment of freely propagating internal tides; that is, it incorporates the tidal mixing scheme of de Lavergne et al. (2020) with the added contribution of shallow internal tides (E_{sha}), implemented as described above. Experiment TRA is identical to NEW but includes the additional contribution of subinertial internal tides (E_{tra}). The third experiment, termed OLD, includes a constant background diffusivity of 10^{-5} m^2 s^{-1} and local bottom-intensified mixing at internal tide generation sites (Simmons et al. 2004). This bottom-intensified mixing is specified by assuming that: (i) one-third of the power input to internal tides mapped by Nycander (2005) fuels turbulence production in the local water column; and (ii) turbulence production decays exponentially with height above bottom, with a uniform 500 m decay scale (St Laurent et al. 2002).

The depth-integrated turbulence production implied by each of the three tidal mixing representations is mapped in Figure 2. For the OLD experiment, the power implicitly consumed by the background diffusivity is included, and calculated as the vertical integral of $\rho_0 K_\rho N^2 R_f^{-1}$ with ρ_0 = 1026 kg m^{-3} the reference density of seawater and N the annual mean buoyancy frequency from the first simulation year. The global total power amounts to 1.12 TW in OLD, 1.28 TW in NEW and 1.40 TW in TRA. Although these totals are of the same order of magnitude, they hide substantial differences in geographical patterns of mixing (Fig.2). Explicit representation of remote tidal mixing creates a much more heterogeneous mixing distribution, reflecting the heterogeneous sources and sinks of internal tide energy. Inclusion of trapped internal tides raises power availability poleward of 30° and most conspicuously in the subarctic Pacific, Arctic and Southern Oceans (Figs. 1a and 2b,c).

Similarities and differences between the three mixing representations are further illustrated in Figure 3, which shows turbulence production summed over depth and longitude (Fig.3a)

or along geopotential model layers (Fig.3b). The latitudinal profiles highlight the similarity of bulk mixing rates across the three simulations. Most important relative differences occur at high latitudes, where TRA has the highest power input to mixing, except north of 70°N; the background diffusivity of OLD sustains unrealistically high mixing in the Arctic pycnocline (Nguyen et al. 2009). The depth profiles highlight the large proportion of power contained in the top 500 m: contrary to common perception, internal tide-driven mixing is prominent in the upper ocean, not only in the deep ocean (Kunze et al. 2006, de Lavergne et al. 2020). The tidal mixing parameterization in NEW and TRA generates more mixing than OLD in the ocean's top kilometer, while the opposite is true between 1 and 3 km depth.

It must be emphasized that power consumed by tidal mixing in OLD is not fixed in time: it evolves with stratification changes. The total power effectively consumed in our OLD experiment increases by 1.5% over the full length of the simulation; a relatively small change that reflects the small drift in stratification. However, should stratification increase rapidly, for example under a strong greenhouse forcing scenario, the power consumed by the constant background diffusivity could increase substantially (de Lavergne et al. 2020). The map and curves shown for OLD in Figures 2 and 3 are thus only applicable to the initial state of our experiment: the same diagnostics applied to a different model state would generate different magnitudes and patterns. These considerations underline the inadequacy of static diffusivities: they ignore energy constraints and do not allow for a realistic response of mixing to forcing or stratification changes (Eden et al. 2014, Sigman et al. 2010).

2.4 Ideal age and offline simulation

To investigate ventilation timescales, the simulations include an ideal age tracer. This tracer is advected and diffused using the same velocities, diffusivities and numerical schemes as those transporting temperature and salinity. Ideal age is restored to zero in the top 10 m of ocean, and increases by 1 year per year deeper than 10 m. It is initialized with uniform null concentrations. After 1,000 years, it is still far from equilibrium in the deep ocean, despite relative stabilization of the circulation and stratification (Fig.4). In order to quantify deep ventilation rates in the near steady state, we extend the simulations of ideal age in offline mode, for an extra 3,000 years. The offline simulation uses physical variables (velocities, diffusivities, layer thicknesses, temperature and salinity) from the last year of the full simulation to evolve the passive tracer distribution. In detail, we output physical variables from year 1,001 of each experiment at five-day frequency, and simulate ideal age as in the online simulation, except that physics are not computed but instead read from this five-day output and time-interpolated at each time step.

3. Results

3.1 Drift

The global mean ocean temperature increases by 0.29 °C in OLD, 0.34 °C in TRA and 0.35 °C NEW over 1,000 years (Fig.4a). The drift is not linear and slows progressively. Over the last century of the simulations, global mean temperature increases only by 1.5 x 10^{-3} °C in OLD,

8.6 x 10^{-3} °C in NEW and 4.3 x 10^{-3} °C in TRA; increases in mean deep ocean temperature are similar or smaller. By construction (section 2.1), the salt content of the global ocean is constant over the simulation. Redistribution between layers can nonetheless occur: over the whole simulation length and across the experiments, the mean salinity in the upper km decreases by 0.022-0.050 g kg^{-1} whereas the mean salinity in the deeper ocean increases by 0.007-0.016 g kg^{-1}. Overall, the drift toward warmer and saltier deep waters can largely be explained by a warm and salty bias at North Atlantic Deep Water (NADW) formation sites, which is progressively communicated to the global deep ocean (see section 3.3).

The overturning circulation shows relatively rapid stabilization: the Atlantic Meridional Overturning Circulation (AMOC) and the lower cell of the MOC reach a near-steady strength after a few hundred years (Fig.4c-e) in all three experiments. The strength of the lower cell is diagnosed in density coordinate and shown both for the latitude of peak strength (64°S; Fig.4d) and a middle latitude (30°S; Fig.4e). The eastward transport through Drake Passage, which is a key indicator of Southern Ocean circulation and stratification, is relatively stable in all three experiments (Fig.4b; mind the small y-axis range). Specifically, it increases from 163 Sv (1 Sv is 10^6 m^3 s^{-1}) in the initial year to 172 Sv, 174 Sv and 181 Sv at the end of the TRA, NEW and OLD experiments, respectively. The positive drift over the tenth century is largest in TRA but lesser than 0.4 Sv. Observational estimates of the Drake Passage transport range between 134 Sv and 174 Sv (Cunningham et al. 2003, Donohue et al. 2016, Xu et al. 2020); our simulations thus lie near the high end of observations.

To bring out the level of equilibration of the model stratification and circulation in the final state of our experiments, we extended experiment TRA for an additional 500 years. The extended time series show that the circulation of TRA is quasi steady by year 1000 (Fig.4b-e). Only the global mean ocean temperature displays a persistent, weak drift of 3.6 x 10^{-3} °C per century (Fig.4a). Given the small degree of variability and drift present in the analyzed time series near the end of our millennial integrations (Fig.4), we focus hereafter on simulation characteristics averaged over years 991-1000 of each experiment. When discussing anomalies, we will take NEW as the reference experiment and examine differences between OLD and NEW (OLD – NEW) or between TRA and NEW (TRA – NEW).

3.2 Surface boundary layer

The surface mixed layer is central to ocean ventilation, being the layer that is effectively in contact with the atmosphere. The depth of this layer, and its spatial and seasonal variations, contribute to shape water-mass characteristics and transports throughout the ocean (Marshall and Nurser 1991, Williams et al. 1995). Figure 5 compares the mixed layer depth (MLD) in experiment NEW to the observational map of Sallée et al. (2021). MLD is defined here as the depth at which potential density exceeds its 10 m value by 0.03 kg m^{-3} (de Boyer Montégut et al. 2004). The broad geographical patterns are well captured by the model for each season. The main difference is a tendency to overestimate MLD at high latitudes in winter and spring, indicative of overestimated winter deep convection and possibly underestimated spring restratification. Main deep convection sites in the model are the Labrador Sea, Irminger Sea, Norwegian Sea, southern Weddell Sea and a band along the northern edge of the Antarctic Circumpolar Current (ACC).

Overall, the simulated MLDs are weakly sensitive to the representation of tidal mixing. Principle differences between experiments occur in winter. Figure 6 shows the annual maximum MLD of NEW and anomalies in OLD and TRA relative to NEW. In the North Atlantic, OLD has shallower winter deep convection than NEW (Fig.6b), consistent with weaker NADW formation and a weaker AMOC. On the other hand, OLD has deeper winter mixed layers in the polar oceans (Arctic and near-Antarctic), which we attribute to higher levels of mixing within polar haloclines (Figs. 3 and 7) that precondition winter convection (Nguyen et al. 2009, Morawitz et al. 1996). Significant anomalies in subantarctic MLDs are also apparent, with an overall shoaling in the Atlantic and Indian sectors and deepening in the Pacific sector (Fig.6b). These changes are suggestive of slight frontal shifts in the ACC, combined to local preconditioning of deep convection by interior mixing (Sloyan et al. 2010).

Southern Hemisphere anomalies in TRA are qualitatively similar to those in OLD, albeit weaker. This similarity suggests that the MLDs are sensitive to the bulk mixing across the high-latitude permanent pycnocline. Both TRA and OLD have stronger average mixing across the Southern Ocean pycnocline than NEW: OLD has higher mixing throughout most of the upper ocean while TRA has higher mixing along continental slopes (Fig.7). In the Northern Hemisphere, differences between TRA and NEW are mostly found in the subpolar North Atlantic. In particular, MLDs deepen in the Irminger Sea and central Labrador Sea, possibly contributing to a slightly stronger AMOC (Fig.4c).

Sea ice coverage exerts a profound influence on deep ocean stratification and ventilation, particularly in the Southern Ocean (Goosse and Fichefet 1999, Haumann et al. 2016, Klocker et al. 2023), and can be sensitive to deep ocean mixing (Tatebe et al. 2018). In our forced ocean experiments, sea ice is insensitive to the chosen tidal mixing scheme in both hemispheres (Fig.8). The seasonal expansion and retreat of the sea ice pack is reasonably well represented, despite Antarctic sea ice dropping too low in summer and retreating too late during the warming season (Fig.8b). Simulated deep mixed layers in southern polar waters are not associated with openings in the sea ice (Fig.5f,h). We will show in the next section that bottom waters are produced on Antarctic shelves rather than in open ocean convection zones.

3.3 Water-mass characteristics

The zonal mean temperature simulated by NEW in the Atlantic shows a warm bias at mid-depths (1.5 to 3 km) and a cold bias in the deeper abyssal layer (Fig.9a,b). These biases reflect important biases in NADW, which is too warm and salty (Fig.10), and which does not reach as deep as in the observations. Lack of realistic overflows from the Nordic Seas into the Irminger and Iceland basins may partly explain this enduring bias of ocean general circulation models (Danabasoglu et al. 2014, Heuzé 2021). Lack of the densest varieties of NADW can also stem from the use of climatological atmospheric forcing: interannual variations in atmospheric conditions are key to produce water-mass extremes and to simulate realistic ventilation patterns in the subpolar North Atlantic (Marzocchi et al. 2021). The absence of NADW in the abyss allows Antarctic Bottom Water (AABW) to take over this volume, leading to the cold and fresh bias deeper than 3.5 km. The density of bottom waters in NEW compares well with observations (Fig.10), so that the shallow bias of NADW

cannot be attributed to overly dense AABW. More generally, temperature and salinity biases tend to have opposing effects on density, so that the density distribution matches observations more closely than temperature or salinity (Fig.10).

In the OLD experiment, deep hydrographic biases in the Atlantic are slightly enhanced: NADW is about 0.1 °C warmer and AABW is 0.2 °C colder than in NEW (Fig.9c). Nonetheless, at high southern latitudes, in the Weddell Sea, the colder temperatures of OLD bring the model closer to observations. In the TRA experiment, Atlantic biases are faintly reduced compared to NEW (Fig.9d): NADW reaches a few hundred meters deeper, leading to warmer temperatures below 3 km depth; and the subsurface temperature maximum in the Southern Ocean is reduced, diminishing the warm bias there. The addition of mixing by subinertial internal tides barely affects the main thermocline (Fig.9d), as expected from its geographical distribution (Fig.1a).

In the Pacific Ocean, all three experiments show smaller biases than in the Atlantic (Figs.10 and 11). The main bias is an overly strong temperature stratification in the subarctic Pacific, which is about 0.2 °C too cold deeper than 4 km and 2-3 °C too warm between 200 and 1500 m (Fig.11a,b). Analysis of the emergence of subarctic Pacific biases during the first decades of the simulations shows that the anomalous subsurface warmth comes from the subtropical gyre, pointing to overestimated northward heat transport across the subtropical-subpolar gyre boundary in the North Pacific. The inclusion of mixing by bottom-trapped internal tides, which is particularly strong in the Kuril straits and along the Aleutian arc, alleviates subarctic Pacific temperature biases both in the abyss and upper ocean, but is insufficient to eliminate them (Fig.11d). The OLD experiment, on the other hand, simulates slightly colder Pacific bottom waters, as well as a colder thermocline and slightly colder North Pacific intermediate waters. The latter differences can be attributed to a smaller mean diapycnal diffusivity in the main thermocline of the Pacific, due to the absence of explicit mixing by the energetic low-mode internal tides of the western Pacific (Fig.2, de Lavergne et al. 2019).

In the Southern Ocean, the Pacific sector zonal mean shows again that OLD and TRA have colder subsurface waters than NEW (Fig.11c,d). The spatial pattern of this mixing-driven cooling is unveiled in Figure 12, which shows the maximum temperature of each grid column south of 50°S. Experiment NEW has too warm Circumpolar Deep Water (CDW) in the high-latitude Southern Ocean (Fig.12a,b). This bias is slightly reduced in OLD (Fig.12c), where stronger background mixing in the pycnocline of subpolar seas contributes to vent CDW heat to the atmosphere. Mixing by subinertial internal tides is even more efficient at cooling CDW (Fig.12d): the temperature maximum in TRA is reduced throughout the subpolar seas by a few tenths of a degree or more, the effect reaching over 1 °C in some regions adjacent to Antarctica. Thus, bottom-intensified mixing energized by subinertial internal tides erodes the temperature maximum of CDW. The distribution of CDW cooling suggests that the extra mixing accelerates the transfer of CDW heat to the mixed layer and ultimately to the atmosphere, leaving less heat able to interact with Antarctic ice shelves. This effect of tides – CDW alteration by vertical ocean mixing away from sub-ice-shelf

cavities – has the potential to damp other tidal effects that were shown to augment heat exchanges between ocean and ice shelves (Padman et al. 2018, Jourdain et al. 2019).

It is noteworthy that all three experiments have a well preserved subsurface heat reservoir in the high-latitude Southern Ocean (Figs. 9 and 11). This realistic structure owes much to the absence of large open-ocean polynyas. Such polynyas frequently develop in global ocean models and deplete intermittently or permanently the subsurface heat content of southern subpolar seas, while producing AABW (Martin et al. 2013, Heuzé et al. 2015). Here, we find that bottom water production occurs on the shelves, near the observed present-day locations (Fig.13; Silvano et al. 2023). Indeed, the bottom neutral density (Jackett and McDougall 1997) does not peak in areas of deep mixed layers (Fig.5f), but instead at four main shelf sites: the southwestern Weddell Sea, the Prydz Bay area, the Adélie coast and the Ross Sea (Fig.13b). The distribution of bottom density further indicates that dense shelf waters lose a (too) large portion of their density excess as they descend the continental slope, but remain the densest bottom waters. A numerical dye release experiment confirms that bottom waters in the model come from the four shelf sites (Fig.13c,d). The passive 'dye' tracer is restored to 1 in the top 10 meters of the ocean and propagated in offline mode using velocities and diffusivities from the last year of TRA. This tracer reaches the bottom in the locations of dense shelf water formation (bottom neutral density > 28.5 kg m^{-3}) and then spreads along the seafloor downstream of these locations. We find similarly realistic ventilation pathways in OLD and NEW experiments.

3.4 Overturning circulation

The meridional overturning circulation is the leading conveyor of tracer transport between the surface boundary layer and the deep ocean. Viewed globally, it is composed of four principal cells (Lumpkin and Speer 2007) that are well captured by the model (Fig.14e,f): (i) an anticlockwise circulation linking the abyss to near-Antarctic surface waters, known as the lower cell; (ii) an overlying clockwise cell connecting both poles and traversing the upper half of the ocean, known as the AMOC; (iii) two subtropical cells confined to the upper few hundred meters and latitudes lower than 40°, circulating clockwise in the Northern Hemisphere and anticlockwise in the Southern Hemisphere. The coherence of each cell is evident when the overturning streamfunction is calculated as a function of density (Fig.14f) rather than depth (Fig.14e). Here we use simulated σ_2 (potential density referenced to 2000 dbars) to bin meridional velocities and we reproject the resultant streamfunction onto pseudo-depth (e.g., Zika et al. 2012) (Fig.14b,d,f). In the reprojected view, both the AMOC and the lower cell have a magnitude that peaks near the main sinking site and declines monotonously away from this site. In experiment NEW, the lower cell has a peak magnitude of 15 Sv at 64°S, whilst the AMOC has a maximum strength of 21 Sv at 59°N. Subtropical cells reside essentially in the Pacific and Indian basins (Fig.14). When diagnosed in density coordinate, the Indian-Pacific subtropical cells of NEW attain peak strengths of 32 Sv near 10°S and 19 Sv near 5°N.

The decomposition between Atlantic and Indian-Pacific basins reveals that sinking in the lower cell occurs in both sectors of the polar Southern Ocean, at comparable rates, yet the bulk of bottom waters is channeled toward the Indian-Pacific (Fig.14b,d). At 30°S, the lower

cell of NEW has a strength of 2.9 Sv in the Atlantic, 2.4 Sv in the Indian and 4.2 Sv in the Pacific. These transports are of the same order of magnitude but smaller than recent data-constrained estimates (Holzer et al. 2021). The total northward AABW flow at 30°S is 9.5 Sv in NEW, implying that about 5 Sv of AABW upwell between 64°S and 30°S.

In the North Atlantic, the AMOC has a strength that compares well with observational estimates from the RAPID mooring array (Sinha et al. 2018) which monitors the circulation at 26.5°N (Fig.15). At this latitude, the peak magnitude of the streamfunction in NEW is 17 Sv both in depth and density space. At 30°S, the peak magnitude is 16 Sv, indicating little upwelling of NADW across the low-latitude Atlantic pycnocline (Fig.14d). The bulk of NADW upwells in the high-latitude Southern Ocean (Fig.14f). Nonetheless, a significant fraction is inferred to enter the Indian and Pacific basins at mid-depths and ultimately upwell at lower latitudes of the Southern Hemisphere (Fig.14b). Overlap between NADW densities and the return branch of the lower cell precludes a straightforward quantification of each upwelling pathway.

Only the lower cell is thought to rely strongly on mixing in the ocean interior, the other cells being firstly governed by surface momentum and buoyancy exchanges (Nikurashin and Vallis 2012, de Lavergne et al. 2022). In accord with these principles and the moderate perturbations of bulk mixing imposed (Fig.3, section 2.3), we find only weak differences in overturning across the three simulations (Figs. 4 and 15). For example, the modelled Atlantic overturning streamfunction at 26.5°N has a stable structure, with southward flow between about 1 and 4 km depth, biased shallow compared to RAPID observations (Fig.15). The main difference is a 1 Sv increase in peak AMOC strength from OLD to NEW, and a smaller increase from NEW to TRA (Fig.15). The lower cell also shows a very stable structure across the three experiments (not shown), with small differences in magnitude (Fig.4d,e). Differences are largest in the Pacific: OLD has the strongest Pacific AABW inflow at 30°S (5.6 Sv, compared to 4.2 Sv in NEW and 4.6 Sv in TRA), while TRA has the largest overturning rate in the subarctic Pacific abyss (1.1 Sv at 50°N, compared to 0.4 Sv in NEW and OLD). The latter finding implies that mixing by subinertial internal tides in the North Pacific invigorates the flow of AABW into the subarctic Pacific.

3.5 Ventilation rate

Despite small differences in overturning, we find important differences in deep ocean ventilation rates, as measured by ideal age (Fig.16). Indeed, ideal age is not only a function of overturning rate but also of diapycnal and isopycnal mixing rates, which can play a dominant role in ventilating regions where the overturning is weak (Jones and Abernathey 2019, Holzer et al. 2021). The large-scale distribution of ideal age is however closely tied to the overturning structure (Figs. 14b,d and 16a-c): ideal age is low near the sinking branches of the overturning and increases along the circulation cells carrying dense waters away from their sources. The maximum zonal mean age occurs near 3.5-4 km depth in the Atlantic and Indian basins, in the density range that separates NADW and AABW (Fig.16b,c). In the Pacific, the maximum zonal mean age lies further aloft, near 2 km depth (Fig. 16a). This mid-depth zone of the Pacific is relatively isolated from the surface ocean because it is remote from the NADW source and above the abyssal overturning (de Lavergne et al. 2017, Holzer

et al. 2021). In experiment NEW, the maximum zonal mean age reaches about 2400 years in the core of this shadow zone (Fig.16a), where the overturning is largely absent (Fig.14b).

As anticipated, the sensitivity of ideal age to the tidal mixing representation peaks in the Pacific shadow zone, where OLD and TRA have ages up to 250 years lower than NEW (Fig.16d,g), largely due to higher rates of bulk diapycnal mixing within the mid-depth North Pacific (Fig.7). But OLD and TRA also have lower ages than NEW throughout the realm of the lower cell, below about 2.5 km depth, indicating that AABW is younger from its source (Fig.16d-i). We attribute this difference to stronger pycnocline mixing in the subpolar Southern Ocean, which lowers the age (and temperature) of CDW entrained into AABW. The effect is larger in TRA than OLD, consistent with greatest erosion of CDW near Antarctic margins in TRA (cf Fig.12 and section 3.3). Quantitatively, the volume-weighted global mean age below 2 km is 1221 years in TRA, 1237 years in OLD and 1328 years in NEW. The reduction of about 10% of deep-ocean age in TRA relative to NEW is comparable to the percentage difference in tidal mixing power between the two simulations – a rather tight dependence which owes to the strength of subinertial internal tides in the North Pacific and near AABW formation sites (Fig.1a).

The OLD experiment also shows a slight increase of age across much of the upper half of the ocean (Fig.16d-f), consistent with a slower AMOC. Additionally, a pronounced aging is simulated between 1 and 2 km depth in the Indian Ocean (Fig.16e). The higher ages can be explained by a reduced influence of young and fresh Antarctic intermediate waters, which are more rapidly eroded in OLD than NEW (not shown). The same occurs in TRA, but to a lower extent, resulting in about half as large an aging (Fig.16h). This local age increase in TRA relative to NEW demonstrates that increased diapycnal mixing in the ocean interior can produce reduced ventilation rates on a regional scale.

4. Discussion and conclusion

We examined the impact of a comprehensive representation of mixing by breaking internal tides in a 1° global ocean configuration of NEMO. Simulations were ran for 1000 years under COREv2 normal year forcing (Large and Yeager 2009). Replacement of the constant background diffusivity of 10^{-5} m^2 s^{-1} (experiment OLD) by an explicit representation of remote tidal mixing (experiment NEW) increases the tidal power input to mixing from 1.12 to 1.28 TW and generates substantial spatial contrasts in diffusivities (Figs. 2 and 7). The improvement causes only moderate changes in the simulated broad-scale hydrography and circulation: the AMOC strengthens by about 1 Sv, the lower overturning cell weakens by about 1 Sv, salinity changes typically by less than 0.1 g kg^{-1} and temperature by less than 0.5 °C. In general, the simulated hydrographic changes are much smaller than pre-existing model biases. This finding is consistent with the notion that atmospheric forcing and surface boundary layer processes – unchanged across our simulations – play a leading role in setting water-mass characteristics and circulation. Nonetheless, the small sensitivity of hydrography and circulation also owes to the small differences in basin-scale bulk diffusivities between OLD and NEW (Fig.3).

Adding the contribution to mixing of bottom-trapped, subinertial internal tides (experiment TRA, otherwise identical to NEW) augments tidal diffusivities at high latitudes and raises the total tidal power input to 1.40 TW (Figs. 1-3). Again this modification of tidal mixing causes only modest changes to stratification and circulation at basin scale. However it induces some important differences in regional hydrography and deep-ocean ventilation rates, and tends to reduce known biases in our configuration. In particular, the extra mixing by subinertial internal tides causes cooling of CDW in southern subpolar seas, reducing the subsurface ocean heat that surrounds Antarctica (Fig.12), with repercussions for ice-shelf melt (Depoorter et al. 2013). In addition, mixing by subinertial internal tides reduces deep-ocean age by up to 250 years in the Pacific shadow zone and by over 100 years on average deeper than 2 km (Fig.16). This reduction of deep-ocean age has consequences for carbon storage at depths, and more generally for biogeochemical cycles that depend strongly on deep-ocean ventilation timescales (Ödalen et al. 2018, Eggleston and Galbraith 2018).

Parameterized mixing by bottom-trapped internal tides thus has significant regional to global scale impacts on water mass transformation and passive tracer transport. The role of bottom-trapped internal tides in mixing the subsurface Arctic Ocean is well recognized (Rippeth et al. 2015, Fer et al. 2020). Here we find the largest impacts in the subarctic Pacific and high-latitude Southern Ocean. The elevated mixing along Antarctic continental slopes has particular significance because it affects critical water mass transformations occurring in this region, and contributes to shelter Antarctica from subsurface warmth contained in CDW, in synergy with subpolar gyres (Narayanan et al. 2023). This finding calls for new observational and theoretical studies of this mixing process, notably in the subpolar Southern Ocean, in order to reduce uncertainties in the magnitude and distribution of parameterized mixing. In the present study, a model estimate of subinertial internal tide generation (Müller 2013) has been employed to parameterize the associated mixing, assuming local, bottom-intensified dissipation (section 2.3). The accuracy of the resulting mixing distribution should be assessed in future work.

Our results also depend in part on configuration and calibration choices, and the associated model limitations and biases. For example, experiment NEW simulates relatively high ages in the mid-depth Pacific shadow zone (up to 2400 years compared to peak ages of about 1600 years in data-constrained estimates; Gebbie and Huybers 2012, Holzer et al. 2021). This feature could favor strong sensitivity of the regional ideal age to increased diapycnal mixing. Similarly, biased NADW formation processes and sites could affect the diagnosed sensitivity of the AMOC to the representation of tidal mixing. Perhaps more importantly, the absence of an interactive atmosphere and of interannual variability in forcing may damp or amplify some of the sensitivities documented here. For instance, the restoring of sea surface salinity toward observations tends to restrain simulated salinity changes. On the other hand, this forcing protocol helps to achieve relatively realistic hydrography and circulation, and allows to perform millennial simulations at reduced computational cost. Notably, our forcing and calibration choices allow the simulation of AABW production near observed shelf sites (Fig.13), together with realistic and quasi-steady density stratification across the global deep ocean (Fig.10). This makes the present modelling framework suited to further studies of abyssal ocean ventilation and its sensitivity.

References

Abernathey, R., Gnanadesikan, A., Pradal, M.-A., Sundermeyer, M.A., 2022. Chapter 9 - Isopycnal mixing, in: Meredith, M., Naveira Garabato, A. (Eds.), Ocean Mixing. Elsevier, pp. 215–256. https://doi.org/10.1016/B978-0-12-821512-8.00016-5

Adcroft, A., Anderson, W., Balaji, V., Blanton, C., Bushuk, M., Dufour, C.O., Dunne, J.P., Griffies, S.M., Hallberg, R., Harrison, M.J., Held, I.M., Jansen, M.F., John, J.G., Krasting, J.P., Langenhorst, A.R., Legg, S., Liang, Z., McHugh, C., Radhakrishnan, A., Reichl, B.G., Rosati, T., Samuels, B.L., Shao, A., Stouffer, R., Winton, M., Wittenberg, A.T., Xiang, B., Zadeh, N., Zhang, R., 2019. The GFDL Global Ocean and Sea Ice Model OM4.0: Model Description and Simulation Features. Journal of Advances in Modeling Earth Systems 11, 3167–3211. https://doi.org/10.1029/2019MS001726

Albrecht, N., Vennell, R., Williams, M., Stevens, C., Langhorne, P., Leonard, G., Haskell, T., 2006. Observation of sub-inertial internal tides in McMurdo Sound, Antarctica. Geophysical Research Letters 33. https://doi.org/10.1029/2006GL027377

Alford, M.H., 2020. Revisiting Near-Inertial Wind Work: Slab Models, Relative Stress, and Mixed Layer Deepening. Journal of Physical Oceanography 50, 3141–3156. https://doi.org/10.1175/JPO-D-20-0105.1

Axell, L.B., 2002. Wind-driven internal waves and Langmuir circulations in a numerical ocean model of the southern Baltic Sea. Journal of Geophysical Research: Oceans 107, 25-1-25–20. https://doi.org/10.1029/2001JC000922

Bell, T.H., 1975. Topographically generated internal waves in the open ocean. J. Geophys. Res. 80, 320–327. https://doi.org/10.1029/JC080i003p00320

Blanke, B., Delecluse, P., 1993. Variability of the Tropical Atlantic Ocean Simulated by a General Circulation Model with Two Different Mixed-Layer Physics. J. Phys. Oceanogr. 23, 1363–1388. https://doi.org/10.1175/1520-0485(1993)023<1363:VOTTAO>2.0.CO;2

Bouffard, D., Boegman, L., 2013. A diapycnal diffusivity model for stratified environmental flows. Dynamics of Atmospheres and Oceans 61–62, 14–34. https://doi.org/10.1016/j.dynatmoce.2013.02.002

Campin, J.-M., Goosse, H., 1999. Parameterization of density-driven downsloping flow for a coarse-resolution ocean model in z-coordinate. Tellus A 51, 412–430. https://doi.org/10.1034/j.1600-0870.1999.t01-3-00006.x

Chapman, D.C., 1989. Enhanced subinertial diurnal tides over isolated topographic features. Deep Sea Research Part A. Oceanographic Research Papers 36, 815–824. https://doi.org/10.1016/0198-0149(89)90030-7

Chelton, D.B., Schlax, M.G., Samelson, R.M., 2011. Global observations of nonlinear mesoscale eddies. Progress in Oceanography 91, 167–216. https://doi.org/10.1016/j.pocean.2011.01.002

Cunningham, S.A., Alderson, S.G., King, B.A., Brandon, M.A., 2003. Transport and variability of the Antarctic Circumpolar Current in Drake Passage. Journal of Geophysical Research: Oceans 108. https://doi.org/10.1029/2001JC001147

Danabasoglu, G., Yeager, S.G., Bailey, D., Behrens, E., Bentsen, M., Bi, D., Biastoch, A., Böning, C., Bozec, A., Canuto, V.M., Cassou, C., Chassignet, E., Coward, A.C., Danilov, S., Diansky, N., Drange, H., Farneti, R., Fernandez, E., Fogli, P.G., Forget, G., Fujii, Y., Griffies, S.M., Gusev, A., Heimbach, P., Howard, A., Jung, T., Kelley, M., Large, W.G., Leboissetier, A., Lu, J., Madec, G., Marsland, S.J., Masina, S., Navarra, A., George

Nurser, A.J., Pirani, A., y Mélia, D.S., Samuels, B.L., Scheinert, M., Sidorenko, D., Treguier, A.-M., Tsujino, H., Uotila, P., Valcke, S., Voldoire, A., Wang, Q., 2014. North Atlantic simulations in Coordinated Ocean-ice Reference Experiments phase II (CORE-II). Part I: Mean states. Ocean Modelling 73, 76–107. https://doi.org/10.1016/j.ocemod.2013.10.005

D'Asaro, E.A., Lien, R.-C., 2000. The Wave–Turbulence Transition for Stratified Flows. J. Phys. Oceanogr. 30, 1669–1678. https://doi.org/10.1175/1520-0485(2000)030<1669:TWTTFS>2.0.CO;2

de Boyer Montégut, C., 2004. Mixed layer depth over the global ocean: An examination of profile data and a profile-based climatology. Journal of Geophysical Research 109. https://doi.org/10.1029/2004JC002378

de Lavergne, C., Falahat, S., Madec, G., Roquet, F., Nycander, J., Vic, C., 2019. Toward global maps of internal tide energy sinks. Ocean Modelling 137, 52–75. https://doi.org/10.1016/j.ocemod.2019.03.010

de Lavergne, C., Groeskamp, S., Zika, J., Johnson, H.L., 2022. Chapter 3 - The role of mixing in the large-scale ocean circulation, in: Meredith, M., Naveira Garabato, A. (Eds.), Ocean Mixing. Elsevier, pp. 35–63. https://doi.org/10.1016/B978-0-12-821512-8.00010-4

de Lavergne, C., Madec, G., Le Sommer, J., Nurser, A.J.G., Naveira Garabato, A.C., 2016. The Impact of a Variable Mixing Efficiency on the Abyssal Overturning. J. Phys. Oceanogr. 46, 663–681. https://doi.org/10.1175/JPO-D-14-0259.1

de Lavergne, C., Madec, G., Roquet, F., Holmes, R.M., McDougall, T.J., 2017. Abyssal ocean overturning shaped by seafloor distribution. Nature 551, 181–186. https://doi.org/10.1038/nature24472

de Lavergne, C., Vic, C., Madec, G., Roquet, F., Waterhouse, A.F., Whalen, C.B., Cuypers, Y., Bouruet-Aubertot, P., Ferron, B., Hibiya, T., 2020. A Parameterization of Local and Remote Tidal Mixing. Journal of Advances in Modeling Earth Systems 12, e2020MS002065. https://doi.org/10.1029/2020MS002065

Depoorter, M.A., Bamber, J.L., Griggs, J.A., Lenaerts, J.T.M., Ligtenberg, S.R.M., van den Broeke, M.R., Moholdt, G., 2013. Calving fluxes and basal melt rates of Antarctic ice shelves. Nature 502, 89–92. https://doi.org/10.1038/nature12567

Donohue, K.A., Tracey, K.L., Watts, D.R., Chidichimo, M.P., Chereskin, T.K., 2016. Mean Antarctic Circumpolar Current transport measured in Drake Passage. Geophysical Research Letters 43, 11,760-11,767. https://doi.org/10.1002/2016GL070319

Eden, C., Czeschel, L., Olbers, D., 2014. Toward Energetically Consistent Ocean Models. J. Phys. Oceanogr. 44, 3160–3184. https://doi.org/10.1175/JPO-D-13-0260.1

Eden, C., Olbers, D., 2014. An Energy Compartment Model for Propagation, Nonlinear Interaction, and Dissipation of Internal Gravity Waves. J. Phys. Oceanogr. 44, 2093–2106. https://doi.org/10.1175/JPO-D-13-0224.1

Egbert, G.D., Ray, R.D., 2000. Significant dissipation of tidal energy in the deep ocean inferred from satellite altimeter data. Nature 405, 775–778. https://doi.org/10.1038/35015531

Eggleston, S., Galbraith, E.D., 2018. The devil's in the disequilibrium: multi-component analysis of dissolved carbon and oxygen changes under a broad range of forcings in a general circulation model. Biogeosciences 15, 3761–3777. https://doi.org/10.5194/bg-15-3761-2018

Falahat, S., Nycander, J., 2014. On the Generation of Bottom-Trapped Internal Tides. J. Phys.

Oceanogr. 45, 526–545. https://doi.org/10.1175/JPO-D-14-0081.1
Falahat, S., Nycander, J., Roquet, F., Zarroug, M., 2014. Global Calculation of Tidal Energy Conversion into Vertical Normal Modes. J. Phys. Oceanogr. 44, 3225–3244. https://doi.org/10.1175/JPO-D-14-0002.1
Fer, I., Koenig, Z., Kozlov, I.E., Ostrowski, M., Rippeth, T.P., Padman, L., Bosse, A., Kolås, E., 2020. Tidally Forced Lee Waves Drive Turbulent Mixing Along the Arctic Ocean Margins. Geophysical Research Letters 47, e2020GL088083. https://doi.org/10.1029/2020GL088083
Fox-Kemper, B., Ferrari, R., Hallberg, R., 2008. Parameterization of Mixed Layer Eddies. Part I: Theory and Diagnosis. J. Phys. Oceanogr. 38, 1145–1165. https://doi.org/10.1175/2007JPO3792.1
Gaspar, P., Grégoris, Y., Lefevre, J.-M., 1990. A simple eddy kinetic energy model for simulations of the oceanic vertical mixing: Tests at station Papa and Long-Term Upper Ocean Study site. Journal of Geophysical Research: Oceans (1978–2012) 95, 16179–16193.
Gebbie, G., Huybers, P., 2012. The Mean Age of Ocean Waters Inferred from Radiocarbon Observations: Sensitivity to Surface Sources and Accounting for Mixing Histories. Journal of Physical Oceanography 42, 291–305. https://doi.org/10.1175/JPO-D-11-043.1
Gent, P.R., Mcwilliams, J.C., 1990. Isopycnal Mixing in Ocean Circulation Models. J. Phys. Oceanogr. 20, 150–155. https://doi.org/10.1175/1520-0485(1990)020<0150:IMIOCM>2.0.CO;2
Goosse, H., Fichefet, T., 1999. Importance of ice-ocean interactions for the global ocean circulation: A model study. Journal of Geophysical Research: Oceans 104, 23337–23355. https://doi.org/10.1029/1999JC900215
GOURETSKI, V., 2019. A new global ocean hydrographic climatology. Atmospheric and Oceanic Science Letters 12, 226–229. https://doi.org/10.1080/16742834.2019.1588066
Gregg, M.C., 1989. Scaling turbulent dissipation in the thermocline. J. Geophys. Res. 94, 9686–9698. https://doi.org/10.1029/JC094iC07p09686
Gregg, M.C., 1987. Diapycnal mixing in the thermocline: A review. J. Geophys. Res. 92, 5249. https://doi.org/10.1029/JC092iC05p05249
Gregg, M.C., D'Asaro, E.A., Riley, J.J., Kunze, E., 2018. Mixing Efficiency in the Ocean. Annual Review of Marine Science 10, 443–473. https://doi.org/10.1146/annurev-marine-121916-063643
Haumann, F.A., Gruber, N., Münnich, M., Frenger, I., Kern, S., 2016. Sea-ice transport driving Southern Ocean salinity and its recent trends. Nature 537, 89–92. https://doi.org/10.1038/nature19101
Held, I.M., Larichev, V.D., 1996. A Scaling Theory for Horizontally Homogeneous, Baroclinically Unstable Flow on a Beta Plane. Journal of the Atmospheric Sciences 53, 946–952. https://doi.org/10.1175/1520-0469(1996)053<0946:ASTFHH>2.0.CO;2
Heuzé, C., 2021. Antarctic Bottom Water and North Atlantic Deep Water in CMIP6 models. Ocean Science 17, 59–90. https://doi.org/10.5194/os-17-59-2021
Heuzé, C., Ridley, J.K., Calvert, D., Stevens, D.P., Heywood, K.J., 2015. Increasing vertical mixing to reduce Southern Ocean deep convection in NEMO3.4. Geoscientific Model Development 8, 3119–3130. https://doi.org/10.5194/gmd-8-3119-2015
Hieronymus, M., Nycander, J., Nilsson, J., Döös, K., Hallberg, R., 2018. Oceanic Overturning

and Heat Transport: The Role of Background Diffusivity. J. Climate 32, 701–716. https://doi.org/10.1175/JCLI-D-18-0438.1

Holzer, M., DeVries, T., de Lavergne, C., 2021. Diffusion controls the ventilation of a Pacific Shadow Zone above abyssal overturning. Nat Commun 12, 4348. https://doi.org/10.1038/s41467-021-24648-x

Huang, R.X., 1999. Mixing and Energetics of the Oceanic Thermohaline Circulation. Journal of Physical Oceanography 29, 727–746.

IOC, SCOR, IAPSO, 2010. The international thermodynamic equation of seawater—2010: Calculation and use of thermodynamic properties. Intergovernmental Oceanographic Commission, Manuals and Guides. UNESCO (English), [Available at: www.TEOS-10.org.]

Iudicone, D., Madec, G., McDougall, T.J., 2008. Water-Mass Transformations in a Neutral Density Framework and the Key Role of Light Penetration. Journal of Physical Oceanography 38, 1357–1376. https://doi.org/10.1175/2007JPO3464.1

Jackett, D.R., McDougall, T.J., 1997. A Neutral Density Variable for the World's Oceans. J. Phys. Oceanogr. 27, 237–263. https://doi.org/10.1175/1520-0485(1997)027<0237:ANDVFT>2.0.CO;2

Jochum, M., 2009. Impact of latitudinal variations in vertical diffusivity on climate simulations. Journal of Geophysical Research 114. https://doi.org/10.1029/2008JC005030

Jones, C.S., Abernathey, R.P., 2019. Isopycnal Mixing Controls Deep Ocean Ventilation. Geophysical Research Letters 46, 13144–13151. https://doi.org/10.1029/2019GL085208

Jourdain, N.C., Molines, J.-M., Le Sommer, J., Mathiot, P., Chanut, J., de Lavergne, C., Madec, G., 2019. Simulating or prescribing the influence of tides on the Amundsen Sea ice shelves. Ocean Modelling 133, 44–55. https://doi.org/10.1016/j.ocemod.2018.11.001

Kiss, A.E., Hogg, A.M., Hannah, N., Boeira Dias, F., Brassington, G.B., Chamberlain, M.A., Chapman, C., Dobrohotoff, P., Domingues, C.M., Duran, E.R., England, M.H., Fiedler, R., Griffies, S.M., Heerdegen, A., Heil, P., Holmes, R.M., Klocker, A., Marsland, S.J., Morrison, A.K., Munroe, J., Nikurashin, M., Oke, P.R., Pilo, G.S., Richet, O., Savita, A., Spence, P., Stewart, K.D., Ward, M.L., Wu, F., Zhang, X., 2020. ACCESS-OM2 v1.0: a global ocean–sea ice model at three resolutions. Geoscientific Model Development 13, 401–442. https://doi.org/10.5194/gmd-13-401-2020

Klocker, A., Naveira Garabato, A.C., Roquet, F., de Lavergne, C., Rintoul, S.R., 2023. Generation of the Internal Pycnocline in the Subpolar Southern Ocean by Wintertime Sea Ice Melting. Journal of Geophysical Research: Oceans 128, e2022JC019113. https://doi.org/10.1029/2022JC019113

Kunze, E., Firing, E., Hummon, J.M., Chereskin, T.K., Thurnherr, A.M., 2006. Global abyssal mixing inferred from lowered ADCP shear and CTD strain profiles. Journal of Physical Oceanography 36.

Large, W.G., McWilliams, J.C., Doney, S.C., 1994. Oceanic vertical mixing: A review and a model with a nonlocal boundary layer parameterization. Reviews of Geophysics 32, 363–403. https://doi.org/10.1029/94RG01872

Large, W.G., Yeager, S.G., 2009. The global climatology of an interannually varying air–sea flux data set. Clim Dyn 33, 341–364. https://doi.org/10.1007/s00382-008-0441-3

Lucazeau, F., 2019. Analysis and Mapping of an Updated Terrestrial Heat Flow Data Set.

Geochemistry, Geophysics, Geosystems 20, 4001–4024. https://doi.org/10.1029/2019GC008389

Lumpkin, R., Speer, K., 2007. Global Ocean Meridional Overturning. Journal of Physical Oceanography 37, 2550–2562. https://doi.org/10.1175/JPO3130.1

MacKinnon, J.A., Zhao, Z., Whalen, C.B., Waterhouse, A.F., Trossman, D.S., Sun, O.M., St. Laurent, L.C., Simmons, H.L., Polzin, K., Pinkel, R., Pickering, A., Norton, N.J., Nash, J.D., Musgrave, R., Merchant, L.M., Melet, A.V., Mater, B., Legg, S., Large, W.G., Kunze, E., Klymak, J.M., Jochum, M., Jayne, S.R., Hallberg, R.W., Griffies, S.M., Diggs, S., Danabasoglu, G., Chassignet, E.P., Buijsman, M.C., Bryan, F.O., Briegleb, B.P., Barna, A., Arbic, B.K., Ansong, J.K., Alford, M.H., 2017. Climate Process Team on Internal Wave–Driven Ocean Mixing. Bull. Amer. Meteor. Soc. 98, 2429–2454. https://doi.org/10.1175/BAMS-D-16-0030.1

Marshall, J.C., Nurser, A.J.G., 1991. A Continuously Stratified Thermocline Model Incorporating a Mixed Layer of Variable Thickness and Density. J. Phys. Oceanogr. 21, 1780–1792. https://doi.org/10.1175/1520-0485(1991)021<1780:ACSTMI>2.0.CO;2

Martin, T., Park, W., Latif, M., 2013. Multi-centennial variability controlled by Southern Ocean convection in the Kiel Climate Model. Climate Dynamics 40, 2005–2022. https://doi.org/10.1007/s00382-012-1586-7

Marzocchi, A., Nurser, A.J.G., Clément, L., McDonagh, E.L., 2021. Surface atmospheric forcing as the driver of long-term pathways and timescales of ocean ventilation. Ocean Science 17, 935–952. https://doi.org/10.5194/os-17-935-2021

Mashayek, A., Peltier, W.R., 2013. Shear-induced mixing in geophysical flows: does the route to turbulence matter to its efficiency? Journal of Fluid Mechanics 725, 216–261. https://doi.org/10.1017/jfm.2013.176

Mathiot, P., Jenkins, A., Harris, C., Madec, G., 2017. Explicit and parametrised representation of under ice shelf seas in a z* coordinate ocean model NEMO 3.6. Geoscientific Model Development 10, 2849–2874. https://doi.org/10.5194/gmd-10-2849-2017

McDougall, T.J., Barker, P.M., 2011. Getting Started With TEOS-10 and the Gibbs Seawater (GSW) Oceanographic Toolbox, 28 pp., SCOR/IAPSO WG127. https://www.teos-10.org/pubs/Getting_Started.pdf

Melet, A., Legg, S., Hallberg, R., 2015. Climatic Impacts of Parameterized Local and Remote Tidal Mixing. J. Climate 29, 3473–3500. https://doi.org/10.1175/JCLI-D-15-0153.1

Melet, A.V., Hallberg, R., Marshall, D.P., 2022. Chapter 2 - The role of ocean mixing in the climate system, in: Meredith, M., Naveira Garabato, A. (Eds.), Ocean Mixing. Elsevier, pp. 5–34. https://doi.org/10.1016/B978-0-12-821512-8.00009-8

Merino, N., Le Sommer, J., Durand, G., Jourdain, N.C., Madec, G., Mathiot, P., Tournadre, J., 2016. Antarctic icebergs melt over the Southern Ocean: Climatology and impact on sea ice. Ocean Modelling 104, 99–110. https://doi.org/10.1016/j.ocemod.2016.05.001

Morawitz, W.M.L., Sutton, P.J., Worcester, P.F., Cornuelle, B.D., Lynch, J.F., Pawlowicz, R., 1996. Three-Dimensional Observations of a Deep Convective Chimney in the Greenland Sea during Winter 1988/89. Journal of Physical Oceanography 26, 2316–2343. https://doi.org/10.1175/1520-0485(1996)026<2316:TDOOAD>2.0.CO;2

Müller, M., 2013. On the space- and time-dependence of barotropic-to-baroclinic tidal energy conversion. Ocean Modelling 72, 242–252. https://doi.org/10.1016/j.ocemod.2013.09.007

Musgrave, R.C., MacKinnon, J.A., Pinkel, R., Waterhouse, A.F., Nash, J., Kelly, S.M., 2017. The Influence of Subinertial Internal Tides on Near-Topographic Turbulence at the Mendocino Ridge: Observations and Modeling. Journal of Physical Oceanography 47, 2139–2154. https://doi.org/10.1175/JPO-D-16-0278.1

Narayanan, A., Gille, S.T., Mazloff, M.R., du Plessis, M.D., Murali, K., Roquet, F., 2023. Zonal Distribution of Circumpolar Deep Water Transformation Rates and Its Relation to Heat Content on Antarctic Shelves. Journal of Geophysical Research: Oceans 128, e2022JC019310. https://doi.org/10.1029/2022JC019310

Nasser, A.-A., Madec, G., de Lavergne, C., Debreu, L., Lemarié, F., Blayo, E., 2023. Sliding or Stumbling on the Staircase: Numerics of Ocean Circulation Along Piecewise-Constant Coastlines. Journal of Advances in Modeling Earth Systems 15, e2022MS003594. https://doi.org/10.1029/2022MS003594

NEMO System Team, 2022. NEMO ocean engine, scientific notes of climate modelling center, 27, ISSN 1288-1619 Institut Pierre-Simon Laplace (IPSL), Zenodo [software]. https://doi.org/10.5281/zenodo.6334656.

Nguyen, A.T., Menemenlis, D., Kwok, R., 2009. Improved modeling of the Arctic halocline with a subgrid-scale brine rejection parameterization. Journal of Geophysical Research: Oceans 114. https://doi.org/10.1029/2008JC005121

Nikurashin, M., Vallis, G., 2012. A Theory of the Interhemispheric Meridional Overturning Circulation and Associated Stratification. J. Phys. Oceanogr. 42, 1652–1667. https://doi.org/10.1175/JPO-D-11-0189.1

Nycander, J., 2005. Generation of internal waves in the deep ocean by tides. Journal of Geophysical Research 110. https://doi.org/10.1029/2004JC002487

Ödalen, M., Nycander, J., Oliver, K.I.C., Brodeau, L., Ridgwell, A., 2018. The influence of the ocean circulation state on ocean carbon storage and CO_2 drawdown potential in an Earth system model. Biogeosciences 15, 1367–1393. https://doi.org/10.5194/bg-15-1367-2018

Osborn, T.R., 1980. Estimates of the Local Rate of Vertical Diffusion from Dissipation Measurements. J. Phys. Oceanogr. 10, 83–89. https://doi.org/10.1175/1520-0485(1980)010<0083:EOTLRO>2.0.CO;2

Padman, L., Siegfried, M.R., Fricker, H.A., 2018. Ocean Tide Influences on the Antarctic and Greenland Ice Sheets. Reviews of Geophysics 56, 142–184. https://doi.org/10.1002/2016RG000546

Plueddemann, A. J., Farrar, J.T., 2006. Observations and models of the energy flux from the wind to mixed-layer inertial currents. Deep-Sea Res. II, 53,5–30. https://doi.org/10.1016/j.dsr2.2005.10.017.

Pollmann, F., Eden, C., Olbers, D., 2017. Evaluating the Global Internal Wave Model IDEMIX Using Finestructure Methods. J. Phys. Oceanogr. 47, 2267–2289. https://doi.org/10.1175/JPO-D-16-0204.1

Redi, M.H., 1982. Oceanic Isopycnal Mixing by Coordinate Rotation. Journal of Physical Oceanography 12, 1154–1158. https://doi.org/10.1175/1520-0485(1982)012<1154:OIMBCR>2.0.CO;2

Reichl, B.G., Hallberg, R., 2018. A simplified energetics based planetary boundary layer (ePBL) approach for ocean climate simulations. Ocean Modelling 132, 112–129. https://doi.org/10.1016/j.ocemod.2018.10.004

Rippeth, T.P., Lincoln, B.J., Lenn, Y.-D., Green, J.A.M., Sundfjord, A., Bacon, S., 2015. Tide-mediated warming of Arctic halocline by Atlantic heat fluxes over rough topography.

Nature Geosci advance online publication. https://doi.org/10.1038/ngeo2350
Rousset, C., Vancoppenolle, M., Madec, G., Fichefet, T., Flavoni, S., Barthélemy, A., Benshila, R., Chanut, J., Levy, C., Masson, S., Vivier, F., 2015. The Louvain-La-Neuve sea ice model LIM3.6: global and regional capabilities. Geoscientific Model Development 8, 2991–3005. https://doi.org/10.5194/gmd-8-2991-2015
Sadourny, R., 1975. The dynamics of finite-difference models of the shallow-water equations. Journal of the Atmospheric Sciences, 32(4), 680–689. https://doi.org/10.1175/1520-0469(1975)032<0680:TDOFDM>2.0.CO;2
Sallée, J.-B., Pellichero, V., Akhoudas, C., Pauthenet, E., Vignes, L., Schmidtko, S., Garabato, A.N., Sutherland, P., Kuusela, M., 2021. Summertime increases in upper-ocean stratification and mixed-layer depth. Nature 591, 592–598. https://doi.org/10.1038/s41586-021-03303-x
Sigman, D.M., Hain, M.P., Haug, G.H., 2010. The polar ocean and glacial cycles in atmospheric CO2 concentration. Nature 466, 47–55. https://doi.org/10.1038/nature09149
Silvano, A., Purkey, S., Gordon, A.L., Castagno, P., Stewart, A.L., Rintoul, S.R., Foppert, A., Gunn, K.L., Herraiz-Borreguero, L., Aoki, S., Nakayama, Y., Naveira Garabato, A.C., Spingys, C., Akhoudas, C.H., Sallée, J.-B., de Lavergne, C., Abrahamsen, E.P., Meijers, A.J.S., Meredith, M.P., Zhou, S., Tamura, T., Yamazaki, K., Ohshima, K.I., Falco, P., Budillon, G., Hattermann, T., Janout, M.A., Llanillo, P., Bowen, M.M., Darelius, E., Østerhus, S., Nicholls, K.W., Stevens, C., Fernandez, D., Cimoli, L., Jacobs, S.S., Morrison, A.K., Hogg, A.M., Haumann, F.A., Mashayek, A., Wang, Z., Kerr, R., Williams, G.D., Lee, W.S., 2023. Observing Antarctic Bottom Water in the Southern Ocean. Front. Mar. Sci. 10. https://doi.org/10.3389/fmars.2023.1221701
Simmons, H.L., Jayne, S.R., Laurent, L.C.St., Weaver, A.J., 2004. Tidally driven mixing in a numerical model of the ocean general circulation. Ocean Modelling 6, 245–263. https://doi.org/10.1016/S1463-5003(03)00011-8
Sinha, B., Smeed, D.A., McCarthy, G., Moat, B.I., Josey, S.A., Hirschi, J.J.-M., Frajka-Williams, E., Blaker, A.T., Rayner, D., Madec, G., 2018. The accuracy of estimates of the overturning circulation from basin-wide mooring arrays. Progress in Oceanography 160, 101–123. https://doi.org/10.1016/j.pocean.2017.12.001
Sloyan, B.M., Talley, L.D., Chereskin, T.K., Fine, R., Holte, J., 2010. Antarctic Intermediate Water and Subantarctic Mode Water Formation in the Southeast Pacific: The Role of Turbulent Mixing. J. Phys. Oceanogr. 40, 1558–1574. https://doi.org/10.1175/2010JPO4114.1
Stroeve, J., Meier, W.N., 2018. Sea ice trends and climatologies from SMMR and SSM/I-SSMIS, Version 3. Boulder, Colorado USA. NASA National Snow and Ice Data Center Distributed Active Archive Center. Accessed on October 7, 2021. https://doi.org/10.5067/IJ0T7HFHB9Y6.
St. Laurent, L.C., 2002. Estimating tidally driven mixing in the deep ocean. Geophysical Research Letters 29. https://doi.org/10.1029/2002GL015633
Tanaka, T., Yasuda, I., Tanaka, Y., Carter, G.S., 2013. Numerical study on tidal mixing along the shelf break in the Green Belt in the southeastern Bering Sea. Journal of Geophysical Research: Oceans 118, 6525–6542. https://doi.org/10.1002/2013JC009113
Tanaka, Y., 2023. Energy Conversion Rate from Subinertial Surface Tides to Internal Tides. Journal of Physical Oceanography 53, 1355–1374. https://doi.org/10.1175/JPO-D-22-

0201.1
Tatebe, H., Tanaka, Y., Komuro, Y., Hasumi, H., 2018. Impact of deep ocean mixing on the climatic mean state in the Southern Ocean. Sci Rep 8, 1–9. https://doi.org/10.1038/s41598-018-32768-6
Tuerena, R.E., Williams, R.G., Mahaffey, C., Vic, C., Green, J.A.M., Naveira-Garabato, A., Forryan, A., Sharples, J., 2019. Internal Tides Drive Nutrient Fluxes Into the Deep Chlorophyll Maximum Over Mid-ocean Ridges. Global Biogeochemical Cycles 33, 995–1009. https://doi.org/10.1029/2019GB006214
Vancoppenolle, M., Rousset, C., Blockley, E., NEMO Sea Ice Working Group, 2023. SI3 – Sea Ice modelling Integrated Initiative – The NEMO Sea Ice Engine, Zenodo [software]. https://doi.org/10.5281/zenodo.7534900.
Vic, C., Garabato, A.C.N., Green, J.A.M., Waterhouse, A.F., Zhao, Z., Melet, A., Lavergne, C. de, Buijsman, M.C., Stephenson, G.R., 2019. Deep-ocean mixing driven by small-scale internal tides. Nature Communications 10, 2099. https://doi.org/10.1038/s41467-019-10149-5
Visbeck, M., Marshall, J., Haine, T., Spall, M., 1997. Specification of Eddy Transfer Coefficients in Coarse-Resolution Ocean Circulation Models. Journal of Physical Oceanography 27, 381–402. https://doi.org/10.1175/1520-0485(1997)027<0381:SOETCI>2.0.CO;2
Vladoiu, A., Bouruet-Aubertot, P., Cuypers, Y., Ferron, B., Schroeder, K., Borghini, M., Leizour, S., Ismail, S.B., 2019. Mixing efficiency from microstructure measurements in the Sicily Channel. Ocean Dynamics 69, 787–807. https://doi.org/10.1007/s10236-019-01274-2
von Storch, J.-S., Lüschow, V., 2023. Wind Power Input to Ocean Near-Inertial Waves Diagnosed From a 5-km Global Coupled Atmosphere-Ocean General Circulation Model. Journal of Geophysical Research: Oceans 128, e2022JC019111. https://doi.org/10.1029/2022JC019111
Walin, G., 1982. On the relation between sea-surface heat flow and thermal circulation in the ocean. Tellus 34, 187–195. https://doi.org/10.1111/j.2153-3490.1982.tb01806.x
Williams, R.G., Marshall, J.C., Spall, M.A., 1995. Does Stommel's Mixed Layer "Demon" Work? J. Phys. Oceanogr. 25, 3089–3102. https://doi.org/10.1175/1520-0485(1995)025<3089:DSMLW>2.0.CO;2
Xu, X., Chassignet, E.P., Firing, Y.L., Donohue, K., 2020. Antarctic Circumpolar Current Transport Through Drake Passage: What Can We Learn From Comparing High-Resolution Model Results to Observations? Journal of Geophysical Research: Oceans 125, e2020JC016365. https://doi.org/10.1029/2020JC016365
Zhai, X., Greatbatch, R.J., Eden, C., Hibiya, T., 2009. On the Loss of Wind-Induced Near-Inertial Energy to Turbulent Mixing in the Upper Ocean. J. Phys. Oceanogr. 39, 3040–3045. https://doi.org/10.1175/2009JPO4259.1
Zika, J.D., Le Sommer, J., Dufour, C.O., Molines, J.-M., Barnier, B., Brasseur, P., Dussin, R., Penduff, T., Iudicone, D., Lenton, A., Madec, G., Mathiot, P., Orr, J., Shuckburgh, E., Vivier, F., 2012. Vertical Eddy Fluxes in the Southern Ocean. J. Phys. Oceanogr. 43, 941–955. https://doi.org/10.1175/JPO-D-12-0178.1

Tidal constituent	M_2	S_2	K_1	O_1	All
Power E_{tra} (GW)	1.7	0.2	60	45	113
Power E_{sha} (GW)	149	25	37	20	236
Scaling factor	1.050	1.086	1.126	1.046	

Table 1: Total power input to subinertial internal tides (E_{tra}) and shallow internal tides (E_{sha}). These barotropic-to-baroclinic conversion rates, based on Müller (2013), are given for each of four tidal constituents and for the sum of the eight most important constituents (last column). The scaling factors used to obtain the sum for all eight constituents are given in the last row.

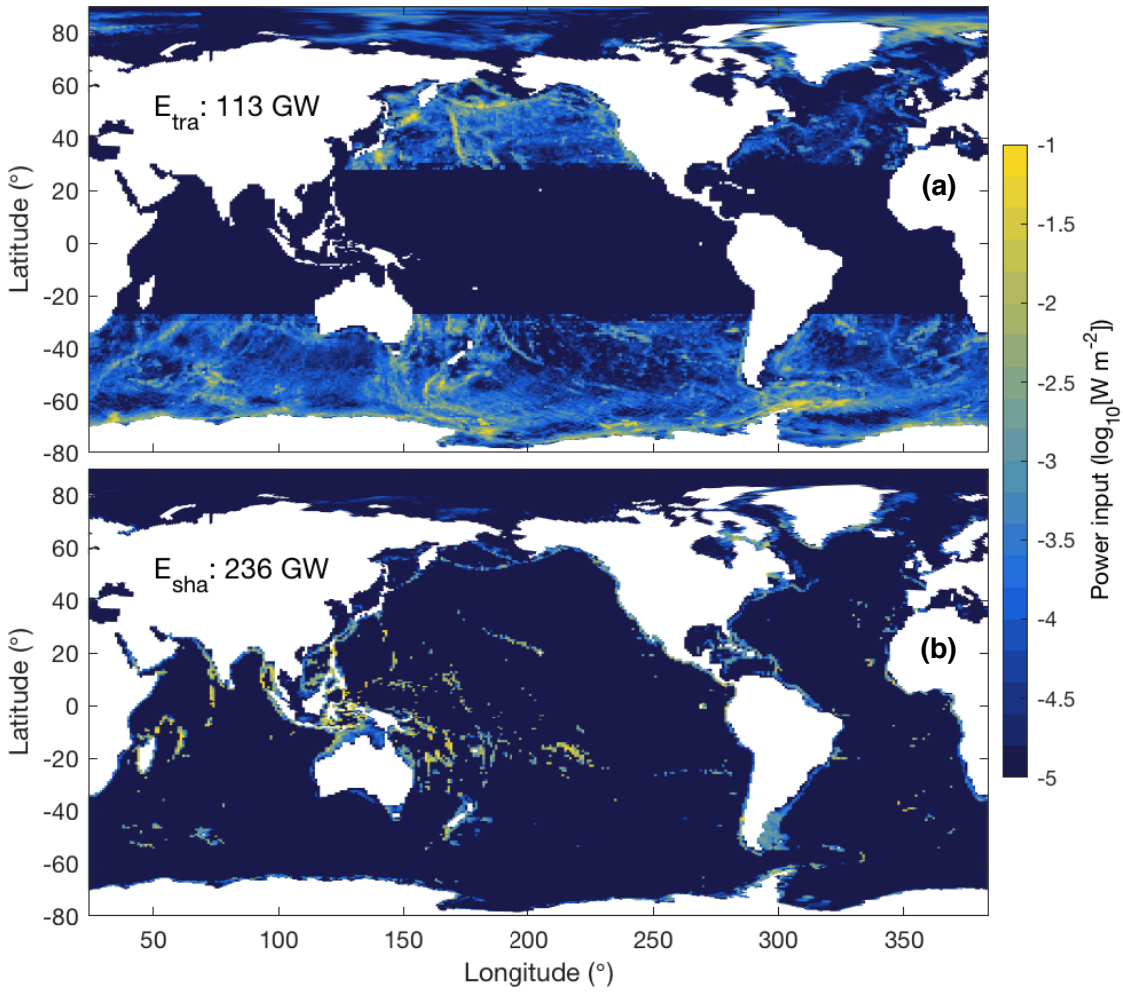

Figure 1: Depth-integrated turbulence production by subinertial internal tides **(a)** and shallow internal tides **(b)** remapped onto the model grid. The total power in each field is indicated at the top left of each panel. Note the power is shown on a $\log_{10}$ scale.

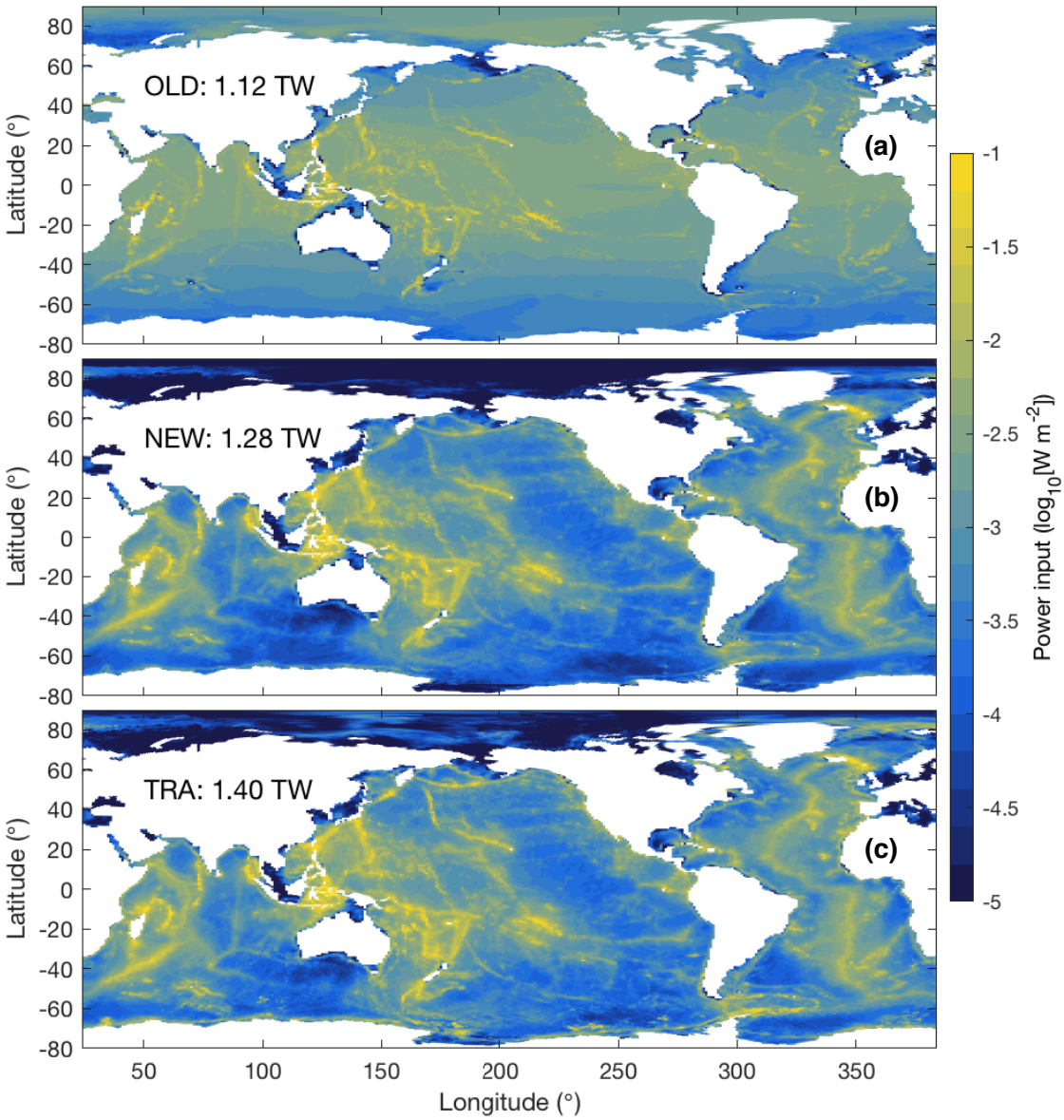

Figure 2: Depth-integrated turbulence production implied by each tidal mixing scheme. For experiment OLD **(a)**, the power shown includes the specified near-field dissipation of internal tides and the contribution of the background diffusivity (calculated as the vertical integral of ρ_0 K_ρ N^2 R_f^{-1} with K_ρ = 10^{-5} m^2 s^{-1}, ρ_0 = 1026 kg m^{-3} , R_f = 1/6, and N the annual-mean buoyancy frequency from the first simulation year). Experiment NEW **(b)** has no background diffusivity: all tidal mixing derives from the specified internal tide energy dissipation. Experiment TRA **(c)** is identical to NEW except for the addition of subinertial internal tides. Note the power is shown on a $\log_{10}$ scale.

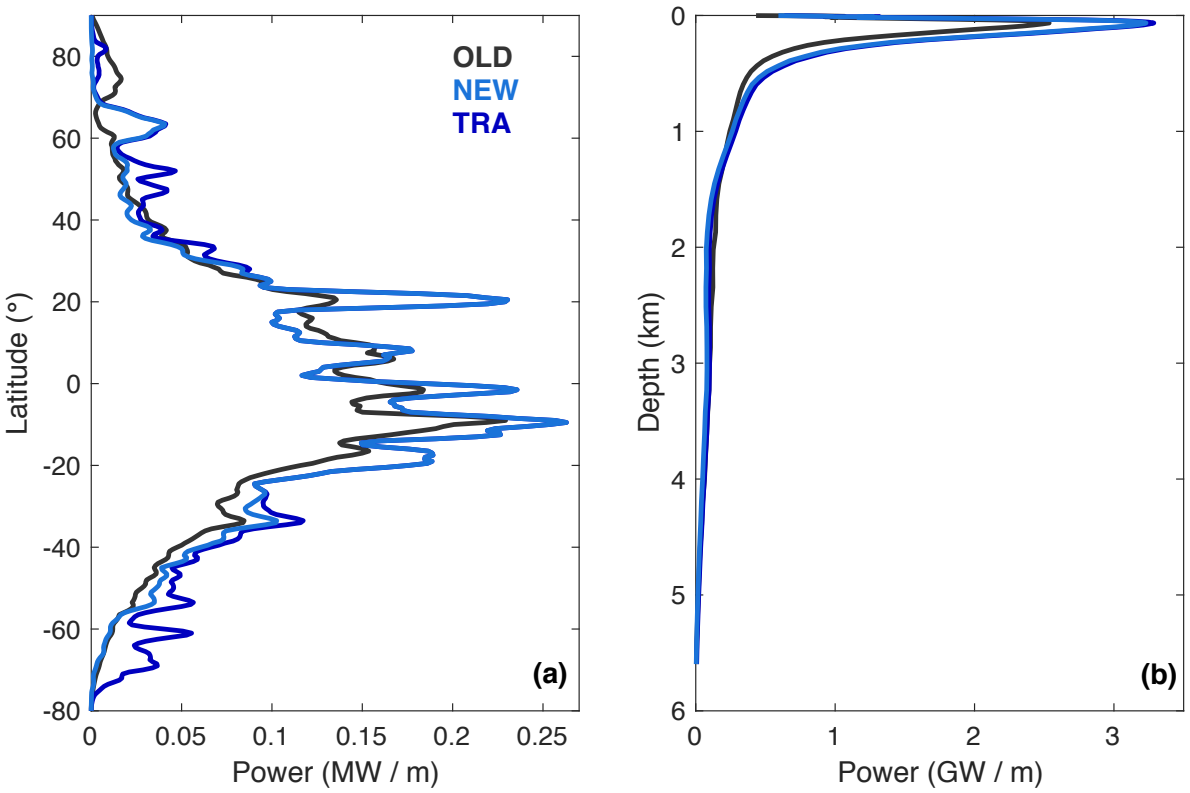

Figure 3: Turbulence production implied by each tidal mixing scheme, summed over depth and longitude **(a)** or over geopotential model layers **(b)**. Experiment OLD is shown in black, experiment NEW in light blue and experiment TRA in dark blue.

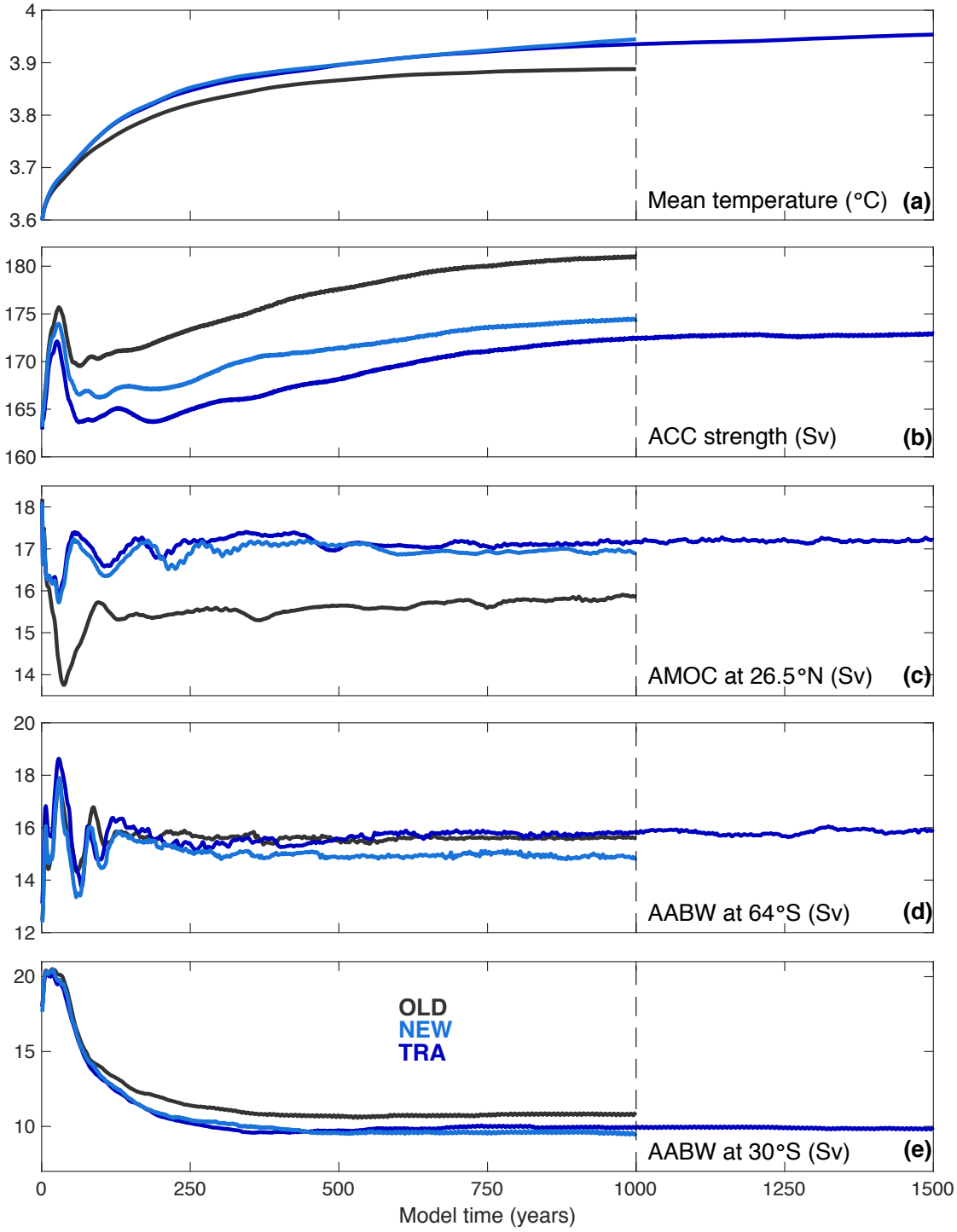

Figure 4: Evolution of global mean ocean temperature **(a)**, Drake Passage eastward volume transport **(b)**, maximum of the Atlantic meridional overturning streamfunction at 26.5°N **(c)**, and northward Antarctic Bottom Water (AABW) transport at 64°S **(d)** and 30°S **(e)**. Experiments OLD, NEW and TRA are shown in black, light blue and dark blue, respectively. AABW transport is the maximum northward transport underneath a given σ_3 isopycnal (for $\sigma_3 > 1041.4$ kg m^{-3}).

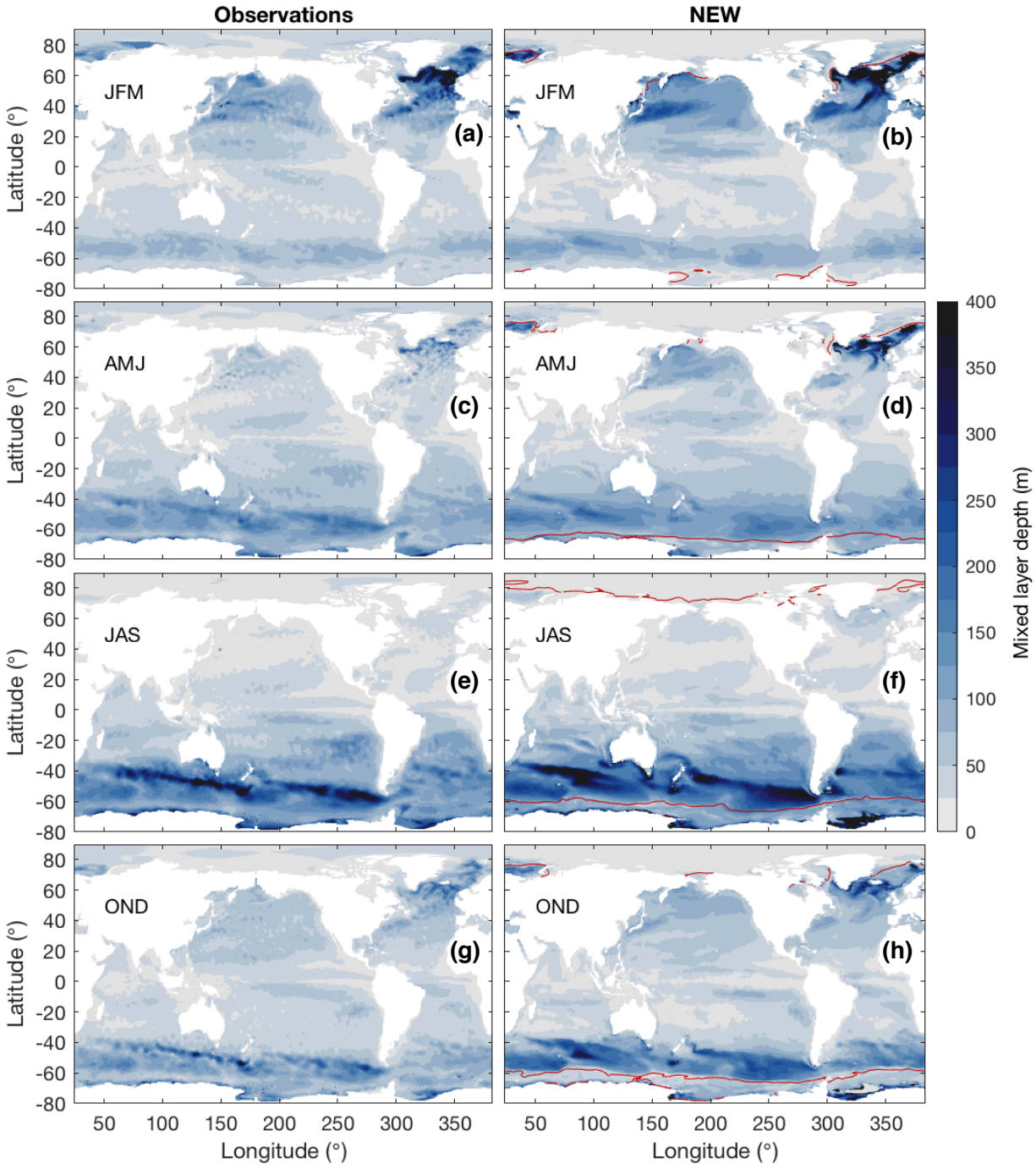

Figure 5: Mixed layer depth in observations and experiment NEW, averaged over January-February-March **(a,b)**, April-May-June **(c,d)**, July-August-September **(e,f)** and October-November-December **(g,h)**. The left column (panels **(a)**, **(c)**, **(e)**, **(g)**) corresponds to the observational climatology of Sallée et al. (2021), the right column (panels **(b)**, **(d)**, **(f)**, **(h)**) to experiment NEW. In the right column, we also show as red contours the modelled 50% sea ice concentration averaged over the central month of each season.

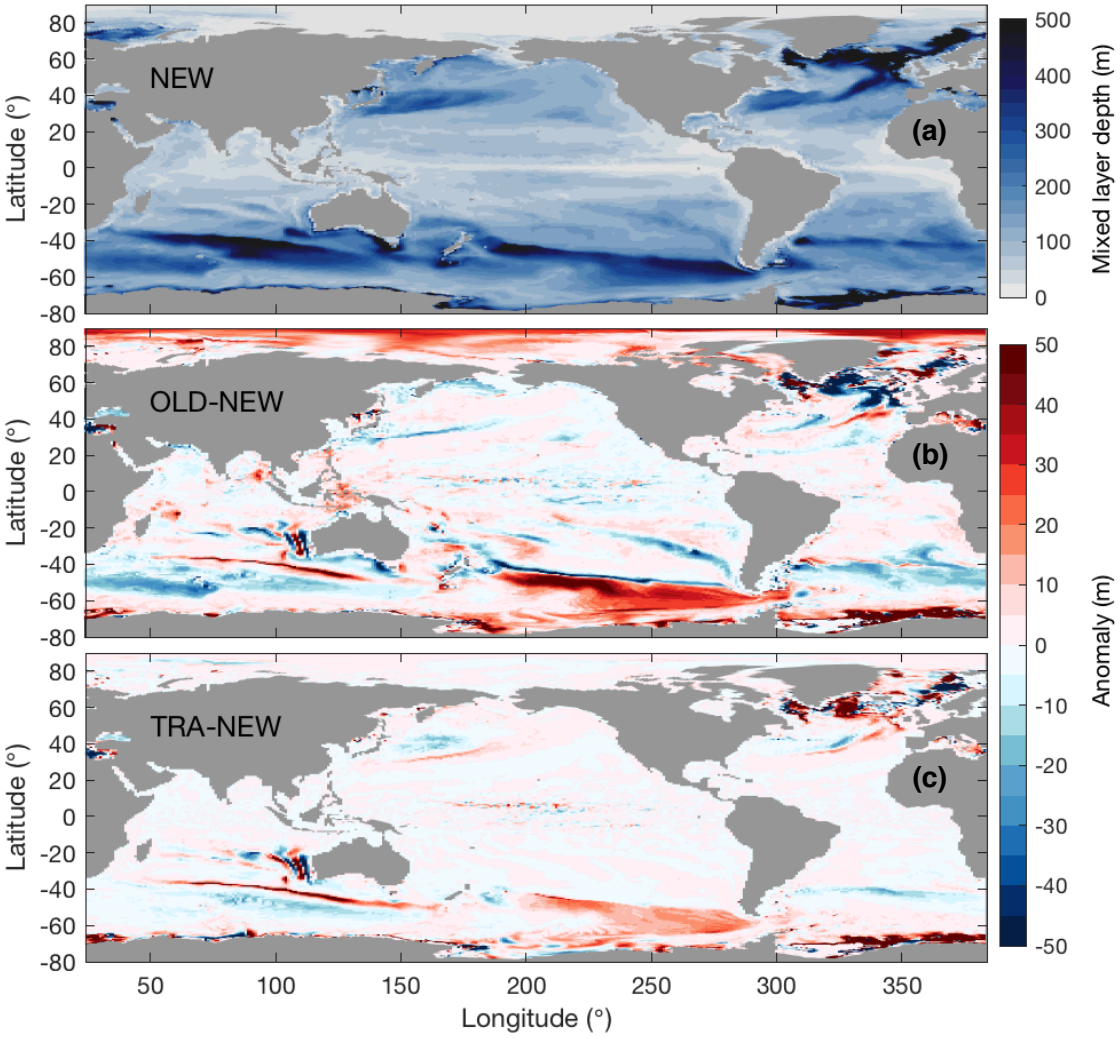

Figure 6: Maximum mixed layer depth in experiment NEW **(a)**, and anomalies in OLD **(b)** and TRA **(c)** with respect to NEW. The maximum is calculated from monthly-mean output over the last decade of each experiment.

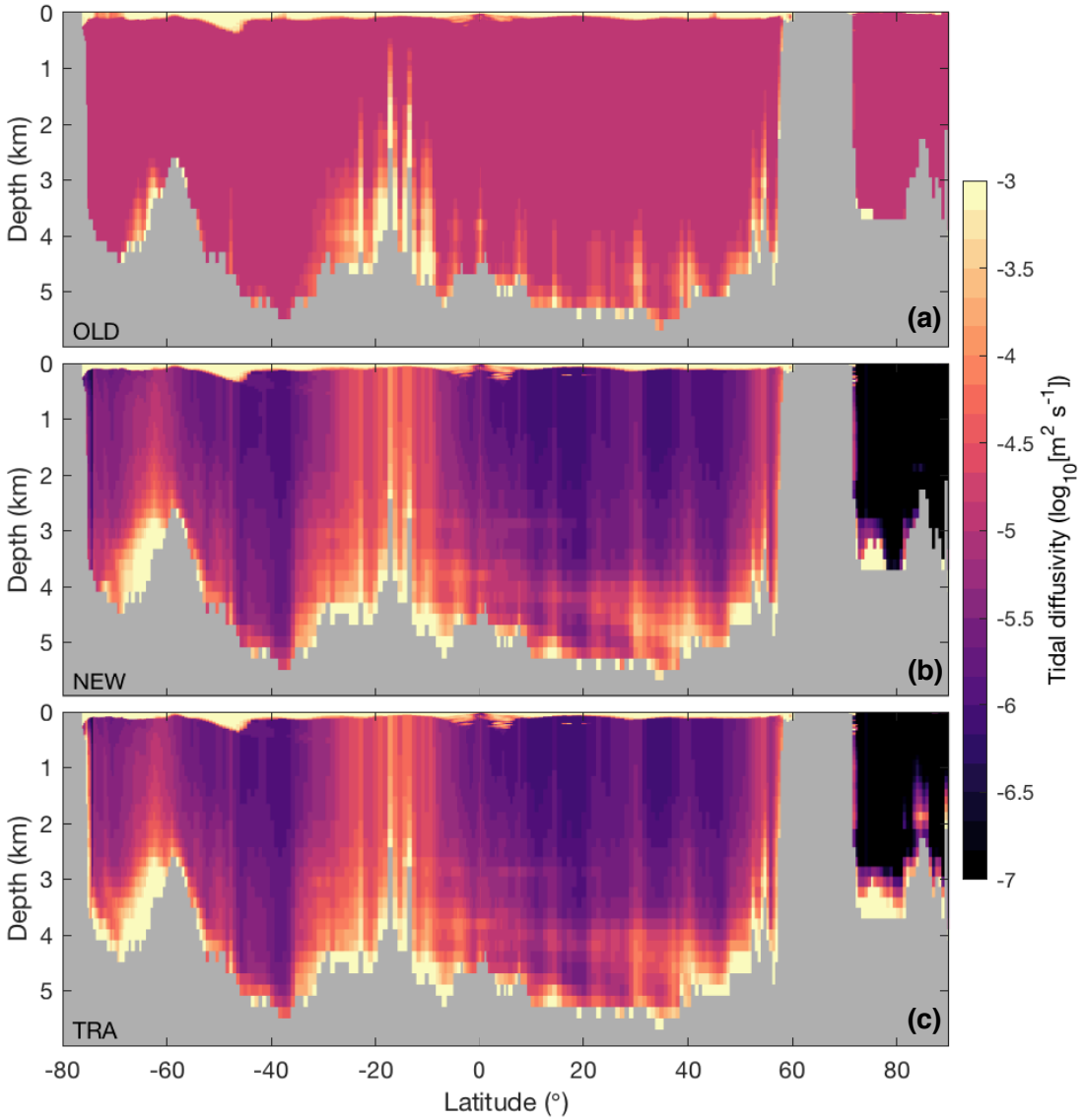

Figure 7: Tidal vertical diffusivity at 210°E (or 150°W), in experiments OLD **(a)**, NEW **(b)** and TRA **(c)**. This diffusivity is that produced by the tidal mixing parameterization in each experiment, including the background diffusivity in the case of OLD. Note the diffusivity is shown on a $\log_{10}$ scale.

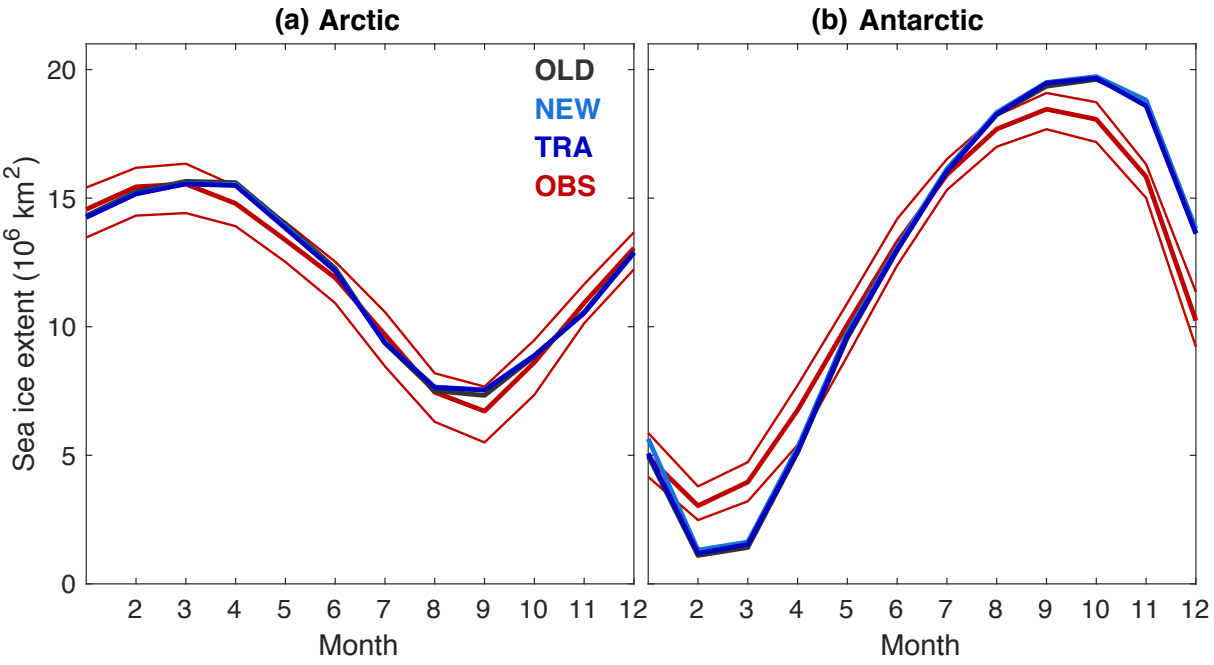

Figure 8: Seasonal evolution of Arctic **(a)** and Antarctic **(b)** sea ice extents in satellite observations (red) and experiments OLD (black), NEW (light blue) and TRA (dark blue). Observations, from the National Snow and Ice Data Center (Stroeve and Meier 2018), are monthly averages over the period 1979-2019; the thick red curve corresponds to the climatological mean while thin red curves denote the observed range for that period.

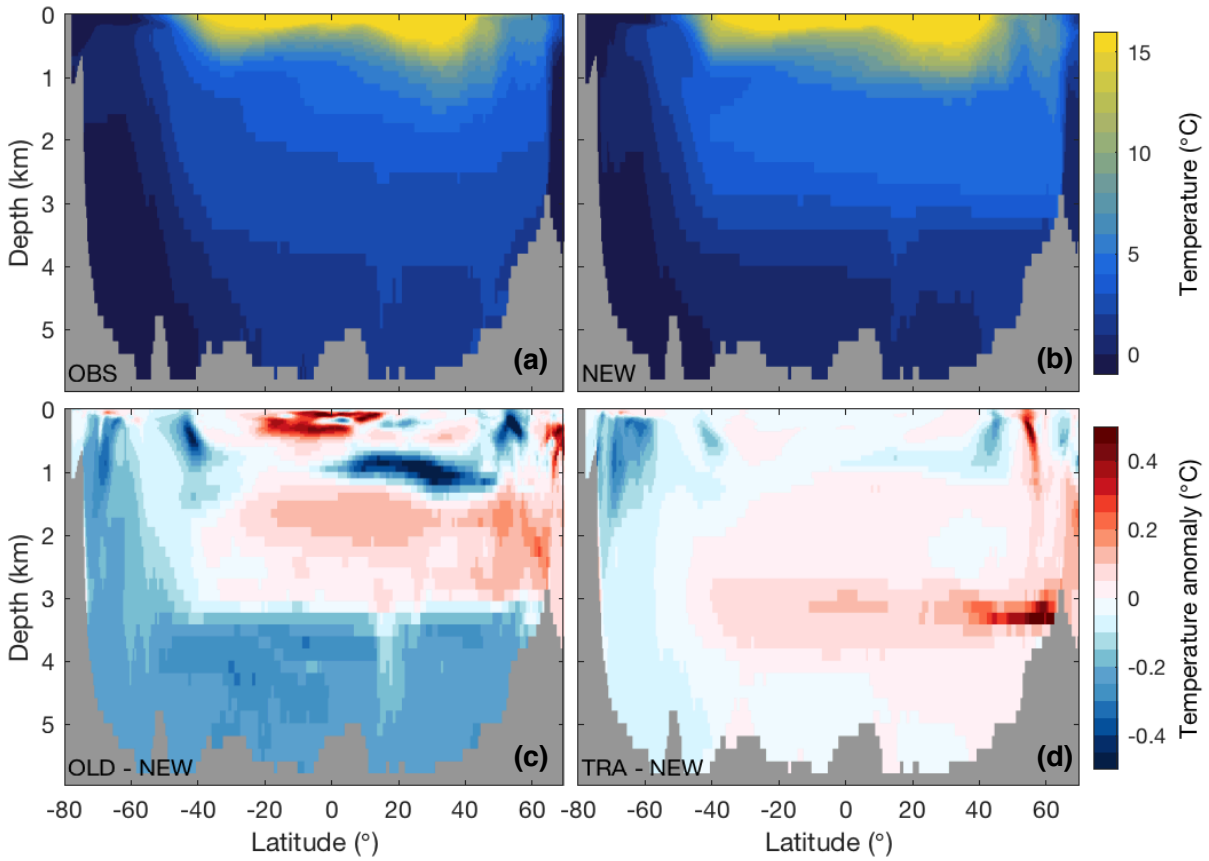

Figure 9: Atlantic zonal mean temperature in the observational climatology of Gouretski (2019) **(a)** and experiment NEW **(b)**. Anomalies in experiments OLD **(c)** and TRA **(c)** with respect to NEW are also shown.

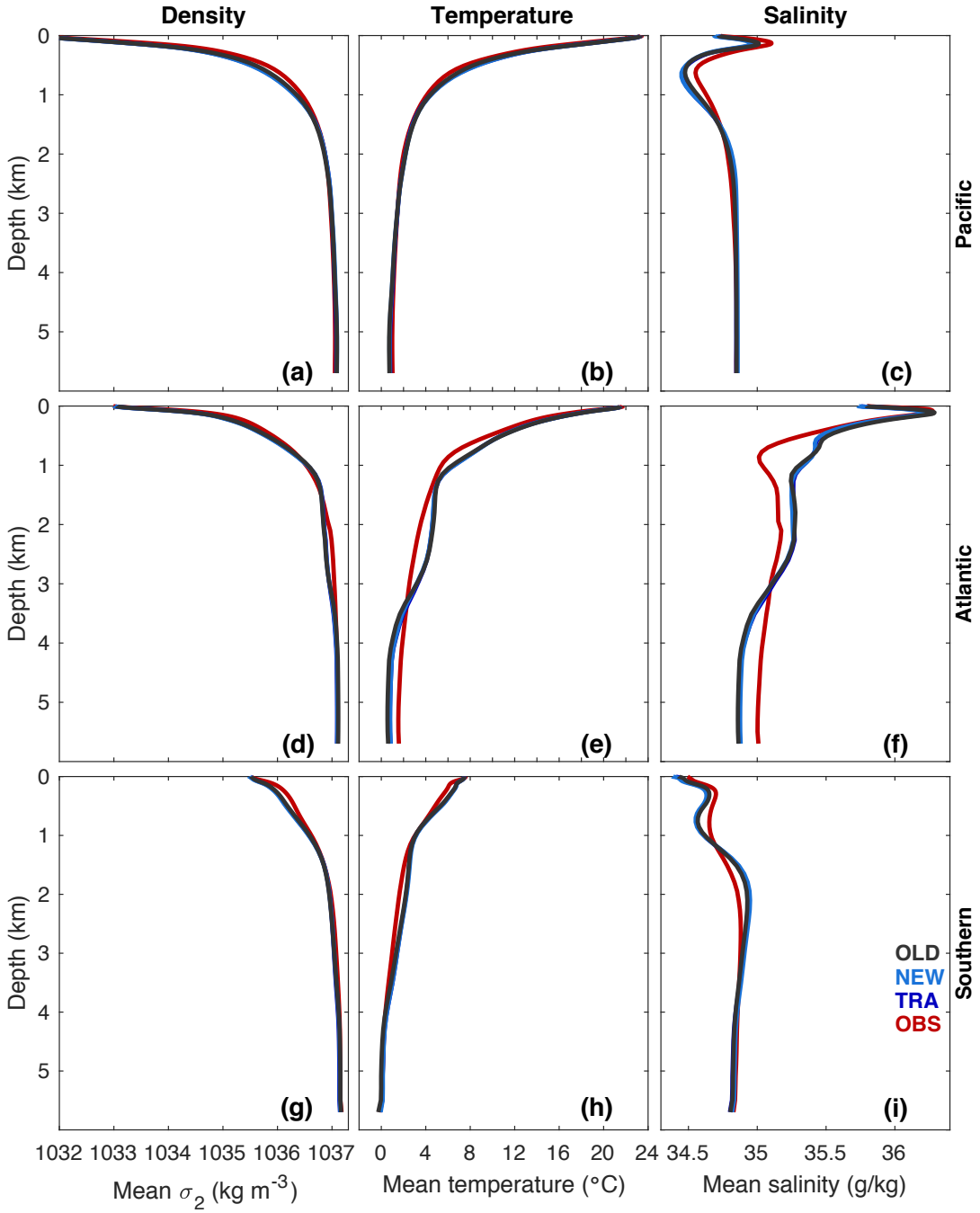

Figure 10: Basin-averaged density **(a,d,g)**, temperature **(b,e,h)** and salinity **(c,f,i)** profiles in the observational climatology of Gouretski (2019) (red) and in model experiments OLD (black), NEW (light blue) and TRA (dark blue). The Pacific Ocean (33°S-65°N) is shown in panels **(a-c)**, the Atlantic Ocean (33°S-65°N) in panels **(d-f)** and the Southern Ocean (80°S-33°S) in panels **(g-i)**. Density is measured as σ_2, the potential density referenced to 2000 dbars.

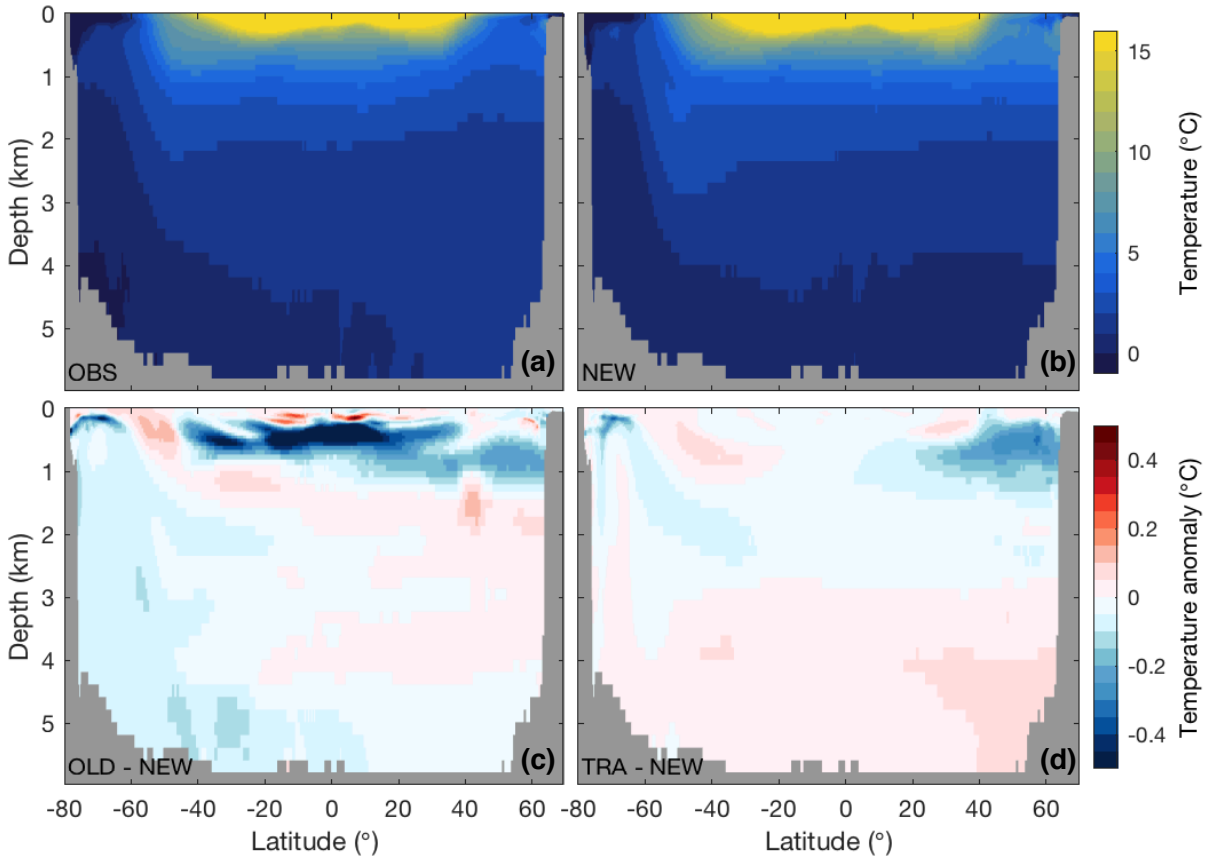

Figure 11: Pacific zonal mean temperature in the observational climatology of Gouretski (2019) **(a)** and experiment NEW **(b)**. Anomalies in experiments OLD **(c)** and TRA **(d)** with respect to NEW are also shown.

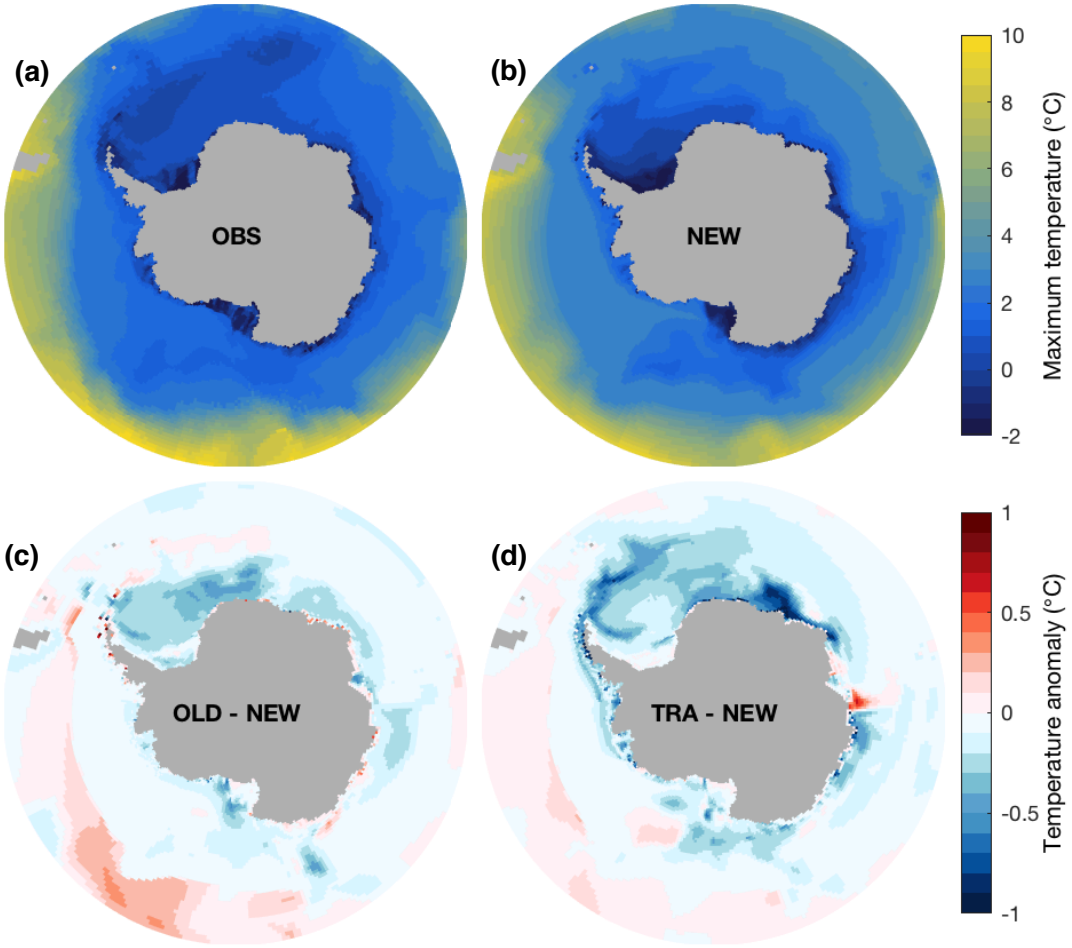

Figure 12: Maximum temperature of the water column in the observational climatology of Gouretski (2019) **(a)** and experiment NEW **(b)**, shown as a stereographic projection south of 50°S. Anomalies in experiments OLD **(c)** and TRA **(d)** with respect to NEW are also shown.

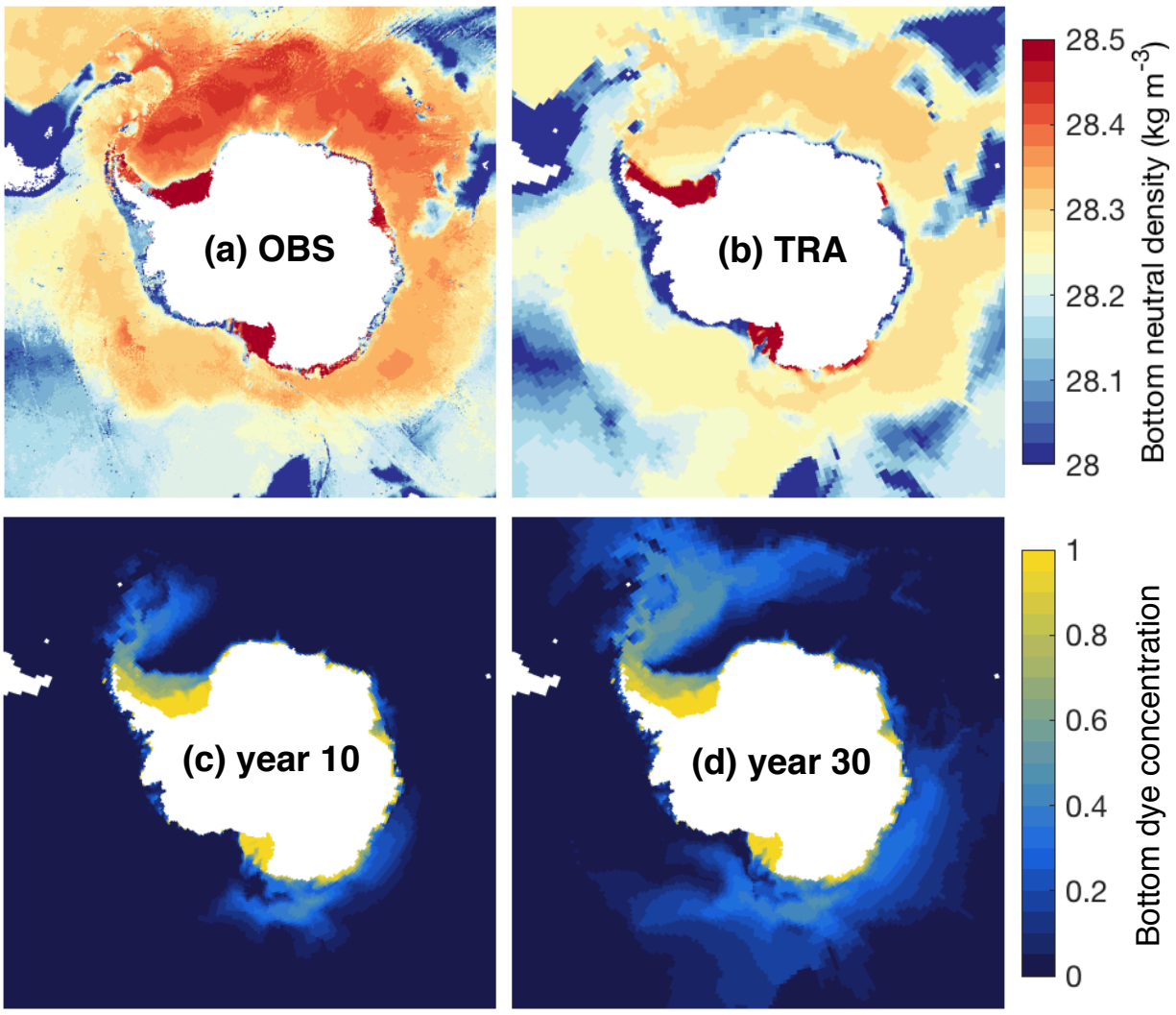

Figure 13: Annual maximum neutral density at the seafloor in the observational climatology of Gouretski (2019) **(a)** and in experiment TRA **(b)**. Panels **(c)** and **(d)** show the concentration of an artificial dye tracer in the bottom grid cell of the model (experiment TRA), respectively 10 years and 30 years after initialization. The dye tracer is restored to 1 in the top 10 meters of the model and propagates as a conservative tracer in the deeper ocean. This dye simulation was done in offline mode using five-day output from year 1,001 of experiment TRA. It shows that the bottom ocean fills from the four sites where dense shelf waters (neutral density > 28.5 kg m^{-3}) are formed.

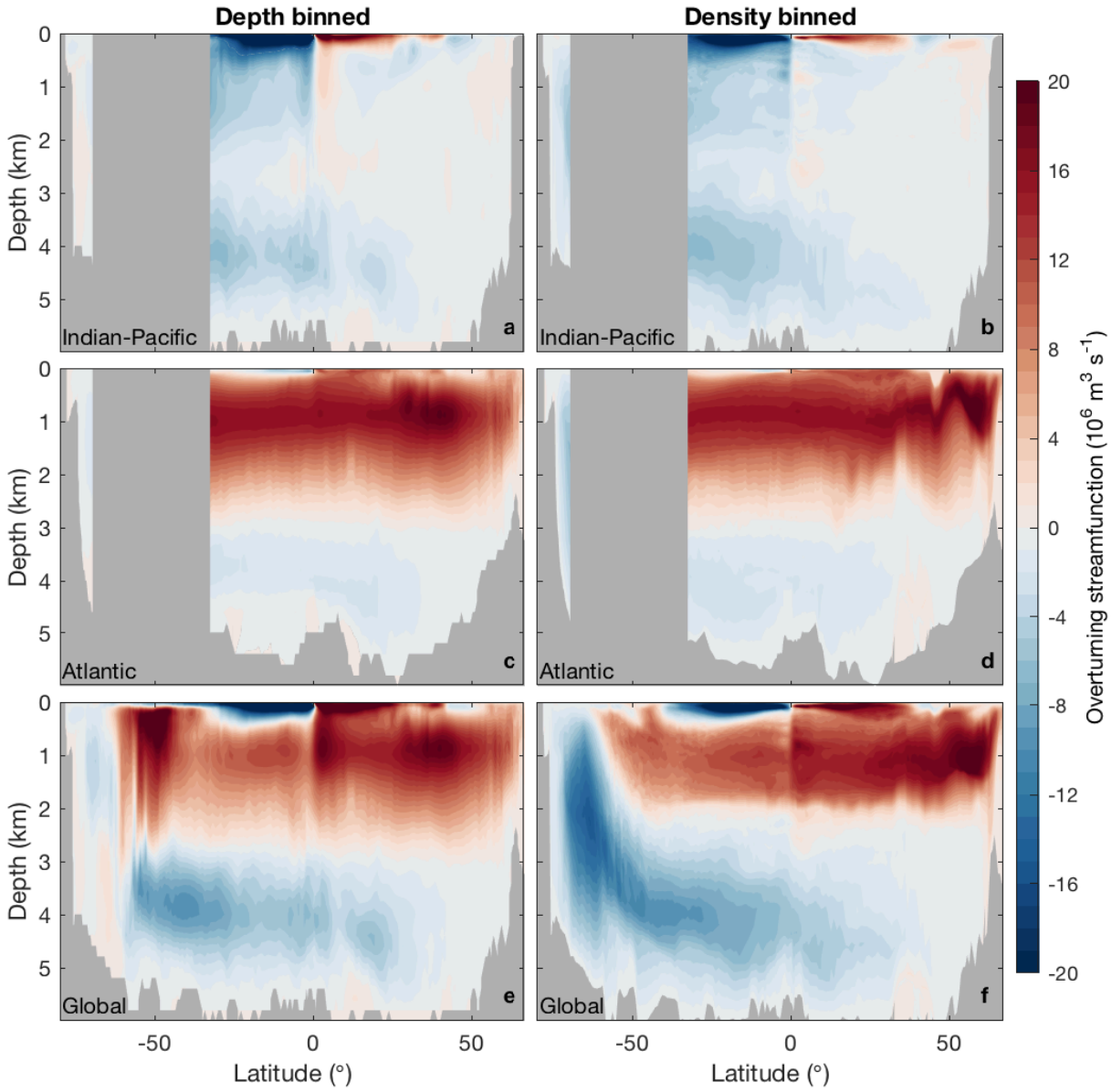

Figure 14: Meridional overturning streamfunction in experiment NEW. The streamfunction is shown for the Indian-Pacific **(a,b)**, Atlantic **(c,d)** and global **(e,f)** oceans. It was computed both in depth coordinate **(a,c,e)** and density (σ_2) coordinate **(b,d,f)**. The density-coordinate streamfunction is reprojected to depth using the pseudo-depth of isopycnal surfaces. The pseudo-depth of an isopycnal surface within a given latitude band is the geopotential which has the same volume beneath it (e.g., Zika et al. 2012).

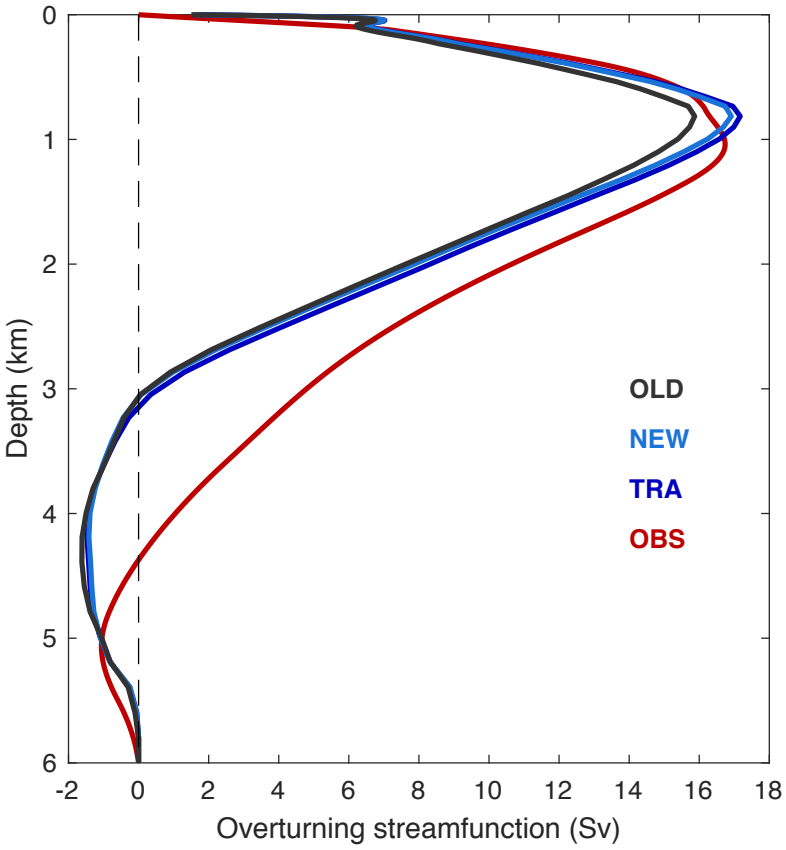

Figure 15: Meridional overturning streamfunction at 26.5°N in the Atlantic. RAPID observations (Sinha et al. 2018) are shown in red, experiment OLD in black, experiment NEW in light blue and experiment TRA in dark blue.

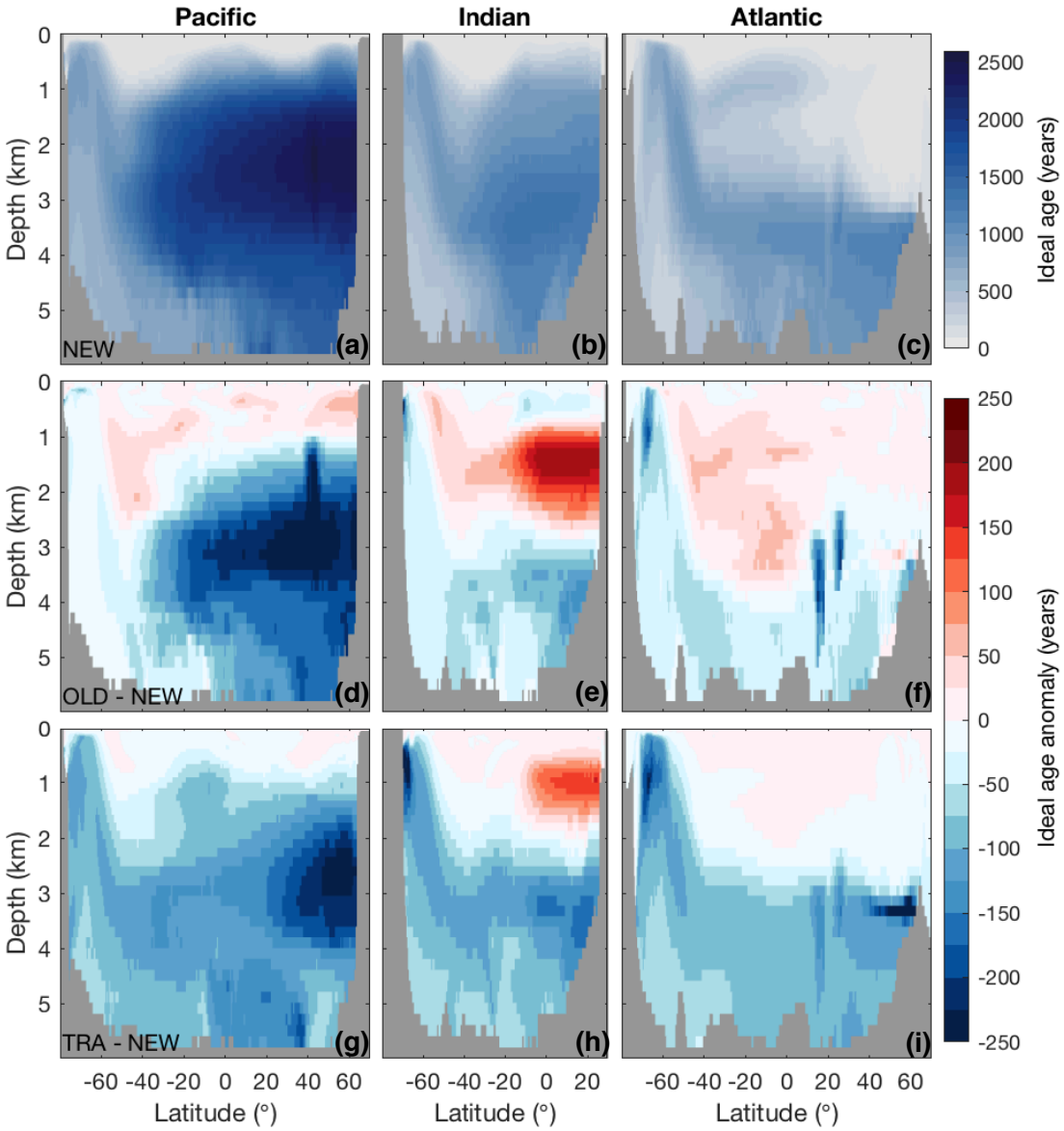

Figure 16: Zonal mean ideal age simulated by experiment NEW **(a-c)**. Anomalies in OLD **(d-f)** and TRA **(g-i)** with respect to NEW are also shown. The zonal average was taken over the Pacific **(a,d,g)**, Indian **(b,e,h)** or Atlantic **(c,f,i)** basin, each extended due south to Antarctica.

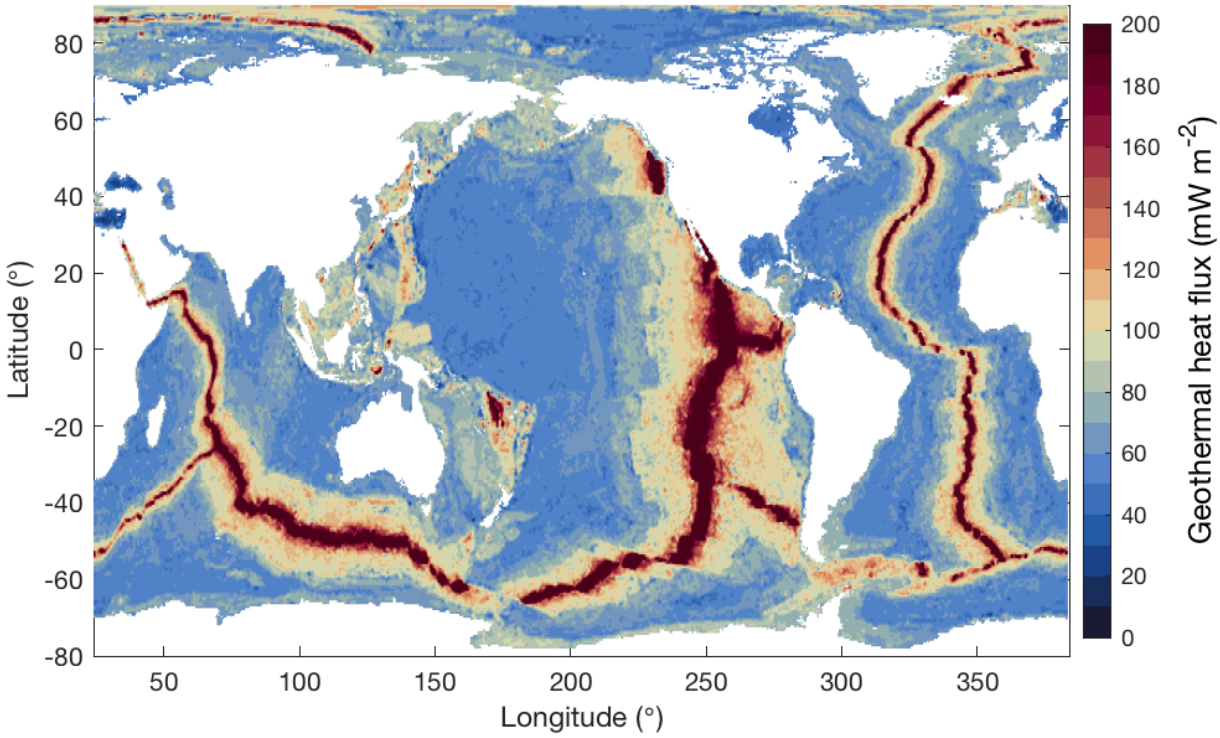

Supplementary Figure S1: Geothermal heat flux through the seafloor from Lucazeau (2019). This flux is included as a bottom thermal forcing in all three experiments.

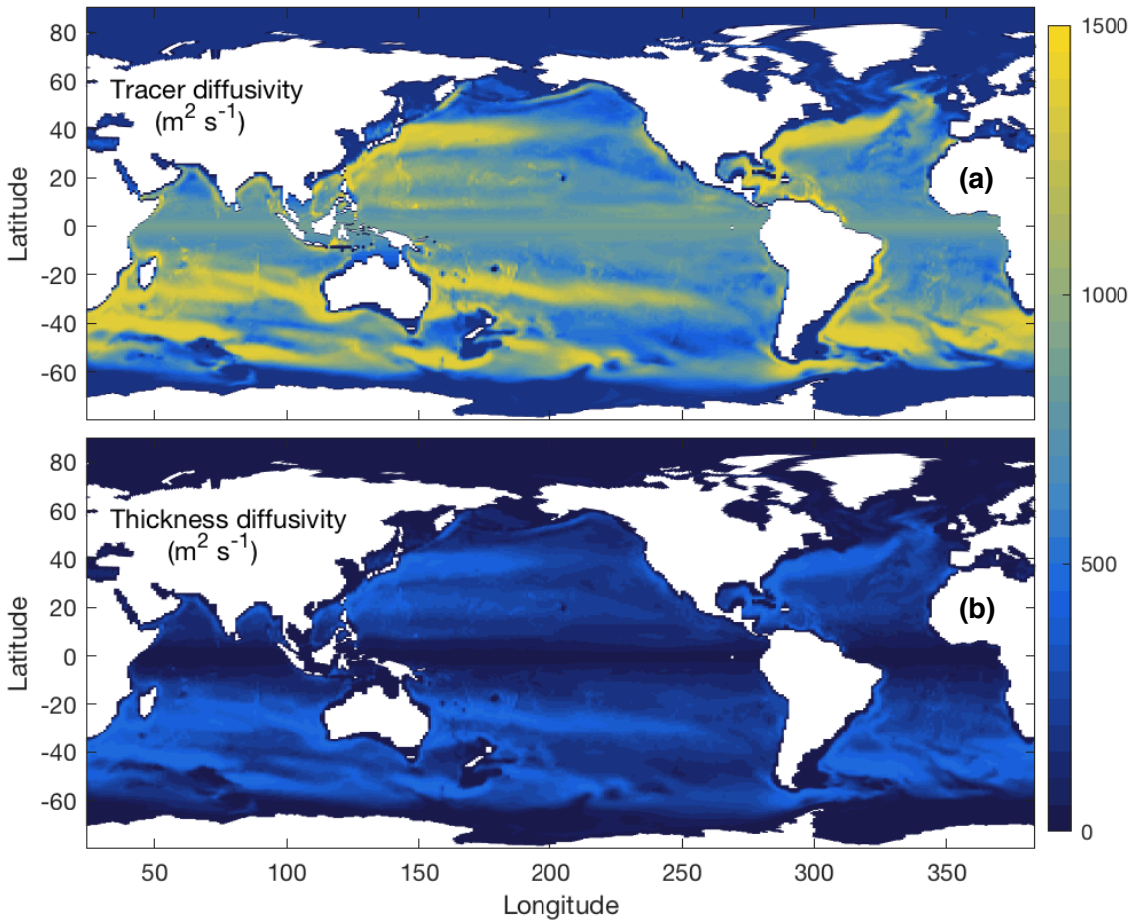

Supplementary Figure S2: Map of the isopycnal tracer diffusivity **(a)** and isopycnal thickness diffusivity **(b)** averaged over the last decade of experiment TRA. Both diffusivities are independent of depth but vary horizontally with the simulated stratification.

CHAPTER III

NEMO SIMULATION: EVALUATION OF A TEMPERATURE BIAS IN THE SUBARCTIC PACIFIC

The upwelling of abyssal tracers in the modern subarctic Pacific was inferred in Chapter I. In Chapter II we examined model outputs to study global ocean ventilation volumes, rates and pathways. Ventilation rates in the deep Pacific were poorly represented in analysed NEMO experiment: the ideal age there far exceeded that deduced from radiocarbon observations and from inverse models that assimilate those observations. Figure 3.1 shows the depth profile of potential density referenced to 2000 dbars (σ_2), conservative temperature and absolute salinity, horizontally averaged over the subarctic Pacific (40-65°N), in the different NEMO experiments explored in Chapter II and in the observational climatology of Gouretski (2019). This figure shows that the hydrography of the subarctic Pacific is also poorly represented in these NEMO experiments: a strong warm bias is present in the upper 2 km.

Warren (1983) inferred the upwelling of deep waters was necessary in the North Pacific to explain low surface temperatures and evaporation rates. In this region NEMO experiments display a warm bias in upper waters and an old bias in deep waters. Both age and temperature biases could potentially be explained by a lack of deep water upwelling, since stronger upwelling of relatively cold and young abyssal waters may rejuvenate and cool shallower waters. Diapycnal mixing could play a role in causing the ascent of deep waters to the surface (Sarmiento et al., 2004). A lack of diapycnal mixing in NEMO is a plausible candidate given that its degree of 'diffusiveness' quantified in Chapter II is lower than that of data-constrained inverse models. A lack of wind-driven upwelling is also plausible: cyclonic wind stress within the subpolar gyre promotes upwelling, and coastal upwelling phenomena could occur along the northern rim of the Pacific (Toggweiler et al., 2019).

Both hypotheses have been partly tested in Chapter II:

- The addition of mixing by sub-inertial internal tides (DIALOW → REF, see Chapter II) proved to have a substantial impact on ventilation rates, but it was insufficient to eliminate the age bias. Meanwhile,

the impact of mixing by subinertial internal tides on the subarctic Pacific temperature bias is weak, even though it shifts the profile towards a better estimate (Figure 3.1).

- Figure 16 of Chapter II showed that no major differences could be observed within the North Pacific between the wind stress of a state-of-the-art reanalysis product and the wind stress forcing in our NEMO experiments. The parameterized eddy-driven vertical velocities were found to be weak in this region in NEMO, and are therefore unlikely to cause a muted response to wind-driven Ekman pumping. Thus, wind-driven upwelling in the subpolar gyre is probably not to blame for temperature and age biases of NEMO.

These findings indicate that: (i) diapycnal mixing and wind-driven upwelling are likely not the only processes underpinning the observed biases in the subarctic Pacific; (ii) the age and temperature biases, although possibly reinforcing each other, may be largely decoupled. In this chapter, we will diagnose and assess the processes that lead to the subarctic Pacific temperature bias in NEMO.

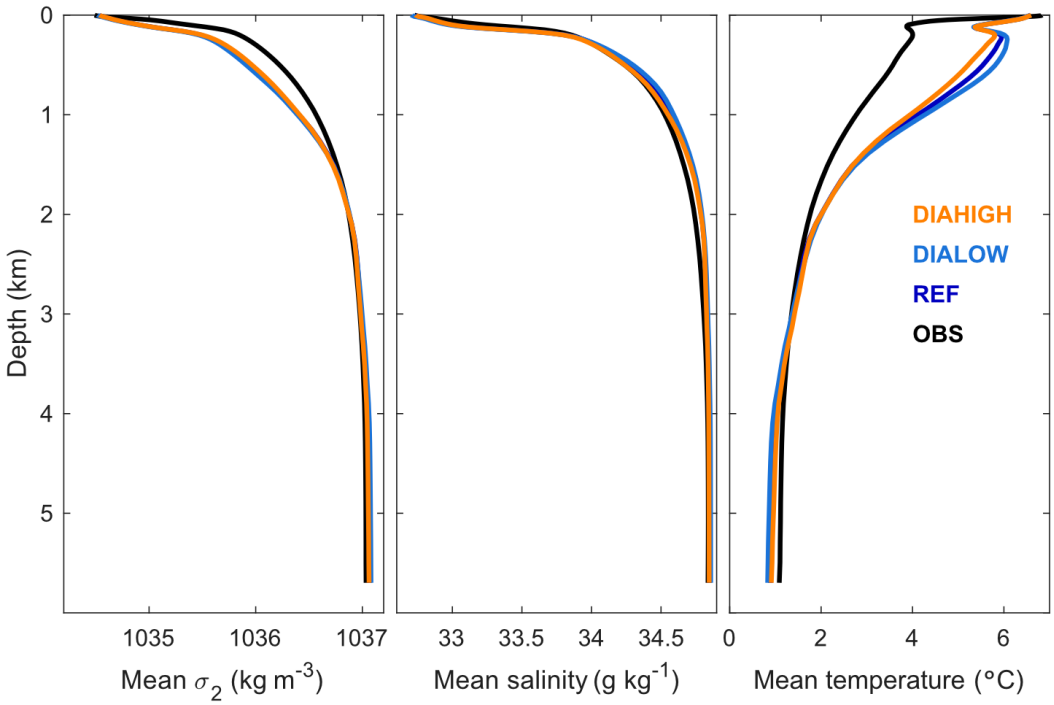

Figure 3.1: Vertical profile of potential density referenced at 2000 m (σ_2), absolute salinity and conservative temperature, horizontally averaged over the subarctic Pacific (40-65°N), in DIAHIGH (orange), DIALOW (light blue), and REF (dark blue) from Chapter 2, and in the observational climatology of Gouretski (2019) (black).

1 . Introduction

The biological pump is highly dependent on nutrient availability in the shallow ocean. This nutrient availability is contingent on the upwelling of nutrient-rich deep water at high-latitudes, in the Southern Ocean (Toggweiler and Samuels, 1993) and in the North Pacific (Sarmiento et al., 2004; Toggweiler et al., 2019). Those upwelled nutrients are advected into the thermocline via mode waters in the Southern Hemisphere and North Atlantic and via North Pacific Intermediate Water (NPIW) in the North Pacific (Sarmiento et al., 2004). Correctly modelling the dynamics of the North Pacific is thus essential to adequately represent marine biogeochemical cycles.

Next, we will present the dynamics of the North Pacific, including an overview of NPIW formation and properties both in observations and in NEMO experiments. Finally, we will identify the source of the temperature bias in NEMO simulations before giving some perspectives.

2 . Methods

In addition to NEMO outputs that have been presented in Chapter 2, we will use annual-mean temperature and salinity from the WOCE global hydrographic climatology Gouretski and Koltermann (2004). Additionally, we will use the reanalysis products from E.U. Copernicus Marine Service Information, specifically gridded fields of horizontal velocities (https://doi.org/10.48670/moi-00021) and wind stress (https://doi.org/10.48670/moi-00185). Horizontal velocities that we will show are averaged over the years 2010 to 2014, while surface wind speeds and wind stress are averaged over years 2013-2014.

The wind stress field is used to show the boundary between the subtropical and subpolar gyres. Let us define the wind stress at the sea surface τ with its northward and eastward components, τ_N and τ_E. The curl of τ is directly linked to Ekman upwelling, and the gyre boundary is often taken as the line of zero wind stress curl:

$$\overrightarrow{rot}\,\tau = 0 \tag{III.1}$$

In order to compute average properties of NPIW water masses that we will define, we use a volume-weighted average. Thus the average water mass property C is computed as:

$$C = \frac{\sum_i C_i \times V_i}{V} \tag{III.2}$$

where the index i refers to grid cells, C_i is the tracer value within each cell of volume V_i, and V is the volume summed over all considered cells.

3 . Results

3.1 . Presentation of the North Pacific ocean dynamics

Ocean dynamics in the shallow North Pacific are largely driven by winds. The mid-latitude westerlies (peaking around 35°N) tend to separate the basin into two zones: an anticyclonic (clockwise) wind-stress zone called the subtropical gyre (ranging from 10-35°N) and a cyclonic (anti-clockwise) one called the subpolar gyre (from around 35°N to 65°N). Figure 3.2 represents temperature and salinity at the surface and at 350 m depth in the North Pacific, as estimated in the WOCE climatology (Gouretski and Koltermann, 2004). The white dashed line in this figure represents the gyre boundary taken as the zero line of the curl of the wind stress (see Methods). Figure 3.2 illustrates that surface waters in the subtropical gyre are warm and salty whereas the ones of the subpolar gyre are cold and fresh. This contrast remains true for water at a depth of 350 m, although the magnitude of the differences is less important. Interestingly, the absolute salinity at 350 m (Figure 3.2d) presents a local salinity maximum along the Aleutian Arc, which reveals deep waters upwelling at this location, as this signal cannot originate from the fresh subpolar surface waters. This upwelling is potentially caused by the winds or enhanced diapycnal mixing near the topography, and could be an important component of the North Pacific mass balance (Warren, 1983).

A local salinity minimum can be observed around 40°N, at 350 m depth east of Japan (Figure 3.2d): it is the signature of North Pacific Intermediate Water (NPIW). Hasunuma (1978) describes this salinity minimum formed at the junction of the Kuroshio and Oyashio currents, as the vertical boundary between the subtropical and subpolar waters. NPIW is usually defined as the salinity minimum in the North Pacific at depths of 300-700 m, within the neutral density range $26.7 \leq \gamma \leq 26.9$, and is thought to be formed by mixing between subtropical and subpolar waters (Talley, 1993). Subpolar waters influencing the intermediate depths sink during wintertime when they are cooled, such that the wintertime temperature of these subpolar waters ultimately sets the NPIW formation density (Talley, 1993).

Surface temperatures of subpolar waters being too warm would result in a warmer type of NPIW than expected, which could ultimately warm the upper Pacific Ocean. We display in Figure 3.3 the annual mean conservative temperature and absolute salinity difference between the REF NEMO experiment and the WOCE climatology, at the surface and at 350 m depth. NEMO-simulated subpolar temperatures are too cold at the surface, and too warm at 350 m depth (Figure 3.3c). Surface temperature biases can thus be ruled out as a direct cause of excess subsurface warmth. The salinity of subpolar surface waters is overestimated along the continental margins and in the Okhotsk Sea (Figure 3.3d), possibly linked to underestimated local freshwater sources. This surface salinity bias does not propagate to the entire basin at greater depths, although salinity at 350 m depth is overestimated in the Okhotsk Sea and near the NPIW formation region (Figure 3.3e). At 350 m depth, biases in both salinity and temperature are maximum in the NPIW formation region and in the Okhotsk Sea (Figure 3.3b,e), suggesting a role for one of those two regions in setting the subarctic temperature bias in NEMO.

3.2 . NPIW formation and properties

The formation of NPIW seems to be either the cause or the direct consequence of the subsurface temperature bias in NEMO. We thus examine in more detail its formation and properties. Neutral density is not readily available from NEMO output, thus the density that we will compare between NEMO and WOCE is potential density with a reference pressure of 0 dbar (σ_0). Nevertheless, neutral density is useful to track NPIW in observations, and we idendify NPIW in the WOCE climatology as the density range $26.7 \leq \gamma \leq 26.9$ in the North Pacific north of $20°$N. The associated (T, S) properties are shown in

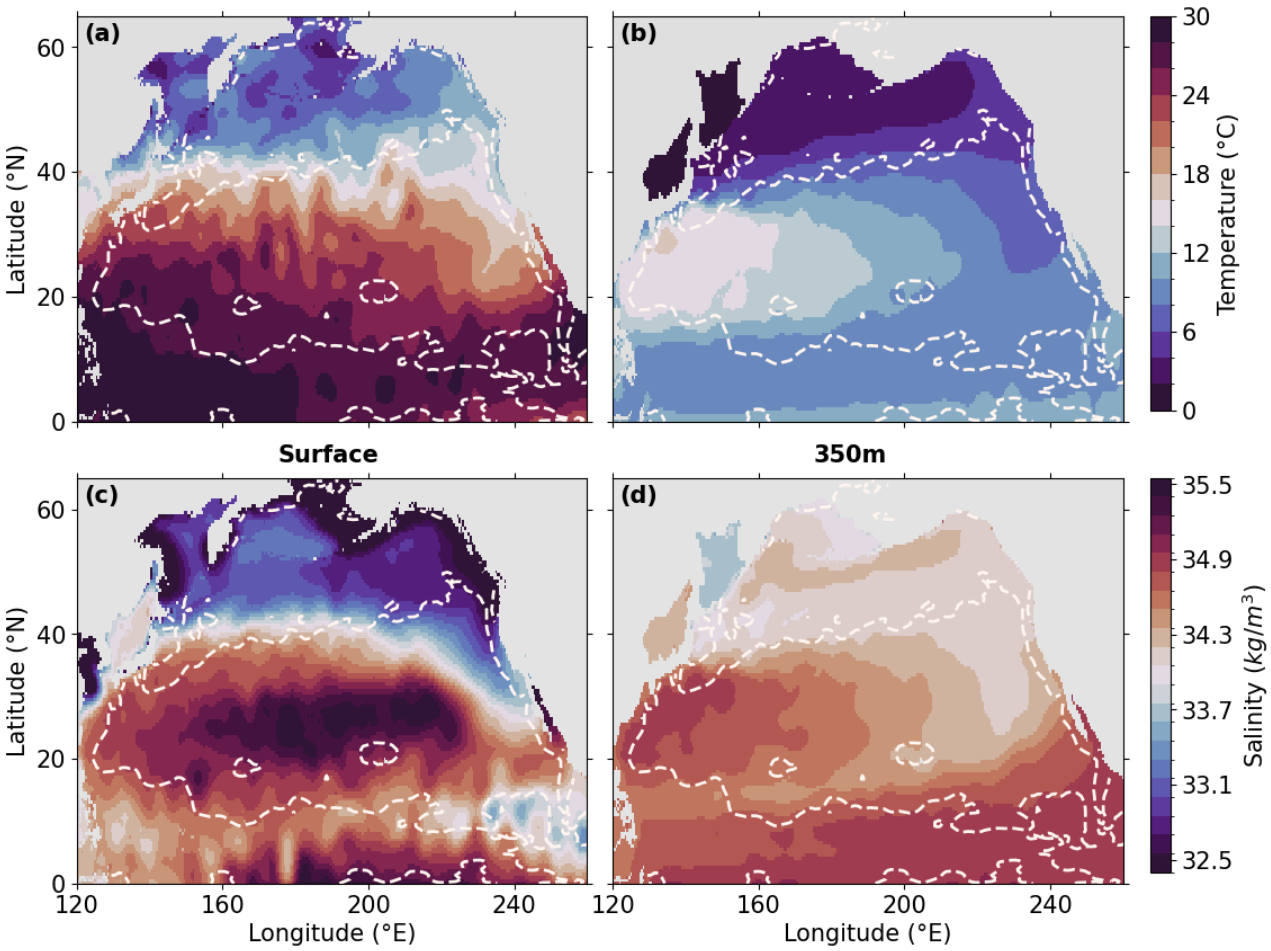

Figure 3.2: Maps of conservative temperature (first row) and absolute salinity (second row) at the surface (first column) and at 350 m depth (second column) in the North Pacific ocean. The white dashed line represents the gyre boundary based on NEMO wind stress forcing.

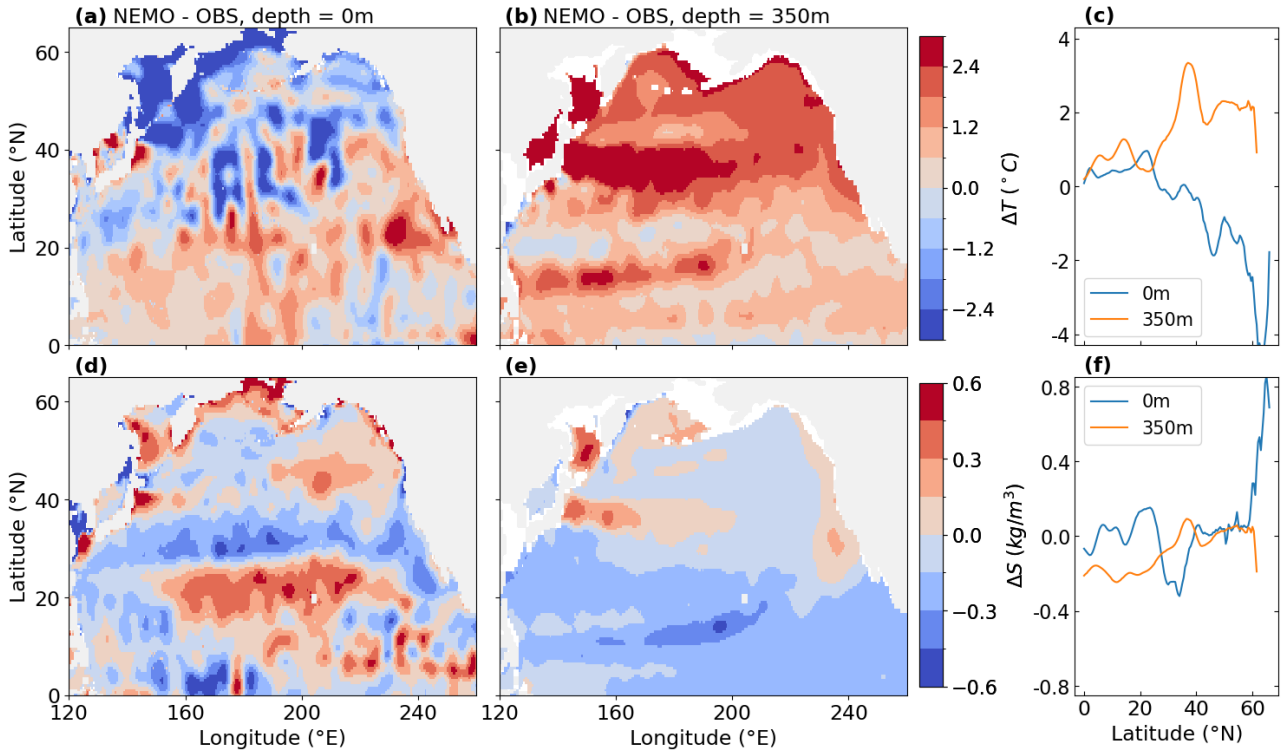

Figure 3.3: Conservative temperature (first row) and absolute salinity (second row) difference between the final state of the REF NEMO experiment and the WOCE climatology, at the surface (first column) and at 350 m depth (second column). In the third column (panels **(c, f)**) we show zonal mean differences as a function of latitude.

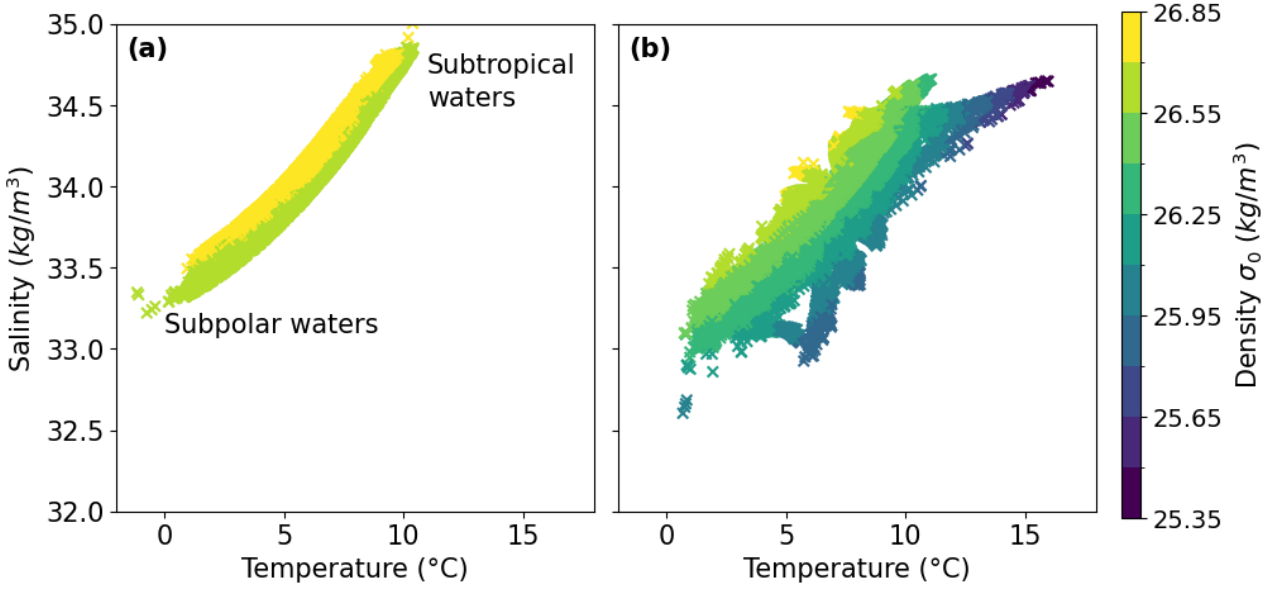

Figure 3.4: Panel **(a)** shows a scatter plot of conservative temperature against absolute salinity of NPIW, defined via its neutral density range in the WOCE climatology. We use the same spatial mask to exhibit water properties at the same locations in NEMO in panel **(b)**. Colours show σ_0.

Figure 3.4a. A clear mixing curve can be seen between fresh and cold subpolar waters and warm and salty subtropical waters. We examine the water properties at similar locations in NEMO (Figure 3.4b) and find that the properties are much more heterogeneous: the density range is wider (see Table 1, 'WOCE' and 'NEMO mask γ') and the mixing line between the two different types of waters is less well defined.

This relative heterogeneity in NEMO-simulated water properties suggests that NPIW in NEMO is not present at the same location as in the WOCE climatology. We thus look for NPIW in our NEMO simulation by looking at different σ_0 ranges. First, we select the water in NEMO that has the same σ_0 density range as the NPIW in WOCE ('NEMO mask σ_0' in Table 1): for the neutral density range mask that we previously described ('WOCE'), we compute the σ_0 associated and define the range of σ_0 representing these waters. The associated NPIW in NEMO ('NEMO mask σ_0') is slightly too warm, salty, and deep, but the averaged properties are fairly close to our reference from the WOCE climatology (Figure 3.5a,b). However, the mixing curve between subpolar and subtropical waters is not correctly represented; we infer that those waters do not satisfy the formation mechanism of NPIW. We thus look for a more faithful definition of NPIW in NEMO, using a similar range of potential density (as in 'NEMO mask σ_0'), shifting this range until the (T, S) curve resembles that of observations. Figure 3.5c shows the associated NPIW properties, referenced as 'NEMO best' in Table 1. The volume-weighted salinity and depth are the same as in 'WOCE', but the conservative temperature differs by about 2°C. Closer comparison of the 'WOCE' and 'NEMO best' NPIW (Figure 3.5a,c) indicates that subtropical waters are too warm and subpolar waters too fresh in the latter, consequently NEMO is unable to reproduce the correct NPIW density.

Figure 3.5d illustrates another possible definition of NPIW, slightly warmer than 'NEMO best'. This example shows that there is no unambiguous definition of NPIW in NEMO. Nonetheless, the spatial distribution of NPIW in 'NEMO best' is most similar to 'WOCE' (see Supplementary Information, Figure S3.1).

	σ_0 (kg/m^3)			$T(°C)$	S (PSU)	depth (m)
	min	max	mean			
WOCE	26.58	26.81	26.7	6.38	34.15	425
NEMO mask γ	25.36	26.79	26.42	8.28	34.15	428
NEMO mask σ_0	26.58	26.81	26.7	6.76	34.22	506
NEMO best	26.32	26.55	26.44	8.2	34.15	425
NEMO ex	26.18	26.41	26.3	8.95	34.12	396

Table 1: Table referencing the minimum, maximum and mean density, as well as the averaged conservative temperature, absolute salinity and depth for the different NPIW definitions we use. Averaged values are volume-weighted means. 'WOCE' stands for the NPIW found with the WOCE climatology, 'NEMO mask γ' for the NPIW defined with the same spatial mask (based on neutral density) used in WOCE, 'NEMO mask σ_0' for NPIW defined with the same σ_0 as in WOCE, 'NEMO best' as the NPIW designed to have a similar salinity and depth as in observations, and 'NEMO ex' for another example of a possible definition.

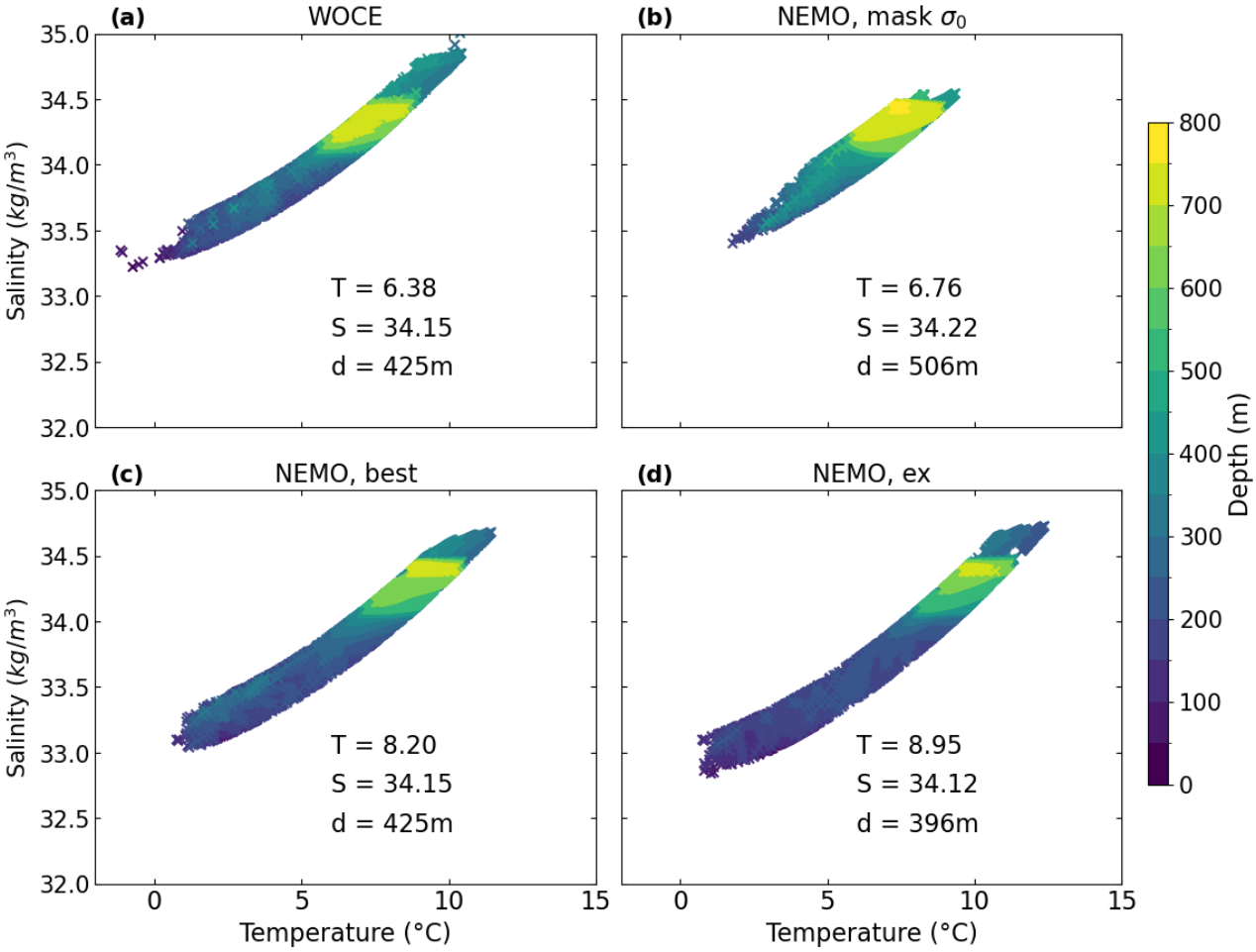

Figure 3.5: Scatter plot of temperature against salinity for the different NPIW definitions of Table 1.

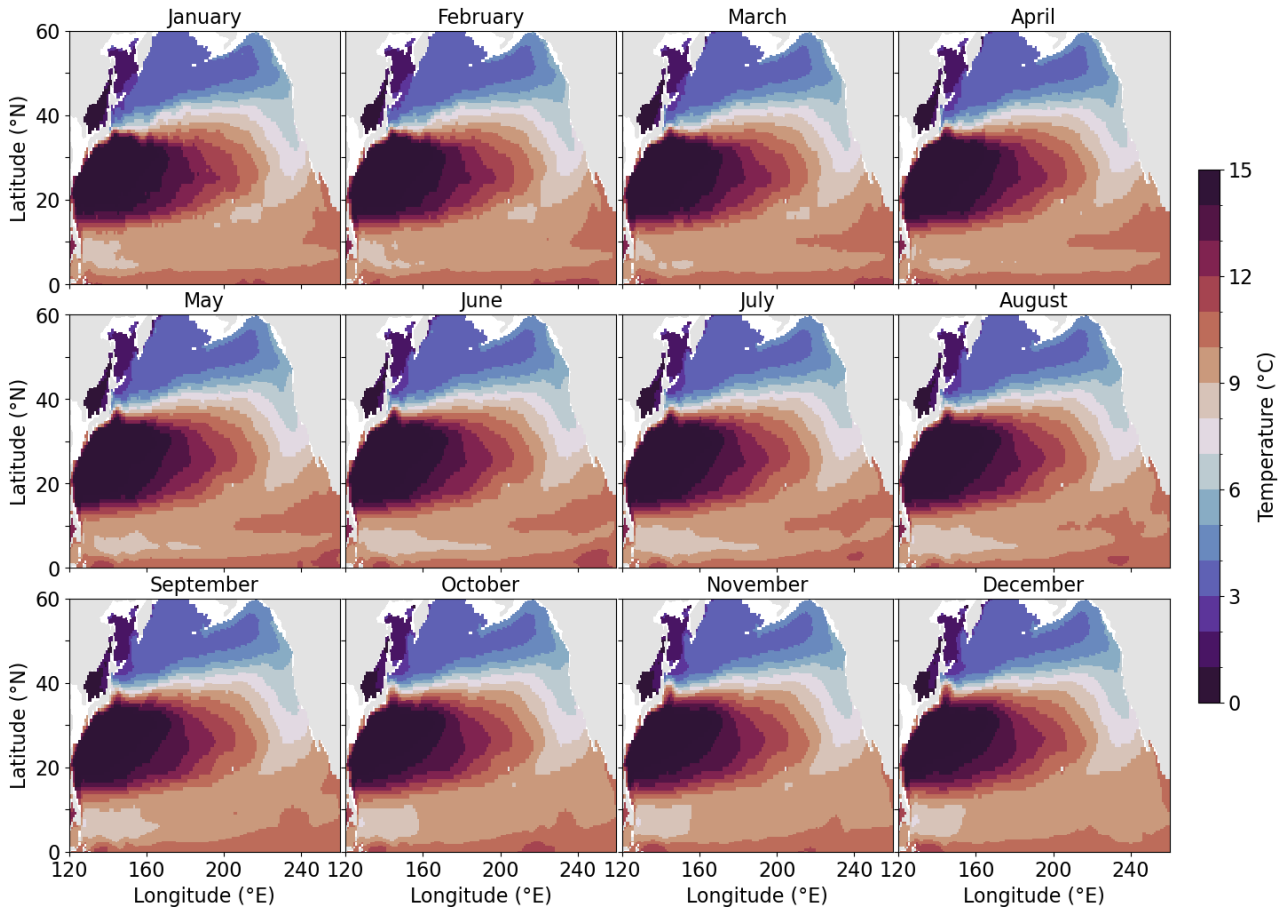

Figure 3.6: Monthly mean conservative temperature at 334 m depth during the first year of the REF online NEMO simulation.

Regardless, our analysis shows that the model generated NPIW is too light, primarily because it is too warm.

Excessive warmth of subtropical waters is not the cause: Figure 3.3 shows that the largest temperature excess is in the NPIW formation region and in the Okhotsk Sea, and that the subtropical waters are not very different from the observations. Hence, biases in circulation and mixing, including NPIW formation processes, must be at play. We next investigate how subtropical and subpolar waters mix during the early spin-up stages of the NEMO REF experiment.

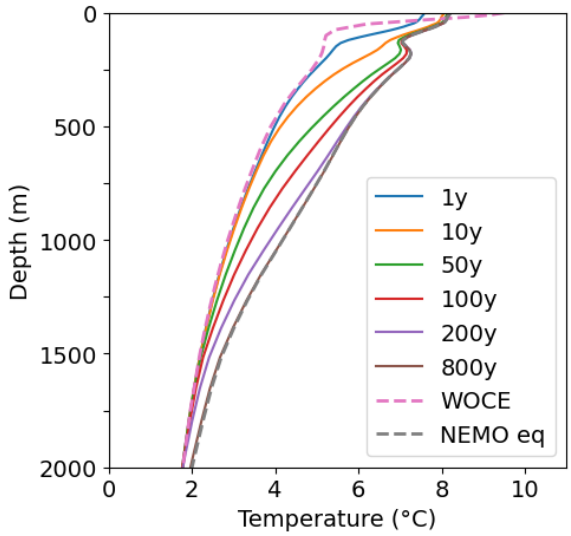

Figure 3.7: Subarctic Pacific ($lat \geq 40°$N) averaged conservative temperature profiles. The WOCE profile and the equilibrium NEMO profile are represented as pink and black dashed curves, respectively. Solid curves depict intermediate stages of the REF online NEMO simulation: year 1 (blue), year 10 (orange), year 50 (green), year 100 (red), year 200 (purple) and year 800 (brown).

3.3 . Origin of the temperature bias

We represent the monthly averaged conservative temperatures at 334 m depth, for the first year of the REF NEMO simulation, in Figure 3.6. This figure shows that a tongue of warm subtropical waters gradually forms and extends northward along the east coast of Japan. This warm water intrusion occurs at the junction of the Kuroshio and Oyashio currents and thus near the NPIW formation region. Can this circulation-driven bias explain the long-term drift toward higher temperature that we observe in the upper subarctic Pacific? What could cause this drift?

The mean temperature profile of the subarctic Pacific (north of 40°N) in the equilibrated state of REF is warm-biased in the upper 2 km. In Figure 3.7 we show the mean temperature profile of the subarctic Pacific (excluding marginal seas) in the WOCE climatology, in the final state of REF and at different stages of the spin-up of this simulation. At the start of the REF simulation (year 1), the temperature profile is very close to the WOCE climatology, as expected since REF was initialized from observations. As the simulation progresses, the averaged temperature profile moves toward the equilibrium state, very quickly in the shallow ocean, and more gradually at greater depths. By year 800, the hydrography in the top 2 km has reached equilibrium (Figure 3.7). The evolution of the profiles suggests that the warm bias first establishes in shallow (subsurface) waters and then diffuses downward over centuries.

The temperature bias seems to emerge at the junction of the Kuroshio and Oyashio currents. To evaluate the quality of the representation of these currents in the model, we use the horizontal seawater velocities of the reanalysis product from Mercator Océan International. We compute the current speed v from zonal (u_x) and meridional (u_y) velocities as $v = \sqrt{u_x^2 + u_y^2}$. Maps of current speed at 334 m are shown in Figure 3.8, together with the zonal average computed over the North Pacific. The reanalysis product shows an important current that flows along the east coast of Japan and that leaves the shore below 38°N. This

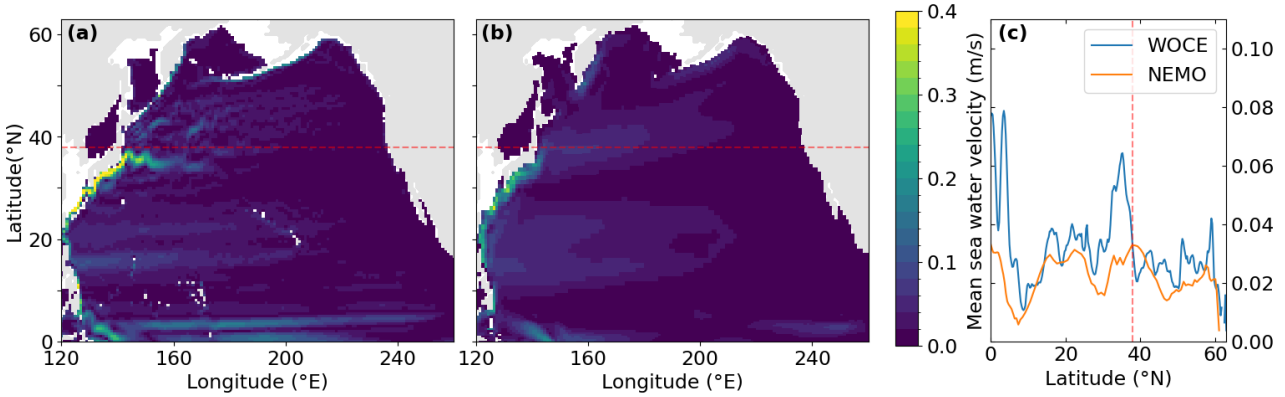

Figure 3.8: Maps of current speed at 334 m depth in the Mercator reanalysis **(a)** and in the final state of REF **(b)**. Panel **(c)** shows the zonal mean current speed in the North Pacific (excluding marginal seas). In all three panels the red dashed line marks the 38°N parallel.

current is also present in NEMO although less strong (Figure 3.8c). Crucially, the Kuroshio in NEMO does not turn sharply toward the east at 37°N, and instead extends further north while feeding a broad eastward current centered around 39°N (Figure 3.8b). This misrepresentation of the structure and position of the Kuroshio current very likely contributes to an excessive penetration of subtropical waters into the subpolar gyre. Representation of western boundary currents like the Kuroshio in coarse (1-degree) ocean models is a well-known difficulty (e.g., Penduff et al., 2007). Subduction at major fronts, such as the one separating subtropical and subpolar waters near 38°N off Japan, is also notoriously challenging to simulate, because it is influenced by mesoscale and submesoscale phenomena (e.g., Garabato et al., 2001). Our analysis indicates that these expected difficulties in capturing Kuroshio and frontal dynamics have large repercussions on the simulated hydrography of the subarctic Pacific.

Misrepresentation of dynamics associated with the Kuroshio seems to be a major factor behind the North Pacific temperature bias. However, it might not be the only factor. In particular, biases in isopycnal diffusion may also play a role in amplifying or spreading the bias across the subpolar gyre. Figure 3.9 shows maps at 334 m of the isopycnal tracer diffusivity in REF and in the observation-based climatology of Groeskamp et al. (2020) (used in the ISO3D offline simulation in Chapter 2). Whereas REF has isopycnal diffusivities that peak within the front between modelled subpolar and subtropical waters near 39°N (Figure 3.9a,c), the observation-based estimate has weaker diffusivities within the observed front (Figure 3.9b,d). A bias in the magnitude and spatial structure of the isopycnal tracer diffusivity in REF is thus likely, and could contribute to excessive north diffusion of subtropical warmth across the gyre boundary. Unfortunately, we do not have an online NEMO simulation with the isopycnal diffusivity of Groeskamp et al. (2020) to quantify the effect. Nonetheless, we hypothesize that suppression of meridional isopycnal diffusion by the swift zonal Kuroshio extension (Ferrari and Nikurashin, 2010), which is accounted for by Groeskamp et al. (2020) but not by the mixing scheme of REF, is an important process in this region that awaits faithful representation in NEMO.

4 . Perspectives

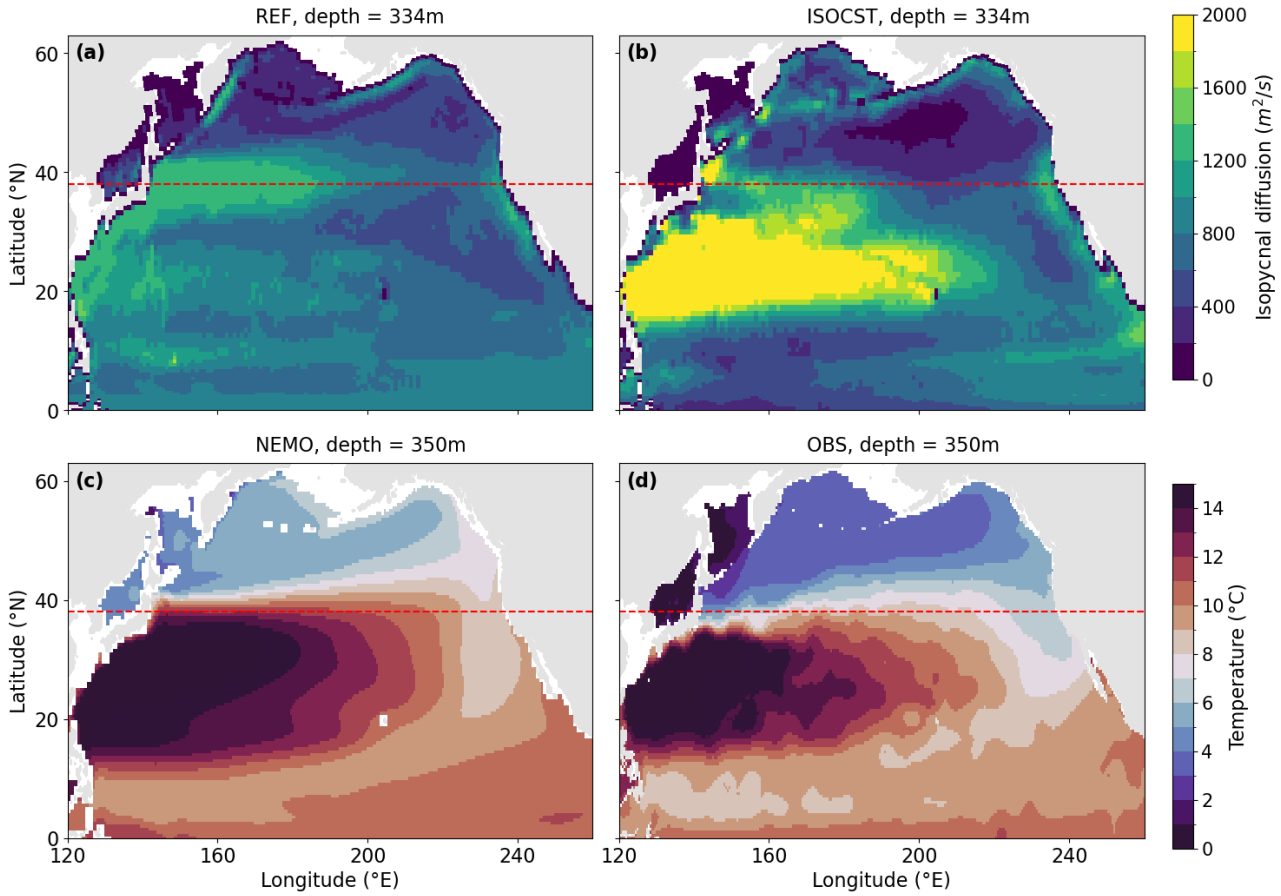

Figure 3.9: Isopycnal tracer diffusivity at 334 m deoth in the REF experiment **(a)** and in the climatology of Groeskamp et al. (2017) **(b)**. The second row showsconservative temperature at 350 m depth in REF **(c)** and in the WOCE climatology **(d)**.

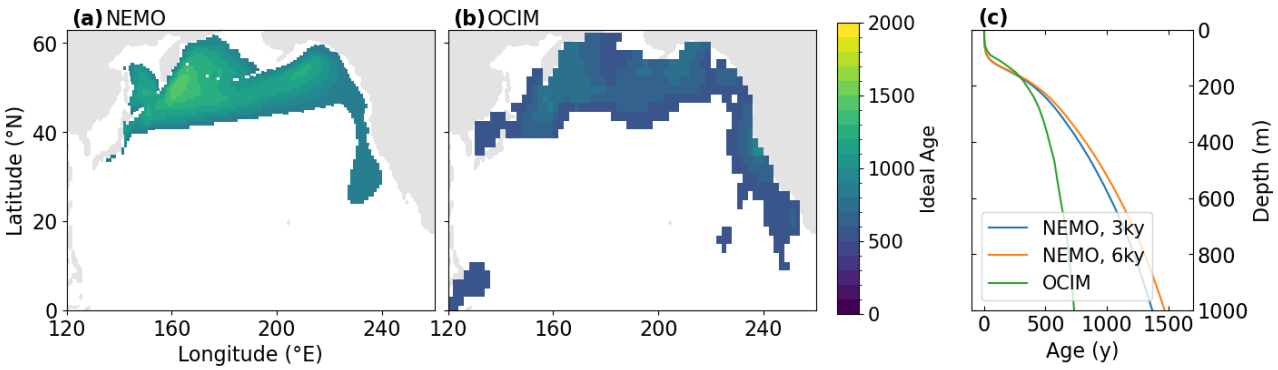

Figure 3.10: Maps of ideal age at 500 m depth in NEMO **(a)** and OCIM **(b)**, over the area where age exceeds 800 years and 500 years, respectively. The area of upwelling was defined as the area where the age is superior at 800y in NEMO and 500y in OCIM. Panel **(c)** shows the age profile averaged over these areas, in OCIM (green) and in REF after 3000 years (blue) and 6000 years (orange) of offline simulation.

Our understanding of the subarctic Pacific temperature and age biases in NEMO has improved but several questions remain. Regarding the temperature bias, an online simulation with the best up-to-date isopycnal mixing scheme would be welcome, to diagnose the impact on stratification and hydrography. Additionally, improving numerics influencing the representation of the Kuroshio current (e.g., Nasser et al., 2023) could reveal key in mitigating the simulated temperature bias. Such experiments could also bring additional information on the effect of the temperature bias on the age bias in the North Pacific: it is more difficult for waters to ascend if the stratification is too strong in the upper ocean.

The Pacific age bias of our NEMO experiments has not been addressed in this chapter. A detailed analysis of dynamics and numerics along the northern rim of the North Pacific would be a first step. Simulations with perturbed wind stress over the subpolar North Pacific or with a strengthened Pacific abyssal overturning could also shed light on likely factors underpinning the systematic overestimation of age in the deep ocean. Figure 3.10 illustrates the areas of deep water upwelling in OCIM and in the REF offline NEMO experiment, and shows age profiles averaged over this area. Upwelling areas, as defined here, are fairly similar in the two models (Figure 3.10a,b). The age profiles are, however, very different (Figure 3.10c). The age bias in NEMO is higher after 6000 years than after 3000 years, and it increases with depth. This suggests that the age bias may originate in the abyss and may progressively diffuse upward in the water column. Whether a lack of upwelling and/or a lack of abyssal overturning is to blame for the emergence of the bias remains unanswered.

BIBLIOGRAPHY

Ferrari, R., & Nikurashin, M. (2010). Suppression of eddy diffusivity across jets in the southern ocean. *Journal of Physical Oceanography*, *40*(7), 1501 –1519. https://doi.org/10.1175/2010JPO4278.1

Garabato, A. C. N., Leach, H., Allen, J. T., Pollard, R. T., & Strass, V. H. (2001). Mesoscale subduction at the antarctic polar front driven by baroclinic instability. *Journal of Physical Oceanography*, *31*(8), 2087 –2107. https://doi.org/10.1175/1520-0485(2001)031<2087:MSATAP>2.0.CO;2

Gouretski, V. (2019). A new global ocean hydrographic climatology. *Atmospheric and Oceanic Science Letters*, *12*(3), 226–229. https://doi.org/10.1080/16742834.2019.1588066

Gouretski, V., & Koltermann, K. P. (2004). Woce global hydrographic climatology. *Berichte des BSH*, *35*, 1–52.

Groeskamp, S., LaCasce, J., McDougall, T., & Roge, M. (2020). Full-depth global estimates of ocean mesoscale eddy mixing from observations and theory. *Geophysical Research Letters*, *47*(18). https://doi.org/10.1029/2020GL089425

Groeskamp, S., Sloyan, B. M., D., Z. J., & McDougall, T. J. (2017). Mixing inferred from an ocean climatology and surface fluxes. *Journal of Physical Oceanography*, *47*(3), 667 –687. https://doi.org/10.1175/JPO-D-16-0125.1

Hasunuma, K. (1978). Formation of the intermediate salinity minimum in the northwestern pacific ocean. *Bull. Ocean Res. Inst*, *9*, 47.

Nasser, A.-A., Madec, G., de Lavergne, C., Debreu, L., Lemarié, F., & Blayo, E. (2023). Sliding or stumbling on the staircase: Numerics of ocean circulation along piecewise-constant coastlines [e2022MS003594 2022MS003594]. *Journal of Advances in Modeling Earth Systems*, *15*(5), e2022MS003594. https://doi.org/10.1029/2022MS003594

Penduff, T., Le Sommer, J., Barnier, B., Treguier, A.-M., Molines, J.-M., & Madec, G. (2007). Influence of numerical schemes on current-topography interactions in 1/4°deg; global ocean simulations. *Ocean Science*, *3*(4), 509–524. https://doi.org/10.5194/os-3-509-2007

Sarmiento, J. L., Gruber, N., Brzezinski, M. A., & Dunne, J. P. (2004). High-latitude controls of thermocline nutrients and low latitude biological productivity. *Nature*, *427*(6969), 56–60. https://doi.org/10.1038/nature02127

Talley, L. D. (1993). Distribution and formation of north pacific intermediate water. *Journal of Physical Oceanography*, *23*(3), 517 –537. https://doi.org/10.1175/1520-0485(1993)023<0517:DAFONP>2.0.CO;2

Toggweiler, J., Druffel, E. R., Key, R., & Galbraith, E. D. (2019). Upwelling in the ocean basins north of the acc: 1. on the upwelling exposed by the surface distribution of Δ14c. *Journal of Geophysical Research: Oceans*, *124*(4), 2591–2608. https://doi.org/10.1029/2018JC014794

Toggweiler, J. R., & Samuels, B. The global carbon cycle (M. Heimann, Ed.). In: *The global carbon cycle* (M. Heimann, Ed.). Ed. by Heimann, M. Berlin: Springer, 1993, pp. 333–366.

Warren, B. A. (1983). Why is no deep water formed in the north pacific? *Journals of Marine Research*, *41*, 327–347. https://doi.org/10.1357/002224083788520207

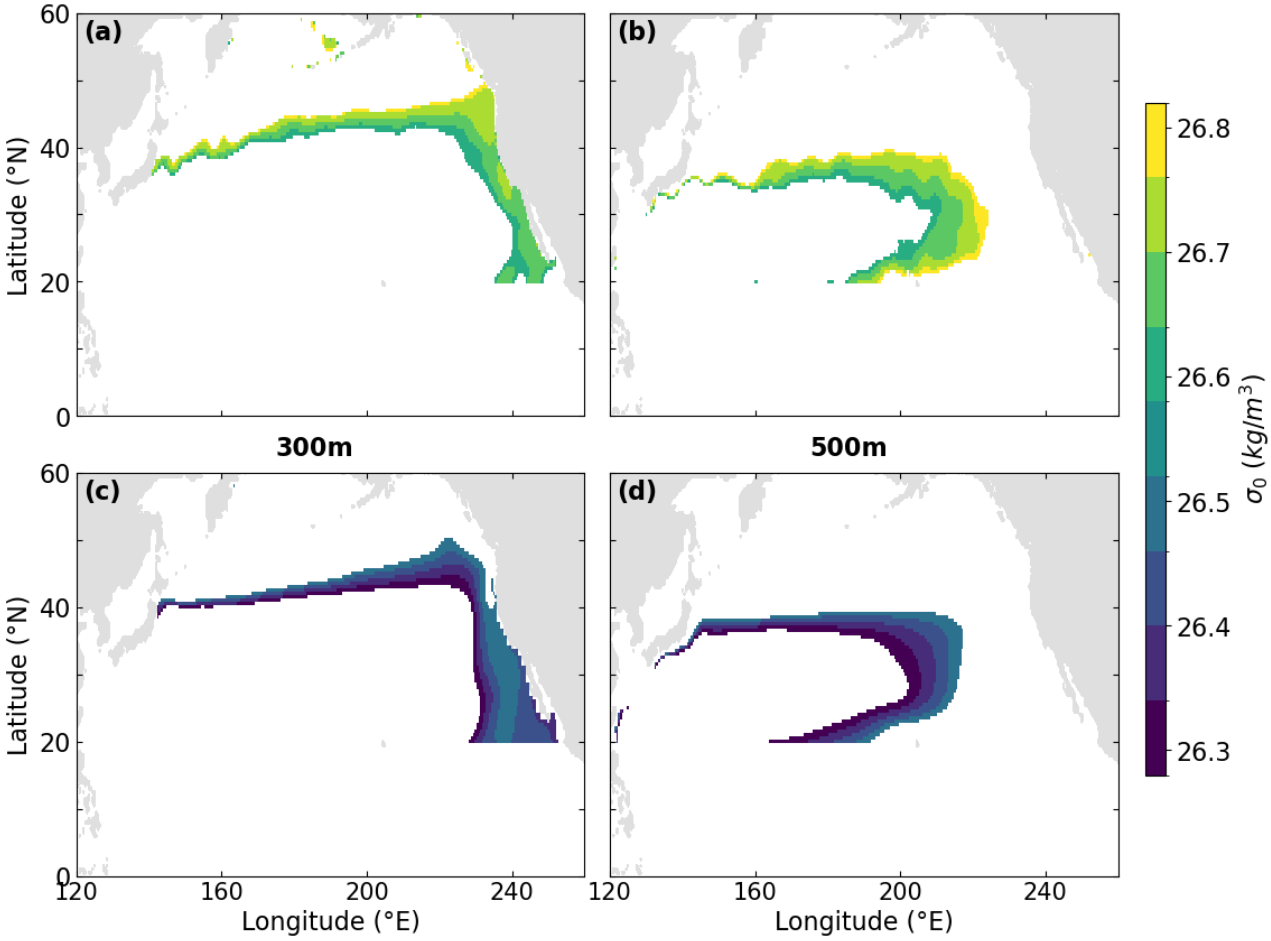

Figure S3.1: Maps at 300 m depth (first column) and 500 m depth (second column) showing the NPIW density σ_0, where NPIW is defined from neutral density in the WOCE climatology (first row) and as in 'NEMO best' (second row).

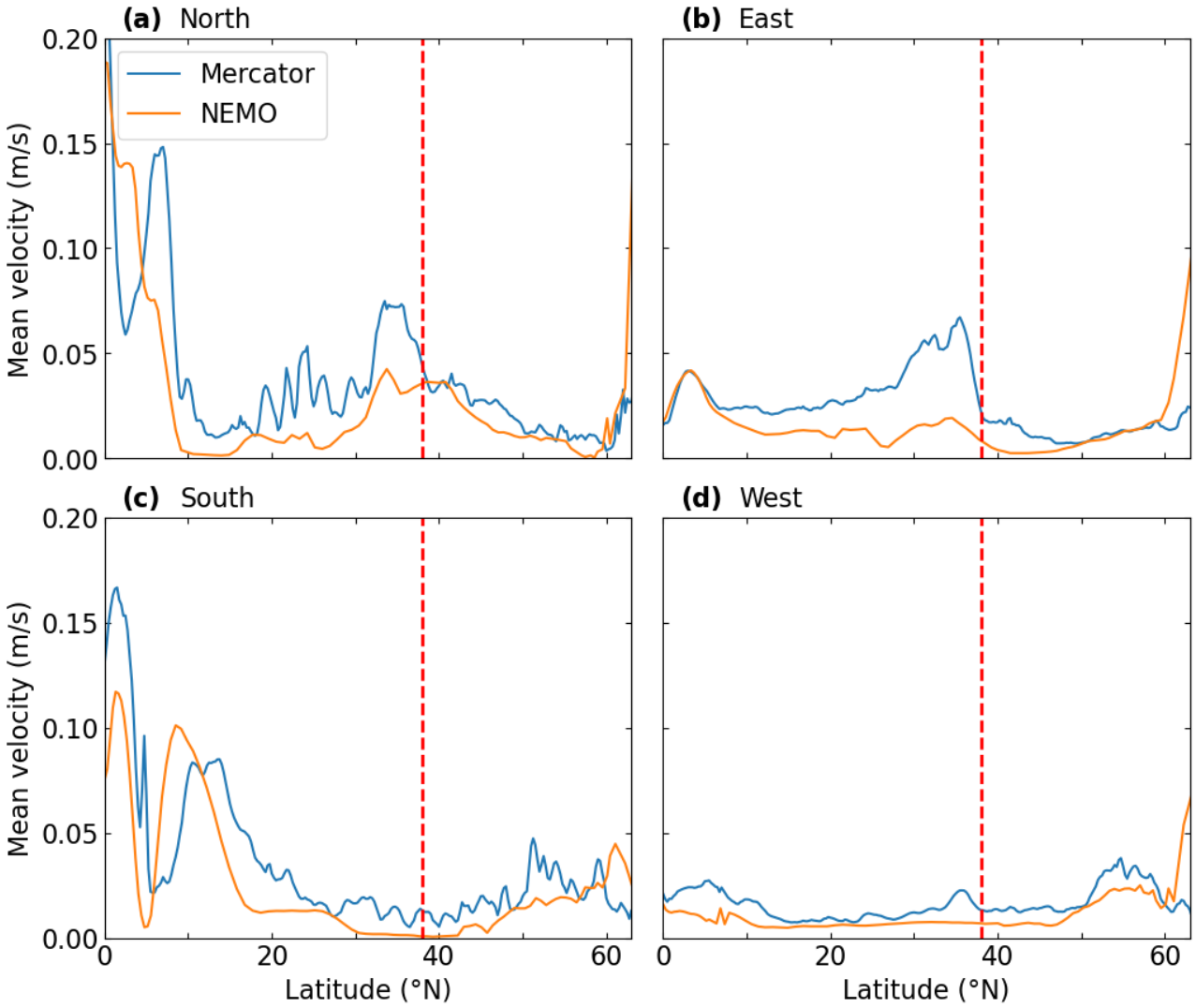

Figure S3.2: Figure showing the mean velocity averaged over the North Pacific as a function of latitude in each of the 4 cardinal directions: north **(a)**, east **(b)**, south **(c)**, and west **(d)**. On each panel the 38°N parallel was represented.

CHAPTER IV

THE OXYGEN ISOTOPE RATIO OF SEAWATER IN THE MODERN DEEP OCEAN: A CLEAR MARKER OF WATER ORIGIN?

In the Chapter II, we saw that the North Atlantic passive tracer progressively erodes as it travels farther away from the North Atlantic sector. A maximum in the vertical of its dye concentration is seen around the Southern Ocean at mid-depth (or mid-densities). Yet, uncertainties remain on the dilution and removal of this passive tracer across different models, and thus on the North Atlantic's role for ventilating the global ocean. Assessing the amount of North Atlantic waters ventilating the Southern Ocean and the other basins, could be key to quantify mixing of this water mass along its pathway.

Southern Ocean waters ventilated by the North Atlantic (NA) lie between freshly ventilated waters formed in the Southern Ocean: intermediate waters often referred as Antarctic Intermediate Water (AAIW) and the deep Antarctic Bottom Water (AABW) (cf ventilation desert in Figure 2.7 of Chapter II). Those waters circulate around the Southern Ocean and subsequently influence the Indian and Pacific Oceans (Chapter I). In Chapter II, models show that the presence of a mid-depth maximum of NA dye concentration in the Pacific is possible, yet its magnitude varies across the models. The sustained thesis is that the $\delta^{18}O_{sw}$ enrichment in the mid-depths of the Pacific, observed in Chapter I, is attributable to the influence of North Atlantic waters.

In this Chapter, I show the potential of $\delta^{18}O_{sw}$ to constrain ocean ventilation. I first show and discuss $\delta^{18}O_{sw}$ data that I produced during this thesis and that I compiled from various databases. In the mid-densities of the different ocean basins, a mid-depth $\delta^{18}O_{sw}$ can be observed that we attribute to the difference in the surface regions of the AABW and NADW ventilation regions. Then, we use the $\delta^{18}O_{sw}$ data compiled in the Southern Ocean and the OCIM-simulated dyes of Chapter II, to constrain end-member values for the different surface patches associated to the dyes. This results in a 3D gridded $\delta^{18}O_{sw}$ product which convincingly represents the structure of $\delta^{18}O_{sw}$ in the deep ocean. The discussion focuses on the

validation of this product by comparing it to the LeGrande and Schmidt (2006) $\delta^{18}O_{sw}$, and the data that we compiled. Finally, we discuss the potential of the $\delta^{18}O_{sw}$ to further constrain deep ocean ventilation, from individual datasets to the implementation of this tracer in inverse models.

1 . Introduction

Waters last ventilated in the Labrador and Nordic Seas, referred as NADW, flow and diffuse southward in the Atlantic before rejoining and upwelling in the Southern Ocean (Kuhlbrodt et al., 2007; Lumpkin and Speer, 2007; Schmitz Jr., 1995; Talley, 2013). They provide a key inflow for the formation of dense waters along the Antarctic margin, and a fraction of NADW is incorporated into the dense shelf waters cascade down the continental slope; this mixture is referred to as AABW (Anilkumar et al., 2021; Orsi et al., 1999; Silvano et al., 2023). Tamsitt et al. (2017) showed that the upwelling of NADW in the Southern Ocean occurred in a south-eastward direction. Using an idealized model, Jones and Abernathey (2019) links the amount of NADW upwelling and the strength of isopycnal mixing in the Southern Ocean. The inherent uncertainties associated to the parameterizations of mixing in the models thus limit our understanding of the fate of the NADW in the Southern Ocean.

The deep Pacific and Indian Ocean share similar ventilation patterns: an abyssal overturning cell and a south to north diffusion-dominated ventilation in the mid-depths (see Introduction; de Lavergne et al., 2017; Millet et al., 2023). Notable differences between the two basins include: (1) the Indian Ocean is overall shallower than the Pacific (the abyssal plains are narrower) (2) it is closer to the Atlantic Ocean, which means that the waters coming from the south that ventilate the Indian mid-depths may have a stronger Atlantic signature, (3) the Indian Ocean does not extend as far north as the Pacific, (4) the Indian is divided into many sub-basins, so that its abyssal circulation is quite complex (Huussen et al., 2012; Solodoch et al., 2022), and (5) a small advective portion of NADW gets through the Aghulas leakage (Talley, 2013).

The oxygen isotope ratio of seawater ($\delta^{18}O_{sw}$) is a conservative tracer, which means that it is only affected by mixing and advection, making it an ideal water mass tracer. The introduction of the thesis pointed out the difference in $\delta^{18}O_{sw}$ values for the NADW and AABW end-members, thus highlighting the potential of using $\delta^{18}O_{sw}$ to measure the influence of NADW versus AABW on modern ocean ventilation. This difference is due to the different mechanisms leading to water mass sinking in the North Atlantic and near Antarctica. NADW is ultimately derived from evaporated tropical waters (Talley, 2013), which make them enriched in $\delta^{18}O$, while AABW is depleted in $\delta^{18}O$, as it is formed largely by brine rejection and ocean-ice interactions in ice-shelf cavities (see Introduction; Schlosser et al., 1990; Weiss et al., 1979; Weppernig et al., 1996).

The sparsity and uneven distribution of the $\delta^{18}O_{sw}$ measurements (from dense to sparse sampling) between the surface and the deep ocean and between the Atlantic and Pacific basins makes it such that the structure of $\delta^{18}O_{sw}$ in the deep Pacific is very uncertain, especially given the deep gradient appears to be the lowest of all the ocean basins. Although uncertain, the observed mid-depth $\delta^{18}O_{sw}$ maximum within the Pacific does seem to be robust as it is present in multiple individual datasets (e.g. Herguera et al., 1992; Keigwin, 1998; McCave et al., 2008). Millet et al. (2023) used $\delta^{18}O_{sw}$, in conjunction with other conservative tracers, to show that the Pacific mid-depths are largely ventilated by isopycnal diffusion. Here we try to constrain the contribution of AABW vs NADW in the Southern, Indian and Pacific oceans, by compiling existing $\delta^{18}O_{sw}$ data. The compilation of $\delta^{18}O_{sw}$ measurements is made difficult by inter-laboratory offsets which leads to uncertainties in the absolute $\delta^{18}O_{sw}$ values of the deep ocean, and the impact of these offsets will be frequently commented on.

This study will try to reconstruct the path that the North Atlantic ventilated waters take once they leave the Atlantic for the Southern Ocean and measure the extent to which they influence other basins. We

will do so by using $\delta^{18}O_{sw}$, both data that we compiled, and new Pacific measurements that were made at the LOCEAN laboratory. In a second step, we will use the OCIM fractions presented in Chapter II to construct a deep $\delta^{18}O_{sw}$ product. This product will be compared to a $\delta^{18}O_{sw}$ product produced by OCIM using the LeGrande and Schmidt (2006) surface values that are being propagated in the model to the deep ocean, and the product from LeGrande and Schmidt (2006). This comparison will give us the opportunity to discuss in more depth the magnitude and extent of the $\delta^{18}O_{sw}$ mid-depth maximum in the Pacific. The new $\delta^{18}O_{sw}$ product will logically lead to a qualitative assessment of the OCIM fractions, and the $\delta^{18}O_{sw}$ product of LeGrande and Schmidt (2006).

2 . Methods

In this chapter we will represent the $\delta^{18}O_{sw}$ alternatively as a function of depth or density. This change in representation depends only on the basin where we represent the data. In the Southern Ocean, the isopycnals are strongly tilted in the meridional direction, which makes the depth coordinate less relevant, as water masses tend to follow isopycnals. In the Indian or Pacific Ocean, mid-depth isopycnals are largely level (de Lavergne et al., 2017), thus the representation along density is no longer necessary. An obvious parallel will be made between the mid-densities in the Southern Ocean and the mid-depths in the other basins.

2.1 . Measurements at LOCEAN

The $\delta^{18}O_{sw}$ in the deep Pacific ocean is largely under-sampled (166 data points in total for the deep Pacific and Indian oceans in LeGrande and Schmidt, 2006), which motivated the addition of new measurements. The samples measured were obtained by serendipity:

- The first samples originate from the SR-2113 cruise that sailed in 2021. It was a cruise of opportunity, and the sample collection for the analysis of the $\delta^{18}O_{sw}$ was not the aim of it, and the sample location is not ideal for our purposes.
- The second set of samples were collected in the GP15 cruise that sailed in 2018 which collected samples along the 152°W meridian. This cruise is one of the various legs of the GEOTRACES legs through the Pacific (specifically designed to look at the distribution of tracers in the ocean). The GP15 samples could not be analyzed after the cruise due to pandemic issues; when we decided to analyze them, they had been preserved in a fridge for 5 years in a non-optimal storage. Multiple GEOTRACES legs were supposed to be used for new $\delta^{18}O_{sw}$ measurements in this thesis but they eventually never materialised due to the COVID19 pandemic.

The location of the two stations measured from SR-2113 and the four stations measured from GP15, ranging from 0 to 32°N, are represented in Figure 4.1. Some of the samples measured were quality-controlled for possible evaporation using the 'd-excess' (Reverdin et al., 2022).

I made the measurements using a Picarro, in the LOCEAN laboratory, which is a cavity ring-down spectrometer which is exhaustively described in Reverdin et al. (2022). The measured standard deviation averaged across the samples is of 0.063‰ for $\delta^{18}O_{sw}$, and 0.28‰ for the δD. The data that we produced can be found on the latest version of the LOCEAN-CISE database (https://doi.org/10.5194/essd-14-2721-2022 SEANOE, 2023).

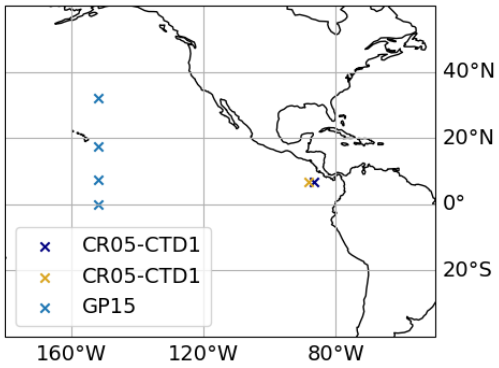

Figure 4.1: A map of the different stations that were measured at LOCEAN.

2.2 . Data compilation

Most of the data we use come from the GISS compilation and the datasets are accessible at: https://data.giss.nasa.gov/o18data/ (Schmidt et al., 1999). The data compiled in this database originates from different laboratories so it might be hard to compare absolute values due to inter-laboratory offsets. This is why most of the figures that we will show represent individual datasets and we will focus more on the shape of the profiles than on the absolute $\delta^{18}O_{sw}$ values.

Additionally, we will use $\delta^{18}O_{sw}$ data kindly provided by Helen Bostock from the TAN1302 cruise which occurred in 2013, and measured by Bass et al. (2014). The cruise was supported by the National Institute of Water and Atmospheric Reseach of New Zealand.

In the following, we will investigate different basins to look at the distribution of $\delta^{18}O_{sw}$. For practical purposes, we define the Southern Ocean as south of 40°S. We thus assume that waters to the north of 40°S belong either to the Atlantic (70°W-20°E), Indian (20°E-120°E) or Pacific basins (150°E-70°W), using natural boundaries between these.

3 . Results

First, we will present the different datasets that have been found in the GISS database, the data we produced at LOCEAN as well as data coming from collaborators. Secondly, we will use the OCIM product previously described (Chapter II), and the data presented, to construct a climatology of $\delta^{18}O_{sw}$. The quality assessment of this product will be made as a part of the discussion.

3.1 . Presentation of the $\delta^{18}O_{sw}$ data

The data that we will show in this part comes from different laboratories, which use different standards for their measurements; the isotopic data will thus have inter-laboratory offsets.

3.1.1 . Southern Ocean

The subset for the Southern Ocean ($lat \leq 40°S$) in the GISS database gives a compilation which contains 23 different individual datasets. Each dataset is uniquely identified by a specific combination of cruise and the laboratory where it was measured. Out of those 23 datasets, only 8 of them have isotope data spanning the density range of interest ($27 \leq \gamma \leq 28.6$) at a useful resolution and with acceptable variability. To select them the datasets were quality-checked visually and those that appeared overly noisy compared to the expected variability and typical analytical uncertainty were excluded. Based on their geographical dispersion we have subdivided some of the quality controlled datasets leading to 12 different datasets. Figure 4.2 shows those 12 profiles of $\delta^{18}O_{sw}$ plotted as a function of neutral density in the Southern Ocean, and a map representing the locations of these profiles. Neutral density for each bottle was computed using the climatology of Gouretski and Koltermann (2004), and interpolated at the bottle location. The numbering on Figure 4.2 has been done in such a way that the further we move southward and eastward away from the Atlantic sector, the greater the number, prioritizing in a first order the meridional displacement, and in a second order the zonal displacement.

All profiles in Figure 4.2 exhibit a local maximum in $\delta^{18}O_{sw}$ at mid-density ($27.93 \leq \gamma \leq 28.15$), associated with a maximum in salinity. The closer the dataset is to the Antarctica margin, the higher the density gets for the associated $\delta^{18}O_{sw}$ maximum ($1 \rightarrow 2 \rightarrow 4, 8 \rightarrow 7$). A similar variation can be observed in salinity, where the salinity associated to the $\delta^{18}O_{sw}$ maximum decreases as we get closer to Antarctica. The salinity highlights the impact of the North Atlantic in ventilating and setting up the $\delta^{18}O_{sw}$ maximum, most conspicuously in the datasets that are closest to the Atlantic sector, where we observe the highest salinity values (profiles 1, 2, 8). The compilation also shows an eastward decrease in the salinity associated to the $\delta^{18}O_{sw}$ maximum ($1 \rightarrow 8 \rightarrow 9 \rightarrow 12$). This decrease is consistent with the eastward decrease of the NA dye in the Southern Ocean seen in Chapter II, and probably signals the continuous mixing with AABW and AAIW that eventually leads to freshening of the North Atlantic-origin waters. The southward erosion of the salinity and higher associated density can be linked to gradual transformation during upwelling, including diffusive downwelling fluxes of fresher and lower $\delta^{18}O_{sw}$ surface water at densities $\gamma < 28$ (Naveira Garabato et al., 2017).

The map of the stations in Figure 4.2 clearly shows the uneven sampling of the Southern Ocean, with only a few stations measured in the Pacific sector. Dataset (12), that represents the Southern Ocean in the Pacific sector, is the only profile which does not display a clear mid-depth maximum. Nonetheless, this seems to be mainly due to the high isotopic signature of the intermediate waters at this location, as a gradient can still be observed between the mid and high densities, which represents the NADW/AABW contribution difference for the ventilation. In order to fill the gap in the GISS compilation between dataset (11) and (12), we present new data from Helen Bostock that were measured but never published (see Bass et al. (2014) for methodology). Figure 4.3, shows the stations which were selected, as well as their $\delta^{18}O_{sw}$. We selected only stations that have a maximum depth exceeding 3000m to avoid complex features near the Antarctic margin. The represented dataset displays a maximum in $\delta^{18}O_{sw}$ at a comparable density to those from the GISS database. The presence of this pronounced mid-density maximum in the $\delta^{18}O_{sw}$ so close to the Pacific sector, confirms the idea that waters last ventilated in the North Atlantic reach the Pacific sector of the Southern Ocean.

Waters last ventilated in the North Atlantic reach into the Southern Ocean, spiral and upwell in a southeastward direction (Tamsitt et al., 2017), so that most reach the near-surface or Antarctic margins

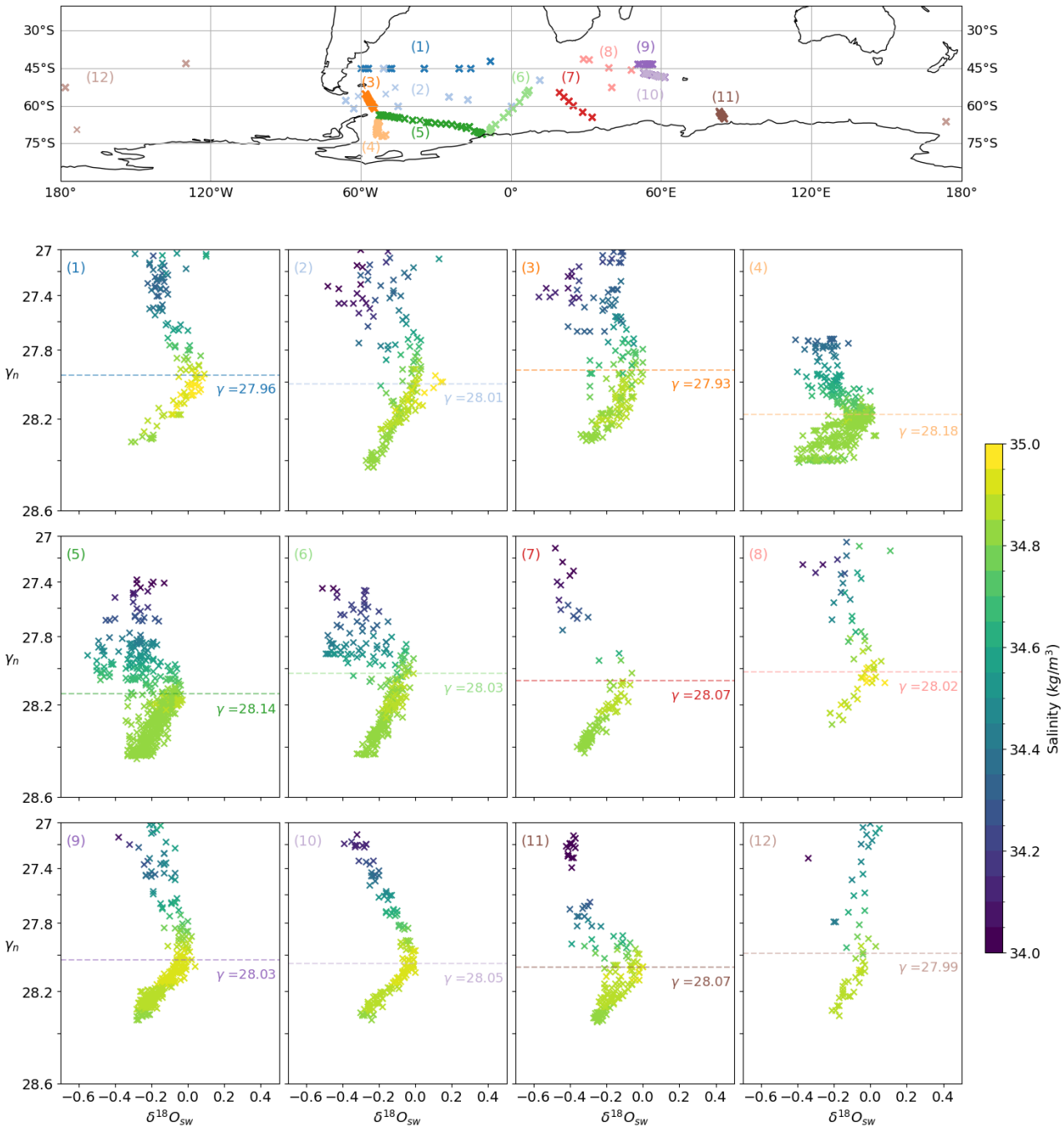

Figure 4.2: The top panel displays the geographical distribution of our 12 datasets in the Southern Ocean, found from the GISS database. For each numbered dataset, we then show measured $\delta^{18}O_{sw}$ as a function of neutral density in the lower set of panels. The dataset number is given in the top-left corner of each panel, and the shading shows salinity. The dashed horizontal line in each panel marks the density where $\delta^{18}O_{sw}$ peaks.

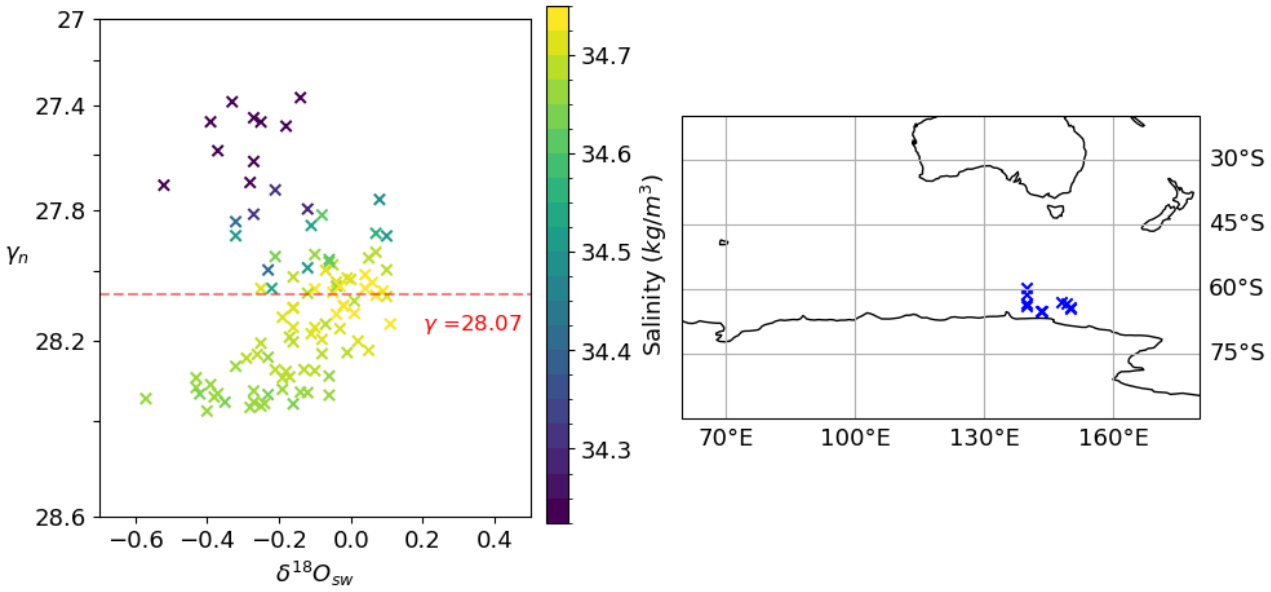

Figure 4.3: $\delta^{18}O_{sw}$ profile of the stations near the Antarctic margin shared by Helen Bostock (left) and the associated map of the measured bottles (right).

west of Drake Passage (DP). As such, datasets (2) and (3) from our Southern Ocean compilation yield some interesting information. The dataset (2) includes both stations sampled within the Drake Passage and stations sampled in the Atlantic sector of the Southern Ocean. As these locations may not represent the same bodies of water, we have separated them in Figure 4.4, where dataset (3) is also represented. The waters in the Drake Passage (panels (3) and (2) DP) show a slight mid-density $\delta^{18}O_{sw}$ maximum. This maximum advocates for the persistence of the NA dye (or waters being ventilated by the NA), throughout the circumpolar current. In the other panel, dataset (2) Atl represents the Atlantic sector, and we observe the high salinity-heavy $\delta^{18}O_{sw}$ signal at mid-densities typical of the NADW. One can also note that the density at which the $\delta^{18}O_{sw}$ maximum is present in the DP is around 27.93, within the density range of UCDW and matching the $\delta^{18}O_{sw}$ maximum in the Pacific in Chapter I.

Therefore, it would seem that the influence of the North Atlantic for the ventilation of deep waters can be observed all around the Southern Ocean. The next step is thus to look at the influence of the North Atlantic on the other basins, which occurs via the Southern Ocean, the cross-roads of the World Ocean.

3.1.2 . Indian Ocean

The basin next influenced by waters last ventilated in the North Atlantic is the Indian Ocean. In Chapter II, we mainly focused the discussion on the NA dye diffusion in both the Southern and Pacific Oceans, leaving the Indian out. Figure 4.5 shows the zonal mean of the NA dye from the 3 previously studied models (NEMO, OCIM, TMI) averaged over the Indian Ocean. All 3 models show a maximum in the NA dye at mid-depth, in contrast to the Pacific where TMI did not. For NEMO and OCIM the mid-depth maximum of the NA dye is stronger in the Indian basin than in the Pacific. This may be due to two factors: (i) a direct advective transport of NADW near the Aghulas (Talley, 2013), (ii) erosion of the NA dye as it moves away from the Atlantic. For OCIM, the maximum extends up to the northern boundary of the basin, again contrasting

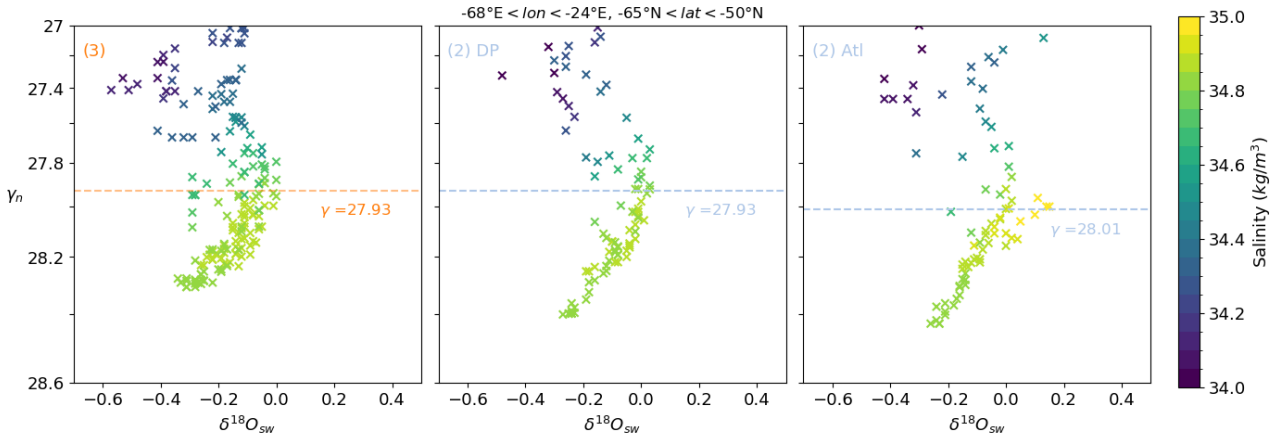

Figure 4.4: Figure showing dataset (3) and (2), from Figure 4.2. Dataset 2 was separated into an Atlantic sector, *(2) Atl*, and a Drake Passage sector, *(2) DP*.

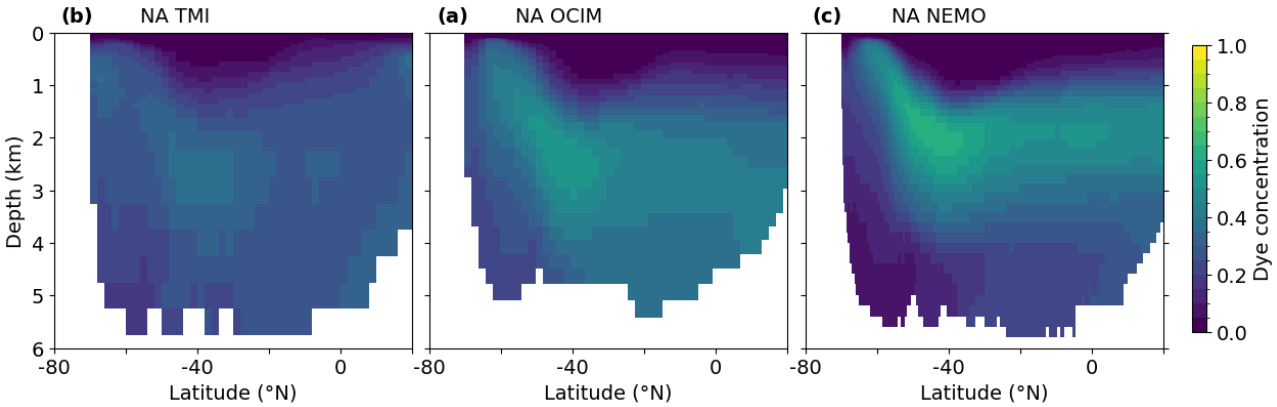

Figure 4.5: Zonal mean over the Indian Ocean of the NA dye in TMI **(a)**, OCIM **(b)** and NEMO **(c)**.

with the Pacific. The 3 models show the major role of the NA dye in ventilating the deep Indian Ocean (> 1km) as they contribute to 40, 38 and 29% respectively in NEMO, OCIM and TMI; and especially for the mid-depths ($1.5 \leq depth \leq 3$km) as this contribution reaches up to 50, 42, and 31 %. The NA influence decreases as waters diffuse northward. As a consequence of the deep NA dye structure in the Indian Ocean, we expect a maximum for $\delta^{18}O_{sw}$ in the mid-depths that decreases as we move away from the Southern Ocean.

Figure 4.6 shows the two datasets in the GISS database (Schmidt et al., 1999) that we found suitable to represent the deep Indian Ocean: one near Madagascar around 30°S and another one that has multiple stations across the Indian Ocean. The first dataset originates from the same study as Southern Ocean dataset (9) from Figure 4.2 previously shown, and we represent it with dataset (9) as well on Figure 4.6.(1). It shows the equivalence of displaying the profile in depth-space or density-space for the Indian Ocean, and it also shows the meridional decrease of the $\delta^{18}O_{sw}$ maximum. Indeed, dataset (1) shows a mid-depth maximum relative to the abyss that is weaker than for dataset (9) which is located about 15° (1600 km)

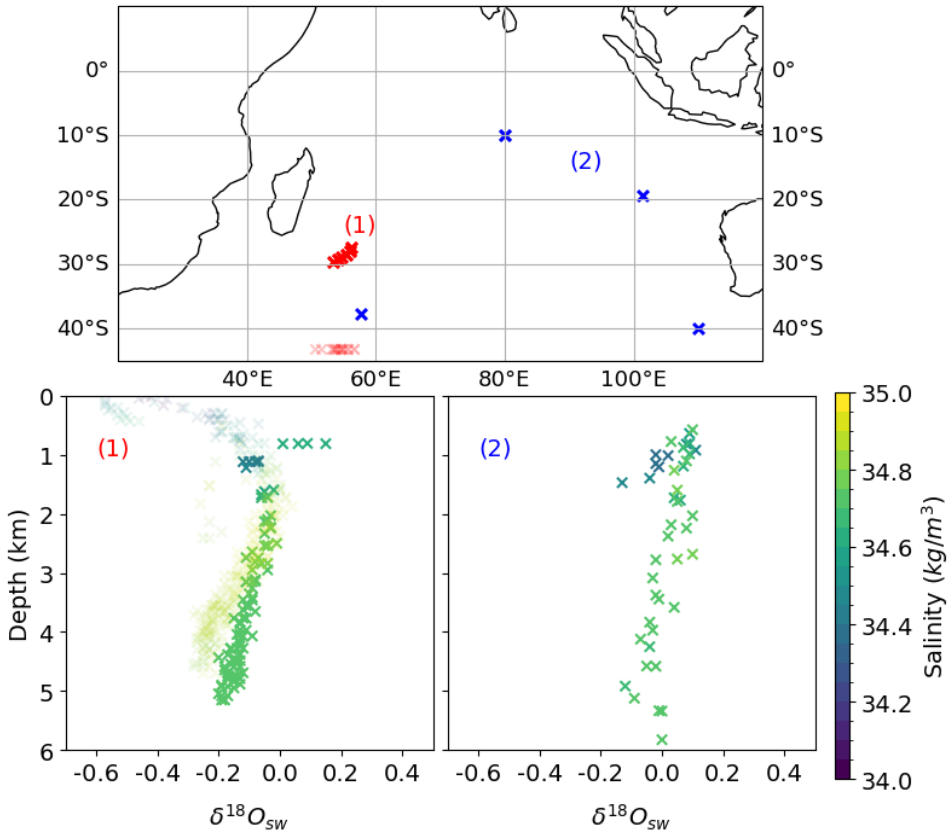

Figure 4.6: The top panel represent the geographical distribution of the 2 datasets in the Indian Ocean, extracted from the GISS database. For each numbered dataset, we then show measured $\delta^{18}O_{sw}$ as a function of neutral density in the lower set of panels. The dataset number is given in the top-left corner of each panel, and the shading shows salinity. The transparent data points in panel (1), and on the map, represent data from the Dataset (9) of the Southern Ocean compilation, which originates from the same lab.

southward. The northward reduction of the difference between the abyss and the mid-depth presumably reflects vertical mixing. Above 1.5km, the isotope values show different water masses: AAIW with light $\delta^{18}O_{sw}$ and low salinity in the south, and intermediate waters which are saltier and heavier in $\delta^{18}O_{sw}$ further north, where they are influenced by low latitude waters (Figure 4.6, intermediate depths of the left panel). Additionally, high-salinity waters coming from the Persian Gulf spread southward in the basin influencing the upper km of the Indian Ocean. The influence of those heavy $\delta^{18}O_{sw}$ waters is not visible in dataset (9).

The second dataset does not show a clear pattern in the upper part of the water column due to the spatial dispersion of the dataset resulting in different intermediate waters at the stations. Nonetheless, the $\delta^{18}O_{sw}$ gradient between the abyss and the mid-depth persists. The Indian Ocean thus presents an isotope maximum at mid-depths, with a northward decrease in its maximum value. This reduction is likely due to vertical mixing which erodes tracer maxima.

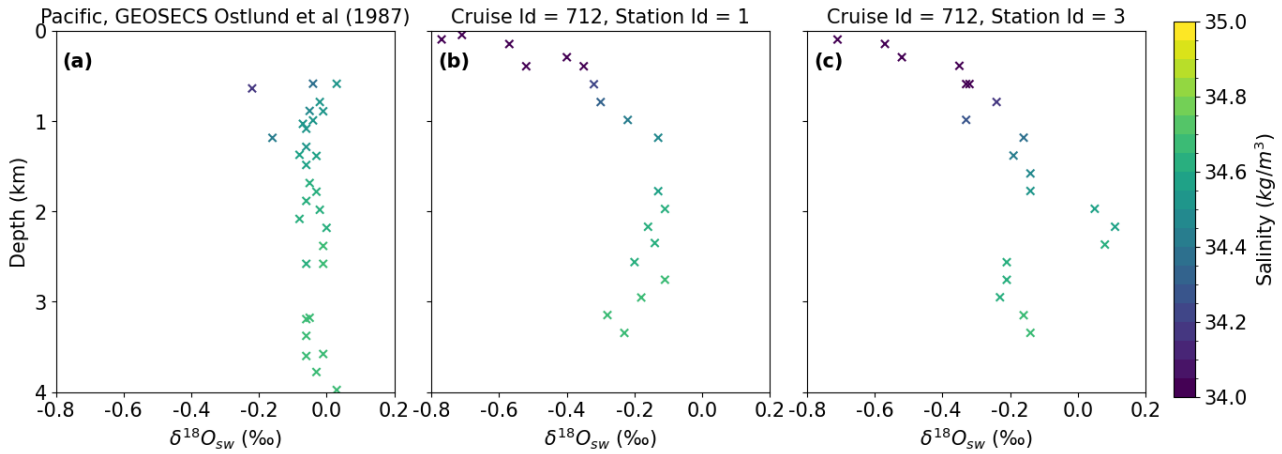

Figure 4.7: Figure representing the Pacific profiles that were found in GISS **(a)** and two stations from Glodap **(b)**, **(c)**. The stations coordinates of the Glodap profiles are 43.99°N and 153.51°E **(b)** and 44.99°N and 152.81°E **(c)**.

3.1.3 . Pacific

As the Pacific is located farther away from the Atlantic Ocean (in terms of the major flow path of deepwaters), one can wonder to what degree and manner it is impacted by NA waters. Figure 4.7 represents three datasets that contain $\delta^{18}O_{sw}$ data found in the North Pacific in the GISS dataset **(a)**, and in Glodap (Key et al., 2015; Olsen et al., 2016) **(b)** and **(c)** near the Kamchatka trench. Here the $\delta^{18}O_{sw}$ mid-depth maximum relative to the abyss is less evident than in the other basins, as the expected signal becomes close to analytical uncertainties. Hence, more data is required to resolve the expected signals within the analytical noise (yet there is less data compared to the other basins). It is hard to know if the mid-depth enrichment relative to the abyss observed in (b) and (c) is due to the diffusion of NA ventilated waters from the south, analytical noise, or possibly some influence of intermediate waters with high $\delta^{18}O_{sw}$. In order to try and resolve this issue, we decided to measure some more oxygen isotope data.

Figure 4.8 shows the $\delta^{18}O_{sw}$ data generated for this study. The two stations measured near Cocco's Ridge are represented on the same panel, given their geographical (see Figure 4.1) and $\delta^{18}O_{sw}$ values proximity. The errorbars on the Figure represent the standard deviation of the Picarro associated to each measurement. A clear gradient between the abyss and the mid-depth cannot be seen: any signal would be masked out by the uncertainties associated to the measurement. However, the trend in the data suggests a possible enrichment between 2-3km relative to the underlying waters. It is noteworthy to point out that the densest waters of the ocean (AABW, $\gamma \geq 28.11$) do not flow into the East Pacific (east of the East Pacific Rise, see Extended Data, Figure 1 de Lavergne et al., 2017), which could cause higher $\delta^{18}O_{sw}$ bottom waters there than in the other basins. The East Pacific being shallower than the main Pacific basin could also explain a faster northward erosion of the $\delta^{18}O_{sw}$ maximum: the depth-distribution of the seafloor in this region can be expected to produce more mixing between abyssal and mid-depth waters.

The second set of data Figure 4.8b represents stations that were collected during the GP15 cruise (see Figure 4.1). Stations to the south and north of the represented stations were measured in Calstate Sacramento. Replicate measurements to compare laboratories were measured in LOCEAN and suggested

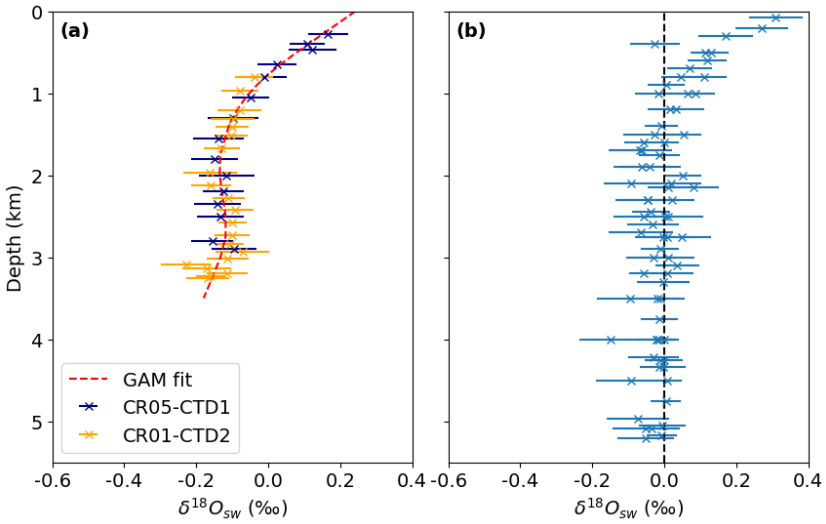

Figure 4.8: Figure representing $\delta^{18}O_{sw}$ data that were produced near Cocco's Ridge **(a)**, and along the 152°W meridian **(b)**. In **(a)**, the different stations measured were highlighted by using different colors, and a GAM fit was passed through the data. In **(b)**, a dashed lines was plotted at zero to show the relative enrichment of the $\delta^{18}O_{sw}$ in the mid-depths.

major issues with the measurements done in Sacramento; the measurements made in Sacramento were thus considered too unreliable to be used. Sadly, the unavailability of a complete north-south transect of $\delta^{18}O_{sw}$ from the Pacific weakened the initial idea of following the decay of the mid-depth maximum in the Pacific. A more detailed description of the differences between the two methodologies (Calstate, Sacramento and LOCEAN, Paris) as well as the subsequent analysis can be found in the Supplementary Information. Like in Figure 4.8a, no clear gradient is observed; nonetheless, more positive values are observed in the mid-depths relative to the abyss. Although not statistically significant this result points to a potential $\delta^{18}O_{sw}$ maximum in the East Pacific mid-depths. Together, given the spatial sampling and analytical noise, the new data remain inconclusive as to the existence of a mid-depth $\delta^{18}O_{sw}$ maximum in the main Pacific basin.

3.2 . Reconstruction of the $\delta^{18}O_{sw}$ with OCIM fractions

Our $\delta^{18}O_{sw}$ compilation allowed us to show the persistence of the North Atlantic ventilated waters across the Southern Ocean and its incursion in the Indian Ocean. The magnitude of the incursion in the Indian and Pacific Oceans can still be questioned however. In this part, we will use the inverse model OCIM and our $\delta^{18}O_{sw}$ compilation to constrain the deep $\delta^{18}O_{sw}$ structure. We are going to study two different products: one that propagates the surface ocean $\delta^{18}O_{sw}$ product of LeGrande and Schmidt (2006) directly with OCIM, and a second one that we will construct from the fractions studied in Chapter II and that we call RECONS.

3.2.1 . OCIM $\delta^{18}O_{sw}$ product

The product of LeGrande and Schmidt (2006), hereafter referred as the LS product, was made using salinity-$\delta^{18}O_{sw}$ relationships for different end-members. This product is more accurate at the surface than in the deep ocean, due to the low data density in the latter. OCIM can be used to map the surface origin of any interior ocean grid point; that is, it allows quantify the volume contribution of each surface grid point to every interior ocean grid cell (Holzer et al., 2021). Coupled with the surface $\delta^{18}O_{sw}$ from the LS product, OCIM can thus produce an estimated 3D gridded field of $\delta^{18}O_{sw}$ in the ocean, that we call OCIM-LS. We will use the previously shown $\delta^{18}O_{sw}$ data compilation to assess the quality of such a reconstruction.

The Southern Ocean is the ideal basin to study the $\delta^{18}O_{sw}$ reconstruction, as major deep ocean water masses can all be found there (see Chapter II). Figure 4.9 displays the 12 compiled datasets for the Southern Ocean and the OCIM-LS values associated to the samples locations of each dataset. The reconstruction appears to be acceptable at first order: the structure is overall correct, it reproduces roughly the shape of the profile, and the values are about the same as the original data. However, one pattern stands out: the $\delta^{18}O_{sw}$ mid-density maximum is not pronounced enough and the densest waters have an isotopic signature that is too heavy. Hence, the $\delta^{18}O_{sw}$ gradient between the mid and high densities is too small in the OCIM reconstruction. This bias may be caused by (1) inaccuracy of OCIM-predicted ventilation, with an over-estimation (respectively under-estimation) of AABW (respectively NADW) in the mid-densities of the Southern Ocean, and reversely at high densities, (2) the surface $\delta^{18}O_{sw}$ values used as end-members being incorrect, or (3) processes such as subsurface glacial meltwater input that are not captured by the OCIM-LS reconstruction. From here on, we will assume that the ventilation patterns of OCIM are correct and investigate hypothesis (2). Hypothesis (3) will be a part of the discussion. Finally, in the conclusions we emphasize that the $\delta^{18}O_{sw}$ might be used to further constrain the ventilation of inverse models.

3.2.2 . Reconstructing the deep $\delta^{18}O_{sw}$ structure

In order to test the hypothesis in which the surface $\delta^{18}O_{sw}$ values are the primary cause of the bias we devise a method to modify and optimize end-member values using the surface patch water fractions detailed in Chapter II. This method therefore reduces the precision of OCIM's ventilation, since only 5 patches are used to constrain it. Our reconstructed product aims at correctly representing the deep (or dense) waters $\delta^{18}O_{sw}$ variability, and the end-member values found are designed to correctly represent the $\delta^{18}O_{sw}$ signatures of the different deep water masses rather than surface end-member values. Such differences are expected given the relevance of sub-surface processes in setting the $\delta^{18}O_{sw}$ of water masses (discussed later). Here, the LL and MS patches of Chapter II are combined into a single patch referred to as LLH.

Before reconstructing the deep $\delta^{18}O_{sw}$ profile with the computed fractions of OCIM, we need to verify first that a reconstruction using a single end-member value for those large surface patches (which in reality are definitely not homogeneous) is sufficient to represent the deep $\delta^{18}O_{sw}$ variability. In order to test this, we use the previously presented OCIM-LS reconstruction ($\delta^{18}O_p$), to investigate if we can roughly reconstruct its deep structure with the OCIM fractions (f_i) and associated end-member values ($\delta^{18}O_{sw}(i)$) so that we have: $\delta^{18}O_p \approx \sum_i f_i \times \delta^{18}O_{sw}(i)$.

Figure 4.10 shows the reconstructed profiles with the 5 dyes and the $\delta^{18}O_{sw}$ of OCIM, at 3 different locations; one in the Atlantic near the Southern Ocean, another in the North Pacific, and one in the Southern Ocean. The $\delta^{18}O_{sw}$ values of the different surface patches, referenced in Table 1, were manually found so that the deep structure of the various profiles would be correct. An optimization to find the best

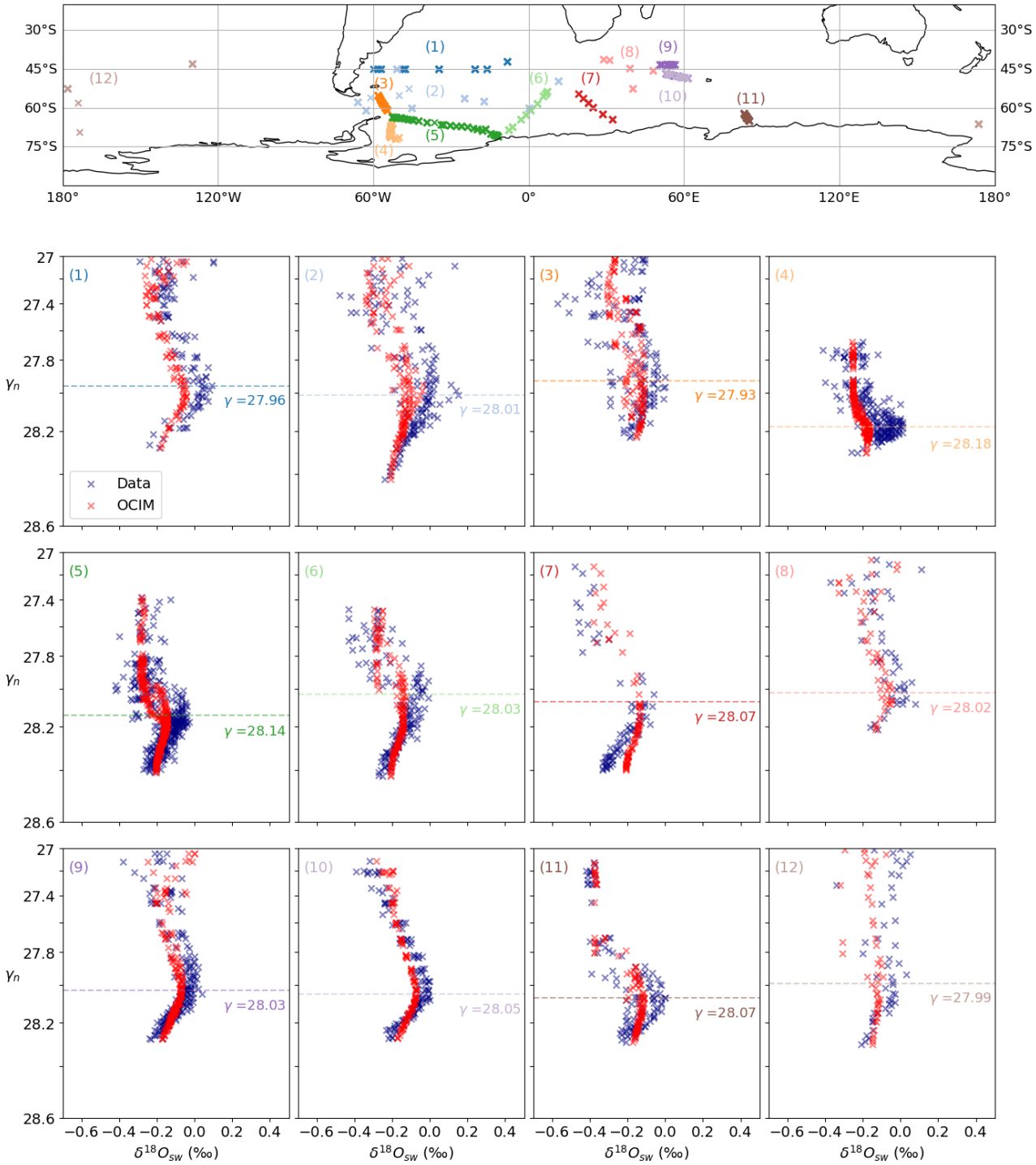

Figure 4.9: Figure representing the data compiled and first showed in Figure 4.2. The colouring based on salinity was removed from this figure and we instead show in red the $\delta^{18}O_{sw}$ predicted by the OCIM-LS reconstruction at the measurement locations.

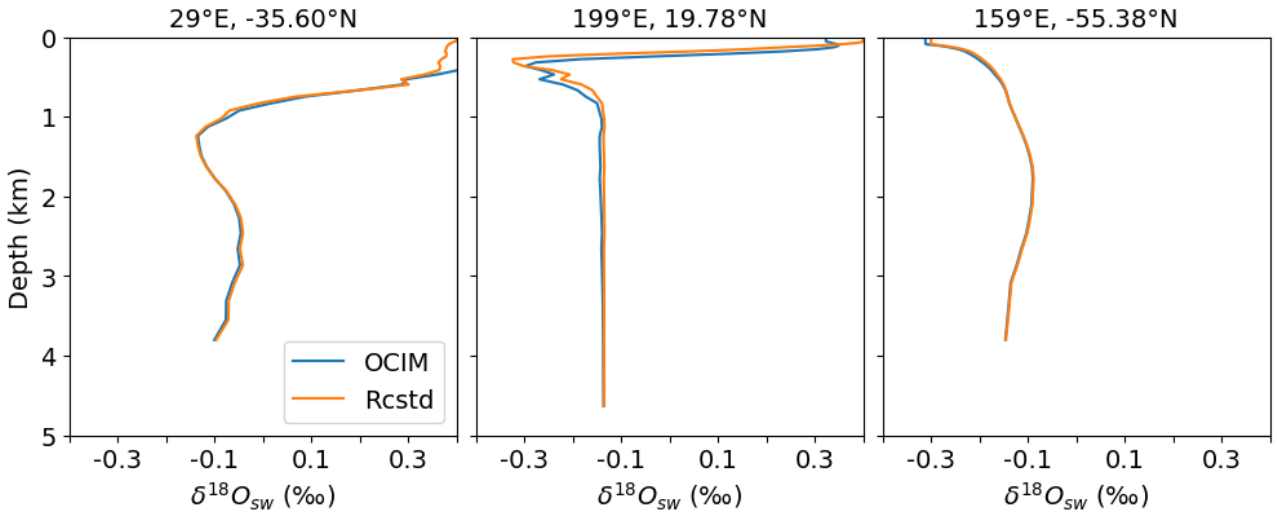

Figure 4.10: Figure representing 3 different $\delta^{18}O_{sw}$ profiles that represent different locations, South Atlantic (left), North Pacific (middle) and in the Southern Ocean (right). Each panel show the $\delta^{18}O_{sw}$ depth profile of the OCIM product (blue) and the associated reconstructed profile using 5 surface patches and end-member values referenced in Table 1.

End-member	AA	HS	NP	NA	LLH
$\delta^{18}O_{sw}$ OCIM	-0.3	-0.3	-0.35	0.08	0.4
$\delta^{18}O_{sw}$ mean optimization	-0.45	-0.29	***	0.31	***

Table 1: Table referencing the values that were manually selected to correctly reconstruct the $\delta^{18}O_{sw}$ product of OCIM with only 5 surface patches, and the end-member $\delta^{18}O_{sw}$ values found from our optimization.

values was not made here, because of the complexity of representing the whole world ocean by 5 surface patches, but it should give a result somewhat similar. The values of $\delta^{18}O_{sw}$ for the NP and LLH surface patches are not so relevant as their influence on deep ventilation is small. The conclusion from this simple reconstruction is that the deep $\delta^{18}O_{sw}$ from OCIM-LS can be theoretically reconstructed using 5 fractions and their associated $\delta^{18}O_{sw}$ surface patch values. However, our reconstruction has limits, as the signal in the shallow and intermediate depths will be badly reconstructed, since more complex processes with a higher degree of spatial variability affect them.

Now we will use our Southern Ocean $\delta^{18}O_{sw}$ compilation, to constrain the $\delta^{18}O_{sw}$ surface values of the 5 patches. For each dataset, we try to minimize the difference between the measured $\delta^{18}O_{sw}$ ($\delta^{18}O_{sw}(meas)$) and the reconstructed $\delta^{18}O_{sw}$ which is computed with the OCIM fractions at the measurement location ($f_{i,meas}$) and the $\delta^{18}O_{sw}$ surface patches values ($\delta^{18}O_{sw}(i)$). Our variables are thus the 5 $\delta^{18}O_{sw}(i)$ values and are found by using the *scipy.optimize* function in python that minimize the following:

$$min \left| \sum_{meas} \delta^{18}O_{sw}(meas) - \left(\sum_{i=1}^{5} f_{i,meas} \times \delta^{18}O_{sw}(i) \right) \right| \quad \text{(IV.1)}$$

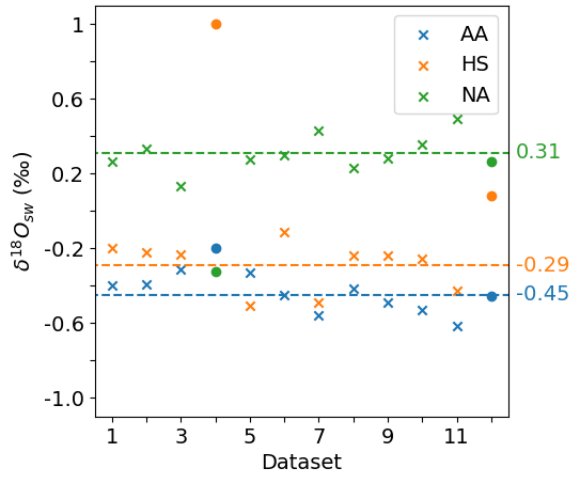

Figure 4.11: Figure representing the different end-member values that were found using our optimization for the 12 datasets compiled in the Southern Ocean. The number of the dataset on the x-axis refers to the numbers in the top-left of the panels of Figure 4.2.

The obtained averaged values are referenced in Table 1. LLH and NP $\delta^{18}O_{sw}$ values are not referenced as they have little impact on the dense-water structure of our Southern Ocean compilation, and the obtained values hold little interest. The surface and subsurface patterns are not meant to be captured by our reconstruction, so in order to compute the surface patch values, bottles that were collected shallower than 150m were left out of the optimization. In addition, we set bounds of (-1, 1) for the $\delta^{18}O_{sw}$ surface patches values, so that the surface patches associated to low fractions (LLH and NP) do not over-impact our optimization. The optimization was performed independently for each dataset, so that our optimization is not affected by potential laboratory offsets.

Figure 4.11 shows the $\delta^{18}O_{sw}$ end-member values obtained for each dataset; the average values over the datasets for each surface patch are represented by dashed lines. Datasets (4) and (12) display some anomalies with respect to the other datasets, so they were left out of the computed average. The optimization gave around the same results for NADW and AABW in Dataset (12), but AAIW exhibited a signal which is too heavy in comparison to the other datasets, as such we do not include it in the average. The standard deviation associated with the 3 averages is of ~ 0.1‰ which seems reasonable (considering lab offsets and the actual differences that can be expected from different sites).

Figure 4.12 shows the Southern Ocean in situ data previously presented that we use to find the surface end-member $\delta^{18}O_{sw}$ values. Furthermore, in each panel, we also represent two reconstructions using the OCIM fractions: one that uses the $\delta^{18}O_{sw}$ end-member values found for each dataset respectively (orange) and another one that uses the average of the end-member values (red) referenced in Table 1. The first reconstruction, which uses the end-member values found for each dataset is thus changing from panel to panel, depending on the end-member values found for each optimization which are represented in Figure 4.11. The reconstruction obtained by using the average of the end-member values is referred to as RECONS. On top of each panel of Figure 4.12, we indicate the root-mean-square error associated to the two reconstructions (that are differentiated by their color). Necessarily, the error is lower for the reconstruction using the end-members found for each dataset rather than the average. Nonetheless, for most datasets the difference

between the two reconstructions is relatively small, and it seems that for most datasets, much of the difference could be explained by a constant offset, potentially originating from inter-laboratory offsets.

The RECONS reconstruction correctly represents the $\delta^{18}O_{sw}$ maximum at mid-densities and the gradient with the abyss seen in the in situ data. The highest variability is observed in the less dense waters, as different intermediate waters may lead to different $\delta^{18}O_{sw}$ values. Overall, we deem that our $\delta^{18}O_{sw}$ reconstructed product is convincing enough in the Southern Ocean, so we look at other basins to verify that our reconstruction extends well in other basins.

Figure 4.13 represents the data (depth $\geq 150m$) that we found for the Indian Ocean as well as the data in the Southern Ocean from Helen Bostock, and the associated maps of the stations. The quality of the reconstruction varies across the 3 datasets: (1) is almost exactly similar to the original data, (2) is badly reconstructed but it would seem that a constant offset between the reconstruction and the original data would be sufficient to explain most of the deviation. Finally, (3) seem to have the overall same structure, but the original data variability is much larger. This does not come as a surprise since we do not expect a 2-degree-resolution inverse model and our simple reconstruction to correctly represent the complexity of the observed signals near Antarctica. Furthermore, instrumental noise and uncertainties associated to the measurements will obviously not be represented by our reconstruction. Overall, the RECONS product seems to agree rather well with the data, which gives us confidence in our reconstruction so that we in turn look at the Pacific basin.

We show the zonal mean of the original $\delta^{18}O_{sw}$ OCIM product, the LS product, and our reconstruction RECONS in Figure 4.14. The OCIM product and the reconstructed product with the average end-members show overall similar structure in the Pacific as tehy derive from similar ventilation patterns. Relative to the OCIM-LS product, RECONS presents a larger gradient between the abyss and the mid-densities in both the Southern Ocean and in the main Pacific. However, the $\delta^{18}O_{sw}$ mid-depth maximum remains much less pronounced in RECONS than in the LS product (Figure 4.14b,c).

It is noteworthy that the HS and AA dye diffuse more in the Indian and Pacific mid-depths, in OCIM than they do in NEMO (Chapter II). This diffusion tend to suppress the potential maximum associated to the NA dye diffusion in the mid-depths. Consistent measurements from the Southern Ocean up to the North Pacific and across the Southern Ocean could provide useful constraints on the amount of waters last ventilated in the North Atlantic in those basins. Furthermore, the intermediate waters of the dataset (12) from Figure 4.2, seem to be heavier in $\delta^{18}O_{sw}$ than the other datasets, potentially linked to a different water mass, but which could contribute to a mid-depth maximum diffusion in the Pacific.

The foregoing analysis leads to different questions, that we will adress in the discussion:

- How confident are we about the surface end-member values used for our $\delta^{18}O_{sw}$ reconstruction?
- How does our product compare to the two previous products in other basins? What could be done to improve it further?
- Where would new measurements of $\delta^{18}O_{sw}$ be most useful to further constrain global ocean ventilation?

4 . Discussion

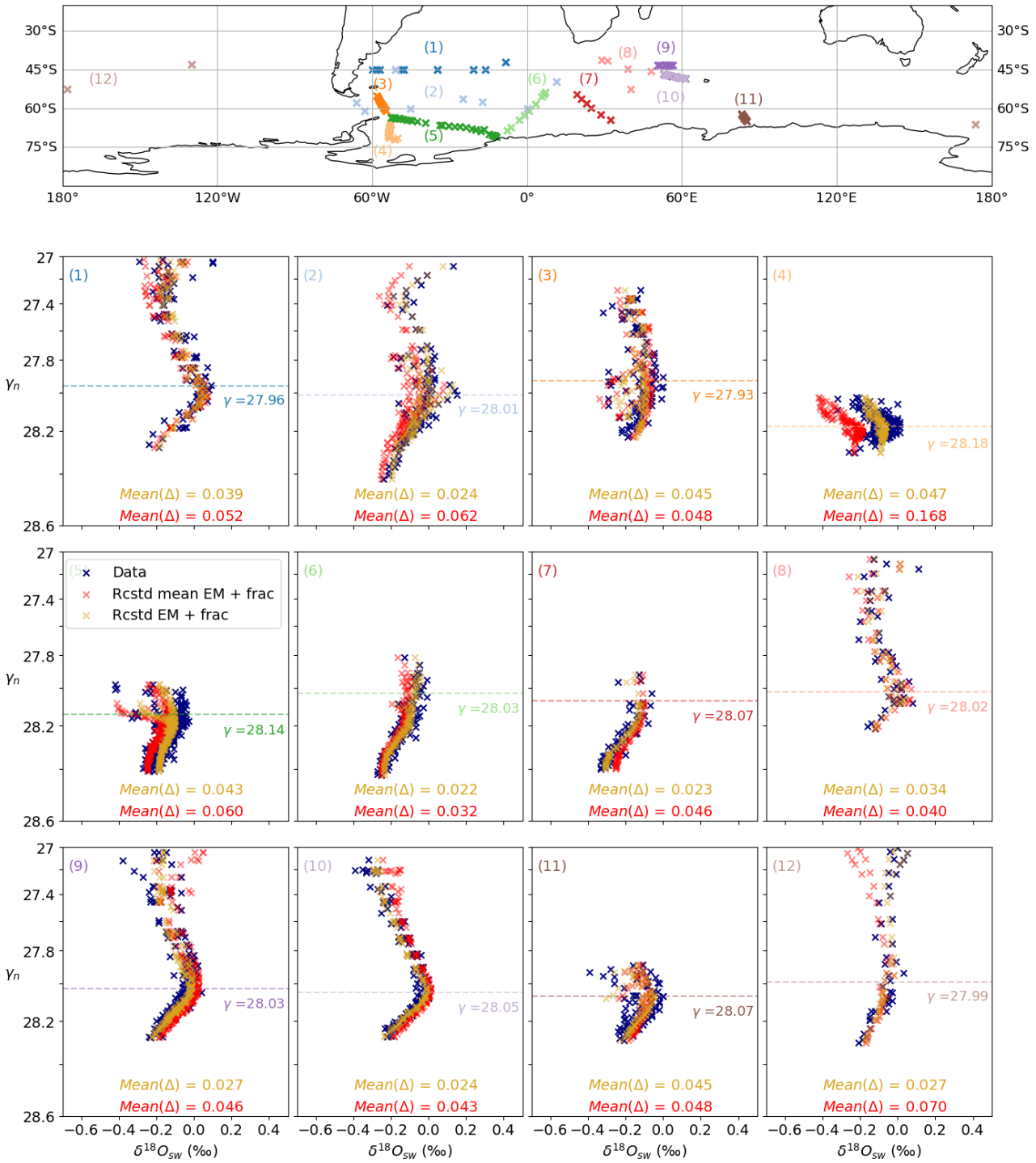

Figure 4.12: Figure representing the 12 datasets shown in Figure 4.2, and the reconstruction made with the end-member $\delta^{18}O_{sw}$ values found through the optimization for each dataset (orange) and with the average end-member values (red). On top of each panel, the mean of the quadratic error between the reconstructed product and the original data is represented in their respective color.

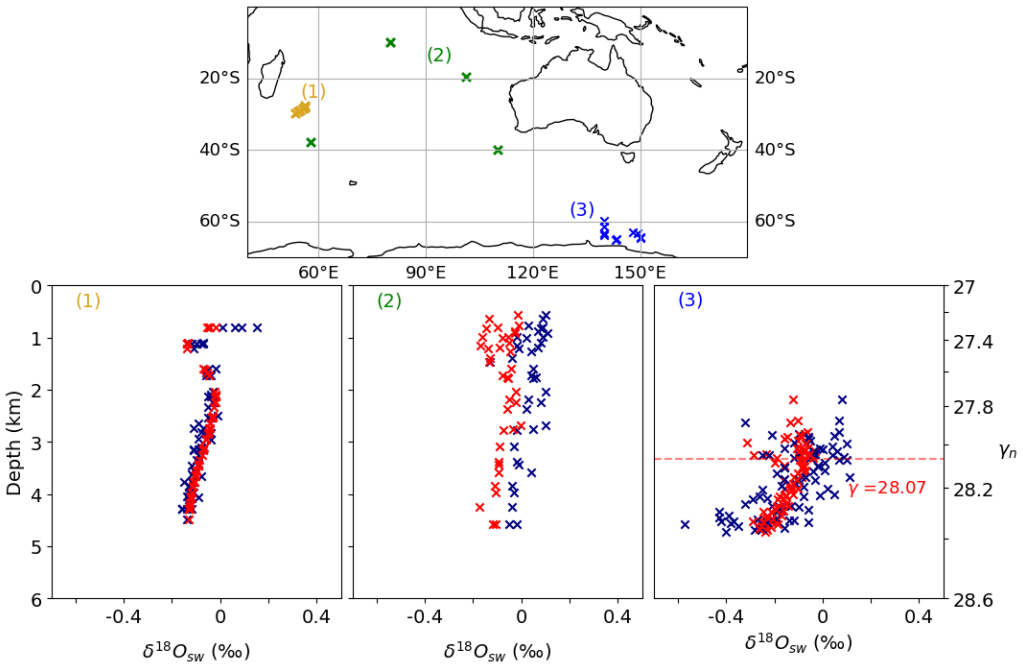

Figure 4.13: On top is the map where the stations were sampled. In the second row, the two datasets from the Indian Ocean, the dataset from the Southern Ocean of Helen Bostock are represented (blue) along our reconstruction with the average $\delta^{18}O_{sw}$ end-member value (red). The first 2 datasets are represented in depth-space and the last, in density-space.

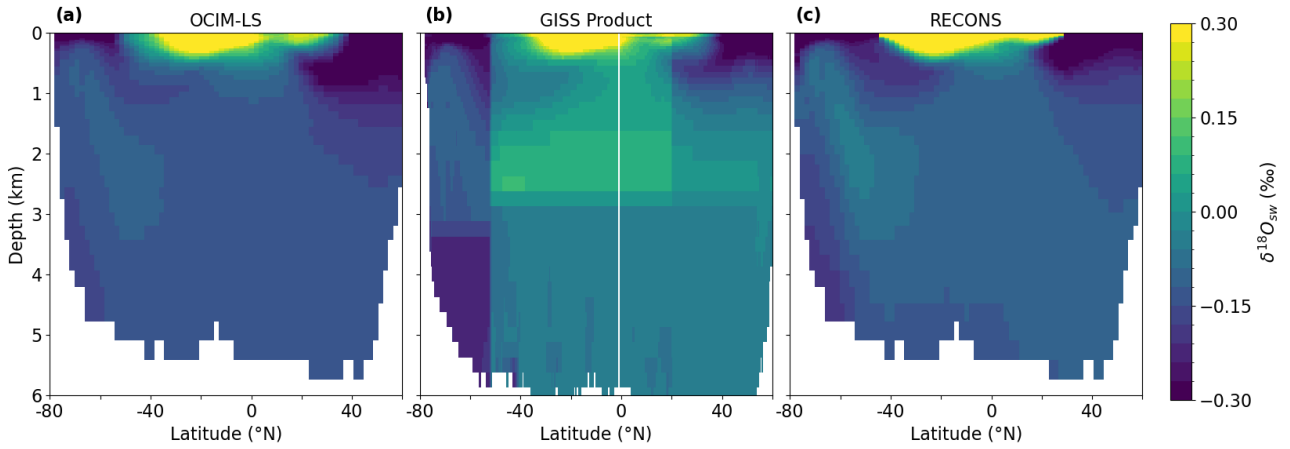

Figure 4.14: Zonal mean of the $\delta^{18}O_{sw}$ in the Pacific from **(a)** the original OCIM product, **(b)** the LS product and **(c)** the reconstructed product with the average end-member $\delta^{18}O_{sw}$ values.

The reconstructed $\delta^{18}O_{sw}$ product presented is based on the steady-state ventilation fractions of OCIM and associated $\delta^{18}O_{sw}$ surface end-member values. The fractions (or regional dye concentrations) of OCIM were assessed in Chapter II: they are deemed an excellent representation of modern ocean ventilation. Thus, we will investigate the plausibility of our end-member $\delta^{18}O_{sw}$ values.

4.1 . Quality assessment of our reconstruction

4.1.1 . Surface end-member values

To assess the quality of the $\delta^{18}O_{sw}$ surface end-member values, one should keep in mind that those values were found to match the deep variability of $\delta^{18}O_{sw}$ in the Southern Ocean, and that they represent a very large surface area. Thus, they cannot realistically represent surface and upper-ocean patterns. Nonetheless, investigating how the deep waters could acquire the resulting $\delta^{18}O_{sw}$ signature, and the apparent gradient between AABW and NADW, is important to assess the feasibility, and thus quality of our product.

The bottom waters formed in the Weddell Sea were long thought to be the main if not the only contributor to AABW formation; a view that has evolved since then as more sources were found in the Ross Sea and off the Adélie Coast and Cape Darnley (Meredith, 2013). Many studies have used $\delta^{18}O_{sw}$ to describe the different water masses leading to AABW formation in the Weddell Sea (Schlosser et al., 1990; Weiss et al., 1979; Weppernig et al., 1996). Weiss et al. (1979) typically gives a $\delta^{18}O_{sw}$ AABW end-member values of -0.2‰, as it results from a mixture between deep waters in the circumpolar current and waters that cascade down the continental slope of Antarctica. Values as depleted in $\delta^{18}O_{sw}$ as the value we found (-0.45‰), can only be found from waters that incorporate significant continental ice melt. The question thus remains, can the surface $\delta^{18}O_{sw}$ value inferred from our optimization be found at the surface?

Aoki et al. (2023) published a new dataset of $\delta^{18}O_{sw}$ off the Antarctic coast between 80 and 150°E. The shallow ocean (depth $\leq 250m$) over the continental shelf exhibits strong longitudinal $\delta^{18}O_{sw}$ variability ranging from -0.2‰ to -0.5‰. From their sections, and the deep $\delta^{18}O_{sw}$ values they infer an AABW value of about -0.25‰ to -0.3‰. This is in agreement with our product that predicts a value of -0.27‰ around

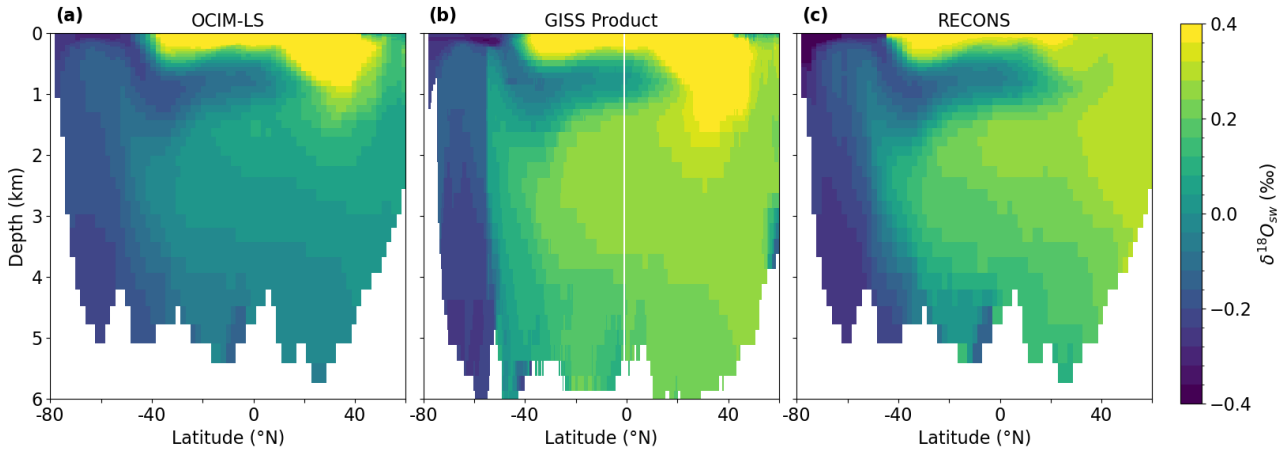

Figure 4.15: Same as Figure 4.14, but in the Atlantic.

these depths, and at this location near the continental slope. It is noteworthy, that the OCIM fractions there already indicate a mixture of around 65% AA, 25% NA and 10%HS.

Solodoch et al. (2022) also highlights the fact that the 4 ventilation sources of AABW do not ventilate the same basins. Our reconstruction was made using the available data around the Southern Ocean but probably represents mainly AABW formed in the Weddell Sea and Cape Darnley, which influence the Atlantic and Indian Ocean more than the Pacific. The Adélie Coast is the only formation region where dense shelf waters do not interact with an ice-shelf cavity (Silvano et al., 2023), so the bulk of AABW should incorporate significant glacial meltwater, that eventually leads to depleted $\delta^{18}O_{sw}$ values.

Similarly to the multitude of AABW sources, NADW is also associated with different sources, questioning its representation using a single surface patch value. Figure 4.15 shows the zonal mean of $\delta^{18}O_{sw}$ in the Atlantic for the three products. RECONS misses the very enriched $\delta^{18}O_{sw}$ values that spread up to 1.5km depth. Those enriched values are caused by (1) low-latitude waters with high $\delta^{18}O_{sw}$ that penetrates deep in the subtropical gyre and (2) waters coming from the Mediterranean Sea. On the other hand, it does a much better job at representing deep $\delta^{18}O_{sw}$ values than the OCIM-LS product (by comparison to the $\delta^{18}O_{sw}$ LS product), thus giving credit to our NA surface patch value. Frew et al. (2000) analysed the $\delta^{18}O_{sw}$ in the North Atlantic and found $\delta^{18}O_{sw}$ surface values of ~ 0.3‰ and deep waters of ~ 0.2‰ which agree well with the values found in RECONS. The distinction between the different deep waters originating from the Nordic Seas and the Labrador Sea could potentially improve our RECONS $\delta^{18}O_{sw}$ product.

The depleted $\delta^{18}O_{sw}$ tongue that can be observed around $\sim$ 800m in the Atlantic in Figure 4.15 corresponds to the penetration of AAIW coming from the Southern Ocean. It seems to penetrate further northward and have a stronger influence in RECONS than in the other products, but a heavier $\delta^{18}O_{sw}$ surface value for the LL patch would suppress this feature (not shown). Additionally, the HS end-member value that was found to reconstruct the OCIM-LS product with the OCIM fractions, and the ones inferred from our optimization are almost similar (see Table 1); thus this HS $\delta^{18}O_{sw}$ value is judged broadly correct.

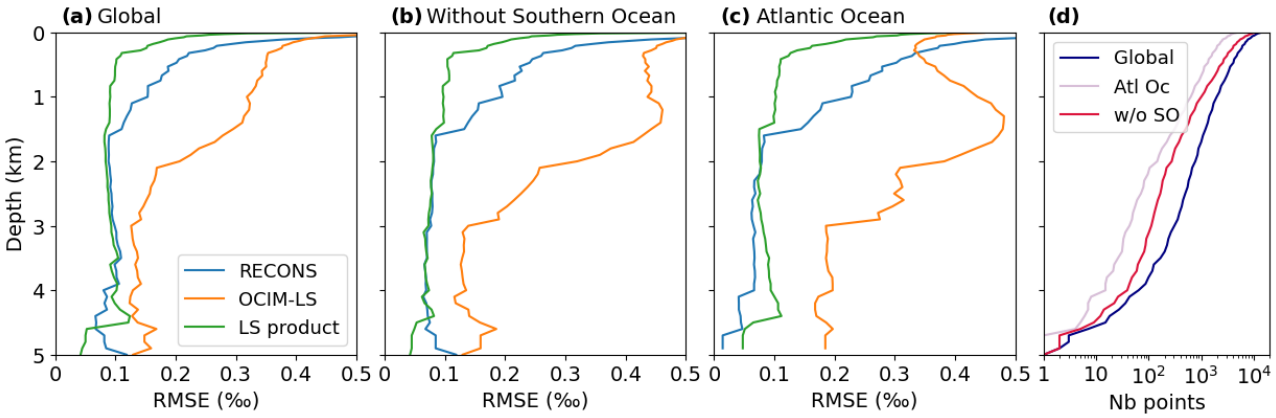

Figure 4.16: Figure showing the averaged depth profile of the root-mean-squared error between the data from GISS and the OCIM, LS and our reconstructed product. The averaged was made over the whole ocean **(a)**, the whole ocean without the Southern Ocean **(b)**, and the Atlantic Ocean **(c)**. Panel **(d)** shows the number of points with which the RMSE was calculated as a function of depth.

4.1.2 . Quantitative inter-comparison of the $\delta^{18}O_{sw}$ products

RECONS is sensitive to the surface patch values, we can thus wonder how our product compares to the others. We expect it to be better constrained in the Southern Ocean, as we use the data there to constrain the surface patch values, but how does it compare elsewhere? Our reconstructed product is designed to represent the deep $\delta^{18}O_{sw}$ structure, so we can wonder if there is a depth below which our product fares better than the other two when it comes to representing the deep $\delta^{18}O_{sw}$ variability. In order to test this, we thus take the GISS database for the whole ocean, and we estimate the difference between the $\delta^{18}O_{sw}$ measured data and the three $\delta^{18}O_{sw}$ products (LS, OCIM-LS, RECONS). For each depth, we compute $f(d)$ which represents the average of the root-mean-square difference between the measured $\delta^{18}O_{sw}$ data ($\delta^{18}O_{sw}(d_i)$) located below this depth (d) and the associated $\delta^{18}O_{sw}$ product values ($\delta^{18}O_p(d_i)$):

$$f(d) = \sqrt{\sum_{d_i \geq d} (\delta^{18}O_{sw}(d_i) - \delta^{18}O_p(d_i))^2} \qquad \text{(IV.2)}$$

Ideally, $f(d)$ gives the depth below which our $\delta^{18}O_{sw}$ reconstructed product is best at representing the $\delta^{18}O_{sw}$ variability. Figure 4.16 shows $f(d)$ computed for the three products over the global ocean, the global ocean without the Southern Ocean and over the Atlantic Ocean alone. Figure 4.16d shows the number of points that were used to compute $f(d)$ at each depth level, obviously decreasing with depth. Overall, Figure 4.16 shows that the OCIM-LS product is the least suitable product to represent $\delta^{18}O_{sw}$ in the ocean. The LS product is evidently superior at representing the $\delta^{18}O_{sw}$ in the upper 1500m of the ocean. Below this depth our reconstructed product and the LS product have overall similar errors (Figure 4.16a). We deemed necessary to represent $f(d)$ using data found anywhere but in the Southern Ocean (Figure 4.16b) as the RECONS product was constructed using the data there, so we expect the error to be much lower in the Southern Ocean. However we find that excluding or not the Southern Ocean does not change the picture (Figure 4.16a,b), and that both products are comparable below 1.5km.

Interestingly, in the Atlantic $f(d)$ is lower below 2km for RECONS than the LS product. Zooming in

on this difference (not shown), we see that the more southern $\delta^{18}O_{sw}$ data are overall too heavy in the LS product, in regard to the measured data, while these locations are correctly represented in RECONS. We think that this must mean that AABW penetration in the South Atlantic is not correctly captured by the LS product. It also emphasizes OCIM's ability to correctly represent the ocean ventilation there.

The differences observed between the RECONS and OCIM-LS products also raise an interesting problem. The fact that the OCIM-LS product error is so large in the Atlantic Ocean (Figure 4.16c) could be explained by multiple reasons: (1) the OCIM ventilation is wrong, (2) the surface $\delta^{18}O_{sw}$ distribution from GISS is wrong in some key locations where deep ventilation occurs in OCIM, (3) the deep ventilation occurs at the wrong place in OCIM (4) OCIM does not account for processes such as subsurface glacial meltwater input. We exclude (1) since RECONS correctly represent the deep $\delta^{18}O_{sw}$, and the RECONS and OCIM-LS products share the same OCIM equilibrated ventilation. The places where deep ventilation occurs in the North Atlantic is thought to be strongly constrained in OCIM, by the CFC measurements that are incorporated in the inverse model, making hypothesis (3) unlikely. Subsurface processes such as glacial meltwater input or brine rejection only act to reduce the $\delta^{18}O_{sw}$, which is already too low in the deep North Atlantic in the OCIM-LS product, thus ruling out hypothesis (4). Differences between the LS and the OCIM-LS product near the continental margins (Groënland, Labrador Sea) seem to quickly (with regard to depth) propagate in the ocean interior (not shown). Representing the processes that influence $\delta^{18}O_{sw}$ could be key to constrain ventilation sources, but may be too complex to parameterize. Not discussed so far, is the resolution of OCIM (2 degrees) which may induce some error in the $\delta^{18}O_{sw}$ that is propagated in the deep ocean, as the mean of this tracer over a 2 degree surface grid-cell may not represent the actual $\delta^{18}O_{sw}$ of deep waters sinking; and especially at the continental margins. Whether the problem is linked to an error of the GISS surface values, a misrepresentation of the deep water formation locations in OCIM, or the resolution of OCIM is of no importance in our reconstruction. Indeed, assigning constant end-member values over the large surface patches allows us to represent the $\delta^{18}O_{sw}$ of the waters contributing to deep water formation, without necessarily finding the origin of the bias.

4.2 . Further constrain ocean ventilation from $\delta^{18}O_{sw}$ observations

Tamsitt et al. (2017) highlight the southeastward upwelling of North Atlantic ventilated waters in the Southern Ocean using Lagrangian particle modelling. The proportion of North Atlantic-originated particles transported around the Southern Ocean thus decreases similarly as the NA dye from Chapter II. Our $\delta^{18}O_{sw}$ compilation presented in Figure 4.2, allowed us to support the fact that waters coming from the North Atlantic penetrate and circumnavigate within the ACC. However, the magnitude of the erosion cannot be assessed with our compilation since it is largely under-sampled from 120°E to 60°W.

Figure 4.17 shows the NA dye maximum found at each longitude below 1km for the 3 models presented in Chapter II. For the three models, we see that the NA dye is maximum in the Atlantic sector of the ACC, and that it decreases as we get farther away from the Atlantic sector. Although, the magnitude and erosion of this maximum varies across the three models. An additional NEMO simulation 'ISO3D', also presented in Chapter II has been added to the plot to highlight the impact of isopycnal mixing schemes on tracer budget in the Southern Ocean: less isopycnal mixing in the Southern Ocean leads to reduced NA dye tracer removal at the Southern Ocean surface (Jones and Abernathey, 2019). ISO3D implements the best isopycnal mixing scheme currently available and this is the simulation where the NA dye is the strongest. Therefore, the North Atlantic signal attenuation in the Southern Ocean is very uncertain and we propose

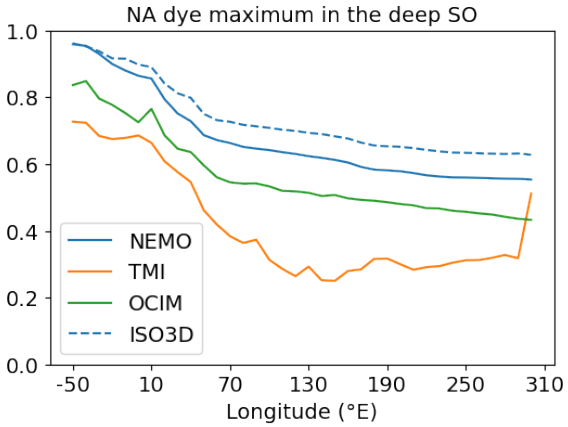

Figure 4.17: The North Atlantic dye maximum found in the Southern Ocean from 60-30°S below 1km is represented as a function of longitude, for NEMO, TMI and OCIM. Another NEMO simulation, ISO3D, is also represented as a dashed line to show the impact of a different isopycnal mixing scheme.

that $\delta^{18}O_{sw}$ could be used to quantitatively constrain it through a targeted $\delta^{18}O_{sw}$ sampling campaign.

Moreover, the ventilation of the mid-depths in the Pacific or Indian Ocean remains poorly characterized (see Introduction and previous chapters). Meridional transects of $\delta^{18}O_{sw}$ measurements from the Southern Ocean, then penetrating in the Indian or Pacific basins, up to the equator, should provide constraints on the relative roles of vertical and isopycnal diffusion for the ventilation of ocean mid-depths. Additionally, it should provide information on the amount, and fate of northward flowing AABW in these basins. Figure 4.18 shows additional data extracted from Reverdin et al. (2022), in the south-west Indian Ocean, from 40-90°E and 60-30°S below 500m, with the zonal mean of the two products on this same spatial range. Separate calculations for both the RECONS and LS product show that to minimize the error between the products and the associated dataset from Reverdin et al. (2022), an offset of 0.15‰ must be applied. The data are thus corrected accordingly on Figure 4.18. The mid-depth $\delta^{18}O_{sw}$ values of both products indicate a maximum, but it would seem that our product is more realistic than the LS product. A systematic sampling could thus highlight the amount of diffusion and add solid constraints on the impact of isopycnal diffusion on tracer budgets in the Indian and Pacific Oceans.

5 . Conclusion and perspectives

In this Chapter, we analyzed pre-existing $\delta^{18}O_{sw}$ measurements and presented new $\delta^{18}O_{sw}$ data to show the utility of this tracer to constrain ocean ventilation. Through this study, we also propose a new $\delta^{18}O_{sw}$ product constructed with the GISS $\delta^{18}O_{sw}$ database as well as the OCIM fractions. Although the absolute $\delta^{18}O_{sw}$ values associated to this dataset can be questioned, we expect the deep $\delta^{18}O_{sw}$ pattern to represent something close to the real ocean structure. Improvements to this product could be made by distinguishing the $\delta^{18}O_{sw}$ values for for the different low-latitude patches, accounting for the difference in the water mass formations sites (different types of NADW, AABW and AAIW), accounting for inter-laboratory offsets, and a more thorough assessment of the NPIW $\delta^{18}O_{sw}$ value.

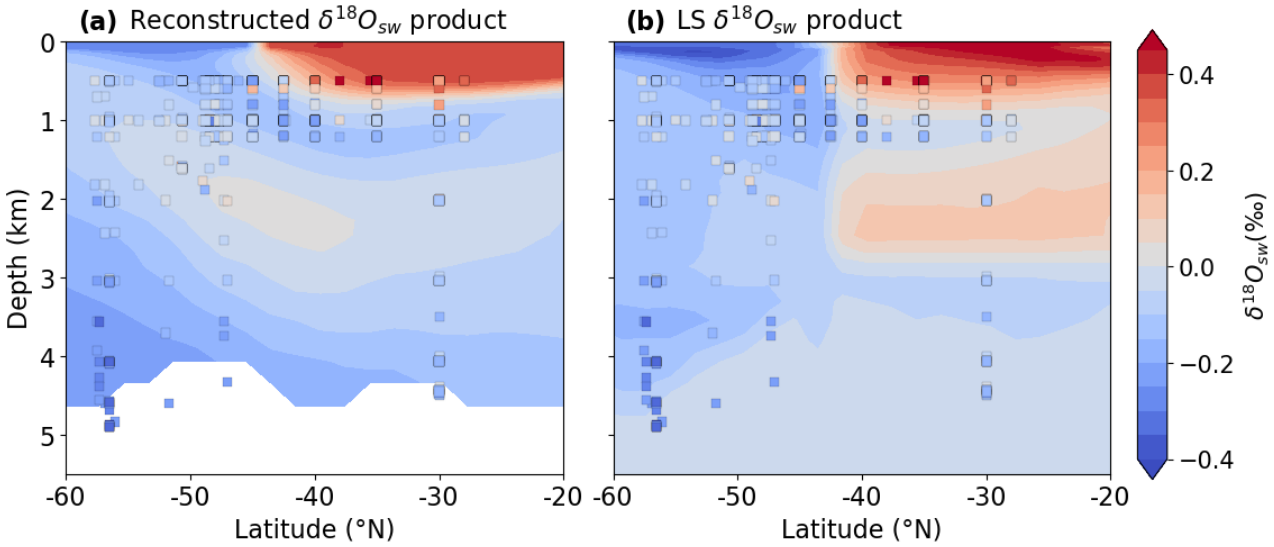

Figure 4.18: Zonal mean (60-30°S, 40-90°E) of the $\delta^{18}O_{sw}$ from the RECONS product **(a)**, and the LS product **(b)**. Measurements from the CISE-LOCEAN database for the same geographic region were added on both plots.

We saw that the deep $\delta^{18}O_{sw}$ structure can be reconstructed with a few fractions and the associated $\delta^{18}O_{sw}$ end-member values. If sufficiently sampled and measured, $\delta^{18}O_{sw}$ should thus give key constraints on deep ocean ventilation. The implementation of $\delta^{18}O_{sw}$ in OCIM could reveal complex, but might prove worthwhile to represent deep ventilation. In addition, intermediate waters show the highest contrast in regard to other water masses. The intermediate waters at low latitudes (LL) or at high-latitudes (AAIW and NPIW) all have characteristic $\delta^{18}O_{sw}$ values. This feature could in turn be used to constrain the diffusion of those water masses in the deep ocean, and thus help place constraints on the magnitude of diapycnal mixing within OCIM (see Chapter II). However, we acknowledge that the many processes that affect the $\delta^{18}O_{sw}$ in the surface ocean might represent a challenge too difficult to overcome.

Additionally, the differences in absolute values between laboratories can be a key issue as seen in this study. However, having comparable full-depth profiles of $\delta^{18}O_{sw}$, which can lead to simple conjectures on their respective offsets. Here we used optimization methods to reduce to a minimum the inter-laboratory offsets and we believe that if done in a systematic way, this approach could lead to a correct representation of absolute $\delta^{18}O_{sw}$ values. The $\delta^{18}O_{sw}$ gradient between the NADW and AABW water masses, both present in the Southern Ocean, offers a really good mean to compute the offset based on the shape of the full-depth profile. Finally we suggest that targeted sampling campaigns zonally in the Southern Ocean and meridionally in the Pacific and Indian could help constrain the patterns and mechanisms of ocean ventilation.

References

Anilkumar, N, Jena, B., George, J. V., P, S., S, K., & Ravichandran, M. (2021). Recent freshening, warming, and contraction of the antarctic bottom water in the indian sector of the southern ocean. *Frontiers in Marine Science*, *8*. https://doi.org/10.3389/fmars.2021.730630

Aoki, S., Yamazaki, K., Hirano, D., Nomura, D., & Murase, H. (2023). Distribution of stable oxygen isotope in seawater and implication on freshwater cycle off the coast from wilkes to george v land, east antarctica. *Progress in Oceanography*, *217*, 103101. https://doi.org/10.1016/j.pocean.2023.103101

Bass, A. M., Munksgaard, N. C., O'Grady, D., Williams, M. J., Bostock, H. C., Rintoul, S. R., & Bird, M. I. (2014). Continuous shipboard measurements of oceanic δ18o, δd and δ13cdic along a transect from new zealand to antarctica using cavity ring-down isotope spectrometry. *Journal of Marine Systems*, *137*, 21–27. https://doi.org/10.1016/j.jmarsys.2014.04.003

de Lavergne, C., Madec, G., Roquet, F., Holmes, R., & McDougall, T. (2017). Abyssal ocean overturning shaped by seafloor distribution. *Nature*, *551*(7679), 181–186. https://doi.org/10.1038/nature24472

Frew, R. D., Dennis, P. F., Heywood, K. J., Meredith, M. P., & Boswell, S. M. (2000). The oxygen isotope composition of water masses in the northern north atlantic. *Deep Sea Research Part I: Oceanographic Research Papers*, *47*(12), 2265–2286. https://doi.org/10.1016/S0967-0637(00)00023-6

Gouretski, V., & Koltermann, K. P. (2004). Woce global hydrographic climatology. *Berichte des BSH*, *35*, 1–52.

Herguera, J. C., Jansen, E., & Berger, W. H. (1992). Evidence for a bathyal front at 2000-m depth in the glacial pacific, based on a depth transect on ontong java plateau. *Paleoceanography*, *7*(3), 273–288. https://doi.org/10.1029/92PA00869

Holzer, M., DeVries, T., & de Lavergne, C. (2021). Diffusion controls the ventilation of a pacific shadow zone above abyssal overturning. *Nature Communications*, *12*(1), 4348. https://doi.org/10.1038/s41467-021-24648-x

Huussen, T. N., Naveira-Garabato, A. C., Bryden, H. L., & McDonagh, E. L. (2012). Is the deep indian ocean moc sustained by breaking internal waves? *Journal of Geophysical Research: Oceans*, *117*(C8). https://doi.org/10.1029/2012JC008236

Jones, C. S., & Abernathey, R. P. (2019). Isopycnal mixing controls deep ocean ventilation. *Geophysical Research Letters*, *46*(22), 13144–13151. https://doi.org/10.1029/2019GL085208

Keigwin, L. D. (1998). Glacial-age hydrography of the far northwest pacific ocean. *Paleoceanography*, *13*(4), 323–339. https://doi.org/10.1029/98PA00874

Key, R. M., Olsen, A., van Heuven, S., Lauvset, S. K., Velo, A., Lin, X., Schirnick, C., Kozyr, A., Tanhua, T., Hoppema, M., Jutterström, S., Steinfeldt, R., Jeansson, E., Ishii, M., Perez, F. F., & Suzuki, T. (2015). Global ocean data analysis project, version 2 (glodapv2). https://doi.org/10.3334/CDIAC/OTG.NDP093_GLODAPv2

Kuhlbrodt, T., Griesel, A., Montoya, M., Levermann, A., Hofmann, M., & Rahmstorf, S. (2007). On the driving processes of the atlantic meridional overturning circulation. *Reviews of Geophysics*, *45*(2). https://doi.org/10.1029/2004RG000166

LeGrande, A. N., & Schmidt. (2006). Global gridded data set of the oxygen isotopic composition in seawater. *Geophysical Research Letters*, *33*(12). https://doi.org/10.1029/2006GL026011

Lumpkin, R., & Speer, K. (2007). Global ocean meridional overturning. *Journal of Physical Oceanography*, *37*(10), 2550 –2562. https://doi.org/10.1175/JPO3130.1

McCave, I., Carter, L., & Hall, I. (2008). Glacial–interglacial changes in water mass structure and flow in the sw pacific ocean. *Quaternary Science Reviews*, *27*(19), 1886–1908. https://doi.org/10.1016/j.quascirev.2008.07.010

Meredith, M. P. (2013). Replenishing the abyss. *Nature Geoscience*, *6*(3), 166–167. https://doi.org/10.1038/ngeo1743

Millet, B., Gray, W. R., de Lavergne, C., & Roche, D. M. (2023). Oxygen isotope constraints on the ventilation of the modern and glacial pacific. *Climate Dynamics*. https://doi.org/10.1007/s00382-023-06910-8

Naveira Garabato, A. C., MacGilchrist, G. A., Brown, P. J., Evans, D. G., Meijers, A. J. S., & Zika, J. D. (2017). High-latitude ocean ventilation and its role in earth's climate transitions. *Philos Trans A Math Phys Eng Sci*, *375*(2102). https://doi.org/10.1098/rsta.2016.0324

Olsen, A., Key, R. M., van Heuven, S., Lauvset, S. K., Velo, A., Lin, X., Schirnick, C., Kozyr, A., Tanhua, T., Hoppema, M., Jutterström, S., Steinfeldt, R., Jeansson, E., Ishii, M., Pérez, F. F., & Suzuki, T. (2016). The global ocean data analysis project version 2 (glodapv2) – an internally consistent data product for the world ocean. *Earth System Science Data*, *8*(2), 297–323. https://doi.org/10.5194/essd-8-297-2016

Orsi, A., Johnson, G., & Bullister, J. (1999). Circulation, mixing, and production of antarctic bottom water. *Progress in Oceanography*, *43*(1), 55–109. https://doi.org/10.1016/S0079-6611(99)00004-X

Reverdin, G., Waelbroeck, C., Pierre, C., Akhoudas, C., Aloisi, G., Benetti, M., Bourlès, B., Danielsen, M., Demange, J., Diverrès, D., Gascard, J.-C., Houssais, M.-N., Le Goff, H., Lherminier, P., Lo Monaco, C., Mercier, H., Metzl, N., Morisset, S., Naamar, A., … Meredith, M. (2022). The cise-locean seawater isotopic database (1998–2021). *Earth System Science Data*, *14*(6), 2721–2735. https://doi.org/10.5194/essd-14-2721-2022

Schlosser, P., Bayer, R., Foldvik, A., Gammelsrød, T., Rohardt, G., & Münnich, K. O. (1990). Oxygen 18 and helium as tracers of ice shelf water and water/ice interaction in the weddell sea. *J Geophys Res C3*, *95*, 3253–3263.

Schmidt, Bigg, G. R., & Rohling, E. J. (1999). Global seawater oxygen-18 database - v1.22.

Schmitz Jr., W. J. (1995). On the interbasin-scale thermohaline circulation. *Reviews of Geophysics*, *33*(2), 151–173. https://doi.org/10.1029/95RG00879

SEANOE (Ed.). (2023). Water isotopes of sea water analyzed since 1998 at locean. https://doi.org/10.17882/71186

Silvano, A., Purkey, S., Gordon, A. L., Castagno, P., Stewart, A. L., Rintoul, S. R., Foppert, A., Gunn, K. L., Herraiz-Borreguero, L., Aoki, S., Nakayama, Y., Naveira Garabato, A. C.,

Spingys, C., Akhoudas, C. H., Sallée, J.-B., de Lavergne, C., Abrahamsen, E. P., Meijers, A. J. S., Meredith, M. P., … Lee, W. S. (2023). Observing antarctic bottom water in the southern ocean. *Frontiers in Marine Science*, *10*. https://doi.org/10.3389/fmars.2023.1221701

Solodoch, A., Stewart, A. L., Hogg, A. M., Morrison, A. K., Kiss, A. E., Thompson, A. F., Purkey, S. G., & Cimoli, L. (2022). How does antarctic bottom water cross the southern ocean? [e2021GL097211 2021GL097211]. *Geophysical Research Letters*, *49*(7), e2021GL097211. https://doi.org/https://doi.org/10.1029/2021GL097211

Talley, L. D. (2013). Closure of the global overturning circulation through the indian, pacific, and southern oceans: Schematics and transports. *Oceanography*, *26*(1), 80–97.

Tamsitt, V., Drake, H. F., Morrison, A. K., Talley, L. D., Dufour, C. O., Gray, A. R., Griffies, S. M., Mazloff, M. R., Sarmiento, J. L., Wang, J., & Weijer, W. (2017). Spiraling pathways of global deep waters to the surface of the southern ocean. *Nature Communications*, *8*(1), 172. https://doi.org/10.1038/s41467-017-00197-0

Weiss, R., Östlund, H., & Craig, H. (1979). Geochemical studies of the weddell sea. *Deep Sea Research Part A. Oceanographic Research Papers*, *26*(10), 1093–1120. https://doi.org/10.1016/0198-0149(79)90059-1

Weppernig, R., Schlosser, P., Khatiwala, S., & Fairbanks, R. G. (1996). Isotope data from ice station weddell: Implications for deep water formation in the weddell sea. *Journal of Geophysical Research: Oceans*, *101*(C11), 25723–25739. https://doi.org/https://doi.org/10.1029/96JC01895

Supplementary Information

I made measurements both in Calstate Sacramento under the supervision of Amy Wagner, and at the LOCEAN under the supervision of Claire Waelbroeck and Gilles Reverdin. The machines used both employed cavity ringdown spectroscopy to perform the $\delta^{18}O_{sw}$ measurements. In Calstate, measurements were made using a Los Gatos Research Liquid Water Isotope Analyzer (LWIA-24d) while in the LOCEAN laboratory I used a Picarro. Methodologies to measure and analyze the raw $\delta^{18}O_{sw}$ data differed between laboratories. A batch of samples that were measured in Sacramento were also taken back to Paris to be measured in LOCEAN. The idea behind this was to potentially measure the difference in $\delta^{18}O_{sw}$ between the laboratories, such that the dataset (comprised of both LOCEAN and Calstate measurements) could be corrected for this offset. Figure S4.1 shows the station that was measured in both labs, and we see that the data obtained do not look alike with a much larger than expected variation in the values from Calstate. Furthermore, they do not have the same shape, and a constant offsets cannot be applied to obtain similar values.

We can wonder as to why those differences originate from. The main difference between the two measurement systems is that the Picarro had a salt trap present before the water vapor is being added into the machine. Single measurement of $\delta^{18}O_{sw}$ for a bottle of seawater are made by injecting the associated vaporized water in a cavity. Based on laser spectrometry, the raw $\delta^{18}O_{sw}$ is then measured; this process is repeated around 8 to 9 times. The first 3 measurements are often ignored due to the memory effect of the machine, and then the raw $\delta^{18}O_{sw}$ are computed from the other measurements.

When the water is being vaporized, residual salt crystals can remain in the pipes of the machine that links the vaporizer to the cavity, if no salt trap is present. The problem associated with residual salt crystals in the machine's pipes is isotope fractionation. In fact, salt crystals can absorb water vapor at any time.

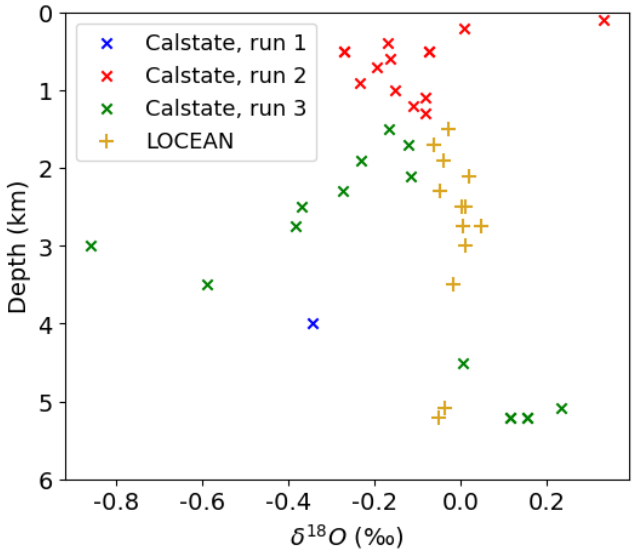

Figure S4.1: Station 14 (32°N) sampled during the GP15 cruise. Measurements were made in Calstate represented by $\times$ sign and in LOCEAN represented by $+$ sign. A coloring was implemented for the measurements made in Sacramento to show the different runs.

These salt crystals can then reject the accumulated water vapour at any time, during other measurements for example, thus distorting the results. In order to avoid the problem caused by salt for $\delta^{18}O_{sw}$ measurements, the method in Calstate was to measure freshwater samples between each seawater measurement. There are two major problems with this approach: (1) the freshwater that was passed had isotopic ratios very different to the one of the seawater possibly leading to large possible memory effects, and (2) it doubles the length of the run.

5.1 . Memory effect

The memory effect is difficult to avoid, and in addition, measuring water samples that have around the same isotopic signature is key to reduce the uncertainties associated to the measurements. Freshwater samples that were passed between each measurement at Calstate had values ~ -11‰ (d18o) and ~ -73‰ (dH). The Pacific signal that we are looking at mid-depths, probably presents a relative maximum between the abyss and the mid-depths that would be of the order of 0.1‰, with absolute values around 0‰. Thus, the presence of 1% of freshwater vapor would explain the magnitude of the signal.

5.2 . Length of the run

Passing freshwater samples between each measurement, doubles the length of the run, and it complicates the measurements, as there is a drift associated with each machine as the number of samples passed increase. This drift, can be measured with the standards that are passed during the run. Figure S4.2 shows the drift associated to both machines, the $\delta^{18}O_{sw}$ offset is computed by taking the difference between the predicted value of the standard (VSMOW) and the raw value of the measurement. The $\delta^{18}O_{sw}$ offset from LOCEAN was put to the same scale, but the absolute values does not hold much information and it is the variations that we are interested about. We see that the range of the variations are about the same, in the first 20 bottles measured, for the different machines (although a bit lower for the Picarro). Afterwards, the drift for the Los Gatos machine drastically increase, which leads to an uncertainty increase to put the measured value on the VSMOW reference.

The uncertainty associated to the length of the run thus increases with the number of bottles measured. Internal standards are measurements that are done within a run on a sample of which we know the $\delta^{18}O_{sw}$ value beforehand. They are made in order to verify the consistency of the method, and that the machine is working alright. Figure S4.3 shows the $\delta^{18}O_{sw}$ values found for the internal standard for each run that was made. We see that the spatial dispersion of this value is big as the standard deviation associated is of 0.22‰ far exceeding expected uncertainties.

Thus we concluded that the method used in Sacramento introduced large artefacts compared to our measurements at LOCEAN. At first, some efforts have been made to try to quality control the dataset, but finally we decided to reject the dataset altogether in order to avoid the risk of biases within the data.

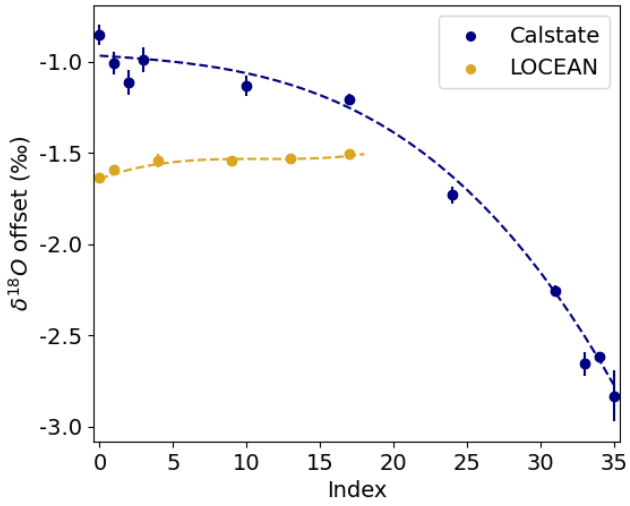

Figure S4.2: Deviation of the standards within a typical run using a Los Gatos instrument (blue) and a Picarro (yellow). The index on the x-axis represent the number of the bottles that has been measured.

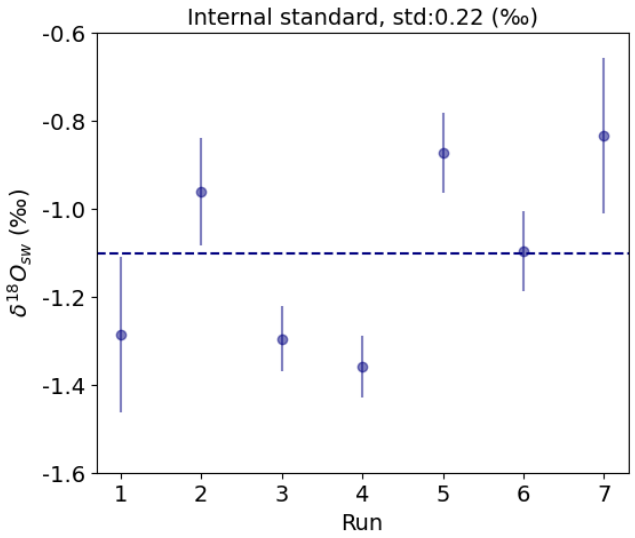

Figure S4.3: The values found for the different runs performed in Sacramento are shown here, with a line indicating the mean vaue of the internal standard. the errorbars displayed indicate the standard deviation for the measurement.

CHAPTER V

GLACIAL CHANGES IN OCEAN VENTILATION: INSIGHTS FROM ISOTOPIC RECORDS AND TEMPERATURE RECONSTRUCTIONS

The modern $\delta^{18}O_{sw}$ distribution was previously used in Chapter IV to show how this tracer can help constrain the fraction of ventilated waters in the deep ocean from the North Atlantic and the Southern Ocean. In Chapter I, we argued that the $\delta^{18}O_{CaCO3}$ is conservative and we used a $\delta^{18}O_{CaCO3}$ compilation in the North Pacific to bring constraints on the glacial ventilation. The UCDW and AABW end-members were defined by using sediment cores found in the South Pacific. We argued that the glacial $\delta^{18}O_{CaCO3}$ gradient that we observed in the North Pacific between the mid-depths and the deeper ocean could be related to the difference in the end-member $\delta^{18}O_{CaCO3}$ values:

- The change in AABW $\delta^{18}O_{CaCO3}$ between the LGM and Holocene should be small, because temperatures associated to the modern AABW are already close to freezing point, and any addition of salt during the LGM should occur via brine rejection which causes little fractionation leaving the AABW end-member relatively depleted in $\delta^{18}O_{sw}$.
- The NADW $\delta^{18}O_{CaCO3}$ change should be large, since modern NADW is relatively warm, allowing glacial temperatures to be much colder. The high density of modern NADW water is obtained through elevated salinity (leaving $\delta^{18}O_{sw}$ relatively enriched).

The argument put forward in Chapter I was thus that the temperature changes between AABW and NADW drive the $\delta^{18}O_{CaCO3}$ changes, and implicitly that the $\delta^{18}O_{sw}$ gradient does not significantly change. A $\delta^{18}O_{sw}$ change of about ~ 1‰ is expected for the global ocean due to the glacial sea level change (Duplessy et al., 2002), but glacial estimates show regional differences in the changes in $\delta^{18}O_{sw}$ between the Holocene and the LGM (Waelbroeck et al., 2002). In the modern ocean, the $\delta^{18}O_{sw}$ and temperature differences

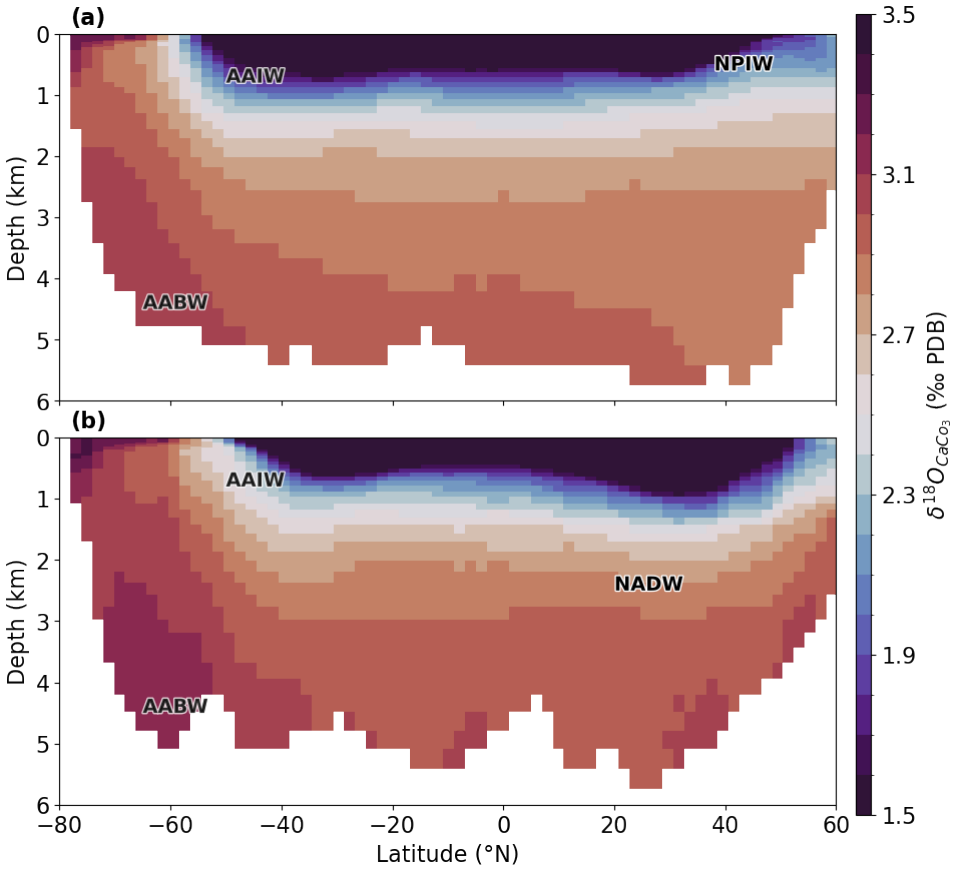

Figure 5.1: Transects at 200°E **(a)** and 25°W **(b)** of the $\delta^{18}O_{CaCO_3}$ of *C. wüellerstorfi* computed with observed temperatures (as used in OCIM) and the $\delta^{18}O_{sw}$ computed in Chapter IV, following Marchitto et al. (2014).

between the AABW and NADW counter-balance each other resulting in a relatively uniform $\delta^{18}O_{CaCO3}$ structure (Figure 5.1). In this Chapter, we will look at the potential of $\delta^{18}O_{CaCO3}$ of the *Cibicidoides* genus to constrain the glacial ocean ventilation.

First, we need to assess the changes in $\delta^{18}O_{CaCO3}$ of the two deep water masses. Figure 5.2 represents the locations of the sediment cores in the World Atlas database of Mulitza et al. (2022) that have a *Cibicidoides* isotopic record. It clearly shows the uneven sampling of the different ocean basins, and we see that the Southern Ocean only has a few sediment cores. The reasoning used for the $\delta^{18}O_{sw}$ in Chapter IV thus cannot be reproduced with $\delta^{18}O_{CaCO3}$, so other means are needed to constrain the end-member $\delta^{18}O_{CaCO3}$ values. In order to find the $\delta^{18}O_{CaCO3}$ signature of the deep glacial water masses, we will try two methods: (1) select sediment cores that "truly" represent the different glacial water masses, (2) infer their values from the glacial $\delta^{18}O_{CaCO3}$ structure in the different ocean basins.

This Chapter will first look at the changes in the $\delta^{18}O_{CaCO3}$ of the end-members, before trying to constrain changes in the LGM ventilation based on $\delta^{18}O_{CaCO3}$ of *Cibicidoides*. In order to tackle these problems, we will use different sediment cores and compilations produced in other studies, and show new data that I generated at the LSCE. We show that the hypothesis made in Chapter I is more uncertain than

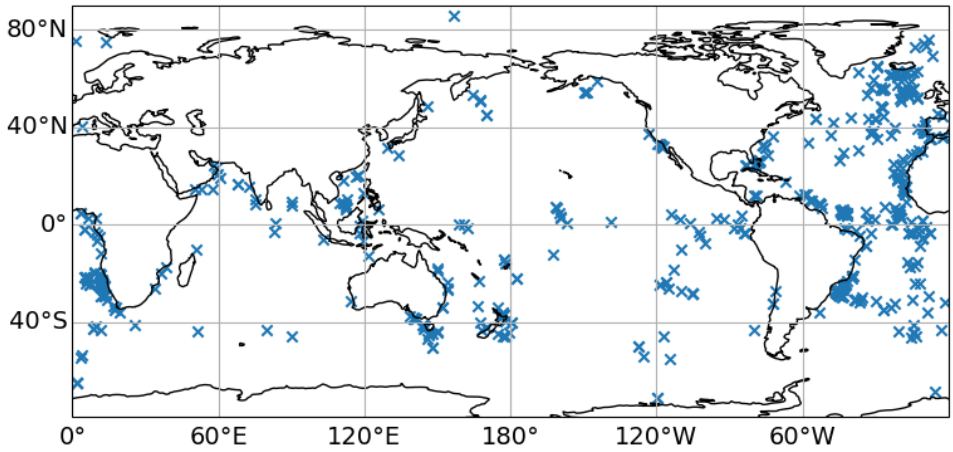

Figure 5.2: Map of the sediment cores with a *Cibicidoides* isotopic record in the World Atlas database (Mulitza et al., 2022).

previously thought. We also show a strong change in the $\delta^{18}O_{CaCO3}$ signal in the mid-depths of the North Atlantic, between the Holocene and the LGM.

1 . Introduction

Changes in the deep ocean ventilation between the LGM and Holocene are still debated. However, the most likely changes are a shallower northern component of deep water formed in the North Atlantic (Curry and Oppo, 2005; Ferrari et al., 2014), and a colder and saltier global ocean, with enhanced deep stratification due to salinity rather than temperature (Adkins et al., 2002). Those combined effect, likely caused by sea ice export, are supposed to drive a disconnection between the upper and lower cell of the glacial ocean, thus isolating deep waters. As a conservative tracer the associated changes in the $\delta^{18}O_{CaCO_3}$ of deep water masses are rarely discussed, but could provide key information for inferring changes in the glacial ocean structure.

We have relatively few constraints on the changes in temperature and $\delta^{18}O_{sw}$ of deep water masses during the LGM (Adkins et al., 2002; Wunsch, 2016), and thus on their relative contribution to the observed $\delta^{18}O_{CaCO3}$ changes. Brine rejection decreases the $\delta^{18}O_{sw}$ of the underlying waters, which could suggest a relative decrease of the $\delta^{18}O_{sw}$ of glacial AABW in respect to other glacial water masses (Introduction). However, the increase in the extent of the Antarctic ice sheet during the LGM may have led to a change in the mechanisms leading to the formation of AABW relative to today (Williams et al., 2019). Today the addition of glacial meltwater within sub-ice-shelf cavities leads to very depleted $\delta^{18}O_{sw}$. This effect may have been suppressed during the LGM due to i) reduced access to continental shelves and sub-ice-shelf cavities, occupied by the expanded ice sheet, and ii) colder Circumpolar Deep Water (CDW), whose heat ultimately drives ice-shelf melting today. Studying the $\delta^{18}O_{CaCO3}$ close to deep water formation sites may help us understand potential changes in water mass formation.

Finding appropriate sediment cores to represent key water masses proved to be complicated. First, because the extent and influence of the different glacial water masses is largely debated. Additionally, high dissolution rates and sea-ice cover complicate the generation of foraminiferal isotopic records in the Southern Ocean. Stefan Mulitza created a database which aims to compile all of the foraminiferal oxygen and carbon isotope data generated to date, and associated radiocarbon ages (Mulitza et al., 2022). Systematic compilation processing of large foraminiferal $\delta^{18}O_{CaCO3}$ databases has proved to be useful for paleo-reconstructions (Gray et al., 2023). The increased number of deep sediment cores should be useful to constrain end-member changes.

Here, I present a series of questions, that try to answer possible changes in the LGM ventilation relative to present. First, I use single sediment cores that I think are the closest to represent a "true" end-member for the glacial AABW and NADW. However, I later discuss the complications and caveats of relying on single locations to determine end member changes, and I show how a quality-checked compilation of isotopic records of sediment cores in the Atlantic can hold significant information on past ventilation changes. Finally, I present a compilation that I generated during this thesis of deep *Cibicidoides* $\delta^{18}O_{CaCO3}$ isotopic records in the Pacific. I also present new isotopic data and temperature reconstructions in the Pacific that I made during this PhD.

2 . End-member change

End-member	NADW	AABW
Holocene value	2.68	3.26
Glacial maximum value	4.84	4.7
Glacial-Holocene difference	2.16	1.44

Table 1: Table referencing the LGM and modern $\delta^{18}O_{CaCO3}$ values found for the NADW and AABW.

First, we try to constrain the $\delta^{18}O_{CaCO_3}$ values of the water masses contributing to the deep glacial ventilation by taking a single, ideally-placed core. Here, I propose two cores, that I think are representative for both the modern and glacial AABW and NADW. Gebbie (2014) shows that the glacial NADW was centered around 2 km in the Atlantic. Those depths in the North Atlantic are also largely ventilated by the modern NADW, so we select the core MD95-2003 (47.45°N, 8.3°W, 2174 m) to represent modern and glacial NADW. Finding a suitable core to represent the AABW does not leave us with many options, since only two cores are available at the Antarctic margin. We take the only one of those two cores that has an isotopic record for *C. wüellerstorfi* with a suitable resolution over the last 30 ky: JR179-TC493 (71.13°S, 119.914°W, 2077 m).

Table 1 provides $\delta^{18}O_{CaCO3}$ values for the Holocene and the LGM for our two cores. For MD95-2002, the Holocene value was selected as the minimum in the last 4 ky. For JR179-TC493, the record does not have sufficient resolution and no representative Holocene value can be extracted. We thus computed the theoretical $\delta^{18}O_{CaCO3}$ value by following Marchitto et al. (2014) using the $\delta^{18}O_{sw}$ value found in Chapter IV, and the ocean freezing point temperature. An alternative definition of modern AABW, more representative of waters along the Antarctic continental margin given by Weiss et al. (1979), that has temperature of -0.4°C and a $\delta^{18}O_{sw}$ of -0.2‰ leads to about the same $\delta^{18}O_{CaCO3}$ value (3.21‰). Using the predicted modern $\delta^{18}O_{CaCO3}$ of Figure 5.1, the Holocene NADW value falls in reasonable range ($\sim$0.05‰) to the observed one. The LGM $\delta^{18}O_{CaCO3}$ value for both end-members was selected as the maximum between 18 to 23 ky. The difference between the end-member glacial values is small, suggesting that the absolute $\delta^{18}O_{CaCO3}$ contrast between the two sources may be difficult to use to reconstruct glacial ventilation changes, although the glacial $\delta^{18}O_{CaCO3}$ value for AABW remains slightly more depleted than that of NADW.

Figure 5.3 depicts the variations of the $\delta^{18}O_{CaCO3}$ from present day to about 30 ky. The scale goes from 0 to about 2, as each record was subtracted from its modern value, referenced in Table 1. The $\Delta\delta^{18}O_{Ca_CO3}$ of the two cores show an interesting contrast: that of NADW shows a variability of 2.16‰, whereas that of AABW varies only by 1.44‰. A change of 1.1‰ is expected from sea level variation alone (see Introduction), and the rest of the change is either due to temperature or $\delta^{18}O_{sw}$. The bigger variation in the $\delta^{18}O_{CaCO3}$ for the North Atlantic core is probably principally due to the changes in temperature.

It would seem that the glacial $\delta^{18}O_{CaCO_3}$ gradient between the two deep water end-members is rather small, and could prove difficult to use to reconstruct past ventilation changes. However, for sediment cores lying in the deep Atlantic, although the glacial $\delta^{18}O_{CaCO3}$ values might not be enough to infer changes in ventilation, the variation between Holocene and LGM may give us insights on ventilation changes. Indeed, a sediment core that is lying in the modern and glacial NADW core should have a variation of about 2‰.

The modern volume fractions predicted by the Ocean Circulation Inverse Model (OCIM) and presented in Chapter II indicate that, at the core location selected to represent the "true" AABW end-member, the

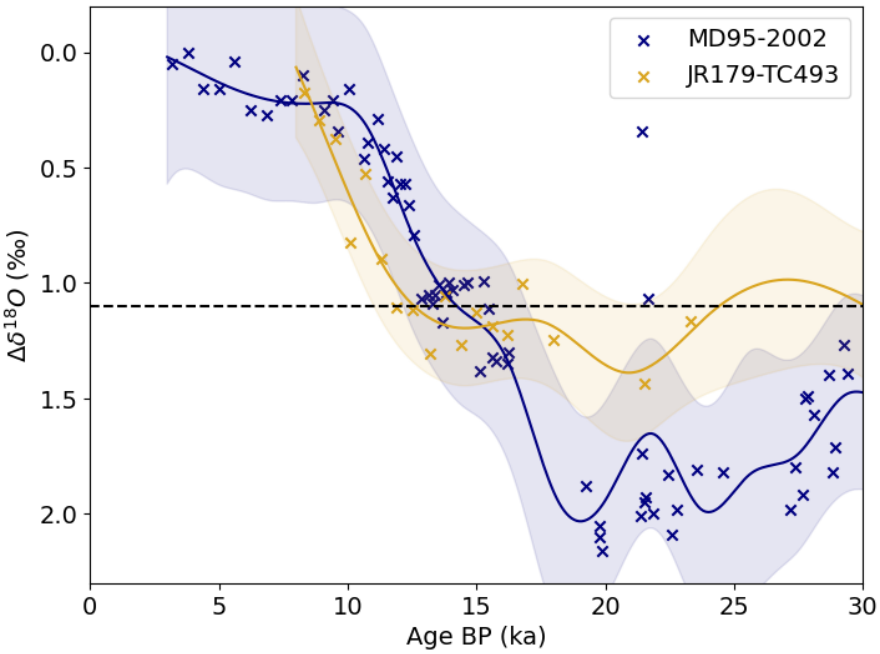

Figure 5.3: The $\delta^{18}O_{CaCO3}$ difference between the Holocene value (referenced in Table 1) and the isotopic record for the sediment cores MD95-2002 (blue) and JR179-TC493 (yellow), representing respectively NADW and AABW. Both time series have been fitted by a GAM, and the dashed line indicates the change of $\delta^{18}O_{CaCO3}$ implied by the sea level change alone.

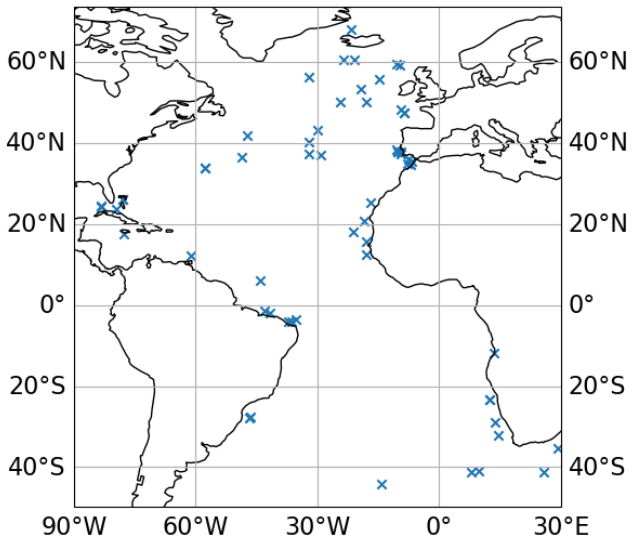

Figure 5.4: Atlantic compilation of the sediment cores used.

Antarctic (AA) fraction is of 56%, the North Atlantic (NA) fraction of 32% and the high-latitude Southern ocean (HS) fraction of 10%. If we assume those fractions to be correct in the modern, then it is already hard to say that this core represents the true Antarctic end-member, while it lies on the Antarctic continental slope. If similar end-member fractions were present at the LGM, then it could explain partly why the change in $\delta^{18}O_{CaCO_3}$ is larger than first expected in Chapter I. Overall, this analysis highlights the difficulty of constraining an end-member value from a single sediment core. The use of multiple cores seems the only viable way to constrain potential changes in ventilation.

3 . Can we observe ventilation changes in the deep Atlantic Ocean?

The Atlantic Ocean has a lot of sediment cores with Cibicidoides (Figure 5.2) and both AABW and NADW water masses should be present at the LGM. Here, we present an Atlantic compilation of sediment cores that have both isotopic records of *Cibicoides wuëllerstorfi, küllenbergi* or *pachyderma* and age models, represented on Figure 5.4. The isotopic record and associated age model of the different sediment cores that we use in this compilation have been manually selected and quality-checked by Waelbroeck et al. (2019). Since every sediment core has an associated age model, we can select a $\delta^{18}O_{CaCO3}$ value for the Holocene and the LGM based on computed ages. The Holocene value is averaged between 0 and 3 ky or 6 ky if there are no values in the first interval. Similarly, the LGM value is obtained by averaging the $\delta^{18}O_{CaCO3}$ between 19 and 21 ky or 18 and 23 ky if the first interval has no data.

Figure 5.5 shows the $\delta^{18}O_{CaCO3}$ values obtained for the Holocene, the LGM and the difference in $\delta^{18}O_{CaCO3}$ ($\Delta\delta^{18}O_{CaCO3}$) between the two periods. The Holocene values show a constant gradient with depth confirming the deep $\delta^{18}O_{CaCO3}$ structure observed in Figure 5.1b. The glacial deep $\delta^{18}O_{CaCO3}$ seems to be fairly uniform below 2 km and no clear gradient can be observed there. However, the $\Delta\delta^{18}O_{CaCO3}$

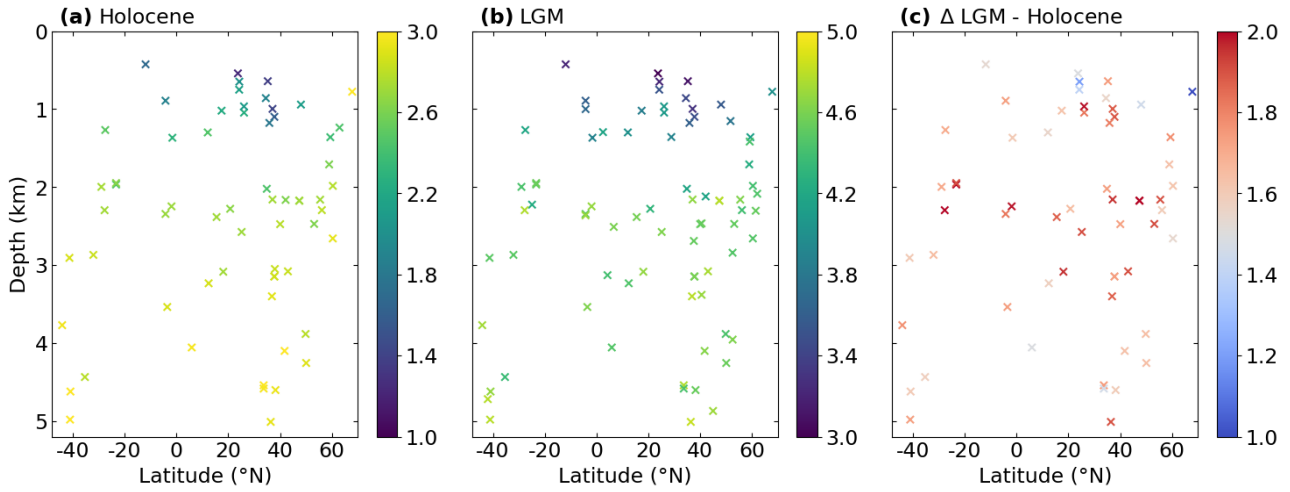

Figure 5.5: $\delta^{18}O_{CaCO3}$ values of the Atlantic sediment cores compilation, for the Holocene **(a)**, the LGM **(b)** and the difference between the two **(c)**.

shows an interesting pattern: between 2 and 3 km, the sediment cores show the biggest difference in $\delta^{18}O_{CaCO3}$. The signal is even clearer if we take the Holocene (respectively LGM) value as the minimum (respectively maximum) and not the average of the Holocene (respectively LGM) age interval (see Figure SI).

This large $\Delta\delta^{18}O_{CaCO_3}$ signal in the mid-depths of the Atlantic coincides with the proposed core of glacial NADW (Gebbie, 2014), and seems logical based on the expected temperature change of glacial NADW. Since this maximum is seen only at mid-depths and not in the deep Atlantic, it begs the question of whether or not this signal can be interpreted as a change in ventilation source in a certain depth range. Indeed, this change cannot be seen in the deepest part of the basin, which may indicate a change of ventilation source there, e.g. shifting from a modern NADW to a glacial AABW. However, as $\Delta\delta^{18}O_{CaCO_3}$ varies both as a function of temperature and $\delta^{18}O_{sw}$, a ventilation change cannot be directly quantified from this: the temperature and $\delta^{18}O_{sw}$ of the modern NADW end-member are not constant with depth, resulting in a non-homogeneous $\delta^{18}O_{CaCO_3}$ in the deep Atlantic (Figure 5.1b).

Figure 5.6 shows the change between the Holocene and LGM in $\delta^{18}O_{CaCO_3}$ and $\delta^{13}C_{CaCO_3}$ of the presented Atlantic compilation. The sediment cores of our compilation were grouped by depth and then averaged to show the $\Delta\delta^{18}O_{CaCO_3}$ signal with depth averaged over the basin. The $\Delta\delta^{13}C_{CaCO_3}$ has the same structure as the 'canonical' structure from Curry and Oppo (2005), that was interpreted as the change from northern source end-member to southern-source end-member for the deep glacial ocean, although this interpretation has been questioned (Gebbie, 2014; Kwon et al., 2012). The averaged $\Delta\delta^{18}O_{Ca_CO3}$ exhibits a gradient between the mid-depths and the deep (excluding the deepest point) of about ∼0.3‰. Following Marchitto et al. (2014), this $\delta^{18}O_{CaCO3}$ change, if driven by temperature alone, would be associated to about 1.5°C change, which coincides with the modern temperature variation between 2 and 4.5 km deep at 30°N in the WOCE climatology (Gouretski and Koltermann, 2004). Thus if glacial temperatures were uniform between these depths, the $\Delta\delta^{18}O_{CaCO3}$ change would be explained only by this temperature change, and not necessarily a change in the ventilation source. If there were a similar temperature difference between

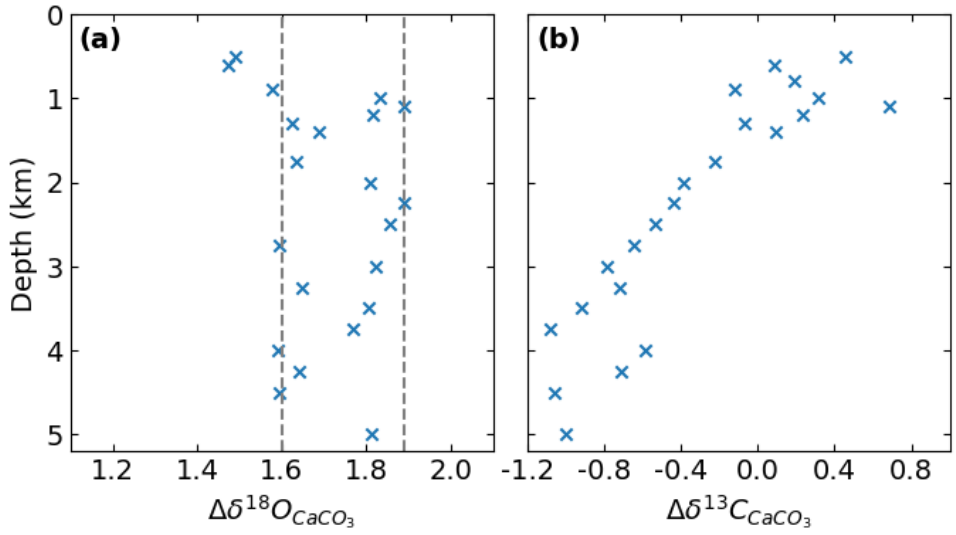

Figure 5.6: Change in $\delta^{18}O_{CaCO3}$ **(a)** and $\delta^{13}C_{CaCO_3}$ **(b)** between the Holocene and LGM of the Atlantic compilation (Waelbroeck et al., 2019) as a function of depth. Sediment cores were grouped by depth and then averaged.

2 and 4.5 km at the LGM than at the present, then this $\Delta\delta^{18}O_{CaCO3}$ change indicate a change of ventilation source (and thus $\delta^{18}O_{sw}$). Hence, the signal we observe in the North Atlantic could indicate two things:

- Deep waters are much more homogeneous in the glacial Atlantic Ocean with almost no gradient between mid-depths and bottom waters.
- NADW was shallower than at present and centered around 2 km depth, and probably replaced in the deep Atlantic by waters last ventilated in the Southern Ocean.

At this point, it is not possible to further argue for one or another hypothesis. However? the use of glacial surface temperature reconstructions coupled with the $\delta^{18}O_{CaCO_3}$ of benthic foraminifera could provide some constraints on the deep $\delta^{18}O_{sw}$ content in the North Atlantic. This would eventually help to confirm or reject either of the above hypotheses.

4 . What do we observe in the Pacific?

The glacial North Pacific sediment cores compilation presented in Chapter I displayed a pronounced $\delta^{18}O_{CaCO3}$ mid-depth maximum. The former hypothesis that this change was due to the glacial $\delta^{18}O_{CaCO3}$ end-members is uncertain because the gradient in sediment cores supposed to represent these end-members cannot be found, or is at least smaller than expected. In the next section, we will focus on the LGM $\delta^{18}O_{CaCO3}$ signal across the Pacific basin, to see if the signal is propagating through the mid-depths as previously thought. We will show data that I produced at the LSCE, as well as some analysis on a compilation of sediment cores that I put together.

	Latitude (°N)	Longitude (°E)	Depth (m)
MD97-2115	-43.1822	-171.8003	2160
MD97-2116	-46.0465	-176.5577	4165
MD01-2385	-0.2200	134.2420	2606
MD98-2183	2.0100	135.0200	4388

Table 2: Location and depth of the different sediment cores that were used to generate new isotopic records.

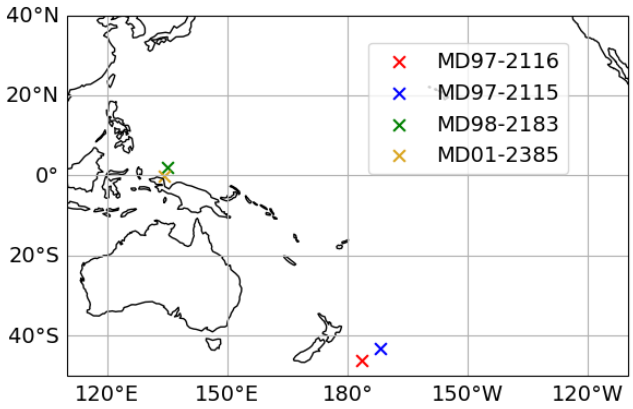

Figure 5.7: Crosses mark the locations of the sediment cores near New Zealand (MD97-2115 and MD97-2116) and near Indonesia (MD01-2385 and MD98-2183).

4.1 . Isotopic records of benthic foraminifera

4.1.1 . New isotopic records produced

Following the North Pacific compilation of Chapter I, and the idea that Upper Circumpolar Deep Water (UCDW) was heavier in $\delta^{18}O_{CaCO_3}$ than AABW, we wanted to track the different water-mass signatures as they diffuse across the Pacific. We thus decided to generate some new benthic isotopic data for two pairs of locations, one in the mid-latitude Pacific near Indonesia, and one in the South Pacific near New Zealand where deep waters "enter" the Pacific. For each location, we analyzed one core at mid-depths (MD97-2115 near New Zealand, and MD01-2385 near Indonesia) supposed to represent UCDW and one near the seafloor (MD97-2116 near New Zealand, and MD98-2183 near Indonesia) supposed to represent AABW. The exact locations and depths of these cores are referenced in Table 2. Figure 5.7 shows their locations.

We analyzed the $\delta^{18}O_{CaCO_3}$, and the $\delta^{13}C_{CaCO_3}$ on different foraminifera species. Here, we only show the data associated to various species of the genus *Cibicidoides* and additional data of the benthic species *Globobulimina affinis* are presented in the Supplementary Information. The different foraminifera species isotopes were measured using a GV Isoprime 100 at the Laboratoire des Sciences du Climat et de l'Environnement (LSCE). The measurements are reported versus Vienna Pee Dee Belemnite (VPDB) standard defined with respect to the NBS19 standard. The mean external reproducibility (1σ) of carbonate standards is ±0.06‰ for $\delta^{18}O_{CaCO_3}$; the different mass spectrometers are regularly inter-calibrated and the data are corrected, depending on the devices, for nonlinearity and the common acid bath.

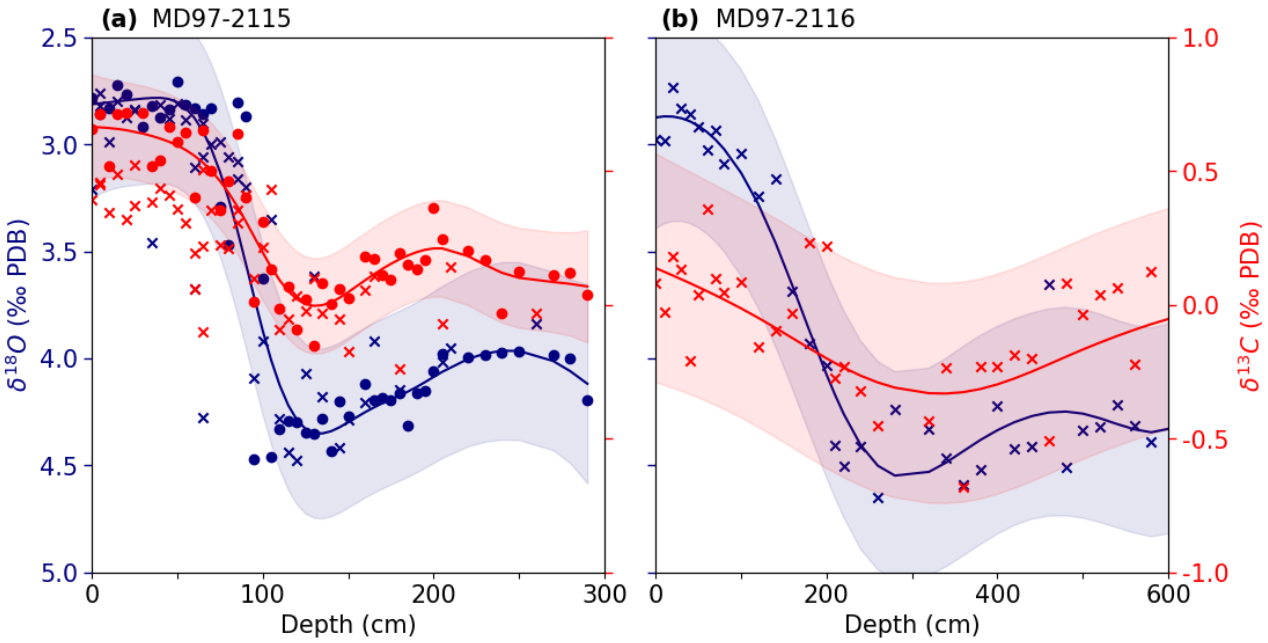

Figure 5.8: The $\delta^{18}O_{CaCO3}$ (represented in blue) and $\delta^{13}C_{CaCO_3}$ (represented in red) of the mid-depth core MD97-2115 **(a)** and the deep core MD97-2116 **(b)** near New Zealand. Circles indicate data points that are associated to *Cibicidoides wüellerstorfi* and crosses indicate *Cibicidoides küllenbergi*. A GAM was passed through the data for both the $\delta^{18}O_{CaCO3}$ and $\delta^{13}C_{CaCO_3}$ of the *C. wüellerstorfi* of MD97-2115 and the *C. kullenbergi* of MD97-2116. The x-axis represents core depth.

We analyzed either *Cibicidoides wüellerstorfi* or *Cibicidoides küllenbergi* that are thought to have about the same $\delta^{18}O_{CaCO3}$ signature. Both species were present in MD97-2115 and a consistent $\delta^{18}O_{CaCO3}$ record does not show a constant difference between the two species (see Figure 5.8a), so we hypothesize that the two species record the same environmental conditions. In Figure 5.8, we present the $\delta^{18}O_{CaCO3}$ and $\delta^{13}C_{CaCO_3}$ associated to our two sediment cores near New Zealand. Both records show the last deglaciation, with a stable $\delta^{18}O_{CaCO3}$ value at the top of the core representing the Holocene, and a maximum around 100 cm for MD97-2115 and 280 cm for MD97-2116, that corresponds to the LGM value. The relative $\delta^{18}O_{CaCO3}$ change between the Holocene and the LGM yields a value of 1.77‰ for the abyssal core and 1.64‰ for the mid-depth core, thus there is a larger change in the abyssal ocean than at mid-depth. Furthermore, the absolute LGM value is also larger for the deeper core. Those results challenge the proposed thesis in Chapter I, which postulated that a $\delta^{18}O_{CaCO3}$ maximum diffused from south to north at mid-depths in the glacial Pacific.

MD97-2115 has relatively low sedimentation rates (twice lower than MD97-2116), and the sediments display indication of major bioturbation in the upper 200 cm (see SI), which raises doubts as to whether the "true" glacial value has been found. We thus look at the other mid-depth core, MD01-2385, to see if we can find a heavy LGM $\delta^{18}O_{CaCO3}$ value. Figure 5.9 shows the $\delta^{18}O_{CaCO3}$ of this record: in comparison to MD97-2115, the $\delta^{18}O_{CaCO3}$ Holocene value is a bit lighter, but the glacial value is of the same order, further questioning the validity of our hypothesis in Chapter I. It is noteworthy, however, that the $\delta^{13}C_{CaCO_3}$ of the record indicates more depleted glacial values for MD01-2385 compared to MD97-2115, consistent

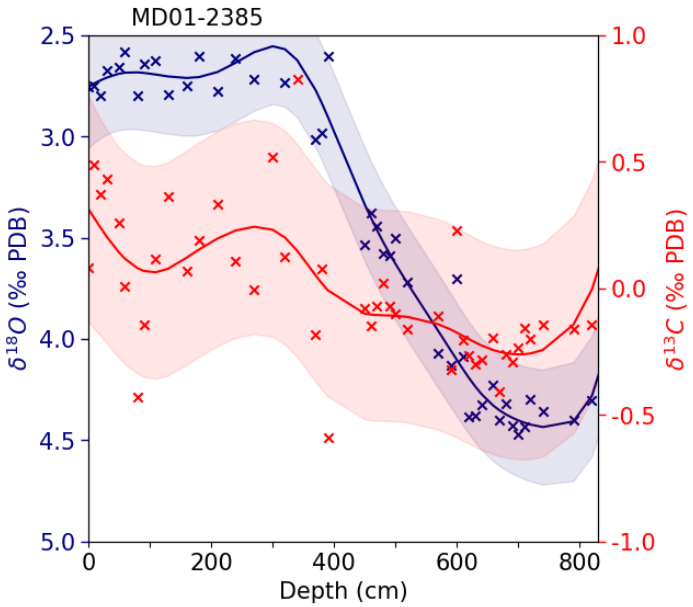

Figure 5.9: $\delta^{18}O_{CaCO3}$ (blue) and $\delta^{13}C_{CaCO_3}$ (red) isotopic records of *C. wüellerstorfi* analyzed in the MD01-2385 sediment core.

with the south to north ventilation of the mid-depth Pacific in the glacial state detailed in Chapter I.

The isotopic records we produced in the Pacific mid-depths thus do not support the idea of a pronounced $\delta^{18}O_{sw}$ mid-depth maximum spreading northward across the glacial Pacific, as hypothesized in Chapter I.

From the isotopic records we produced, and the glacial North Pacific compilation we showed, it is hard to know if a clear $\delta^{18}O_{CaCO3}$ mid-depth maximum could be observed in the Pacific LGM, so we decide to find more isotopic records in the Pacific.

4.1.2 . Pacific compilation of sediment cores

One objective of this PhD was to compile a sufficient number of benthic records to constrain the ventilation of the glacial Pacific. At first, this arduous process was carried out by retrieving data from various databases (NODC, NOAA, PANGAEA...). However, during the course of the PhD, Mulitza et al. (2022) published a large database which aims to compile all the foraminiferal oxygen and carbon isotopes data, and associated radiocarbon ages (the author estimates v1 included around 30% of all available data). Thus, the compilation of *Cibicidoides* that I previously made turned out to be worthwhile in the end because we found over 70 isotopic records of different species that we had and that were not in the original version of the database. In addition to sharing these, I also shared the data that I produced during this PhD to contribute to the v2 of this database (that has a thousand more cores), and became a co-author.

The sediment cores used in our compilation have age models from the different studies where they were published. In the same way as before LGM values were taken as the average over the 19-21 ky age interval. Figure 5.10 shows the map of the sediment core locations and the associated glacial $\delta^{18}O_{CaCO3}$ LGM values in the Pacific as a function of depth and latitude. We see that the high $\delta^{18}O_{CaCO3}$ mid-depth values that we found in the North Pacific (around 50°N) cannot be seen anywhere else, except in the South Pacific where one core exhibits a high value (which was used in Chapter 1 as the UCDW sediment core). It is noteworthy

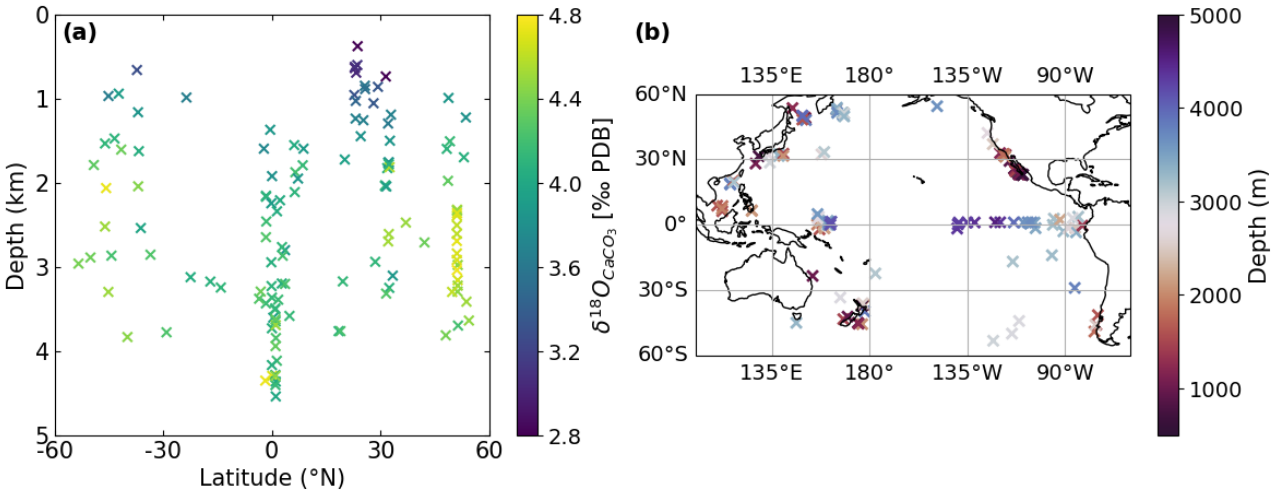

Figure 5.10: **(a)** Pacific $\delta^{18}O_{CaCO3}$ LGM values from our compilation as a function of depth and latitude. **(b)** Locations of the sediment cores included in panel **(a)**, coloured according to seafloor depth.

however that most of the mid-depth sediment cores in the equatorial Pacific may not adequately represent waters ventilating the main Pacific because of their locations: all of these data come from semi-enclosed seas, namely the China Sea, the Panama basin, and the Ontong Java Plateau (Figure 5.10).

4.2 . LGM profiles of BWT and $\delta^{18}O_{sw}$ from the subarctic Pacific

In Chapter I we saw that a depth profile of benthic foraminiferal $\delta^{18}O_{CaCO3}$ in the North Pacific displayed a distinct mid-depth maximum during the LGM. To better understand the temperature and $\delta^{18}O_{sw}$ contributions to this profile we analysed Mg/Ca on benthic foraminifera *Uvigerina* spp from a suite of sediment cores forming a depth transect in the subarctic Pacific used in Chapter I (Keigwin, 1998). Between 10-20 individual benthic forams were picked, cleaned, and measured at the foraminiferal trace element laboratory at LSCE. *Note, because of the time required to learn the methodology that we describe hereafter and the low number of samples that we were going to measure, I did not generate the data myself: the sample preparation and subsequent analysis was performed by Hélène Rebaubier.*

Cleaning followed a modified version of the protocol of Barker et al. (2003). Foraminiferal tests were gently opened between two glass plates and the resulting fragments were loaded into acid leached microvials. Clays were removed through repeated ultrasonic cleaning with 18.2 MΩ water. Fe-Mn oxyhydroxide coatings were removed using the protocol of Boyle and Keigwin (1985). Samples were reductively cleaned in a solution of hydrazine and ammonium citrate for 20 minutes at 80°C. In order to remove potential organic contaminants, the samples were oxidized using a solution of 1% H_2O_2 buffered with 0.1 M NH_4OH for 20 minutes at 80°C. The final cleaning treatment consists in a rapid leaching with 0.001 M HNO_3, before dissolution in 0.15 M HNO_3. Samples are centrifuged immediately after dissolution and transferred to a new acid-leached centrifuge tube, leaving a residual $\sim$ 10 µl, which helps exclude any remaining undissolved contaminants. Trace metal grade (NORMATOM) acids are used throughout and a boron-free MilliQ cartridge is used to generate clean water. All work was carried out in a dedicated laminar-flow hood within an over-pressured clean lab, with boron-free HEPA filters fitted throughout.

A 10 ul aliquot of sample was utilised to determine the calcium concentration. Aliquots of each sample were then diluted to a calcium concentration of 1 mM [Ca], to match that of the bracketing standards. A suite of major and trace elements (Li, B, Na, Mg, Al, Ca, Mn, Sr, Cd, Ba, Nd, U) were analysed on an Analytik Jena PlasmaQuant ELITE quadrupole ICP-MS at LSCE. Analysis followed a modified version of the method of Yu et al. (2005) against in-house standards prepared from single elementary solutions. In order to minimise boron blanks a solution of 0.5 M HNO_3 and 0.3 M HF is used as the matrix for the samples and standards as well as the rinse, following the method of Misra et al. (2014). This results in low and stable boron blanks, with a [B] detection limit typically less than 10 ppt. Instrumental precision was determined based on multiple replicates of a standard solution of known composition. Mg/Ca has a long term precision of <2% (2RSD), and analysis of external standard NIST RM 8301 Foram gives a value of 2.65±0.02 (1σ), in excellent agreement with the stated value of 2.62±0.14 (Stewart et al., 2021). Al/Ca was <20 μmol/mol in all samples indicating efficient removal of clays. Repeated cleaning/analysis (n=10) of the LGM sample from core NES 25-1 GG27 indicates a total analytical uncertainty of ±0.01 mol/mmol (1σ), equivalent to an RSD of <3%.

Mg/Ca was converted to temperature following the equation (Gray, 2014) :

$$Mg/Ca = 0.095 \pm 0.006(BWT) + 0.58 \pm 0.04$$

where BWT stands for Bottom Water Temperature. This equation is based on a global compilation of coretops, including data from the North Pacific; it has a similar temperature sensitivity to existing equations (Elderfield et al., 2006) but indicates no detectable influence of carbonate ion saturation on Mg/Ca in Uvigerina. The standard error is equivalent to a temperature uncertainty of ±1.25 °C.

Another hypothesis to explain the observed mid-depth maximum in $\delta^{18}O_{CaCO3}$ in the North Pacific was a possible inversion in the temperature profile, with abyssal waters warmer than the mid-depth waters due to geothermal heat trapped in the salty abyss (see Chapter I, 4.3). This hypothesis was deemed to be rather unlikely. Here we examine again this hypothesis using the calculated BWTs shown on Figure 5.11. Along with the BWTs, measured coretop temperatures from the sites are around 1°C warmer than instrumental temperatures reconstructions (although falling within the standard error), and we adjust the LGM temperatures by this anomaly; however, we interpret relative changes in temperature with depth only (i.e., the vertical profile). The data show a profile very similar to the modern one, with very little change in temperature with depth. This confirms that the observed changes in the $\delta^{18}O_{CaCO3}$ profile must be driven by changes in $\delta^{18}O_{sw}$, rather than temperature, ruling out the geothermal heat trapping hypothesis. We calculate $\delta^{18}O_{sw}$ using the Uvigerina equation from Marchitto et al. (2014), correcting for the 1 per mil whole ocean change (Adkins et al., 2002). The resulting $\delta^{18}O_{sw}$ profile shows much larger vertical gradients in $\delta^{18}O_{sw}$, with a strong mid-depth maximum, and more depleted values in both the intermediate depths and abyss. Apart from the mid-depth $\delta^{18}O_{CaCO3}$ maximum, we observe a very large gradient in $\delta^{18}O_{sw}$ between 1-2 km depth. Such a large gradient in $\delta^{18}O_{sw}$ can only be driven by the advection of a depleted $\delta^{18}O_{sw}$ water mass in the intermediate depths and indicates the presence of enhanced North Pacific intermediate overturning. The measurements thus point towards enhanced NPIW formation as the driver of the enhanced ventilation of the intermediate North Pacific observed in non-conservative tracers during the LGM (Keigwin, 1998; Matsumoto et al., 2002; Rae et al., 2020). While shoaled NADW is seen as a 'canonical' feature of the LGM ocean, deepened NPIW is not, yet it provides an equally large signal to test the overturning response in climate models under glacial forcings.

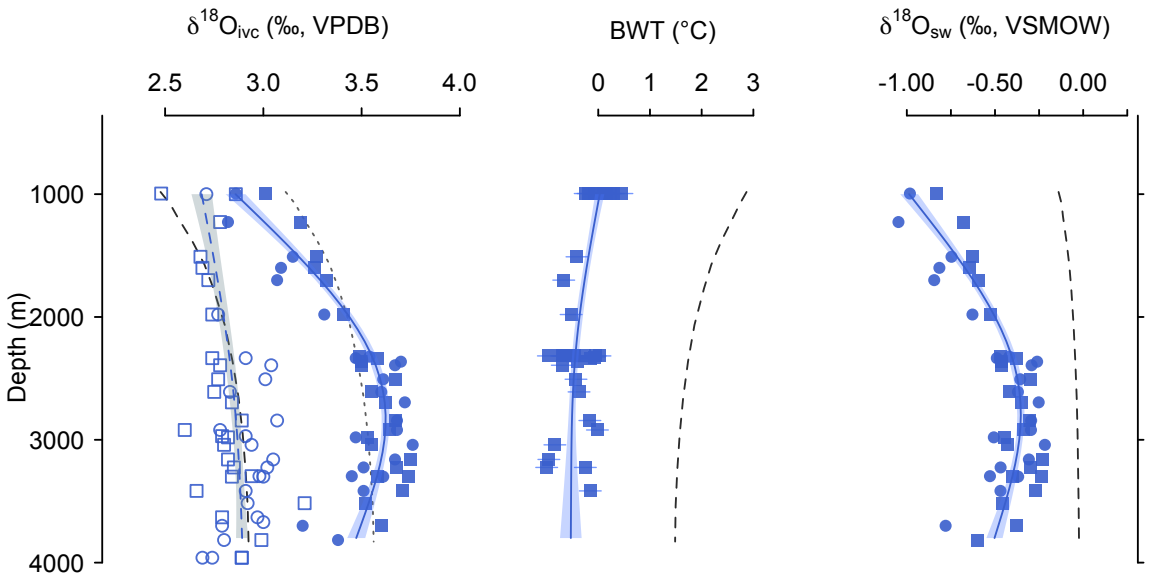

Figure 5.11: Vertical profiles in the subarctic Pacific of (left) $\delta^{18}O_{CaCO3}$ as measured by Keigwin (1998), (center) reconstructed Bottom Water Temperature, and (right) calculated $\delta^{18}O_{sw}$ based on $\delta^{18}O_{CaCO3}$ and BWT profiles combined with the equation of Marchitto et al. (2014). Blue filled points indicate glacial values while the points that are not filled represent modern values. Rectangles indicate that the species used are *Uvigerina peregrina* and circles indicate *Cibicidoides*. Black dashed lines represent the modern profiles, extracted from LeGrande and Schmidt (2006) for $\delta^{18}O_{sw}$, extracted from the WOCE climatology for temperatures, and computed with the latter two for $\delta^{18}O_{CaCO3}$. GAMs have been fitted to the different profiles to help show the different structures. The dotted line shows the modern $\delta^{18}O_{CaCO3}$ profile adjusted by the mean offset between LGM and Holocene.

5 . Conclusion & Perspectives

The first objective of this chapter was to study the causes of the North Pacific LGM $\delta^{18}O_{CaCO3}$ mid-depth maximum commented on in Chapter I. A large compilation of data and generation of new records show that the mid-depth maximum we observe in the northern North Pacific is not observed across the wider basin. It could imply that the mid-depth glacial signal is badly represented by the sediment cores compiled here, or that we initially over-interpreted the North Pacific glacial profile.

Nonetheless, we would like to draw the reader's attention to the fact that the glacial circulation structure proposed in Chapter I is qualitatively compatible with the ventilation patterns simulated by NEMO in Chapter II. NEMO experiments indeed demonstrate that a mid-depth maximum in Pacific conservative tracers generated by isopycnal diffusion of a signal contained in NADW is plausible, even with a modern-like density stratification in the Pacific. In these NEMO experiments, necessary ingredients appear to be merely (i) a small light and shallow bias of NADW relative to modern observations (Rathore et al., 2024), and (ii) relatively weak bulk diapycnal mixing rates (Chapter II, section 3.2).

The emergence of a database that compiles all isotopic records and associated radiocarbon ages leaves room for coherent reconstructions of the glacial properties. We deem crucial to find methods that allow one to treat the sediment cores and associated ages in a systematic way (Supplementary Information). In addition to potentially help constrain ventilation changes, the variation of the different glacial water masses may allow us to understand the changes in the mechanisms that led to the deep water masses.

Furthermore, the strong intermediate $\delta^{18}O_{sw}$ signal in the North Pacific advocates for an expansion of the glacial NPIW. Finding appropriate sediment cores to study the reach and extent of this glacial water mass might be key to infer changes in glacial biogechemical cycles, given its importance in modern cycles (Sarmiento et al., 2004).

References

Adkins, J. F., McIntyre, K., & Schrag, D. P. (2002). The salinity, temperature, and $\delta^{18}O$ of the glacial deep ocean. *Science*, *298*(5599), 1769–1773. https://doi.org/10.1126/science.1076252

Barker, S., Greaves, M., & Elderfield, H. (2003). A study of cleaning procedures used for foraminiferal mg/ca paleothermometry. *Geochemistry, Geophysics, Geosystems*, *4*(9). https://doi.org/10.1029/2003GC000559

Blaauw, M., & Christen, J. A. (2011). Flexible paleoclimate age-depth models using an autoregressive gamma process. *Bayesian Analysis*, *6*(3), 457 –474. https://doi.org/10.1214/11-BA618

Boyle, E., & Keigwin, L. (1985). Comparison of atlantic and pacific paleochemical records for the last 215,000 years: Changes in deep ocean circulation and chemical inventories. *Earth and Planetary Science Letters*, *76*(1), 135–150. https://doi.org/10.1016/0012-821X(85)90154-2

Butzin, M., Köhler, P., & Lohmann, G. (2017). Marine radiocarbon reservoir age simulations for the past 50,000 years. *Geophysical Research Letters*, *44*(16), 8473–8480. https://doi.org/10.1002/2017GL074688

Curry, W. B., & Oppo, D. W. (2005). Glacial water mass geometry and the distribution of δ13c of Σco2 in the western atlantic ocean. *Paleoceanography*, *20*(1). https://doi.org/https://doi.org/10.1029/2004PA001021

Duplessy, J.-C., Labeyrie, L., & Waelbroeck, C. (2002). Constraints on the ocean oxygen isotopic enrichment between the last glacial maximum and the holocene: Paleoceanographic implications [EPILOG]. *Quaternary Science Reviews*, *21*(1), 315–330. https://doi.org/10.1016/S0277-3791(01)00107-X

Elderfield, H., Yu, J., Anand, P., Kiefer, T., & Nyland, B. (2006). Calibrations for benthic foraminiferal mg/ca paleothermometry and the carbonate ion hypothesis. *Earth and Planetary Science Letters*, *250*(3), 633–649. https://doi.org/10.1016/j.epsl.2006.07.041

Ferrari, R., Jansen, M. F., Adkins, J. F., Burke, A., Stewart, A. L., & Thompson, A. F. (2014). Antarctic sea ice control on ocean circulation in present and glacial climates. *Proceedings of the National Academy of Sciences*, *111*(24), 8753–8758. https://doi.org/10.1073/pnas.1323922111

Gebbie, G. (2014). How much did glacial north atlantic water shoal? *Paleoceanography*, *29*(3), 190–209. https://doi.org/10.1002/2013PA002557

Gouretski, V., & Koltermann, K. P. (2004). Woce global hydrographic climatology. *Berichte des BSH*, *35*, 1–52.

Gray. (2014). *The role of the north pacific ocean in the deglacial co2 rise: Insights from trace elements and boron isotopes in biogenic carbonates*. University College London. https://books.google.fr/books?id=RImC0AEACAAJ

Gray, de Lavergne, C., Jnglin Wills, R. C., Menviel, L., Spence, P., Holzer, M., Kageyama, M., & Michel, E. (2023). Poleward shift in the southern hemisphere westerly winds syn-

chronous with the deglacial rise in co2 [e2023PA004666 2023PA004666]. *Paleoceanography and Paleoclimatology*, *38*(7), e2023PA004666. https://doi.org/10.1029/2023PA004666
Hoogakker, B., Elderfield, H., Oliver, K., & Crowhurst, S. (2010). Benthic foraminiferal oxygen isotope offsets over the last glacial-interglacial cycle. *Paleoceanography*, *25*(4). https://doi.org/10.1029/2009PA001870
Hoogakker, B. A. A., Elderfield, H., Schmiedl, G., McCave, I. N., & Rickaby, R. E. M. (2015). Glacial–interglacial changes in bottom-water oxygen content on the portuguese margin. *Nature Geoscience*, *8*(1), 40–43. https://doi.org/10.1038/ngeo2317
Keigwin, L. D. (1998). Glacial-age hydrography of the far northwest pacific ocean. *Paleoceanography*, *13*(4), 323–339. https://doi.org/10.1029/98PA00874
Key, R. M., Kozyr, A., Sabine, C., Lee, K., Wanninkhof, R., Bullister, J., Feely, R., Milero, F., Mordy, C., & Peng, T.-H. (2004). A global ocean carbon climatology: Results from global data analysis project (glodap). *Global Biogeochemical Cycles*, *18*(4), GB4031. https://doi.org/10.1029/2004GB002247
Kwon, E. Y., Hain, M. P., Sigman, D. M., Galbraith, E. D., Sarmiento, J. L., & Toggweiler, J. R. (2012). North atlantic ventilation of "southern-sourced" deep water in the glacial ocean. *Paleoceanography*, *27*(2). https://doi.org/10.1029/2011PA002211
LeGrande, A. N., & Schmidt. (2006). Global gridded data set of the oxygen isotopic composition in seawater. *Geophysical Research Letters*, *33*(12). https://doi.org/10.1029/2006GL026011
Lisiecki, L. E., & Stern, J. V. (2016). Regional and global benthic δ18o stacks for the last glacial cycle. *Paleoceanography*, *31*(10), 1368–1394. https://doi.org/10.1002/2016PA003002
Marchitto, T., Curry, W., Lynch-Stieglitz, J., Bryan, S., Cobb, K., & Lund, D. (2014). Improved oxygen isotope temperature calibrations for cosmopolitan benthic foraminifera. *Geochimica et Cosmochimica Acta*, *130*, 1–11. https://doi.org/10.1016/j.gca.2013.12.034
Matsumoto, K., Oba, T., Lynch-Stieglitz, J., & Yamamoto, H. (2002). Interior hydrography and circulation of the glacial pacific ocean. *Quaternary Science Reviews*, *21*(14), 1693–1704. https://doi.org/10.1016/S0277-3791(01)00142-1
Misra, S., Greaves, M., Owen, R., Kerr, J., Elmore, A. C., & Elderfield, H. (2014). Determination of b/ca of natural carbonates by hr-icp-ms. *Geochemistry, Geophysics, Geosystems*, *15*(4), 1617–1628. https://doi.org/10.1002/2013GC005049
Mulitza, S., Bickert, T., Bostock, H. C., Chiessi, C. M., Donner, B., Govin, A., Harada, N., Huang, E., Johnstone, H., Kuhnert, H., Langner, M., Lamy, F., Lembke-Jene, L., Lisiecki, L., Lynch-Stieglitz, J., Max, L., Mohtadi, M., Mollenhauer, G., Muglia, J., … Tiedemann, R. (2022). World atlas of late quaternary foraminiferal oxygen and carbon isotope ratios. *Earth System Science Data*, *14*(6), 2553–2611. https://doi.org/10.5194/essd-14-2553-2022
Olsen, A., Key, R. M., van Heuven, S., Lauvset, S. K., Velo, A., Lin, X., Schirnick, C., Kozyr, A., Tanhua, T., Hoppema, M., Jutterström, S., Steinfeldt, R., Jeansson, E., Ishii, M., Pérez, F. F., & Suzuki, T. (2016). The global ocean data analysis project version 2 (glodapv2) – an internally consistent data product for the world ocean. *Earth System Science Data*, *8*(2), 297–323. https://doi.org/10.5194/essd-8-297-2016

Rae, J. W. B., Gray, W. R., Wills, R. C. J., Eisenman, I., Fitzhugh, B., Fotheringham, M., Littley, E. F. M., Rafter, P. A., Rees-Owen, R., Ridgwell, A., Taylor, B., & Burke, A. (2020). Overturning circulation, nutrient limitation, and warming in the glacial north pacific. *Science Advances*, *6*(50), eabd1654. https://doi.org/10.1126/sciadv.abd1654

Sarmiento, J. L., Gruber, N., Brzezinski, M. A., & Dunne, J. P. (2004). High-latitude controls of thermocline nutrients and low latitude biological productivity. *Nature*, *427*(6969), 56–60. https://doi.org/10.1038/nature02127

Stewart, J. A., Christopher, S. J., Kucklick, J. R., Bordier, L., Chalk, T. B., Dapoigny, A., Douville, E., Foster, G. L., Gray, W. R., Greenop, R., Gutjahr, M., Hemsing, F., Henehan, M. J., Holdship, P., Hsieh, Y.-T., Kolevica, A., Lin, Y.-P., Mawbey, E. M., Rae, J. W. B., … Day, R. D. (2021). Nist rm 8301 boron isotopes in marine carbonate (simulated coral and foraminifera solutions): Inter-laboratory δ11b and trace element ratio value assignment. *Geostandards and Geoanalytical Research*, *45*(1), 77–96. https://doi.org/10.1111/ggr.12363

Waelbroeck, C., Labeyrie, L., Michel, E., Duplessy, J., McManus, J., Lambeck, K., Balbon, E., & Labracherie, M. (2002). Sea-level and deep water temperature changes derived from benthic foraminifera isotopic records [EPILOG]. *Quaternary Science Reviews*, *21*(1), 295–305. https://doi.org/https://doi.org/10.1016/S0277-3791(01)00101-9

Waelbroeck, C., Lougheed, B. C., Vazquez Riveiros, N., Missiaen, L., Pedro, J., Dokken, T., Hajdas, I., Wacker, L., Abbott, P., Dumoulin, J.-P., et al. (2019). Consistently dated atlantic sediment cores over the last 40 thousand years. *Scientific data*, *6*(1), 165.

Weiss, R., Östlund, H., & Craig, H. (1979). Geochemical studies of the weddell sea. *Deep Sea Research Part A. Oceanographic Research Papers*, *26*(10), 1093–1120. https://doi.org/10.1016/0198-0149(79)90059-1

Williams, T. J., Hillenbrand, C.-D., Piotrowski, A. M., Allen, C. S., Frederichs, T., Smith, J. A., Ehrmann, W., & Hodell, D. A. (2019). Paleocirculation and ventilation history of southern ocean sourced deep water masses during the last 800,000 years. *Paleoceanography and Paleoclimatology*, *34*(5), 833–852. https://doi.org/10.1029/2018PA003472

Wunsch, C. (2016). Pore fluids and the lgm ocean salinity—reconsidered. *Quaternary Science Reviews*, *135*, 154–170. https://doi.org/10.1016/j.quascirev.2016.01.015

Yu, J., Day, J., Greaves, M., & Elderfield, H. (2005). Determination of multiple element/calcium ratios in foraminiferal calcite by quadrupole icp-ms. *Geochemistry, Geophysics, Geosystems*, *6*(8). https://doi.org/10.1029/2005GC000964

Supplementary information

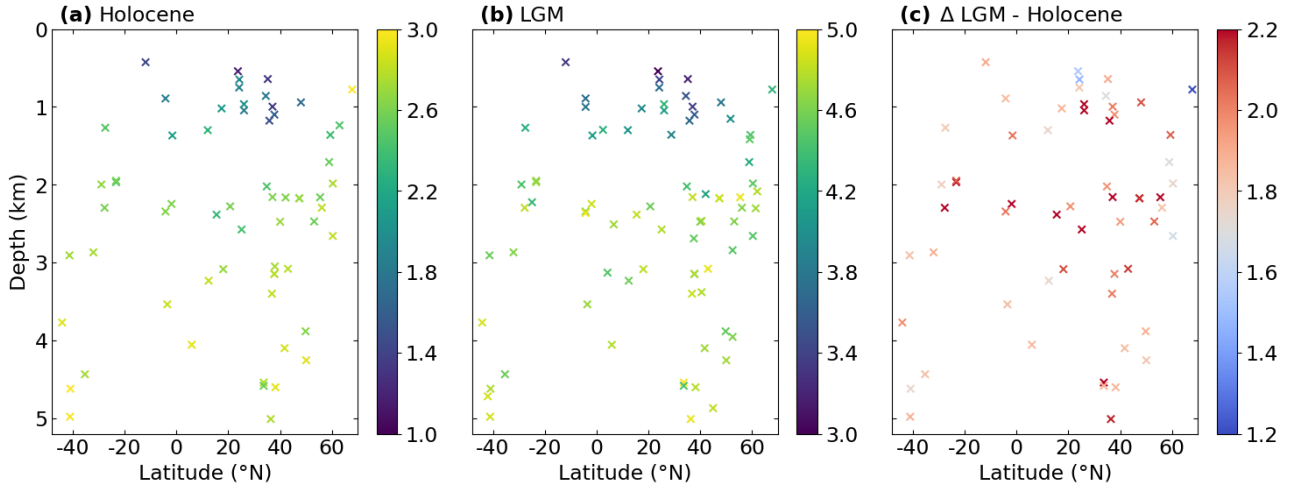

Figure S5.1: Similar to Figure 5.5, but by selecting the LGM and Holocene by taking as the maximum and minimum of their age interval.

Bioturbation in MD97-2115

The results from the sediment core MD97-2115 that we analyzed and on which we put a lot of work suggest in underwent substantial bioturbation. We show evidence of this by first showing the differences in $\delta^{18}O_{CaCO3}$ and $\delta^{13}C_{CaCO_3}$ between two benthic species, and second by showing planktonic and benthic radiocarbon ages.

Differences between *Globobulimina affinis* and *Cibicidoides wüellerstorfi*

While picking Cibicidoides to be analyzed in the sediment of the MD97-2115 core, we came across specimens of the species *Globobulimina affinis*. It was demonstrated that the difference in $\delta^{13}C_{CaCO_3}$ between *G. affinis* and the *C. wüellerstorfi* can be linked to oxygen in Hoogakker et al. (2015). Figure S5.2 shows the difference in $\delta^{13}C_{CaCO_3}$ and d18o between the two species for the MD97-2115 core. The number of *G. affinis* was not constant across the sediment core: a lot more specimens were found near the glacial levels (Depth $\geq$ 100cm) than at the top of the core. Figure S5.2.b show the $\delta^{18}O_{CaCO3}$ difference between the two species for every depth where they were both found. If all specimens lived around the same epoch, then the $\Delta\delta^{18}O_{CaCO3}$ should be a constant line. We see that it is mostly the case (blue points) but some exceptions (red points) are visible and mainly in the first 100cm of the core. In order to compute the mean $\Delta\delta^{13}C_{CaCO_3}$ for both periods, we exclude the levels for which the $\Delta\delta^{18}O_{CaCO3}$ exceeds by 0.3‰ the offset between the two species (Hoogakker et al., 2010, of 0.9‰ following), that are represented by red points for both panels of Figure S5.2.

We find values of oxygen of 173 and 102 µmol/kg for the modern and LGM at the core location. Interpolating the oxygen product of Glodap v2 (Olsen et al., 2016), we find a modern oxygen value of 167

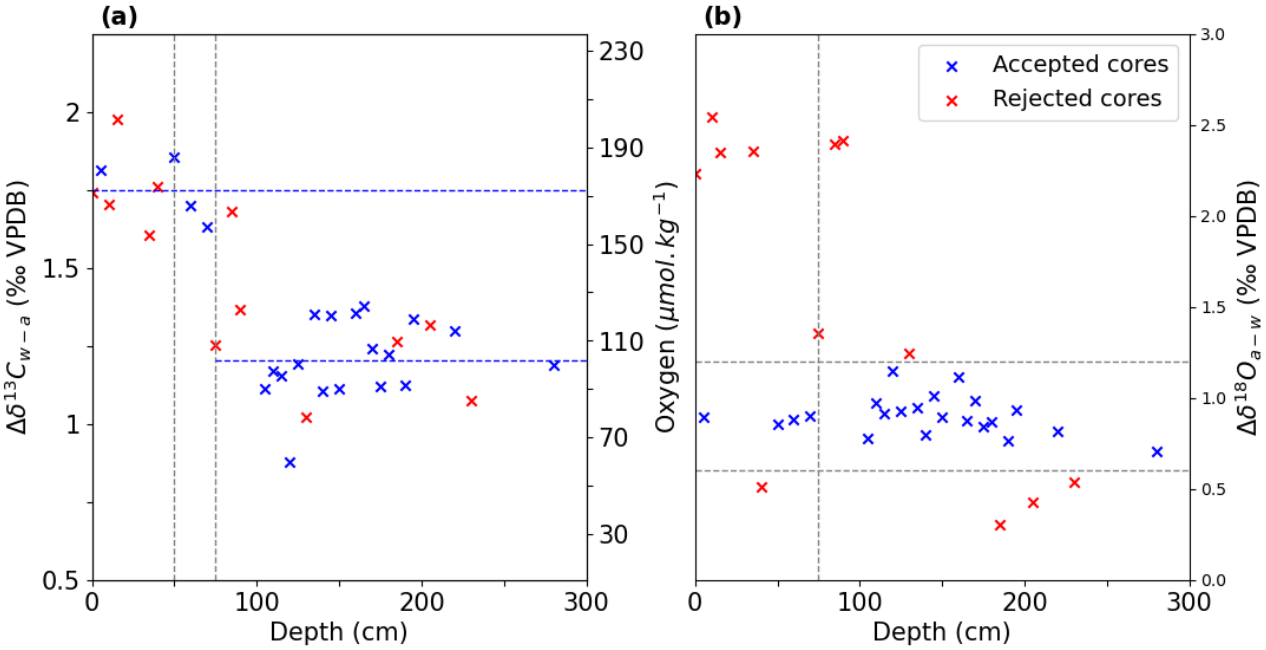

Figure S5.2: $\delta^{13}C_{CaCO_3}$ **(a)** and $\delta^{18}O_{CaCO3}$ **(b)** differences between the *G. affinis* and *C. wüellerstorfi* species. Red points indicate levels that have been rejected based on their $\delta^{18}O_{CaCO3}$ difference and blue points indicate levels that were accepted. The horizontal dashed grey lines in panel **(b)** indicate the $\delta^{18}O_{CaCO3}$ interval that we used to discriminate the different levels. In both panels, the vertical dashed grey line indicate the separation between the Holocene and Glacial intervals.

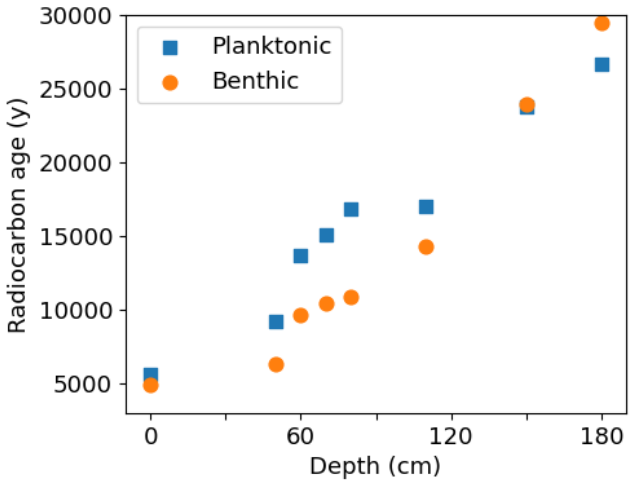

Figure S5.3: Planktonic and benthic radiocarbon ages measured in MD97-2115.

µmol/kg at the core location, giving credit to our result. A 70 µmol/kg decrease in oxygen during the LGM would imply a large increase in the amount carbon stored in these deepwaters by the biological pump.

Benthic and Planktonic ages

Prior to this thesis, radiocarbon ages were measured at the CEA *Globigerina bulloides*, and various benthic foraminifera species which thus led to both planktonic and benthic ages. The ages are not calibrated and are represented on Figure S5.3, and we see that in the upper 150cm of the core, the benthic ages are younger than the planktonic. This is not supposed to happen in theory, as the ^{14}C age is usually older for deep waters than surface waters. This inversion in the ages is attributed to bioturbation caused by worms that live in the sediments and that results in an uneven mixing of the foraminifera species.

Consistent use of the World Atlas

The World Atlas of late Quaternary Foraminiferal Oxygen and Carbon Isotope Ratios (World Atlas) presented in Mulitza et al. (2022) is a database that compiles foraminiferal oxygen and carbon isotopic records. Radiocarbon measurements that allow the calculation of age models associated to the isotopic records are also available in this database: 1001 radiocarbon series will be available in the v2 of the database, associated to the 3047 isotopic records. Reaching this number of isotopic records and radiocarbon series, it becomes really time-consuming to analyze each record independently. A part of this thesis therefore focused on trying to process the database in a systematic way. We think that it is all the more important as each database update adds new isotopic records, and could be instantly processed if adequate methods were implemented. Among the ideas that were investigated are: the systematic calculation of age models based on radiocarbon measurements, and analyzing the differences in timing of the glacial signal between benthic and planktonic species. We will discuss both ideas in turn.

Age models

Radiocarbon series are available in the The World Atlas , but this is not sufficient to get the age model: the ages need to be calibrated. Indeed, the ^{14}C concentration in the atmosphere is not constant through time due to the influence of the Earth's magnetic field and solar activity on long timescale, and more recently nuclear bomb testing and the burning of fossil fuels. In order to calibrate the radiocarbon ages, we use Bacon which is a software that divides a sediment core up into equally-sized sections, and assumes a linear accumulation within each section (Blaauw and Christen, 2011). Accumulation rates can change between the sections, and it can use radiocarbon dates, and calibrates them as it runs. For the calibration, different calibration curves can be used and we use Marine20 in most cases which is the calibration curve for the marine organisms.

In addition to calibrating the age, another thing needs to be accounted for: the reservoir ages. Planktonic foraminifera incorporate the ^{14}C signal of their environment: the surface ocean. The reservoir age thus refers to the concentration difference in ^{14}C between the surface ocean and the atmosphere. The reservoir age varies a lot as a function of latitude, since it depends both on the time that surface waters have to equilibrate their ^{14}C concentration with the atmosphere through sea-gas exchange. Hence, it cannot be approximated to a single value for the surface ocean. It is easily obtained in the modern ocean by taking the ^{14}C value of the surface ocean at the location above the sediment core. This value needs to be corrected however from the anthropogenic ^{14}C emissions, but is available in the product of Key et al. (2004). For other periods such as the LGM and the deglaciation, it is much more complicated to know how surface ^{14}C may have varied. We take the values found by Butzin et al. (2017), that simulated the marine radiocarbon ages of surface waters using a three-dimensional ocean circulation model for the past 50,000 years. For now, we deduced the reservoir age based on the calibrated age that we found using MarineCal and the modern reservoir age. This can be called into question, as the reservoir ages influence the computed ages and can thus affect the calibrating of the ages. A more precise method would be to compute a few iterations of the calibrated ages by correcting it from the reservoir ages calculated from the first iteration, until the corrected and calibrated ages converge to a unique solution. However, given the uncertainties associated to the calibration of the ages we do not think that it will lead to big differences.

Before computing the age models, we excluded the radiocarbon series with a single value. Figure S5.4 shows a typical output of the age model from bacon calibrated and corrected from the reservoir ages. The age model shown derives from many different ^{14}C dates, and the sediment cores has high sedimentation rates (mean at 26.5 yr/cm). However, not all age models are this neat, and we can wonder about the quality of computing the age models without quality checks.

We decided to use the cores from The World Atlas in the Atlantic and the computed age models to try the same exercise as the one presented in Section 3. In Figure S5.5, we present the $\delta^{18}O_{CaCO3}$ of the Holocene, LGM and the difference between the two of these sediment cores, similarly as in Figure 5.5. We see that for the three periods, the patterns that were discussed before are overall noisier, but nonetheless, it would seem that they are still present. Figure S5.6 shows the same information as Figure 5.6 but for the sediment cores of the World Atlas. The $\Delta\delta^{18}O_{CaCO3}$ contrast between the mid-depth and the abyss in the Atlantic is reduced in the World Atlas compilation. We attribute this to isotopic records and age models that are less trustworthy as they were not quality checked.

The limits of our methodology are shown here, as we are unable to reproduce the quality of a manually checked signal. However, finding criteria to discriminate between cores and age models would seem to be the

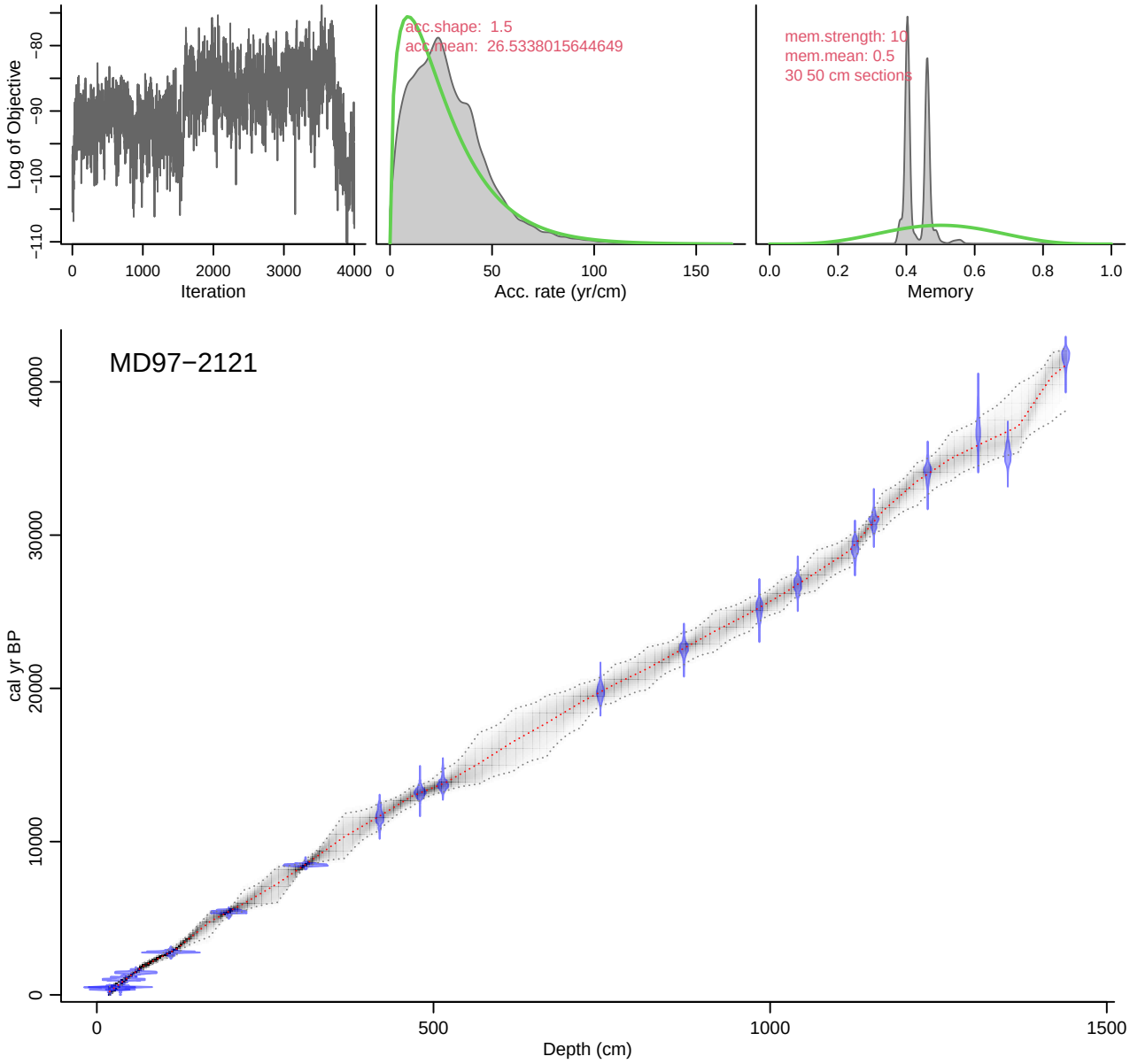

Figure S5.4: The Bacon age model ouput from our calculation for the sediment core MD97-2121.

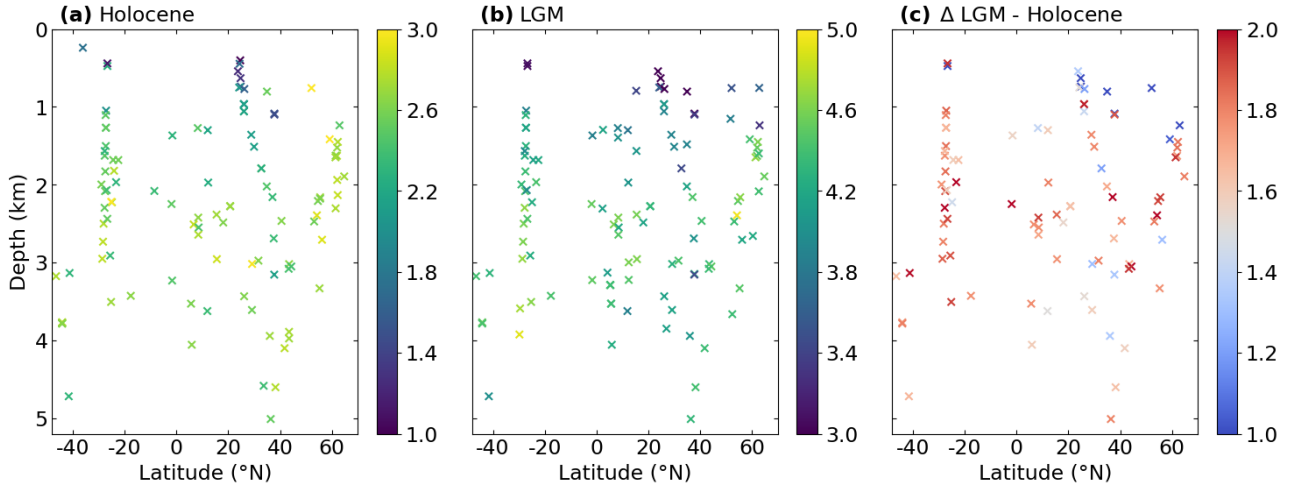

Figure S5.5: $\delta^{18}O_{CaCO3}$ values of the sediment cores found in the Atlantic in the World Atlas database, for the Holocene **(a)**, the LGM **(b)** and the difference between the two **(c)**.

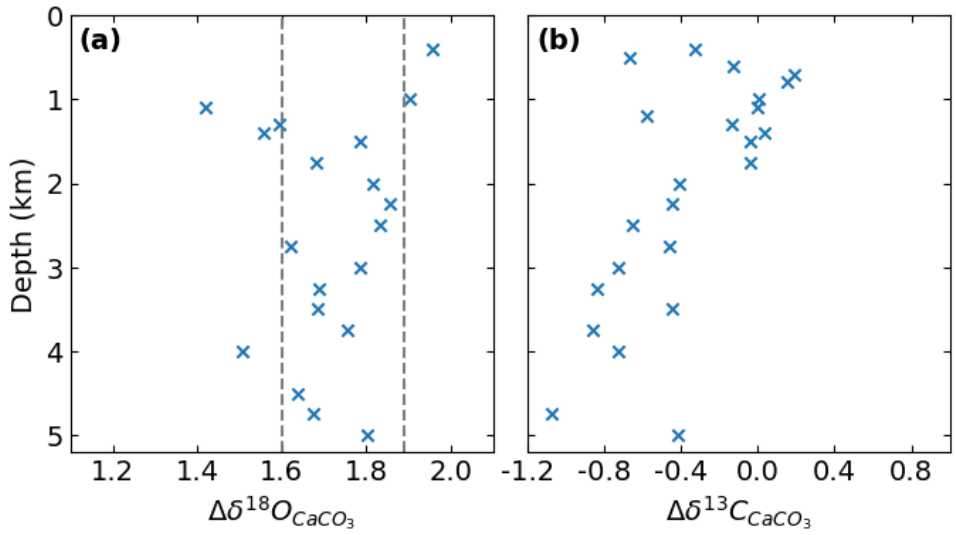

Figure S5.6: Changes in $\delta^{18}O_{CaCO3}$ **(a)** and $\delta^{13}C_{CaCO_3}$ **(b)** between the Holocene and LGM for the the sediment cores found in the Atlantic in the World Atlas database, integrated as a simple depth profile. Grey dashed lines indicate the values that were found for the mid-depth and deep ocean in the previous Atlantic compilation (Figure 5.6).

next logical step to improve the quality of our results. Two basic criterias were imagined to select suitable cores: a minimum sedimentation rate of 5cm/kyr, and a sufficient sampling resolution with at least a point every 3ky through the isotopic record. Some attempts were made to try to measure the "noisiness" of an isotopic record by fitting a GAM through the record, and then measuring the root mean-squared error, but it over-penalized records with many data points, and led to other issues. This thesis did not had time to fully explore the isotopic record processing and age models, but we believe that this is important and that it can lead to significant developments in the automation of generating paleo-climatic reconstructions.

Differences in glacial timing

The LGM $\delta^{18}O_{CaCO3}$ value of an isotopic record is thought to be the most recent $\delta^{18}O_{CaCO3}$ maximum value, even though we refer at a specific time period (19-21ky). Nevertheless, previous studies have shown that the $\delta^{18}O_{CaCO3}$ maximum for deep benthic species could vary across different ocean basins (Lisiecki and Stern, 2016). The idea of looking at possible differences in glacial timing arose after Chapter 2, when the different pathways for the North Atlantic dye to reach the pacific were shown and the resulting long time scale to fill the shadow zone. We wanted to show possible differences in the $\delta^{18}O_{CaCO3}$ glacial timing between the mid-depths and the deep Pacific, but no clear signal with the current isotopic records and age models could be found.

A second idea emerged to show differences in the $\delta^{18}O_{CaCO3}$ glacial timing: using both planktonic and benthic species to show the differences in glacial timing. At first, we wanted to measure the depth difference in the sediment core between the maximum (or LGM) $\delta^{18}O_{CaCO3}$ value between the benthic and planktonic species. However, since the $\delta^{18}O_{CaCO3}$ of planktonic largely reveals temperature patterns, we are not sure that the plantkonic $\delta^{18}O_{CaCO3}$ maximum exactly gives the timing for the LGM. Since we are interested in the difference of glacial timing between the mid-depth and the deep Pacific, we need two cores that are closely located with both benthic and planktonic species. We did the analysis in the cores near New Zealand, and no clear signal could be found. We believe even if a signal was present the bioturbation present in the upper 200cm of the sediment core could not allow us to correctly represent it. In the World Atlas, we did not look yet for closely located mid-depth and deep cores, but the presence of many different foraminifera species for some of the sediment cores means that there must surely be cores validating these conditions.

References

Adkins, J. F., McIntyre, K., & Schrag, D. P. (2002). The salinity, temperature, and $\delta^{18}O$ of the glacial deep ocean. *Science*, *298*(5599), 1769–1773. https://doi.org/10.1126/science.1076252

Barker, S., Greaves, M., & Elderfield, H. (2003). A study of cleaning procedures used for foraminiferal mg/ca paleothermometry. *Geochemistry, Geophysics, Geosystems*, *4*(9). https://doi.org/10.1029/2003GC000559

Blaauw, M., & Christen, J. A. (2011). Flexible paleoclimate age-depth models using an autoregressive gamma process. *Bayesian Analysis*, *6*(3), 457 –474. https://doi.org/10.1214/11-BA618

Boyle, E., & Keigwin, L. (1985). Comparison of atlantic and pacific paleochemical records for the last 215,000 years: Changes in deep ocean circulation and chemical inventories. *Earth and Planetary Science Letters*, *76*(1), 135–150. https://doi.org/10.1016/0012-821X(85)90154-2

Butzin, M., Köhler, P., & Lohmann, G. (2017). Marine radiocarbon reservoir age simulations for the past 50,000 years. *Geophysical Research Letters*, *44*(16), 8473–8480. https://doi.org/10.1002/2017GL074688

Curry, W. B., & Oppo, D. W. (2005). Glacial water mass geometry and the distribution of δ13c of Σco2 in the western atlantic ocean. *Paleoceanography*, *20*(1). https://doi.org/https://doi.org/10.1029/2004PA001021

Duplessy, J.-C., Labeyrie, L., & Waelbroeck, C. (2002). Constraints on the ocean oxygen isotopic enrichment between the last glacial maximum and the holocene: Paleoceanographic implications [EPILOG]. *Quaternary Science Reviews*, *21*(1), 315–330. https://doi.org/10.1016/S0277-3791(01)00107-X

Elderfield, H., Yu, J., Anand, P., Kiefer, T., & Nyland, B. (2006). Calibrations for benthic foraminiferal mg/ca paleothermometry and the carbonate ion hypothesis. *Earth and Planetary Science Letters*, *250*(3), 633–649. https://doi.org/10.1016/j.epsl.2006.07.041

Ferrari, R., Jansen, M. F., Adkins, J. F., Burke, A., Stewart, A. L., & Thompson, A. F. (2014). Antarctic sea ice control on ocean circulation in present and glacial climates. *Proceedings of the National Academy of Sciences*, *111*(24), 8753–8758. https://doi.org/10.1073/pnas.1323922111

Gebbie, G. (2014). How much did glacial north atlantic water shoal? *Paleoceanography*, *29*(3), 190–209. https://doi.org/10.1002/2013PA002557

Gouretski, V., & Koltermann, K. P. (2004). Woce global hydrographic climatology. *Berichte des BSH*, *35*, 1–52.

Gray. (2014). *The role of the north pacific ocean in the deglacial co2 rise: Insights from trace elements and boron isotopes in biogenic carbonates*. University College London. https://books.google.fr/books?id=RImC0AEACAAJ

Gray, de Lavergne, C., Jnglin Wills, R. C., Menviel, L., Spence, P., Holzer, M., Kageyama, M., & Michel, E. (2023). Poleward shift in the southern hemisphere westerly winds synchronous with the deglacial rise in co2 [e2023PA004666 2023PA004666]. *Paleoceanography and Paleoclimatology*, *38*(7), e2023PA004666. https://doi.org/10.1029/2023PA004666

Hoogakker, B., Elderfield, H., Oliver, K., & Crowhurst, S. (2010). Benthic foraminiferal oxygen isotope offsets over the last glacial-interglacial cycle. *Paleoceanography*, *25*(4). https://doi.org/10.1029/2009PA001870

Hoogakker, B. A. A., Elderfield, H., Schmiedl, G., McCave, I. N., & Rickaby, R. E. M. (2015). Glacial–interglacial changes in bottom-water oxygen content on the portuguese margin. *Nature Geoscience*, *8*(1), 40–43. https://doi.org/10.1038/ngeo2317

Keigwin, L. D. (1998). Glacial-age hydrography of the far northwest pacific ocean. *Paleoceanography*, *13*(4), 323–339. https://doi.org/10.1029/98PA00874

Key, R. M., Kozyr, A., Sabine, C., Lee, K., Wanninkhof, R., Bullister, J., Feely, R., Milero, F., Mordy, C., & Peng, T.-H. (2004). A global ocean carbon climatology: Results from global data

analysis project (glodap). *Global Biogeochemical Cycles*, *18*(4), GB4031. https://doi.org/10.1029/2004GB002247

Kwon, E. Y., Hain, M. P., Sigman, D. M., Galbraith, E. D., Sarmiento, J. L., & Toggweiler, J. R. (2012). North atlantic ventilation of "southern-sourced" deep water in the glacial ocean. *Paleoceanography*, *27*(2). https://doi.org/10.1029/2011PA002211

LeGrande, A. N., & Schmidt. (2006). Global gridded data set of the oxygen isotopic composition in seawater. *Geophysical Research Letters*, *33*(12). https://doi.org/10.1029/2006GL026011

Lisiecki, L. E., & Stern, J. V. (2016). Regional and global benthic δ18o stacks for the last glacial cycle. *Paleoceanography*, *31*(10), 1368–1394. https://doi.org/10.1002/2016PA003002

Marchitto, T., Curry, W., Lynch-Stieglitz, J., Bryan, S., Cobb, K., & Lund, D. (2014). Improved oxygen isotope temperature calibrations for cosmopolitan benthic foraminifera. *Geochimica et Cosmochimica Acta*, *130*, 1–11. https://doi.org/10.1016/j.gca.2013.12.034

Matsumoto, K., Oba, T., Lynch-Stieglitz, J., & Yamamoto, H. (2002). Interior hydrography and circulation of the glacial pacific ocean. *Quaternary Science Reviews*, *21*(14), 1693–1704. https://doi.org/10.1016/S0277-3791(01)00142-1

Misra, S., Greaves, M., Owen, R., Kerr, J., Elmore, A. C., & Elderfield, H. (2014). Determination of b/ca of natural carbonates by hr-icp-ms. *Geochemistry, Geophysics, Geosystems*, *15*(4), 1617–1628. https://doi.org/10.1002/2013GC005049

Mulitza, S., Bickert, T., Bostock, H. C., Chiessi, C. M., Donner, B., Govin, A., Harada, N., Huang, E., Johnstone, H., Kuhnert, H., Langner, M., Lamy, F., Lembke-Jene, L., Lisiecki, L., Lynch-Stieglitz, J., Max, L., Mohtadi, M., Mollenhauer, G., Muglia, J., … Tiedemann, R. (2022). World atlas of late quaternary foraminiferal oxygen and carbon isotope ratios. *Earth System Science Data*, *14*(6), 2553–2611. https://doi.org/10.5194/essd-14-2553-2022

Olsen, A., Key, R. M., van Heuven, S., Lauvset, S. K., Velo, A., Lin, X., Schirnick, C., Kozyr, A., Tanhua, T., Hoppema, M., Jutterström, S., Steinfeldt, R., Jeansson, E., Ishii, M., Pérez, F. F., & Suzuki, T. (2016). The global ocean data analysis project version 2 (glodapv2) – an internally consistent data product for the world ocean. *Earth System Science Data*, *8*(2), 297–323. https://doi.org/10.5194/essd-8-297-2016

Rae, J. W. B., Gray, W. R., Wills, R. C. J., Eisenman, I., Fitzhugh, B., Fotheringham, M., Littley, E. F. M., Rafter, P. A., Rees-Owen, R., Ridgwell, A., Taylor, B., & Burke, A. (2020). Overturning circulation, nutrient limitation, and warming in the glacial north pacific. *Science Advances*, *6*(50), eabd1654. https://doi.org/10.1126/sciadv.abd1654

Sarmiento, J. L., Gruber, N., Brzezinski, M. A., & Dunne, J. P. (2004). High-latitude controls of thermocline nutrients and low latitude biological productivity. *Nature*, *427*(6969), 56–60. https://doi.org/10.1038/nature02127

Stewart, J. A., Christopher, S. J., Kucklick, J. R., Bordier, L., Chalk, T. B., Dapoigny, A., Douville, E., Foster, G. L., Gray, W. R., Greenop, R., Gutjahr, M., Hemsing, F., Henehan, M. J., Holdship, P., Hsieh, Y.-T., Kolevica, A., Lin, Y.-P., Mawbey, E. M., Rae, J. W. B., … Day, R. D. (2021). Nist rm 8301 boron isotopes in marine carbonate (simulated coral and foraminifera solutions): Inter-laboratory δ11b and trace element ratio value assign-

ment. *Geostandards and Geoanalytical Research*, *45*(1), 77–96. https://doi.org/10.1111/ggr.12363

Waelbroeck, C., Labeyrie, L., Michel, E., Duplessy, J., McManus, J., Lambeck, K., Balbon, E., & Labracherie, M. (2002). Sea-level and deep water temperature changes derived from benthic foraminifera isotopic records [EPILOG]. *Quaternary Science Reviews*, *21*(1), 295–305. https://doi.org/https://doi.org/10.1016/S0277-3791(01)00101-9

Waelbroeck, C., Lougheed, B. C., Vazquez Riveiros, N., Missiaen, L., Pedro, J., Dokken, T., Hajdas, I., Wacker, L., Abbott, P., Dumoulin, J.-P., et al. (2019). Consistently dated atlantic sediment cores over the last 40 thousand years. *Scientific data*, *6*(1), 165.

Weiss, R., Östlund, H., & Craig, H. (1979). Geochemical studies of the weddell sea. *Deep Sea Research Part A. Oceanographic Research Papers*, *26*(10), 1093–1120. https://doi.org/10.1016/0198-0149(79)90059-1

Williams, T. J., Hillenbrand, C.-D., Piotrowski, A. M., Allen, C. S., Frederichs, T., Smith, J. A., Ehrmann, W., & Hodell, D. A. (2019). Paleocirculation and ventilation history of southern ocean sourced deep water masses during the last 800,000 years. *Paleoceanography and Paleoclimatology*, *34*(5), 833–852. https://doi.org/10.1029/2018PA003472

Wunsch, C. (2016). Pore fluids and the lgm ocean salinity—reconsidered. *Quaternary Science Reviews*, *135*, 154–170. https://doi.org/10.1016/j.quascirev.2016.01.015

Yu, J., Day, J., Greaves, M., & Elderfield, H. (2005). Determination of multiple element/calcium ratios in foraminiferal calcite by quadrupole icp-ms. *Geochemistry, Geophysics, Geosystems*, *6*(8). https://doi.org/10.1029/2005GC000964

CONCLUSION

This thesis explored the processes influencing the ventilation of the deep Pacific and their representation in the OGCM NEMO. Here we propose an answer to the three questions studied in this thesis:

1. What are the processes and pathways of Pacific deep ventilation?
2. What do oxygen isotope observations tell about ventilation of the modern ocean ($\delta^{18}O_{sw}$) and ventilation of the LGM ocean ($\delta^{18}O_{CaCO_3}$)?
3. How well is the modern ocean ventilation represented in OGCMs? Which aspects of OGCMs need to be improved to accurately model the ventilation of the deep Pacific Ocean?

Processes and pathways of deep ventilation in the Pacific: a snail race between isopycnal and diapycnal diffusion

Isopycnal diffusion plays a major role in ventilating the mid-depths (1.5-3 km) of the Pacific. In the abyss, AABW flows northward, upwells and returns back toward the south under the influence of diapycnal diffusion and geothermal heating. Chapter I highlighted an upwelling pathway of tracers from the abyss to the surface in the subarctic Pacific. This upwelling seems to have the largest influence in ventilating the mid-depths north of 35°N. Likely candidates to explain this tracer upwelling are diapycnal mixing and wind-driven upwelling. No firm answer emerged from our study on their respective roles and future work is needed on this aspect.

It was hypothesized in Chapter I that the location of the radiocarbon minimum in the Pacific, which corresponds to the oldest waters in the global ocean, was determined by this combined influence of (1) ventilation by isopycnal diffusion from the south, in the mid-depths and (2) ventilation through tracer upwelling along the northern boundary of the Pacific. The different mixing parameterizations used in NEMO in Chapter II confirmed that the location of the age maximum depends on both isopycnal and diapycnal diffusion. The waters of the deep Pacific are thus ventilated through a balance between isopycnal mixing and diapycnal transports.

Modern conservative tracer distributions are quasi-uniform in the modern deep Pacific. However, the potential of isopycnal diffusion at mid-depths for setting strong tracer gradients in the deep Pacific is shown through the passive tracer representing waters originating from the North Atlantic. Precisely, these tracer differences might have occurred during the LGM, as a clear $\delta^{18}O_{CaCO_3}$ maximum is observed in the North Pacific. The glacial geochemical evidence suggests a stronger layering of the waters during the LGM, with less connection between the abyss and the mid-depths of the Pacific (although, as detailed below, evidence for such changes in the South Pacific is lacking). Interestingly, a density bias in the NADW in our modern NEMO simulations results in a more layered ocean, and suggests a relative disconnection between NADW and AABW water masses is possible even with a small density difference between the two. Overall, our results show the potential of isopycnal diffusion to dominate mid-depth Pacific ventilation under a different climate state.

Constraints on modern and past ocean ventilation using oxygen isotopes

The oxygen isotope ratio of the seawater exhibits large differences between the two major contributors to deep ocean ventilation: AABW and NADW. The difference in their isotopic signature allows for simple reconstructions on their relative contributions in the Southern Ocean. A persistent $\delta^{18}O_{sw}$ maximum is observed throughout the whole Southern Ocean at mid-densities. Moreover, we show that more systematic sampling in the Indian and Pacific basins could help constrain mixing of the Southern Ocean waters as they flow and diffuse in the Indian and Pacific basins. The role that this tracer could play in measuring the penetration of intermediate waters into the ocean has not been fully explored, but could be of major interest. Targeted sampling campaigns zonally in the Southern Ocean and meridionally in the Pacific and Indian could help constrain the patterns and mechanisms of ocean ventilation.

Whether a $\delta^{18}O_{CaCO3}$ gradient exists between the two deep water masses during the LGM remains uncertain. Initially, the observed mid-depth $\delta^{18}O_{CaCO3}$ maximum in the North Pacific advocated for a significant difference between the water masses in the South Pacific. Reconstructions of bottom water temperatures, using trace elements, further support that the observed signal is principally linked to a change in the $\delta^{18}O_{sw}$ profile. However, through systematic exploration across different databases, and the analysis of relevant sediment cores, we do not obtain clear evidence for a $\delta^{18}O_{CaCO3}$ maximum in the South Pacific, required to explain the North Pacific $\delta^{18}O_{CaCO3}$ maximum via diffusion at mid-depths.

Moreover, the analysis of relevant sediment cores show that significant differences may not exist in the $\delta^{18}O_{CaCO3}$ of glacial deep end-members. Uncertainties associated to glacial fractions at the sediment core locations, on top of experimental, sampling and analytical uncertainties further limit this study. We emphasize that the creation of methods to use emerging paleoceanographic data in a systematic way, may be the only way to overcome these inherent hurdles. In Chapter V, we use an Atlantic sediment core compilation to show that the change in $\delta^{18}O_{CaCO3}$ from Holocene to the LGM also holds interesting information and either indicates a change in the glacial temperature gradient relative to present, or that the glacial NADW core was shallower and centered at 2 km depth. Furthermore, the strong glacial intermediate $\delta^{18}O_{sw}$ signal in the North Pacific advocates for an expansion of the glacial NPIW. Finding appropriate sediment cores to study the reach and extent of this glacial water mass might be key to infer changes in the glacial biogechemical cycling.

How well is the modern ocean ventilation represented in OGCMs? Which aspects of OGCMs need to be improved to accurately model the deep Pacific Ocean ventilation?

In Chapter II, we compared a global configuration of the NEMO general circulation model to two data-constrained inverse models, focusing on steady-state ventilation patterns and rates. More precisely, we examined the volumes ventilated by different surface regions and the ideal age distribution of the three model oceans. The three models share several important features, among which the global ventilation volumes: the North Atlantic (north of 30°N), and the Antarctic marginal seas ventilate about a third of the whole ocean volume each; and the Southern Ocean region where the Antarctic intermediate waters and Subantarctic mode waters are formed ventilates about a fifth. In addition, the three models show that it takes about twice the maximum age to actually renew the water at a specific location, which has major implications for

tracer equilibrium. However, major differences between the models exist and reveal important biases and unknowns:

- Ideal ages are consistently higher in the NEMO simulations than in the inverse model states. State-of-the-art maps of isopycnal and diapycnal mixing result in a maximum ideal age in the Pacific over twice the one of the inverse model estimates. A widespread underestimate of both isopycnal and diapycnal mixing rates in the deep ocean of NEMO is deemed likely. A misrepresentation of subarctic Pacific upwelling is likely another key factor for the overestimated age in the North Pacific.

- The numerical dyes diffuse more across the isopycnals in the inverse models than in NEMO. Whether it is related to an overestimation of diapycnal diffusion in the inverse models or only an underestimation in NEMO remains unknown.

Additionally, we showed the impact of isopycnal mixing on tracer distribution, especially in the Southern Ocean where it seems to control to some extent the return path to the surface of deep waters. Overall, NEMO better represents ventilation patterns than ventilation rates. The inability of NEMO to correctly represent ocean ventilation seems to be partly linked to a misrepresentation of turbulent mixing in the ocean and calls for better parameterizations of mixing in the ocean.

The temperatures of the upper 2 km in the subarctic Pacific are poorly represented in NEMO. The Kuroshio boundary current seems to be poorly represented, which, combined with biases in the isopycnal mixing scheme, contributes to this temperature bias. This results in a misrepresentation of the NPIW density and penetration, which is key for biogeochemical cycling in the North Pacific Ocean.

Perspectives

The answers given to the different questions during the thesis, also led to interesting perspectives.

Firstly, key processes in NEMO seem to be badly represented and deserve more attention. When the best mixing parameterizations are implemented in this state-of-the-art ocean model, the maximum of age in the Pacific is correctly located, but the waters are twice as old as the one inferred from the observations. Characterizing what the model is missing to correctly represent ages in the Pacific seems to be a crucial step to our understanding of ocean ventilation.

This thesis highlighted the return path of abyssal tracers to the subarctic Pacific surface. I pointed out in turn the winds or diapycnal mixing to drive this return to the surface, but no consensus could be made on the role of each one. The study of the contribution on each of these mechanisms to tracers upwelling may be key to correctly represent the biogeochemistry of the North Pacific. The sensitivity of this upwelling to the winds has not been tested here, but should provide useful information for the modern and the glacial climate state.

Additionally, the $\delta^{18}O_{sw}$ climatology produced during this thesis could be subject to several improvements. First, separating the surface patch of the low latitudes into three patches, one for each basin, would help representing the regional differences. Second, the product could benefit from distinguishing key regions such as the Mediterranean or the Labrador Sea to better represent the deep Atlantic structure. Third, the deep averaged error of the product relative to the observation below 1.5 km is of about ~ 0.1‰. The analysis that led to the construction of this product showed roughly similar, if not greater, discrepancies

between the data produced in different laboratories, so that it might prove difficult to further lower the error associated to the reconstruction without accounting for this. Finding a method to systematically account for inter-laboratories offset might be the most critical aspect to further improve the product.

Finally, the part that leaves the most doors open is surely the glacial one. The increased number of sediment cores that are becoming available with isotopic records and associated age models leaves room for numerous studies. One of the most interesting one might be the study of the different "time lags" between isotopic signals. Indeed, we saw that the tracers roughly takes about twice the ideal age to equilibrate. Then in the North Pacific mid-depths, where the oldest waters are located, the maximum glacial $\delta^{18}O_{CaCO_3}$ value might occurs several millennias after the glacial deep water masses get their heaviest value. More generally, the "lag" between the time the deep end-members get their maximum value and the time that the different places of the ocean get their maximum value, might indicate ventilation rates of the glacial ocean. I believe that improving the generation of age models, and more generally, methods to treat systematically sediment cores records is the logical next step to reconstruct glacial ocean ventilation.